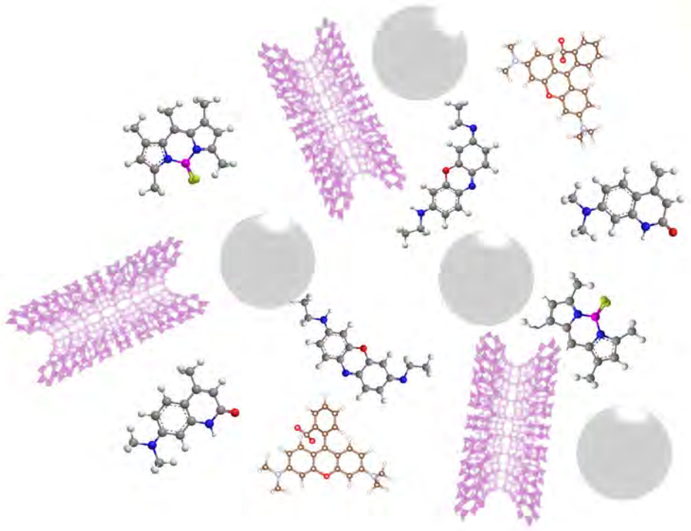

The scope of this thesis deals is the development and description of photoactive nanomaterials and novel multichromophoric arrays as artificial antenna systems. To this aim, the photophysical signatures of luminescent fluorophores (with absorption and emission at different regions of the visible electromagnetic spectrum) encapsulated into inorganic and organic hosts, or assembled in supramolecular structures have been exhaustively characterized. These systems are able to harvest the light over a broad spectral region (ultraviolet-visible) and transfer it to the target place and with a specific energy via successive energy transfer hops. As consequence the excitation can be performed far away from the emission region, improving the photostability of the acceptor emitting dye and lowering the background interferences.

In pursuit of such antennas, different alternatives have been considered, (i) Hybrid materials based on LTL zeolites doped with laser dyes working in the blue, green or red parts of the visible. (ii) Latex nanoparticles doped simultaneously with luminescent fluorophores, leading to stable aqueous colloids. (iii) Molecular cassettes based on energy donor and acceptor dyes covalently linked. All of them undergoing efficient and tunable energy transfer processes, the key factor for a successful development of luminescent antennas.

In conclusion, the herein reported approaches (photoactive materials and novel dyes) towards the development of luminescent antennas are shown to be properly applied in photonic fields such as tunable dye lasers, light modulators or polarity probes.

Molecular Antennas and Photoactive Nanomaterials based on Energy Transfer Processes
Leire Gartzia Rivero 2014

ZTF-FCT
Zientzia eta Teknologia Fakultatea
Facultad de Ciencia y Tecnología

Molecular Antennas and Photoactive Nanomaterials based on Energy Transfer Processes

Leire Gartzia Rivero

Leioa, 2014

eman ta zabal zazu
Universidad del País Vasco
Euskal Herriko Unibertsitatea

Universidad del País Vasco
Euskal Herriko Unibertsitatea

ZTF-FCT
Zientzia eta Teknologia Fakultatea
Facultad de Ciencia y Tecnología

Kimika Fisikoko Saila

Molecular Antennas and Photoactive Nanomaterials based on Energy Transfer Processes

DOCTORAL THESIS

Thesis report submitted by

Leire Gartzia Rivero

for the degree of Doctor

with "INTERNATIONAL DOCTORATE" mention

Supervisors: Dr. Jorge Bañuelos Prieto and Prof. Iñigo López Arbeloa.

Leioa, December 2014

- *Euskal Herriko Unibertsitateko (UPV/EHU) Argitalpen Zerbitzua*
- University of the Basque Country (UPV/EHU) Press
- **ISBN: 978-84-9082-227-2**

e-mail: leire.gartzia@ehu.eus

Gu sortu ginen enbor beretik sortuko dira besteak

(Xabier Lete)

AGRADECIMIENTOS

Lo que en realidad importa es que al final del viaje uno acaba dándose cuenta de que a pesar de haber sido duro merece la pena haberlo recorrido, y mucho. Por ello, en primer lugar querría agradecer a mis directores de tesis Jorge e Iñigo el haber sido las brújulas que han sabido guiarme a través del tiempo y el espacio, dejándome libertad siempre que ha sido necesario. Esto ha permitido dar forma a mis inquietudes mediante los conocimientos que he ido adquiriendo día a día, y a su vez han contribuido a mi desarrollo como científica, por eso y por otras muchas cosas más siempre les estaré agradecida.

También querría dar las gracias al Gobierno Vasco por la concesión de la beca predoctoral, dado que sin ella nada de esto hubiese sido posible. Además, no quisiera olvidarme de los Servicios Generales de la Facultad de Ciencia y Tecnología de la UPV/EHU (SGIKER) por las medidas tan valiosas para el desarrollo de mi tesis.

Además, no me gustaría olvidarme de todos aquellos que fueron partícipes de mi estancia en Fribourg (Suiza), que aunque fuese corta no por eso fue menos intensa. En primer lugar quisiera agradecer al Prof. Peter Belser y todo su grupo (André y Pengpeng) por acogerme con los brazos abiertos en la Facultad de Química de la "Université de Fribourg". Lo que más admiro en él es que pese a su inminente retirada tras toda una vida dedicada la ciencia y la investigación seguía conservando ese brillo especial en sus ojos, sobre todo cuando surgían nuevos enigmas y preguntas sin respuesta.

De hecho, eso es lo que más me fascina de las personas, que sigan manteniendo esa ilusión por saber y descubrir, esa inquietud que emana a borbotones cuando somos niños, pero que poco a poco parece ir diluyéndose con el paso de los años. Por eso, espero conservarla toda mi vida!

No podía faltar la mención a mis compañeras de laboratorio y digo compañeras porque somos mayoría, aunque en realidad pueda referirme a ellas como amigas. A todos y todas, Virginia, Hegoi, Ixone, Nerea, Rebeca, Edu y Teresa, mil gracias por ayudarme y haber hecho que pueda guardar un recuerdo inolvidable de esta etapa de mi vida.

Por su puesto a mis amigas incondicionales, compañeras de carrera, doctorado y del día a día, Eider, Mireia eta Arantza. Eskerrik asko neskak! hamar urte pase dire ia ibilaldi hau hasi gendunetik eta emoten deu atzo izen zala. Bidai hau amaitzear dauela pentse arren badakizue beste horrenbeste ibilbide barri geratzen iakuzela alkarregaz.

Amaitzeko, zelan ez, nire eredu zarien familize, lagunek eta Aitorreri, zueri danori nire eskerrik beroenak ezinbestekoak zarielako nire eguneroko bizizen.

Danontzat mosu handi bana eta besarkada itzela.

ABSTRACT

The herein presented thesis deals with the development and study of photoactive nanomaterials and novel multichromophoric arrays for the obtention of artificial antenna systems. To this aim, a wide variety of luminescent fluorophores have been encapsulated into either inorganic or organic hosts, as well as molecular systems based on scaffolding of laser dyes have been photophysically characterized. The main goal is to design systems which harvest the light over a broad spectral region (in particular the ultraviolet-visible section of the electromagnetic spectrum) and transfer it to the target place and with a desired energy via successive energy transfer hops. As a result, the photostability of the system is ameliorated, since the emitting dye can be indirectly excited. Besides, the possibility of monitoring the emission far away from the excitation avoids background interferences and enhances the detection sensitivity. To this purpose, three different approaches have been considered to develop luminiscent antenna systems:

- Hybrid materials via the occlusion of laser dyes with absorption and emission signatures in the blue (oxazols and carbostyryls), green (BODIPY) or red-edge (oxazines) of the visible, into the nanochannels of the aluminosilicate LTL zeolite, synthesized under microwave heating. As a result, supramolecularly organized photoactive materials are obtained, providing red emission, regardless of the excitation wavelength, or alternatively white-light emission is achievable, by means of Förster-type energy transfer process modulation, which takes place among the encapsulated dyes.
- Dye-doped latex nanoparticles (NPs) in which luminescent fluorophores (rhodamine and oxazine) undergoing intermolecular energy transfer processes are encapsulated. The confinement ensures proximity between dyes and hugely enhances the efficiency of such process, which is also tunable, and at the same time, protects the dye and increases its photostability. As consequence, these aqueous colloids outstand by their bright emission in the long-wavelength part of the visible, regardless of the pumping wavelength.
- Molecular antennas where the donor and acceptor dyes (BODIPYs and rhodamine) are covalently linked through a spacer. The energy transfer is intramolecular and highly efficient (approaching the 100%), due to the promotion of an ultrarapid through-bond mechanism (femtosecond scale). The molecular design plays a key role in the development of these “cassettes”, which also present very high laser efficiencies in the less energetic part of the visible.

The photophysical signatures of all these photoactive materials and dyes have been deeply analyzed and characterized by spectroscopic techniques (light absorption and fluorescence emission, in steady-state and time-correlated in the picoseconds scale) as well as by fluorescence microscopy, which allows the analysis at the single particle level.

Summing up, during this thesis different strategies have been conducted towards the development of luminescent antennas (based on photoactive materials and novel dyes) in which the most convenient alternative can be finely selected for each photonic application field, as tunable dye lasers, light modulators or polarity probes.

LABURPENA

Tesi honetan, sistema antena artifizialak lortzeko hainbat nanomaterial fotoaktibo eta egitura multikromoforiko berritzaile garatu dira. Horretarako, mota ezberdineko fluroforo luminiszenteak matrize organiko zein inorganikoetan barneratu dira. Aldi berean, sistema molekular anitzak eraikitzeko bereziki aukeratutako laser koloratzaileak bateratu dira lotura kobalente sendoen bitartez. Helburu nagusia zera da: espektro eremu zabalean ahalik eta argi kantitate handiena biltzeko gai diren sistemak diseinatzea (zehazki espektro elektromagnetikoaren ultramore-ikusgai eremuan); ondoz ondoko energia transferentzia jarrai baten bidez, energia zehatza behar den tokira garraiatzeko ahamena duten sistemak, hain zuzen. Horren ondorioz, sistemaren fotoestabilitatea nabarmen hobetzen da, izan ere, argia igortzen duen kromoforoa zeharka kitzikatzeko aukera dago. Gainera, emisioa kitzikapen iturritik urrun erregistratu daitekeenez, inguruko interferentziak ekiditen dira; eta ondorioz, detekzio-sentikortasuna areagotu daiteke. Asmo honekin, antena optikoen garapena ahalbidetzeko hiru hurbilketa hausnartu dira:

- Material hibridoak: LTL-zeolita aluminosilikatoaren (mikrouhinen bitartez sintetizatua) nano-kanalak eremu ikusgaiaren esparru ezberdinetan xurgatu eta emititzen duten laser-koloratzaile sorta batez dopatu dira. Esparru urdinerako (oxazol eta karboestiriloak), berderako (BODIPY-ak) eta gorrirako (oxazinak) beharrezko fluoroforoak aukeratuz. Modu horretan, lorturiko material fotoaktiboak ordenamendu supramolekularra aurkezten du. Eta Förster motako transferentzia intermolekularra kontrolatuz gero, emisioa sintonizatu daiteke argi gorria lortuz; edota ikusgai guztia estaltzen duten bandak (urdina, berdea eta gorria) agerrarazi daitezke, argi zuria eskuratuz.
- Koloratzaileez dopaturiko latex nanopartikulak (NP): energia transferentzia prozesuarekiko sentikorrak diren fluoroforo luminiszenteak (errodamina eta nile urdina) latex NP-etan barneratu dira. Molekulak konfinatzean, koloratzailea babestu eta bere fotoestabilitatea areagotzeaz gain, elkarrekiko distantzia nabarmen murriztu egiten da; eta ondorioz, prozesuaren eraginkortasuna hobetu. Hartara, kitzikapena edozein izanda ere, koloide urtsu hauek ikusgaiaren gune gorrian igorpen distiratsua dutelako nabarmentzen dira.
- Antena molekularrak: energia emateko eta hartzeko gai diren kromoforoak (BODIPY-ak eta errodaminak) modu kobalentean lotzen dira tartekari batez bidez. Kasu honetan, energia transferentzia molekula barneko lotura bidez gertatzen da eta oso eraginkorra da; izan ere, prozesua lotura mekanismo ultra-azkar (femtosegundu eskalan) batek bideratuta gertatzen da. Hori dela eta, diseinu molekularrak ezinbesteko rol-a jokatzen du “cassette” hauen garapenean. Gainera, aipatutako diseinuak laser efizientzia nabarmenak aurkezten dituzte ikusgaiaren energia gutxieneko esparruan.

Garatutako fluoroforo eta material fotoaktiben ezaugarri fotofisikoen analisia eta karakterizazioa hainbat teknika espektroskopikoren bidez burutzeaz gain, (argi absortzioa eta fluoreszentziaren igorpena, egoera geldikorrean eta denboran zehar ebatzitakoa), fluoreszentziazko mikroskopiaren bidez aztertu da. Modu horretan partikula bakarreko eskalan lan egiteko aukera izanik.

Laburbilduz, tesian zehar antena luminiszenteak (koloratzaile eta material fotoaktiboetan oinarrituta) eraikitzeko helburua lortzeko hainbat estrategia ezberdin garatu dira. Eta ondoren, estrategia egokiena aukeratu da beharrezkoa den erabilera fotoniko bakoitzerako, hala nola, laser koloratzaileak, argi sintonizagarriak, edota polaritaterako zundak.

RESUMEN

La presente memoria trata sobre el desarrollo de nanomateriales fotoactivos, mediante la encapsulación de fluoróforos en soportes inorgánicos u orgánicos, y el estudio de sistemas multicromóforicos, todos ellos con propiedades antena. El objetivo principal que se persigue es diseñar sistemas capaces de captar luz a lo largo de una amplia región espectral (concretamente la zona ultravioleta-visible del espectro electromagnético) y transferirla al lugar deseado y con la energía requerida mediante sucesivos procesos de transferencia de energía. De esta manera se aumenta la fotoestabilidad del sistema porque el colorante emisor de luz no tiene porque ser directamente excitado y se mejora la sensibilidad en la detección ya que se evitan interferencias al tener la zona de monitorización alejada de la excitación. A tal fin, se han considerado tres alternativas para desarrollar sistemas antena:

- Materiales híbridos mediante la inserción de colorantes con absorción y emisión en la región azul (oxazoles y carboestirilos), verde (BODIPY) o roja (oxacinas) del visible en los nanocanales del aluminosilicato conocido como zeolita L, sintetizado por microondas. Como consecuencia se ha desarrollado un material fotoactivo y altamente ordenado que da lugar a emisión roja, independientemente de la longitud de onda de excitación, o blanca, en base a la modulación de la eficiencia del proceso de transferencia de energía via Förster que tiene lugar.
- Nanopartículas de latex dopadas donde se encapsulan colorantes susceptibles de dar lugar a procesos de transferencia de energía intermolecular (rodamina y oxacina). El confinamiento aumenta enormemente la eficiencia de dicho proceso, que también se puede modular, a la vez que protege el colorante y aumenta su fotoestabilidad. Como consecuencia, estos coloides acuosos se caracterizan por una fuerte emisión láser en la región roja del visible, independientemente de la energía de bombeo.
- Antenas moleculares donde los colorantes dadores y aceptores de energía (BODIPYs y rodamina) están unidos covalentemente mediante un espaciador. La transferencia de energía es intramolecular y altamente eficiente (prácticamente del 100%), ya que se promueve un mecanismo a través del enlace que es ultrarápido (escala de femtosegundos). El diseño molecular previo es esencial en estos “cassettes”, que han mostrado también altas ganancias láser en la región menos energética del visible.

Las propiedades fotofísicas de todos estos materiales y colorantes se han estudiado en profundidad tanto con técnicas espectroscópicas (absorción y emisión fluorescente de luz, en estado estacionario y resuelto en el tiempo en la escala de picosegundos) como por microscopía fluorescente, que permite estudios a nivel de partículas individuales.

Por tanto, se han desarrollado diversas alternativas para la obtención de sistemas antena (bien sean materiales o colorantes) y así poder elegir la más conveniente para su posterior aplicación fotónica como láseres sintonizables de colorante, moduladores de luz o sensores de polaridad.

Table of contents

INTRODUCTION

Sunlight plays an essential role in the daily life of the living organisms inhabiting the earth: all food we eat and all fossil fuels we use as energy sources are a product of photosynthesis, the most sophisticated and important solar energy storage system in the nature. The photosynthetic organisms (plants, algae and a variety of types of bacteria) utilize sunlight to power cellular processes and ultimately derive most or all of their biomass through chemical reactions driven by light. In this process, the light is absorbed by an antenna system of a few hundred chlorophyll molecules arranged in a protein environment (Figure 1) which allows a fast energy transfer from an electronically excited molecule to unexcited neighbour molecules in a way that the excitation energy reaches a specific reaction centre where optical energy is converted to chemical energy [1-6]. The proteins, acting as a host material for the pigments, keep them in a well defined orientation, at short intermolecular distance, and prevent them from forming aggregates, three main prerequisites for fast and efficient radiationless energy transfer. In other words, the very high efficiency of natural photosynthesis is a consequence of the well-defined organization of a multitude of chromophores with distinct optical and redox properties that facilitate the efficient capture of visible light and the subsequent transfer of excitation energy.

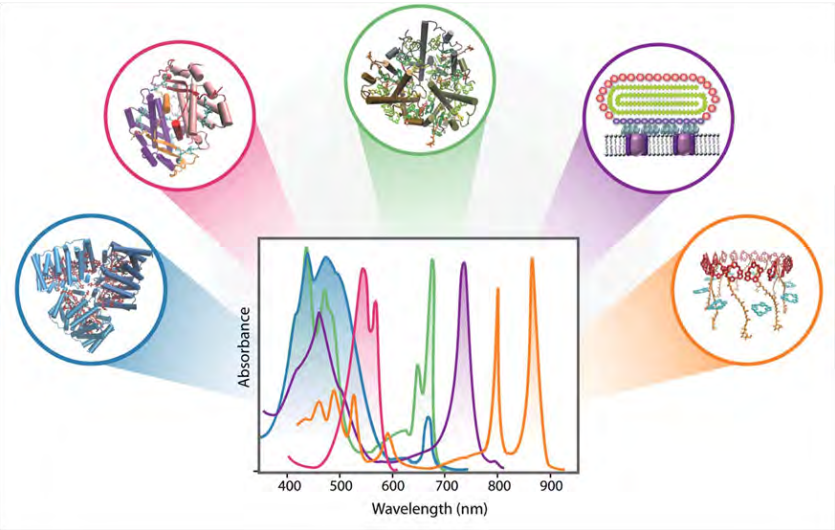

Figure 1. Diversity in light-harvesting antenna systems commonly encountered in photosynthetic organisms, which vary widely in their protein structure and the number and arrangement of pigments utilized. Their respective absorption spectra, shown in matching colours, illustrate how different organisms have evolved to optimize their light-harvesting capabilities in different regions of the visible spectrum. Picture taken from ref [1].

One of the most fascinating topics of the modern photochemistry is the design and construction of artificial photonic antenna systems capable of harvesting and transporting the light to an acceptor component with the desired energy, mimicking the natural process of photosynthesis [7-10]. The excitation energy transfer emerges as one of the key factors ruling the effectiveness of the process. Thus, this implies a profound understanding of the parameters affecting the energy transfer efficiency, such as interchromophore distances and their relative orientations, as well as the exact ratio of donors and acceptors [11]. The fine control of all these factors opens the door to the development of efficient and competitive artificial antenna systems with a huge number of applications. Many imaginative attempts have been tested to build artificial photonic antennas, among them luminescent metal complexes [12,13], dyes in polymer matrices [14,15], dendrimers [16-19], DNA nanoscaffolds [20] and host-guest systems [21,22].

The unique properties and versatility of these artificial antennas make them suitable for developing dye-sensitized solar cells [23-26] and luminescent solar concentrators (LSC) [27,28] with improved absorption capability, increased efficiencies and reduction of the costs. The most popular solar cells on the market are based on crystalline silicon and although their high energy conversion, they show very low absorbance in the visible spectral range, which induces the need of a certain thickness (in the order of 300 micrometer) for absorption of long wavelength light, which raises the price of the device [29]. Some attempts have been accomplished to increase the efficiency by light trapping in thin solar cells [30,31]. Other alternative can be found in dye sensitized solar cells in which the charge separation process performed in the semiconductor is associated to the light absorption by a dye or an antenna system (Figure 2).

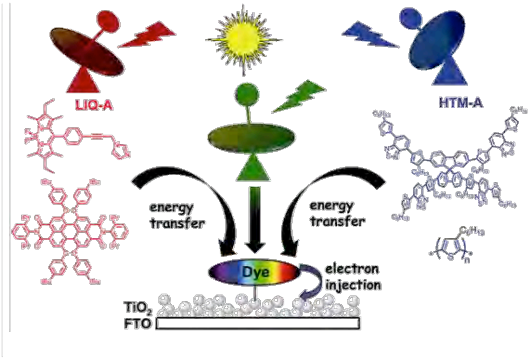

Figure 2. Bio-inspired artificial light-harvesting antennas in dye-sensitized solar cells. Picture taken from ref [32]

Nevertheless, if the light is first absorbed by an artificial antenna system in the UV-Vis range of the electromagnetic spectrum (where the silicon hardly absorbs light) and then transferred radiationless to silicon, a very thin silicon layer would be sufficient, reducing the costs and ameliorating the light absorption capability [32,33].

Moreover, the antenna systems are found as a new approach for solving an old problem of LSC. The simplest version of an LSC is a glass or plastic substrate doped with organic dyes where the incident photons are absorbed by the fluorophores and re-emitted by these centers at a red-shifted wavelength [34]. A fraction of the luminescent light is trapped by total reflection and guided to the edges of the plate, at which is converted to electricity by a photovoltaic device (Figure 3). However, there are several drawbacks affecting their efficiency: e.g. limited stability of the luminescent organic species, high self-absorption, and poor photostability. These handicaps can be overcome by antenna materials undergoing excitation energy transfer processes [35]. That is, the spectral overlap between light absorption and emission is reduced, decreasing the self-absorption and enhancing the photostability by means of indirect excitation of the acceptors.

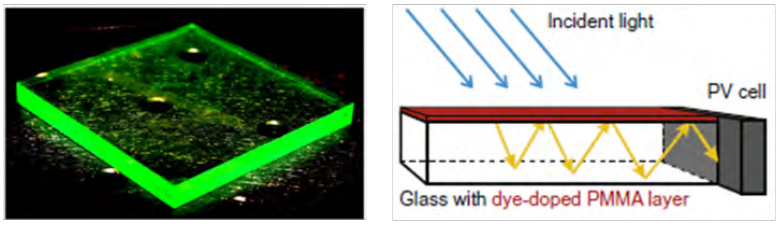

Figure 3. Photographs and principle of operation of a LSC based on a thin dye-doped polymer film. Re-emitted light is guided toward the edges by total internal reflection (yellow arrows). Picture of principle of operation taken from ref [34].

These photonic artificial antennas are not only useful in LSC or as photosensitizers of semiconductors in photovoltaic devices, but are also applicable as tunable dye lasers [36-39] and light modulators in white-light emitting systems [40-43]. In the former case, the wavelength of the laser signal can be modulated over a broad spectral range (Figure 4), against conventional monochromatic lasers, while in the last case the emission wavelength can be tuned over the whole Vis region as a result of the simultaneous blue, green and red emission. This thesis report is focused in the development of artificial antenna systems based on photoactive materials and molecular cassettes undergoing energy transfer processes, subsequently directed to applications in the above technological fields.

Regarding the laser purposes, one of the greatest advantages of this kind of fluorophores or materials with antenna property is that acceptor molecules can be indirectly excited by means of the excitation energy transfer coming from the donor, i.e., a robust dye which in turn enhances the photostability of the luminescent dye and reduces the self-absorption effects. Therefore, the laser performance is hugely improved, especially for lasers working in the red-edge of the visible (› 650 nm), which are usually characterized by a low absorption capability at the standard pump wavelength 532 nm and low photostability [44]. Nowadays, there is considerable interest in long-wavelength fluorescent dyes for biomedical and biophotonic applications because of their ability to penetrate deeper into tissue [45], facilitating their use in surgical and photodynamic therapy [46]. Besides, the light absorption can take place in a spectral region far away from the emission (larger "pseudo" Stokes shift), thereby reducing the background interferences in bioimaging and sensing applications.

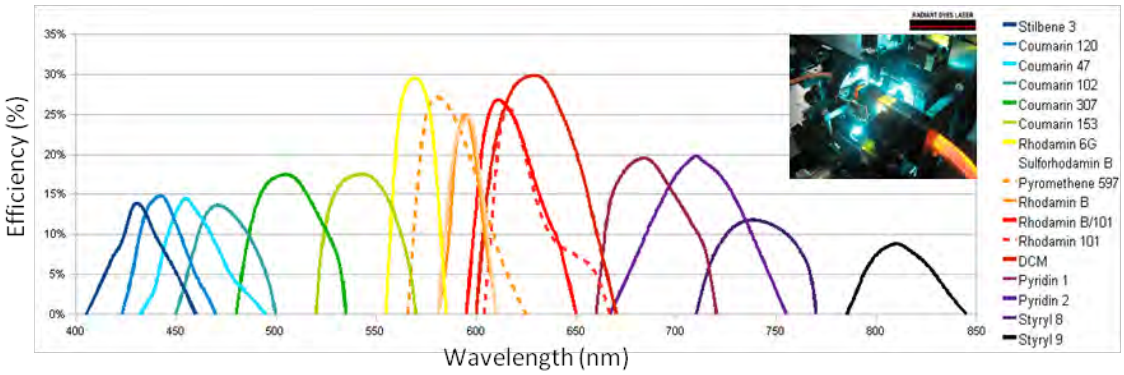

Figure 4. Lasing emission spectra of several dyes with tunable output signals over a broad spectral range. Inset; Rh6G-based dye laser.

Moreover, the combination of the appropriate dyes and the accurate control of the energy transfer efficiency between them could led to a simultaneous emission of the three fundamental colours (blue, green and red), that is, to white-light emission (Figure 5). This allows the development of photoactive materials in which the emission can be finely tuned in the blue, green and red regions by using the proper filters. In fact, white-light emitting materials [47-52] have opened perspectives for the fabrication of a new generation of light emitting devices such as LEDs (light-emitting diodes), also known as color-changing media (CCM), in which white-light emitting diodes (WLEDs) should be highlighted. [53,54].

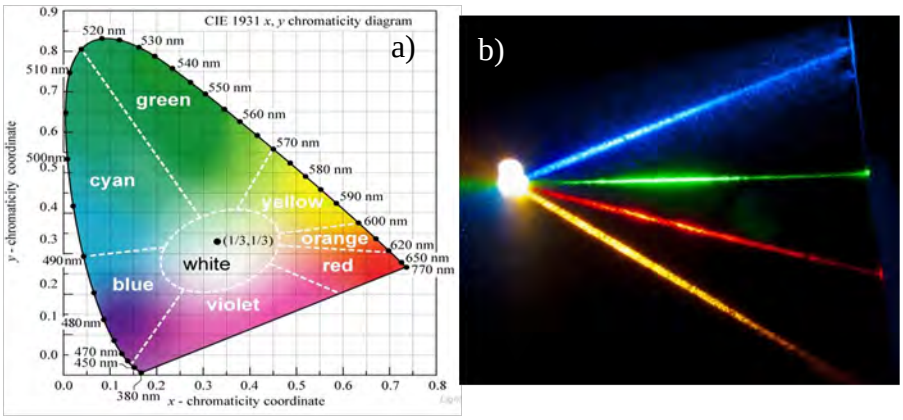

Figure 5. a) CIE chromaticity diagram. b) Four laser beams –yellow, blue, green and red– converge to produce a pleasantly warm white light.

In this context, different approaches have been considered in this thesis for the development of artificial photonic antenna systems undergoing energy transfer process to be applied as dye lasers or white-light emitters. To this aim, a wide variety of suitable laser dyes acting as guests have been allocated in either inorganic (porous LTL zeolite) or organic (polymeric nanoparticles) hosts, as well as molecular systems based on the assembly of laser dyes have been developed and photophysically characterized, looking for tight-fitting their properties to specific applications. Along the following lines, we will briefly describe the designed materials and luminescent fluorophores paying attention to the ongoing energy transfer mechanism, which can be classified in two main types further analyzed in Chapter 1; long-range dipole-dipole coupling or through-space (FRET) and short-range superexchange or through-bond (TBET).

- **Hybrid Materials**

The incorporation of organic photoactive guests into nanostructured inorganic frameworks gives rise to well organized multifunctional dye-doped hybrid materials [55-59]. The aluminosilicate LTL zeolite has been chosen as the ideal solid host [60] owing to its one-dimensional channel system with a pore opening size in which dye molecules fit like a glove (Figure 6). Considering that high-quality LTL zeolite crystals are required for its successful application as hybrid antennas, firstly we have optimized the conventional synthetic hydrothermal route by means of a microwave heating procedure to attain crystals with defined, homogeneous and tunable morphology and size. The geometrical constrains imposed by the zeolitic framework lead to a full alignment of the guest molecules along the zeolitic channels [61]. Moreover, the sequential allocation of luminescent dyes working in the blue (oxazole and carbostyril), green-yellow (BODIPYs) and red-edges (oxazines) of the electromagnetic spectrum

gives rise to a supramolecular organization in which the energy donors are placed in the center of the crystals, while the final acceptor traps are placed in the pore entrances. Accordingly, light over a broad spectral range can be simultaneously harvested and transferred via successive energy transfer hops (FRET mechanism) in a cascade-like unidimensional process from the center to the crystal ends. An accurate control of the energy transfer efficiency allows a fine modulation of the emission window of the system (from predominant red emission to white-light emission) and opens the door to a new generation of photoactive materials capable of modulating the colour light output [62].

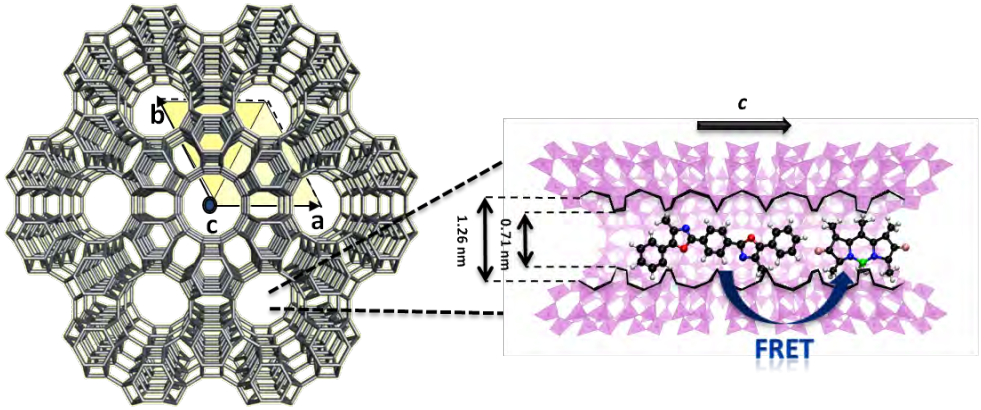

Figure 6. LTL zeolite framework described by unidimensional channels running along the crystal main axis suitable for allocating luminiscent fluorophores.

- **Dye-doped polymeric NPs**

The incorporation of fluorophores into polymeric nanocarriers is a strategy to circumvent the often undesirable sensitivity and interactions of most chromophores with their local environment [63,64], i.e., allowing the use of hydrophobic dyes in a biologically relevant aqueous environment. Against this background, we have studied aqueous colloidal suspensions in which fluorophores are encapsulated into polymeric latex nanoparticles (Figure 7). The dye confinement increases its photostability and enables to manage very high dye concentrations without signs of aggregation, while keeping or even improving the characteristic high fluorescence efficiency of the encapsulated guests [65,66]. Moreover, the confinement ensures a close proximity between donor and acceptor molecules, boosting the probability for excitation energy transfer [67-69]. Thus, the co-encapsulation of suitable pairs of laser dyes (rhodamine 6G and nile blue), capable of undergoing intermolecular FRET processes, should be a good approach to attain improved red laser emission in a high calorific capacity media (as is the water) [70]. The promotion of the red emission from the nile blue through

FRET pathway from the pumped donor rhodamine could be considered as a good strategy to overcome some of the drawbacks of long-wavelength emitting dyes, such as low absorption, low laser efficiency and poor photostability. Therefore, these stable colloidal nanomaterials are highlighted as suitable candidates for developing tunable dye lasers in the red region, surpassing the laser performance of those commercially available.

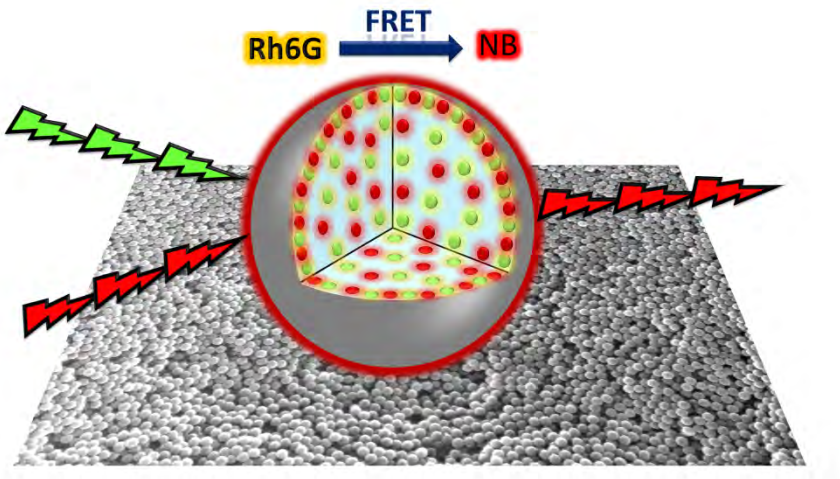

Figure 7. Dye doped latex nanoparticles undergoing FRET process.

- **Molecular Antenna Systems**

Finally, the covalent linkage of the energy donor and acceptor via a spacer in a single supramolecular structure has been considered, leading to molecular antennas or cassettes (Figure 8) [71,72]. Nowadays, the vast knowledge in organic chemistry allows the development of tailor made molecular structures. In this context, BODIPY laser dyes stand out as excellent scaffolds owing to its synthetic versatility and the possibility of shift their emission by the substitution pattern of its core [73]. Thus, we have studied molecular assemblies constituted by different BODIPYs and also by combination of BODIPY with rhodamine. The short donor-acceptor distance in these multichromophoric structures ensure highly efficient intramolecular FRET processes, but also promote an additional energy transfer mechanism, TBET, if the spacer is the adequate (commonly it should be rigid and delocalized to enable such process) [74]. On this point, the molecular engineering is of vital importance since the identity of each fragment must be maintained in the cassette to excite the donor and the acceptor selectively. Accordingly, the energy transfer is very fast and efficient (almost the 100%), and mainly conducted by the ultrafast TBET. Therefore, and in analogy to the above described dye-doped NPs, this would also be a proper strategy to develop

energy transfer dye lasers working exclusively in the red-edge, since no sign of the donor emission is detected, overcoming the drawbacks related to the long-wavelength active media.

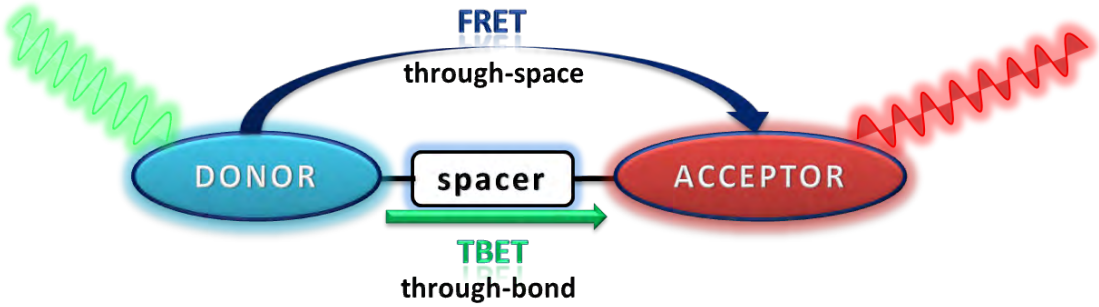

Figure 8. Schematic view of donor-bridge-acceptor multichromophoric array undergoing FRET and TBET processes.

This thesis is based on article compilation and is divided in the following chapters, which will serve to organize and summarize the results of the thesis. Firstly, a brief theoretical background about excitation energy transfer processes (Chapter 1) is carried out. Afterwards, the results and discussion on the photophysical properties of the Dye-doped LTL zeolite Hybrid Materials (Chapter 2), Dye-doped polymeric Photoactive Nanomaterials (Chapter 3) and Molecular Antennas (Chapter 4) are presented. Finally, the main conclusions derived from this work together with some future perspectives are briefly described.

Bibliography

[1] G. D. Scholes, T. Mirkovic, D. B. Turner, F. Fassioli and A. Buchleitner, *Energy Environ. Sci.,* **2012**, 5, 9374-9393.

[2] D. L. Andrews, *Energy Harvesting Materials,* World Scientific, Singapore, **2005**.

[3] G. McDermott, S. M. Prince, A. A. Freer, A. Hawthornthwaite-Lawless, M. Z. Papiz, R. J. Cogdell and N. W. Isaacs, *Nature,* **1995**, 374, 517-521.

[4] T. Ritz, A. Damjanovic and K. Schulten, *ChemPhysChem,* **2002**, 3, 243-248.

[5] Scheer H. and Schneider S., *Photosynthetic Light Harvesting Systems,* Walter de Gruyter, Berlin, **1988**.

[6] G. D. Scholes, G. R. Fleming, A. Olaya-Castro and R. van Grondelle, *Nat. Chem.,* **2011**, 3, 763-774.

[7] M. Choi, T. Yamazaki, I. Yamazaki and T. Aida, *Angew. Chem. Int. Ed.,* **2004**, 43, 150-158.

[8] K. Boeneman, J. R. Deschamps, S. Buckhout-White, D. E. Prasuhn, J. Blanco-Canosa, P. E. Dawson, M. H. Stewart, K. Susumu, E. R. Goldman, M. Ancona and I. L. Medintz, *ACS Nano,* **2010**, 4, 7253-7266.

[9] A. Sautter, K. Başak Kükrer, D. G. Schmid, R. Dobrawa, M. Zimine, G. Jung, van Stokkum, Ivo H. M., L. De Cola, R. M. Williams and F. Würthner, *J. Am. Chem. Soc.,* **2005**, 127, 6719-6729.

[10] V. Balzani, A. Credi and M. Venturi, *Light-Harvesting Antennae,* in Molecular Devices and Machines - A Journey into the Nano World, Wiley-VCH, Weinheim, **2004**.

[11] J. R. Lakowicz, *Principles of Fluorescence Spectroscopy,* Springer, Singapore, **2006**.

[12] P. D. Frischmann, K. Mahata and F. Wurthner, *Chem. Soc. Rev.,* **2013**, 42, 1847-1870.

[13] F. Puntoriero, A. Sartorel, M. Orlandi, G. La Ganga, S. Serroni, M. Bonchio, F. Scandola and S. Campagna, *Coord. Chem. Rev.,* **2011**, 255, 2594-2601.

[14] C. N. Fleming, P. Jang, T. J. Meyer and J. M. Papanikolas, *J. Phys. Chem. B,* **2004**, 108, 2205-2209.

[15] S. E. Webber, *Chem. Rev.,* **1990**, 90, 1469-1482.

[16] W. S. Aldridge, B. J. Hornstein, S. Serron, D. M. Dattelbaum, J. R. Schoonover and T. J. Meyer, *J. Org. Chem.,* **2006**, 71, 5186-5190.

[17] M. Cotlet, T. Vosch, S. Habuchi, T. Weil, K. Müllen, J. Hofkens and F. De Schryver, *J. Am. Chem. Soc.,* **2005**, 127, 9760-9768.

[18] Y. Nakamura, N. Aratani and A. Osuka, *Chem. Soc. Rev.,* **2007**, 36, 831-845.

[19] Y. Zeng, Y. Li, J. Chen, G. Yang and Y. Li, *Chem. Asian J.,* **2010**, 5, 992-1005.

[20] P. K. Dutta, R. Varghese, J. Nangreave, S. Lin, H. Yan and Y. Liu, *J. Am. Chem. Soc.,* **2011**, 133, 11985-11993.

[21] H. Mass and G. Calzaferri, *Angew. Chem. Int. Ed.,* **2002**, 41, 2495-2497.

[22] G. Calzaferri, R. Meallet-Renault, D. Bruehwiler, R. Pansu, I. Dolamic, T. Dienel, P. Adler, H. Li and A. Kunzmann, *ChemPhysChem,* **2011**, 12, 580-594.

[23] H. Xin, F. S. Kim and S. A. Jenekhe, *J. Am. Chem. Soc.,* **2008**, 130, 5424-5425.

[24] T. P. Chou, Q. Zhang, G. E. Fryxell and G. Cao, *Adv. Mater.,* **2007**, 19, 2588-2592.

[25] A. Morandeira, G. Boschloo, A. Hagfeldt and L. Hammarstrom, *J. Phys. Chem. C,* **2008**, 112, 9530-9537.

[26] S. Gunes, H. Neugebauer and N. S. Sariciftci, *Chem. Rev.,* **2007**, 107, 1324-1338.

[27] M. G. Debije and P. P. C. Verbunt, *Adv. Energy Mater.,* **2012**, 2, 12-35.

[28] T. Markvart, L. Danos, L. Fang, T. Parel and N. Soleimani, *RSC Adv.,* **2012**, 2, 3173-3179.

[29] S. W. Glunz, *Sol. Energy Mater. Sol. Cells,* **2006**, 90, 3276-3284.

[30] M. A. Green, *J. Mater. Sci.: Mater. Electron.,* **2007**, 18, S15-S19.

[31] J. Poortmans and V. Arkhipov, *Thin Film Solar Cells: Fabrication, Characterization and Applications,* Wiley, Chichester, **2006**.

[32] F. Odobel, Y. Pellegrin and J. Warnan, *Energy Environ. Sci.,* **2013**, 6, 2041-2052.

[33] S. Huber and G. Calzaferri, *ChemPhysChem,* **2004**, 5, 239-242.

[34] T. Dienel, C. Bauer, I. Dolamic and D. Brühwiler, *Solar Energy,* **2010**, 84, 1366-1369.

[35] Luminiscence concentrators and luminiscence dispersers on the basis of oriented dye-zeolite antennas. patent CH-698333, granted 15.07.2009; pending WO 2010/009560 A1.-

[36] F. J. Duarte and L. W. Hillman, *Dye Laser Principles,* Academic Press, San Diego, **1990**.

[37] F. P. Schäfer, *Dye Lasers,* Springer-Verlag, Berlin, **1990**.

[38] B. H. Soffer and B. B. McFarland, *Appl. Phys. Lett.,* **1967**, 10, 266-267.

[39] C. Grivas and M. Pollnau, *Laser Photonics Rev.,* **2012**, 6, 419-462.

[40] P. Coppo, M. Duati, V. N. Kozhevnikov, J. W. Hofstraat and L. De Cola, *Angew. Chem. Int. Ed.,* **2005**, 44, 1806-1810.

[41] M. Mazzeo, V. Vitale, F. Della Sala, M. Anni, G. Barbarella, L. Favaretto, G. Sotgiu, R. Cingolani and G. Gigli, *Adv. Mater.,* **2005**, 17, 34-39.

[42] V. Vohra, G. Calzaferri, S. Destri, M. Pasini, W. Porzio and C. Botta, *ACS Nano,* **2010**, 4, 1409-1416.

[43] X. Wang, J. Yan, Y. Zhou and J. Pei, *J. Am. Chem. Soc.,* **2010**, 132, 15872-15874.

[44] U. Resch-Genger, M. Grabolle, S. Cavaliere-Jaricot, R. Nitschke and T. Nann, *Nat. Meth.,* **2008**, 5, 763-775.

[45] H. P. Berlien and G. H. Müller, *Applied Laser Medicine,* Springer-Verlag, Landsberg, **2003**.

[46] F. J. Duarte, *Tunable Lasers Applications,* CRC, New York, **2009**.

[47] M. Ganschow, C. Hellriegel, E. Kneuper, M. Wark, C. Thiel, G. Schulz-Ekloff, C. Braeuchle and D. Woehrle, *Adv. Funct. Mater.,* **2004**, 14, 269-276.

[48] X. Guo, C. Qin, Y. Cheng, Z. Xie, Y. Geng, X. Jing, F. Wang and L. Wang, *Adv. Mater.,* **2009**, 21, 3682-3688.

[49] W. Ki, J. Li, G. Eda and M. Chhowalla, *J. Mater. Chem.,* **2010**, 20, 10676-10679.

[50] J. Kido, M. Kimura and K. Nagai, *Science,* **1995**, 267, 1332-1334.

[51] Y. Li, A. Rizzo, R. Cingolani and G. Gigli, *Adv. Mater.,* **2006**, 18, 2545-2548.

[52] P. Nandhikonda and M. D. Heagy, *Chem. Commun.,* **2010**, 46, 8002-8004.

[53] P. Lee, S. L. Hsu and J. Lee, *J. Polym. Sci. , Part A: Polym. Chem.,* **2007**, 46, 464-472.

[54] C. Sun, X. Wang, X. Zhang, C. Qin, P. Li, Z. Su, D. Zhu, G. Shan, K. Shao, H. Wu and J. Li, *Nat. Commun.,* **2013**, 4, 2717-2725.

[55] M. E. Davis, *Nature,* **2002**, 417, 813-821.

[56] Y. Tao, H. Kanoh, L. Abrams and K. Kaneko, *Chem. Rev.,* **2006**, 106, 896-910.

[57] M. Busby, H. Kerschbaumer, G. Calzaferri and L. De Cola, *Adv. Mater.,* **2008**, 20, 1614-1618.

[58] L. Gigli, R. Arletti, G. Tabacchi, E. Fois, J. G. Vitillo, G. Martra, G. Agostini, S. Quartieri and G. Vezzalini, *J. Phys. Chem. C,* **2014**, 118, 15732-15743.

[59] N. Mizoshita, Y. Goto, T. Tani and S. Inagaki, *Adv. Mater.,* **2009**, 21, 4798-4801.

[60] D. W. Breck, *Zeolite Molecular Sieves,* John Wiley & Sons, New York, **1974**.

[61] E. Fois, G. Tabacchi, A. Devaux, P. Belser, D. Bruhwiler and G. Calzaferri, *Langmuir,* **2013**, 29, 9188-9198.

[62] D. Pisignano, M. Mazzeo, G. Gigli, G. Barbarella, L. Favaretto and R. Cingolani, *J. Phys. D: Appl. Phys.,* **2003**, 36, 2483-2486.

[63] R. E. Hermes, T. H. Allik, S. Chandra and J. A. Hutchinson, *Appl. Phys. Lett.,* **1993**, 63, 877-879.

[64] S. Bhattacharyya, S. Prashanthi, P. R. Bangal and A. Patra, *J. Phys. Chem. C,* **2013**, 117, 26750-26759.

[65] V. Martín, J. Bañuelos, E. Enciso, I. López-Arbeloa, A. Costela and I. García-Moreno, *J. Phys. Chem. C,* **2011**, 115, 3926-3933.

[66] E. Enciso, A. Costela, I. García-Moreno, V. Martin and R. Sastre, *Langmuir,* **2010**, 26, 6154-6157.

[67] Z. Tian, J. Yu, C. Wu, C. Szymanski and J. McNeill, *Nanoscale,* **2010**, 2, 1999-2011.

[68] A. Reisch, P. Didier, L. Richert, S. Oncul, Y. Arntz, Y. Mély and A. S. Klymchenko, *Nat. Commun.,* **2014**, 5, 4089-4098.

[69] C. Martin, S. Bhattacharyya, A. Patra and A. Douhal, *Photochem. Photobiol. Sci.,* **2014**, 13, 1241-1252.

[70] L. Cerdan, E. Enciso, V. Martin, J. Banuelos, I. Lopez-Arbeloa, A. Costela and I. García-Moreno, *Nat. Photon.,* **2012**, 6, 621-626.

[71] A. Harriman, G. Izzet and R. Ziessel, *J. Am. Chem. Soc.,* **2006**, 128, 10868-10875.

[72] R. Ziessel and A. Harriman, *Chem. Commun.,* **2011**, 47, 611-631.

[73] H. Lu, J. Mack, Y. Yang and Z. Shen, *Chem. Soc. Rev.,* **2014**, 43, 4778-4823.

[74] Y. Ueno, J. Jose, A. Loudet, C. Pérez-Bolívar, P. Anzenbacher and K. Burgess, *J. Am. Chem. Soc.,* **2011**, 133, 51-55.

CHAPTER 1

Excitation Energy Transfer

Interaction between excited and ground states of two molecular chromophores remains being a subject of considerable interest nowadays due to its manifestation in a broad range of processes; chemical reactions, complex formation, and photophysical processes such as excitation energy transfer (EET). These processes play a key role in chemistry, biology, and physics and occur at distances ranging from 1 Å to more than 50 Å, and on time scales from femtosecond to milliseconds, which open a wide range of applications [1,2].

When the energy is transferred from an excited molecule (donor) to another that is chemically different (acceptor) according to

$$D^* + A \rightarrow D + A^*$$

it is called heterotransfer. This process becomes feasible thanks to the partial spectral overlap between donor emission and acceptor absorption bands.

Differently, if the donor and acceptor are identical, the energy transfer is termed homotransfer:

$$D^* + D \rightarrow D + D^*$$

Such transfer typically occurs for fluorophores which display small Stokes shifts. When the process can repeat itself so that the excitation migrates over several molecules, it is called *excitation transport* or *energy migration*.

1.1. Radiative vs Non-Radiative Transfer

It is important to distinguish between radiative and non-radiative transfer. Radiative energy transfer (RET) corresponds to the absorption by a molecule A (or D) of a photon emitted by a molecule D, supposing an average distance between D and A (or D) larger than the wavelength. Such a transfer does not require any interaction

between the partners, but it depends on the spectral overlap and on the concentration. In contrast, non-radiative transfer occurs without emission of photons at distances less than the wavelength and results from short- or long-range interactions between molecules. For instance, non-radiative transfer by dipole-dipole interaction is possible at distances up to 80-100 Å. Consequently, it can be used as a tool for determining distances of a few tens of Angströms between chromophores.

The impact of the radiative and non-radiative transfers on the characteristics of fluorescence emission from the donor is quite divergent and allows the statement of the type of mechanism taking place in the energy transfer process. Tables 1.1 and 1.2 summarize their effects for heterotransfer and homotransfer EET [3].

Table 1.1. Effect of the hetero-energy transfer on the fluorescence characteristics of the donor.

Characteristics of donor emission	Radiative transfer	Non-radiative transfer
Fluorescence spectrum	Modified in the region of spectral overlap	Unchanged
Steady-state fluorescence intensity	Decreased in the region of spectral overlap	Decreased by the same factor whatever λ_{em}
Fluorescence decay	Unchanged	Shortened

Table 1.2. Effect of the homo-energy transfer on the fluorescence characteristics of the donor.

Characteristics of donor emission	Radiative transfer	Non-radiative transfer
Fluorescence spectrum	Modified in the region of spectral overlap	Unchanged
Steady-state fluorescence intensity	Decreased in the region of spectral overlap	Decreased by the same factor whatever λ_{em}
Fluorescence decay	Slower	Unchanged
Steady-state emission anisotropy	Decreased	Strongly decreased
Decay emission anisotropy	Faster	Much faster

Apart from the spectral overlap, which is required for radiative and non-radiative energy transfers, the factors governing the efficiency of each one are not the same, as it is collected in Table 1.3.

Table 1.3. Factors governing the efficiency of radiative and non-radiative transfers.

	Spectral overlap	λ_{exc} and λ_{em}	Φ_D	r_{DA} or r_{DD}	Viscosity	Experimental arrangement
Radiative	Yes	Yes	No	No	No	Yes
Non-radiative	Yes	No	Yes	Yes	Yes	No

1.1.1. Radiative energy transfer

Radiative energy transfer (RET) is a two-step process: a photon emitted by a donor D is absorbed by an acceptor that is chemically different (A) or identical (D)

$$D^* \rightarrow D + h\upsilon$$

$$h\upsilon + A \rightarrow A^* \text{ or } h\upsilon + D \rightarrow D^*$$

This process is often called *trivial* because of the simplicity of the phenomenon, but in reality the quantitative description is quite complicated because it depends on the experimental arrangement, i.e., on size and shape of the sample and its configuration with respect to excitation and emission detection.

Radiative transfer results in a decrease of the donor fluorescence intensity in the region of spectral overlap (Tables 1.1 and 1.2). Such distortion of the fluorescence spectrum is called the inner filter effect (i.e., re-absorption and re-emission effect). In the case of radiative transfer between identical molecules, the fluorescence decays more slowly as a result of successive re-absorptions and re-emissions (Table 1.2).

1.1.2. Non-radiative energy transfer

Non-radiative transfer of electronic excitation energy requires some interaction between an excited donor molecule D^* and an acceptor molecule A, as well as an overlap between the emission spectrum of the donor and the absorption spectrum of the acceptor, so that several vibronic transitions in the donor have practically the same energy as the corresponding transitions in the acceptor (Figure 1.1). That means that the transitions can be coupled or in resonance and the energy transfer process does not involve the appearance of a photon. Thus, the commonly used expression of *fluorescence resonance energy transfer* is not correct at all because it is not the

fluorescence that is transferred but the electronic energy of the donor. Nevertheless, it is possible to maintain the FRET term referring to Förster Resonance Energy Transfer, one of the energy transfer mechanisms later considered.

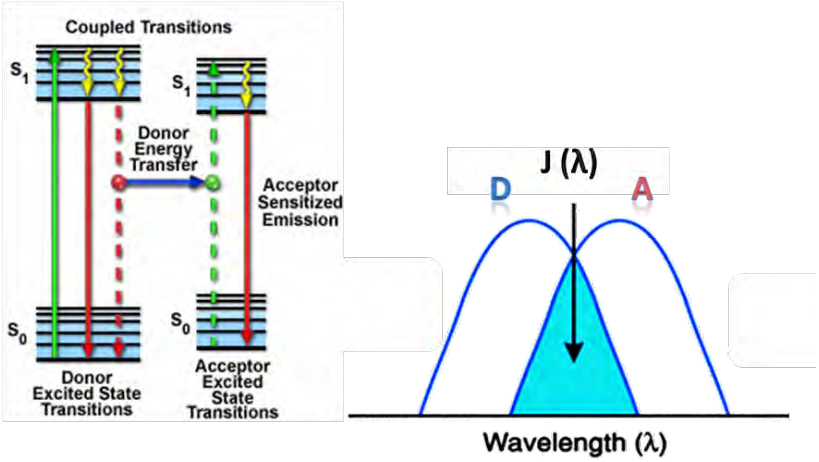

Figure 1.1. Jablonski diagram of donor and acceptor molecule at nanometer separation. Absorption and emission transitions are represented by straight vertical arrows (green and red, respectively), while vibrational relaxation is indicated by wavy yellow arrows. The coupled transitions are drawn with dashed lines. The donor fluorophore can transfer excited state energy (blue arrow) directly to the acceptor without emitting a photon as result of the integral overlap $J(\lambda)$ between the emission spectrum of the donor and the absorption of the acceptor.

A radiationless energy transfer process occurs when a zero-order state decays faster through this coupling than by the competing radiative process. The electronic energy transfer may be an intermolecular process which can be described in terms of bimolecular quenching process

$$D^* + A \xrightarrow{k_q} D + A^*$$

where the bimolecular quenching rate constant k_q is related to an intermolecular energy transfer rate constant k_{EET} by:

$$k_{EET} = k_q[A] \qquad \text{(eq. 1.1)}$$

Intramolecular EET processes are also feasible in bicromophoric molecules and are usually described in terms of the process [1]

$$D^* - B - A \xrightarrow{k_{EET}} D - B - A^*$$

where the excitation energy is transferred from an excited donor D^* chromophore moiety to a ground-state acceptor moiety A, resulting in quenching of D^* fluorescence

and sensitization of A. B denotes a molecular spacer bridge connecting the two cromophores. This bridge can play a role in promoting the transfer process (see section 1.3).

In most cases k_{EET} is attributed to two possible contributions, i.e. to different interaction mechanisms. The interactions may be *Coulombic* and/or due to *intermolecular orbital overlap*.

The Coulombic interactions consist of long-range dipole-dipole interactions (Förster's mechanism) and short-range multi-polar interactions. The interactions due to intermolecular orbital overlap, which include electron exchange (Dexter's mechanism) and charge resonance interactions, are of course only short range (Figure 1.2). It should be mentioned that for singlet-singlet energy transfer all types of interactions are involved, whereas for triplet-triplet energy transfer an orbital overlap is required. In this way, the Coulombic interaction is predominant for allowed transitions on D and A even at short distances. In contrast, for forbidden transitions, as in the transfer between triplet states, the Coulombic interaction is almost negligible, whereas the exchange mechanism prevails over the others, but just at shorts distances (< 10 Å) because an overlap of the molecular orbital is required [3].

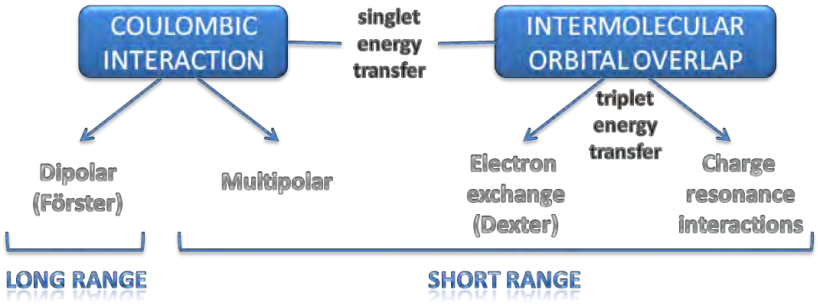

Figure 1.2. Types of interactions involved in non-radiative transfer mechanisms.

The Coulombic term corresponds to the energy transfer in which the initially excited electron on the donor D returns to the ground state orbital on D, while simultaneously an electron on the acceptor A is promoted to the excited state (Figure 1.3, bottom). The exchange mechanism in turn, corresponds to an energy transfer process associated with an exchange of two electrons between D and A (Figure 1.3, top).

Dexter [4] and Förster [5] developed the theory of energy-transfer induced electron exchange interactions and dipole-dipole interactions, respectively. In honor of the developers of the theories for energy transfer, electron exchange energy transfer is sometimes referred to in the literature as "Dexter" energy transfer and dipole-dipole energy transfer is sometimes referred to in the literature as "Förster" Resonance Energy Transfer (FRET) [6].

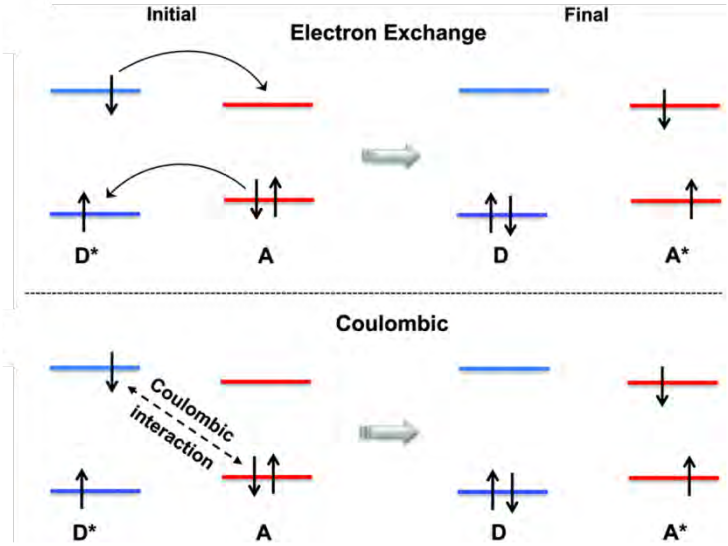

Figure 1.3. Comparison of the dipole-dipole and exchange mechanism of electronic energy transfer.

The magnitude of the interaction is even more important than its nature, and consequently it is convenient to distinguish between three main classes of coupling (proposed by Förster): strong, weak and very weak [3].

Strong coupling: the coupling is called *strong* when the intermolecular interaction is much larger than the interaction between the electronic and nuclear motions within the individual molecules. These systems are characterized by large differences between their absorption spectra and those of their components, and the excitation energy is not localized on one of the molecules but is truly delocalized over the two components (or more in multi-cromophoric systems).

Weak coupling: when the interaction energy is much lower than the absorption bandwidth but larger than the width of an isolated vibronic level, then it is denoted as weak coupling. The electronic excitation in this case is more localized than under strong coupling and the absorption spectrum is less altered. The formation of aggregates or complexes is a clear example of weak coupling.

Very weak coupling: when the interaction energy is much lower than the vibronic bandwidth it can be denominated as a very weak coupling. In this case, there is little or no alteration of the absorption spectra and the initial excitation is localized. For dipole-dipole interaction, that is, transfer between molecules in which donor and acceptor transitions are dipole-allowed (Förster), the distance dependence is thus r^{-6} instead of r^{-3} for the preceding cases [5,6].

The more or less extended delocalization of the excitation in strong and weak couplings makes impossible to define a clear transfer rate of the process. It is only in the case of very weak coupling that a transfer rate can be defined unequivocally. Indeed, this is the scope of this thesis. In the following section we will describe in detail the main mechanisms of non-radiative energy transfer in the very weak coupling regime: the Förster or dipole-dipole coupling mechanism (also called as long range energy transfer), the Dexter mechanism (also known as exchange energy transfer), and a further extension of the last one, the superexchange.

1.2. FÖRSTER FORMULATION: LONG-RANGE DIPOLE-DIPOLE TRANSFER

The theory for resonance energy transfer is moderately complex, and similar equations have been derived from classical and quantum mechanical considerations [5]. We will consider only the derived final equations by Förster [7,8]. This theory is best understood by considering a single donor and acceptor separated by a distance *r*. In this picture the rate of transfer from a donor to an acceptor is given by:

$$k_{ET}(r) = \frac{\phi_D \kappa^2}{\tau_D r^6}\left(\frac{9000(\ln 10)}{128\pi^5 N n^4}\right)\int_0^\infty I_D(\lambda)\varepsilon_A(\lambda)\lambda^4 d\lambda \qquad \text{(eq. 1.2)}$$

where ϕ_D is the quantum yield of the donor in the absence of acceptor, *n* is the refractive index of the medium, *N* is Avogadro's number, and τ_D is the lifetime of the donor in the absence of the acceptor. $I_D(\lambda)$ is the corrected fluorescence intensity of the donor in the wavelength range λ to $\lambda+\Delta\lambda$ respect to the total intensity (area under the curve) normalized to unity. $\varepsilon_A(\lambda)$ is the absorption coefficient of the acceptor at λ, which is typically in units of M^{-1} cm^{-1}. The term κ^2 is a factor describing the relative orientation of the transition dipoles of the donor and acceptor.

The overlap integral ($J(\lambda)$) expresses the degree of spectral overlap between the donor emission and the acceptor absorption:

$$J(\lambda) = \int_0^\infty I_D(\lambda)\varepsilon_A(\lambda)\lambda^4 d\lambda = \frac{\int_0^\infty I_D(\lambda)\,\varepsilon_A(\lambda)\lambda^4 d\lambda}{\int_0^\infty I_D(\lambda)d\lambda} \qquad \text{(eq. 1.3)}$$

The overlap integral has been defined in several ways, each with different units but the units of nm or cm for the wavelength and units of $M^{-1}cm^{-1}$ for the molar absorption coefficient are more recommendable so as to avoid any possible confusion.

The distance at which FRET is 50% efficient is called the Förster distance R_0, or Förster radius, defined as the donor-acceptor separation for which the donor emits and transfers (to the acceptor) its energy with the same probability. R_0 depends on the photophysical properties of the donor and the acceptor and is given by:

$$R_0^{\,6} = \frac{9000(\ln 10)\,\phi_D \kappa^2}{128\pi^5 N n^4} \int_0^\infty I_D(\lambda)\varepsilon_A(\lambda)\lambda^4 d\lambda \qquad \text{(eq. 1.4)}$$

R_0 is generally in the range of 15-60 Å and it is important to recognize that these distances are usually reported for an assumed value of κ^2. The orientation factor κ^2 plays an important role in the energy transfer rate and is given by

$$\kappa^2 = (\cos\theta_{DA} - 3\cos\theta_D \cos\theta_A)^2 = (\sin\theta_D \sin\theta_A \cos\phi - 2\cos\theta_D \cos\theta_A)^2 \qquad \text{(eq. 1.5)}$$

where θ_{DA} is the dihedral angle between the donor and acceptor transition moments, and θ_D and θ_A are the angles of each transition moment with the normal linking the mass centers and ϕ is the angle between the planes (Figure 1.4).

As it is shown in Figure 1.4 (right), κ^2 can in principle take values from 0 (perpendicular transition moments) to 4 (collinear transition moments). When the transition moments are parallel, $\kappa^2 = 1$. Nevertheless, when the molecules are free to rotate at a rate that is much faster than the decay excitation rate of the donor, i.e., a random disposition of the donor and the acceptor, the average value of κ^2 is 2/3. Alternatively, in a rigid medium one may assume that a range of static donor-acceptor orientations are present and that these orientations do not change during the lifetime

of the excited state. In this case, for randomly distributed acceptors, where rotation is much slower than the donor decay, $\kappa^2 = 0.476$.

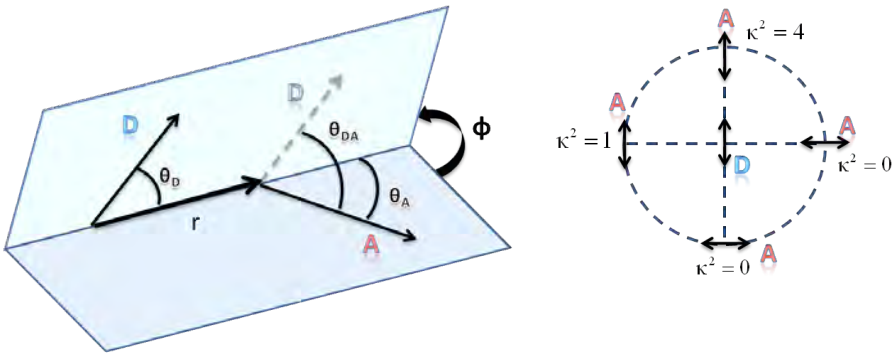

Figure 1.4. Angles involved in the definition of the orientation factor κ^2 (left) and examples of values of κ^2 (right).

Once the value of R_0 is known the rate of energy transfer can be easily calculated using

$$k_{EET}(r) = \frac{1}{\tau_D}\left(\frac{R_0}{r}\right)^6 \qquad \text{(eq. 1.6)}$$

and as consequence the rate of EET via Förster mechanism depends markedly on the donor-acceptor distance.

1.2.1. Energy transfer efficiency

The efficiency of energy transfer (ϕ_{EET}), i.e., the fraction of photons absorbed by the donor which are transferred to the acceptor, is controlled by the ratio r/R_0:

$$\phi_{EET} = \frac{1}{1+(r/R_0)^6} \qquad \text{(eq. 1.7)}$$

This equation shows that the transfer efficiency is 50% when the donor-acceptor distance is equal to the Förster critical radius. Besides, this expression allows the determination of the mean distance between a donor and an acceptor (r) by means of the efficiency of the transfer. Indeed, this energy transfer process is also known as a "spectroscopic ruler" and is widely applied in biochemistry to measure

distances between donor and acceptor molecules strategically placed in specific parts of biomolecules [7].

There are different experimental methods that can be used to determine the efficiency of the energy transfer. The most common used methods can be divided in the basis of steady-state and time-resolved techniques respectively [3].

Among the steady-state methods two of them are widely used.

Method 1: Decrease in donor fluorescence

The energy transfer from the donor to the acceptor causes the decrease of the donor quantum yield. Consequently, this reduction of the fluorescence capacity of the donor can be used to determine the efficiency

$$\phi_{EET} = 1 - \frac{\phi_{DA}}{\phi_D} \qquad \text{(eq. 1.8)}$$

where ϕ_{DA} and ϕ_D are the donor quantum yields in the presence and absence of the acceptor, respectively.

Method 2: Enhancement of the acceptor fluorescence

The fluorescence intensity of the acceptor increases thanks to the energy transfer coming from the donor. Comparing it with the intensity in the absence of the donor provides the transfer efficiency:

$$\phi_{EET} = \frac{A_A(\lambda_D)}{A_D(\lambda_D)}\left[\frac{I_{AD}(\lambda_D, \lambda_A^{em})}{I_A(\lambda_D, \lambda_A^{em})} - 1\right] \qquad \text{(eq. 1.9)}$$

where A_A and A_D are the absorbances at the excitation wavelength λ_D and I_A and I_{AD} the fluorescence intensities of the acceptor in the absence and presence of the donor.

Time-resolved emission of the donor or acceptor fluorescence also provides accurate information of the transfer rate, avoiding difficulties such as inner filter effects directly connected to concentration and configuration factors.

Method 3: Decay of the donor fluorescence

The energy transfer efficiency can be obtained from the comparison of the fluorescence decay curves of the donor in the absence $(I_f{}^{D}(t))$ and presence $(I_f{}^{D+A}(t))$ of the acceptor as

$$\phi_{EET} = 1 - \frac{\int_0^\infty I_f{}^{D+A}(t)dt}{\int_0^\infty I_f{}^{D}(t)dt} \qquad \text{(eq. 1.10)}$$

when the donor decay in the absence of acceptor is not a single exponential (i.e., due to some heterogeneity of the microenvironment of the donor) it can be empirically modeled as a sum of exponentials.

$$I_f(t) = A_0 + \sum A_i \exp(-t/\tau_i) \qquad \text{(eq. 1.11)}$$

In this case and for the sake of simplicity the energy transfer efficiency can be estimated according to the amplitude-average lifetimes of the donor alone and donor in presence of the acceptor as

$$\phi_{EET} = 1 - \frac{\langle\tau\rangle_{D,A}}{\langle\tau\rangle_{D}} \qquad \text{(eq. 1.12)}$$

where the amplitude-averaged lifetimes are defined as

$$\langle\tau\rangle = \sum A_i \tau_i \qquad \text{(eq. 1.13)}$$

being the coefficients A_i the weight of each contribution to the lifetime in the multiexponential.

1.3. DEXTER FORMULATION: EXCHANGE ENERGY TRANSFER

In any region of orbital overlap, i.e., when the participants in the reaction are sufficiently close each other that their electron clouds overlap significantly (the separation of the colliding partners is slightly smaller than their van der Waals radii), electron exchange can occur.

For the simple case of two spherical orbitals of D^* and A, the overlap between the orbitals falls off exponentially as the separation r_{DA} between D^* and A increases. This exponential falloff is related with the distance dependence of orbital overlap. Since the degree of exchange for energy transfer is directly related to the orbital overlap of D^* and A, the rate constant for exchange energy transfer (k_{ET}) is also expected to decrease as an exponential function of the distance separating D^* and A. Besides the dependence of the separation distance, the rate of the energy transfer will also be directly related to the spectral overlap integral *(J)*, which, as expected from the golden rule for energy transfer between states, is a measure of the number of states that are capable of satisfying the resonance conditions, once D^* and A are coupled by the electron exchange interaction. The rate constant of energy transfer by electron exchange can be written as [2,3]:

$$k_{ET}(\text{exchange}) = KJ\exp(-2r_{DA}/r_{DA}^{0}) \qquad \text{(eq. 1.14)}$$

where *K* is a parameter related to the specific orbital interactions, such as the dependence of orbital overlap on the instantaneous orientations of D^* and A and J is the normalized spectral overlap. The separation of D^* and A is given by r_{DA} and r_{DA}^{0} is the separation of D^* and A when they are in van der Waals contact.

1.4. SUPEREXCHANGE OR THROUGH-BOND INTRAMOLECULAR EET

Overall, Dexter and Förster mechanism are the pathways of intermolecular EET, however both can also take place intramolecularly in a donor-acceptor assembly. Indeed, a bicromophoric molecule may be defined as a molecule built of two distinguishable molecular units connected by a molecular bridge, where the properties of the bridge determine the characteristics of the whole bicromophoric structure (Figure 1.5). The bridge can serve as a molecular spacer unit which does not influence the basic π electronic system of the two chompophores, i.e., preventing intrachromophore interaction in their ground state. This allows a very weak coupling limit where the Förster and Dexter mechanism are feasible.

However, electronic excitation of either fluorophore may lead to intramolecular electronic interactions between the molecular units. There are many experiments, in particular photoinduced intra-electron transfer studies [1], that indicate strong

interactions between donor and acceptor moieties at D^* and A separated even by a set of σ bonds, at a distance much larger than the sum of their van der Waals orbital radii.

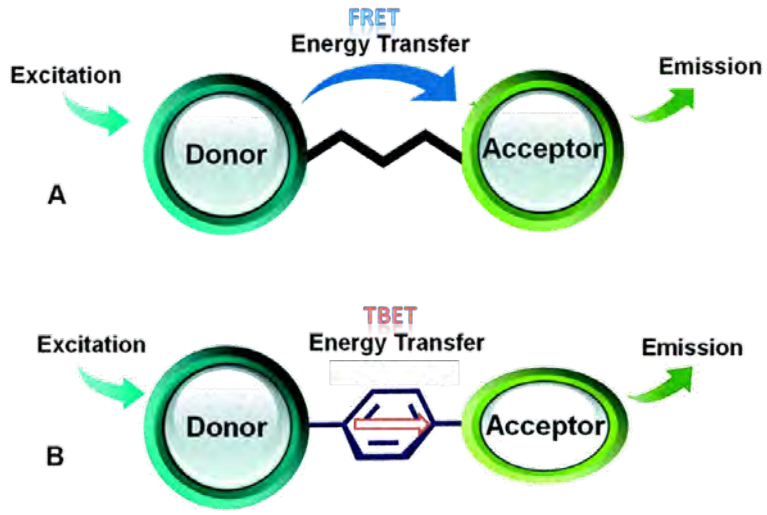

Figure 1.5. Sketch representing the A) through-space and B) through-bond energy transfer mechanisms.

An obvious question arising from the evidence of this phenomenon would be how does the electron move from the donor to the acceptor when the intervening bridge is a set of σ bonds that have a very little electron affinity and posses a high excitation energy for promotion of an electron to a σ^* orbital?

One mechanism to achieve electronic coupling between D^* and A would be trough the usual electron exchange interaction that occurs from overlap of the wave functions of D^* and A. This mechanism is termed the normal electron exchange interaction mechanism. However, electronic wave functions are not expected to overlap significantly when the donor and acceptor are separated by distances ~10 Å because of the exponential decrease in energy transfer rate as a function of separation (Eq. 1.14). The very high values of k_{ET} determined for molecules separated by › 10 Å, makes the orbital overlap interaction unlikely as a mechanism for electron transfer. When selection rules exclude the possibility of dipole-dipole interaction, the proposed mechanism is a superexchange interaction operating beyond the actual orbital overlap region, usually mediated by electronic coupling of the interchromphore bridge orbitals [1,3]. This mechanism uses the wave functions of the σ and σ^* orbitals of the spacer to assist in the propagation of the electronic coupling interaction between D^* and A and is usually termed as "electron superexchange" or "through bond" electronic coupling

(Figure 1.5). These mechanisms may operate simultaneously with FRET (also called "through-space" in intramolecular processes), but are usually much faster.

Accordingly, short–range intra-EET described in terms of Dexter exchange interaction picture should be slightly modified due to the incorporation of through-bond (TB) superexchange interactions. The basic idea of through-bond coupling is shown in Figure 1.6 where the LUMO orbital of the donor overlaps with the σ^* orbital of the nearest bond of the bridge. This interaction propagates through the bridge until it is adjacent to the LUMO orbital of the acceptor. At this point, the electron has a finite probability of being on the acceptor, giving rise to an electron transfer through-bond interaction. Alternatively, the half-filled HOMO of the donor overlaps with the σ orbital of the nearest bond on the bridge and this interaction propagates through the bridge until it is adjacent to the HOMO of the acceptor. As a result, the electrons in the HOMO of the acceptor have a finite probability of being in the HOMO of the donor, leading to a hole transfer [3]. Anyway, though these two mechanisms have been proposed by the experts for describing the through-bond energy transfer, which involve an orbital overlap with the s orbitals of the spacer to promote an "electron" or "hole transfer, the true mechanism is still unclear [1].

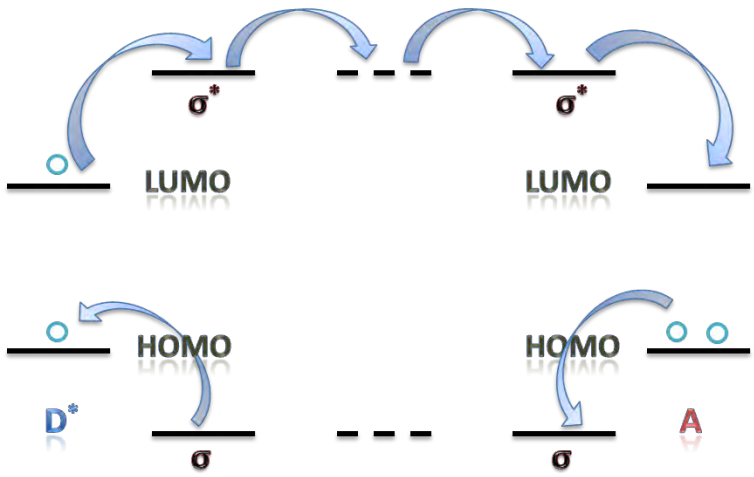

Figure 1.6. Schematic of through-bond coupling for an electron hole (or energy) transfer.

For an excited state electron transfer (ET) to occur, the electron to be transferred is initially in the LUMO of the D^* and must eventually be transferred to the LUMO of A. The donor and acceptor are attached to each other by a sequence of σ bonds that make up the spacer. To each σ, we can associate a filled HOMO and an empty LUMO. As it can be appreciated from the Figure 1.6, the σ HOMOs of the spacer

bonds have a lower energy than the HOMO of the donor, and the σ^* LUMOs of the spacer bonds have a higher energy than of the donor and acceptor.

The through-bond mechanism predicts (in a qualitative way) that the rate of electron transfer decreases as the number of σ bonds between the donor and the acceptor increase, since the degree of overlap falls off as the number of orbitals involved increases. The stereochemistry of the bonds attaching to D and A is also important, and there is an exponential dependence of the rate constant on the number of σ bonds between D and A only for a series of the same stereochemistry. Of course, the transfer is boosted when an alternation of σ and π electrons is present in the structure of the bridge (as for the phenyl spacer of Figure 1.5), as would be our particular case.

Bibliography

[1] S. Speiser, *Chem. Rev.,* **1996**, 96, 1953-1976.

[2] N. J. Turro, V. Ramamurthy and J. C. Scaciano, *Modern Molecular Photochemistry of Organic Molecules,* University Science Books, Sausalito, **2010**.

[3] B. Valeur and M. N. Berberan-Santos, *Molecular Fluorescence: Principles and Applications,* Wiley-vch, Weinheim, **2013**.

[4] D. L. Dexter, *J. Chem. Phys.,* **1953**, 21, 836-850.

[5] T. Förster, *Naturwissenschaften,* **1946**, 33, 166-175.

[6] R. S. Knox, *J. Biomed. Opt.,* **2012**, 17, 0110031-0110036.

[7] J. R. Lakowicz, *Principles of Fluorescence Spectroscopy,* Springer, Singapore, **2006**.

[8] I. Medintz and N. Hildebrandt, *FRET-Förster Resonance Energy Transfer,* Wiley-vch, Singapore, **2014**.

CHAPTER 2

Nanostructured Hybrid Antenna Systems. Laser Dyes in LTL Zeolite

The allocation of organic fluorophores into nanostructured solid frameworks is a very active area of research due to the forward-possibility to monitor the characteristics of the surrounding solid host and additionally improve the properties of the enclosed guest in order to develop advanced smart materials [1]. In this last regard, we pretend to insert laser dyes into channeled frameworks and take advantage of the cage protecting effect of the constrained solid host to build up ordered photoactive materials susceptible to be used as antenna systems. Accordingly, suitable dyes, with absorption and emission properties in different spectral regions and capable to give rise to excitation energy transfer (EET) processes were sequentially enclosed into the unidimensional channels of Linde Type L (LTL) zeolite (Figure 2.1). The final aim consists in a customized design of a well organized antenna material in which light over a wide spectral region is efficiently absorbed and transported to the desired place, via successive energy transfer hops and with a given energy (i.e., red emission).

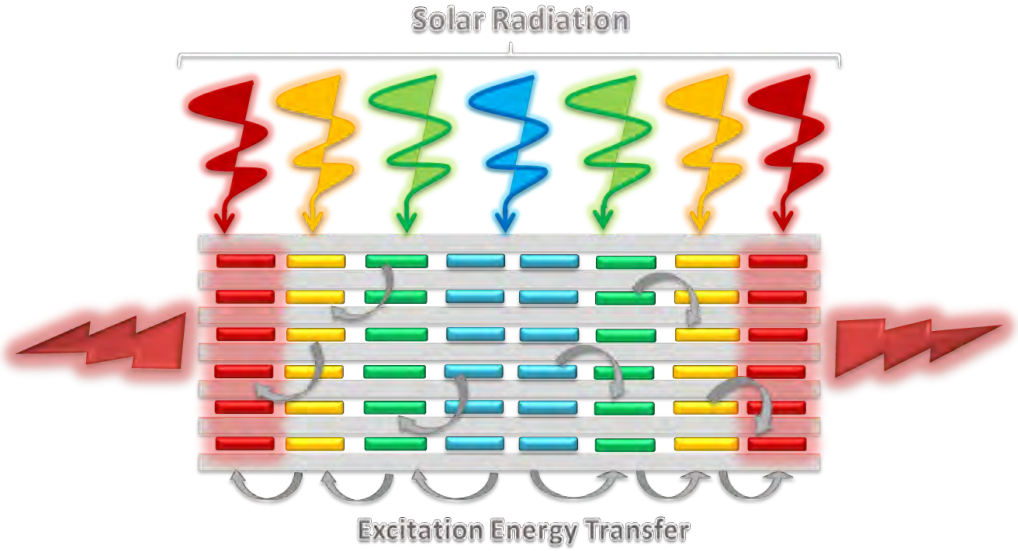

Figure 2.1. Schematic overview of an artificial photonic antenna.

In the following sections, we first present a brief description of the procedure developed for the synthesis of the inorganic framework (LTL Zeolite), and afterwards we get immerse into the shaping of tailor-made hybrid antenna systems by allocating carefully chosen organic molecules (guests) which are also photophysically characterized in depth. More detailed information can be found in the published articles attached to the chapter.

2.1. LTL Zeolite. Microwave Assisted Hydrothermal Synthesis

Nowadays, there are available a wide variety of inorganic molecular sieves [2]. The aluminosilicates known as zeolites have deserved considerable attention from the scientific community due to their well defined and diverse frameworks (from cavities to pores) [3]. Among them, Linde Type L (LTL) zeolite, which presents unidimensional channels, fits well to our scope and has been chosen as the ideal host to allocate organic fluorophores [4]. In fact, LTL zeolite is a very versatile material that can be applied in a broad range of fields, including catalytic processes, ion exchange and separation, antenna materials, photosensitizers in solar cells or light-emitting diodes, luminescent solar concentrators, and also in bio-medicine, where it is widely used [5-11].

LTL zeolite is a crystalline aluminosilicate of well-defined three-dimensional framework and a hexagonal symmetry (Figure 2.2). It is formed by corner sharing TO_4 tetrahedra (T being aluminum or silicon), which leads to a three dimensional network (cancrinite cages). The presence of the trivalent aluminum infers an anionic character to the framework and charge compensating cations are required to balance the charge of the tetrahedra. This is why the stoichiometry of LTL zeolite with monovalent charge compensating cations M^+ is $M_9[Al_9Si_{27}O_{72}]\cdot nH_2O$, where the number of water molecules n per unit cell equals 21 in fully hydrated materials and is about 16 at 20% relative air humidity. The connection of the cancrinite units give rise to one-dimensional channels running along the c-axis of the crystals and with a pore opening diameter of 7.1 Å (Figure 2.2) [4]. Therefore, this kind of framework is an excellent candidate for shape-selective hosting of guests (such as ions, metals or organic molecules).

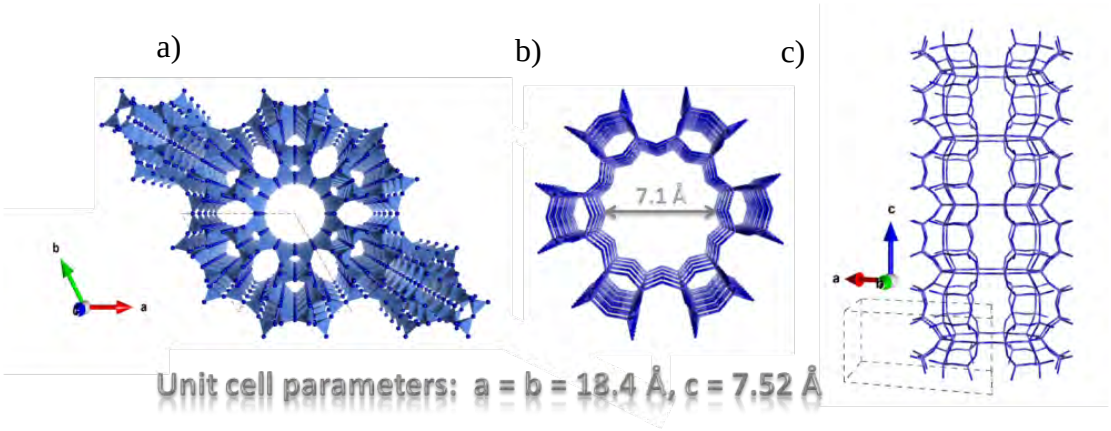

Figure 2.2. a) Top view of LTL zeolite framework, illustrating the hexagonal structure. b) Pore opening of LTL zeolite viewed along the c axis. c) Side view of a channel that consist of 0.75 nm long unit cells with a van der Waals opening of 0.71 nm at the smallest and 1.26 nm at the widest place.

LTL zeolites are usually achieved by hydrothermal synthesis, in which an aqueous suspension containing the silica source and a solution containing the aluminum source in a basic environment are mixed to form a milky gel phase. Afterwards, the gel is heated at reaction temperatures generally above 100ºC in a sealed high pressure politetrafluoroethylene (PTFE) vessel for a certain period of time (suitable for each kind of zeolite) (Figure 2.3) [12]. The size and morphology of the obtained LTL zeolite crystals can be modulated in a large range by changing the source of reactants, composition of the starting gel (water content, alkalinity or oxide proportions) as well as the heating conditions (heating rate or temperature) and aging time of the gel (Figure 2.3) [13-15].

Recently, the use of microwave heating has arisen as a valuable alternative in modern synthesis of nanoparticles and nanostructures [16-19]. It provides an accurate control of the heating, which ensures a fine control of the temperature without gradients within the oven and samples. As consequence, the heating process is more efficient, the reaction times are significantly reduced, and the side reactions are prevented in great extent. This means an improvement in the yield and reproducibility of the process and should allow the acquisition of LTL zeolite crystals with higher quality in comparison to those obtained using conventional ovens. It is noteworthy that high quality crystals (which means homogeneous and narrow size distribution, high crystallinity and defined morphology) are essential for the development of competitive and customized materials.

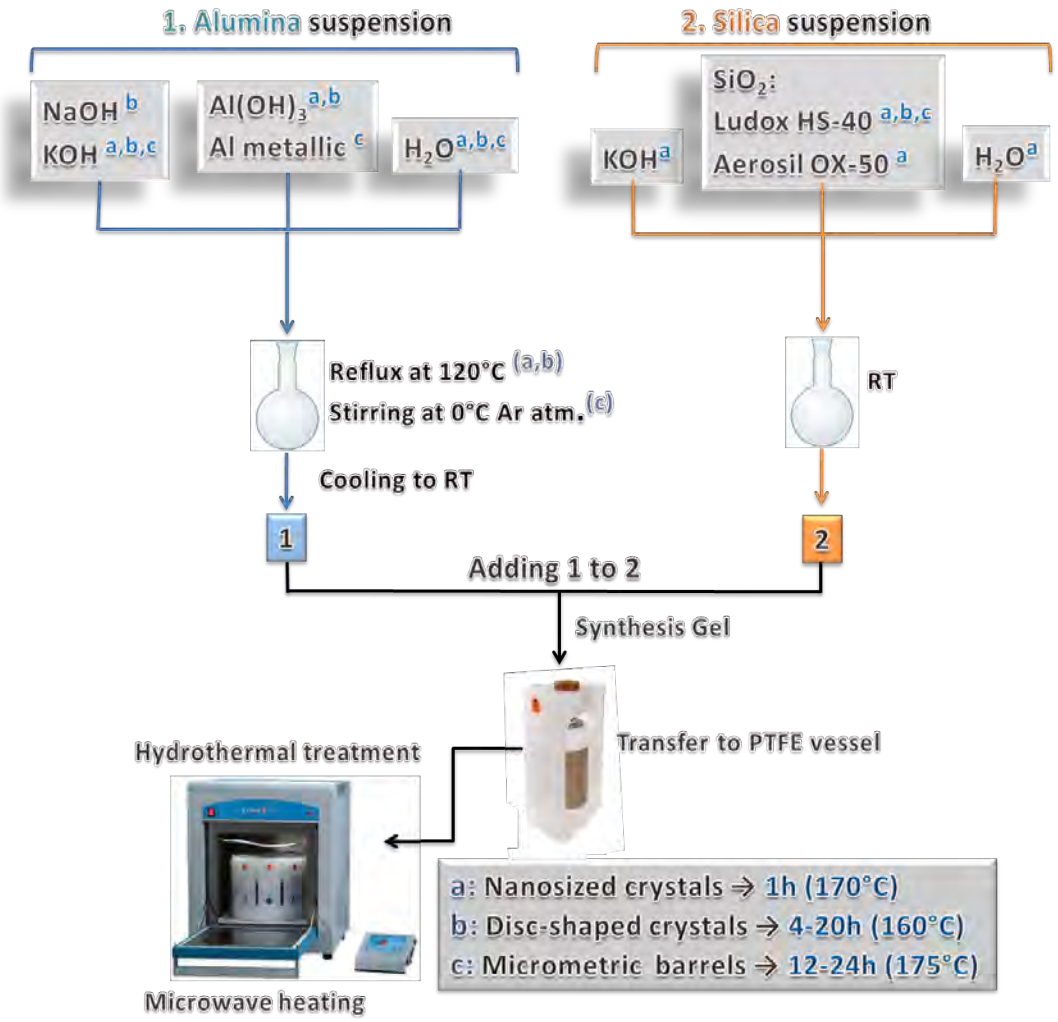

Figure 2.3. Scheme of the hydrothermal synthesis route for a) nanosized, b) disc-shaped and c) micrometric barrel-shaped LTL crystals.

Against this background, we have adapted the optimal synthetic conditions previously reported to grow LTL crystals with conventional ovens [20] to microwave heating. Thus, LTL zeolite ranging from nanometers (15 nm) to micrometers (3 μm), with coin, disc or barrel-shape has been synthesized from a suitable gel composition and synthesis conditions for each kind of zeolite. The effect of the reaction conditions (heating rate, temperature and time) and gel pre-treatment into the size and morphology of the resulting crystals have been analyzed. The main characteristics of the herein developed materials have been summarized in Table 2.1. In all cases, microwave heating reduced the synthesis time up to 90% with regard to conventional ovens (days to hours) and the consequent energy savings.

Table 2.1: Synthesis and material characteristics.

	Length c-axis (nm)	Aspect ratio[a]	Gel composition $K_2O:Al_2O_3:SiO_2:H_2O$	Crystallization				Silica source[d]	Variation
				h.r.[b]	t/h	T/°C	cond.[c]		
Nanozeolites	15-20	2.5	9.34:1.00:20.20:412.84	10′	1	170	d	L	Synthesis conditions
	15-20	2.5	9.34:1.00:20.20:412.84	10′	1	170	a	L	
	40-50	3.5	9.34:1.00:20.20:412.84	10′	1	170	s	L	
	55-65	3.3	9.34:1.00:20.20:412.84	10′	1	170	s	AO	Silica source
Disc or Coin	200	0.3	5.40:*5.50*:1.00:30.00:416.08[e]	1h	4	160	s	L	NaOH addition and increase of reaction time
	160	0.2	5.40:*5.50*:1.00:30.00:416.08[e]	1h	6	160	s	L	
	140	0.15	5.40:*5.50*:1.00:30.00:416.08[e]	1h	8	160	s	L	
	130	0.11	5.40:*5.50*:1.00:30.00:416.08[e]	1h	12	160	s	L	
	180	0.15	5.40:*5.50*:1.00:30.00:416.08[e]	1h	20	160	s	L	
Large crystals	1500-3000	1.4-2.0	2.21:1.00:9.00:164.60[f]	10′	12	175	s	L	Increase of heating rate
		1.5-1.9	2.21:1.00:9.00:164.60[f]	20′	12	175	s	L	
		1.6-1.8	2.21:1.00:9.00:164.60[f]	1h	12	175	s	L	Increase of reaction time
		1.6-2.0	2.21:1.00:9.00:164.60[f]	1h	18	175	s	L	
		1.8-2.2	2.21:1.00:9.00:164.60[f]	1h	24	175	s	L	

[a] Calculated from the ratio between the mean length and the mean diameter; [b] Heating rate; [c] crystallization conditions: d = dynamic, s = static, a= aging of the gel; [d] L = Ludox, AO = Aerosil OX-50; [e] 5.40 K_2O-5.50 Na_2O-1.00 Al_2O_3-30.00 SiO_2-427.00 H_2O; [f] Aluminum metallic as aluminum source.

Following, we will briefly describe the synthesis and principal characteristics of each kind of LTL zeolite: nanozeolite, disc or coin shaped, and large crystals.

2.1.1. Nanozeolites

Small zeolites provide a much easier diffusion of guest molecules (i.e., organic molecules, metal complexes, etc.) into the nanochanneled structure of the host, as well as a larger surface area, suitable for employing it as supports in adsorption processes [21,22]. The obtained particle dimensions (Table 2.1) range from 15 to 50 nm and the nanocrystals were straightaway identified by the X-ray diffraction (XRD) pattern (Figure 2.4.a). The size distribution analysis was not viable because of their general tendency to agglomerate into larger clusters of 80–100 nm.

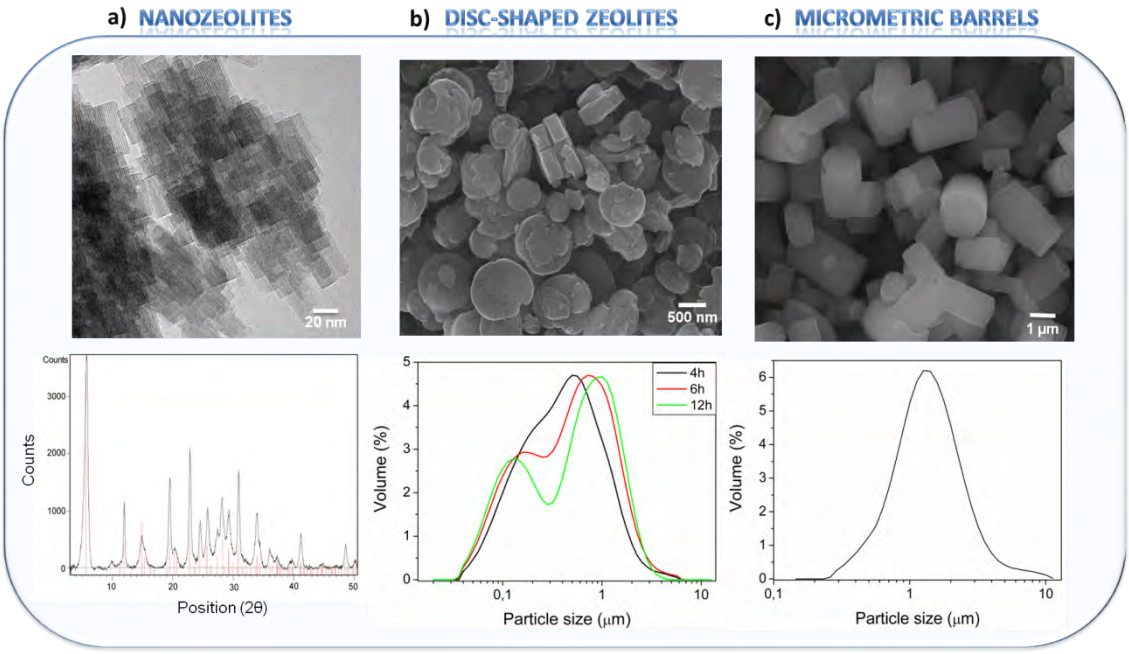

Figure 2.4. a) Transmission electron microscopy (TEM) image of LTL zeolite nanocrystals (top), and the corresponding X-ray diffraction pattern (bottom) for phase identification (powder diffraction file from the database in red is included for comparison). b) SEM image of disc-shaped LTL zeolite crystals and the particle size distribution by DLS for crystals synthesized under different reaction times. c) SEM image of micrometer barrel LTL zeolite crystals together with the corresponding representation of particle size distribution.

The growth of crystals can be controlled by several factors: (i) static/dynamic conditions during synthesis, (ii) previous aging of the gel before heating or with (iii) different silica sources (Table 2.1):

(i) Although stirring during the synthesis of LTL zeolite had almost negligible impact in the crystal size using conventional ovens [23], smaller crystals (around 15–20 nm) have been achieved using microwaves with dynamic conditions. The crystallization process is thermally activated, thus the heating method has a crucial role in it, particularly the rate and uniformity of the heat applied to the reaction mixture, which is enhanced by microwave heating. Therefore, stirring hampers crystal growing and favours the formation of more seeds, leading to smaller crystals.

(ii) The aging of the synthesis gel at room temperature before crystallization also promotes the formation of abundant uniformly distributed nuclei rather than their growth, giving rise to an average reduction of the crystal size from 40 to 20 nm.

(iii) Finally, the effect of different silica sources has been also checked: a water silica suspension (LUDOX HS-40) or a suspension prepared from silica powder (Aerosil OX-50). The latter one yielded slightly larger crystals as confirmed by the average crystal size estimated by the Scherrer equation:

$$\beta_{hkl} = k\lambda/L_{hkl} \cos\theta \qquad \text{(eq. 2.1)}$$

where k is a dimensionless shape factor (k = 0.9), λ is the X-ray wavelength (λ = 1.54 Å), L_{hkl} the line broadening at half maximum intensity (β_{Inst} = 0.1°), and θ is the Bragg angle. Indeed, it has been reported that crystallization using Ludox HS-40 produces a very sharp crystallization curve due to rapid nucleation of the desired structured after 5 h [24]. Thus, Ludox HS-40 provides more nuclei, which implies a high number of crystals with a smaller size.

Therefore, smaller nanocrystals were obtained using Ludox as the silica source, dynamic conditions or previously aged gel (Table 2.1).

2.1.2. Disc-shaped LTL Zeolites

This type of zeolites are characterized by a large basal surface with regard to the coat of the crystal (aspect ratio ‹ 1, defined as length/diameter ratio), a desirable morphology to ease their coupling with external devices, and to build uniform and well-organized monolayers or membranes [25]. The synthesis of thin platelets with minimal diffusion pathlengths and large external porous surface area (around 100 000 channels in a crystal with diameter of 600 nm) allow the optimization of properties critical in catalysis, photonic devices, and biomedical applications [26]. That is, the fine tuning of the diameter and thickness of the crystal can be used as a valuable tool to control the accessibility and diffusion of the guest.

The characteristics of the obtained disc and coin shaped LTL zeolite crystals have been collected in Table 2.1. DLS analysis (Figure 2.4.b) show two main populations: one assigned to the length (between 130-200 nm) and the other to the diameter (ranging from 600-1200 nm), pursuant to the crystal surface pierced by the laser radiation.

The thickness can also be adjusted by varying the synthesis conditions: (i) heating rate and (ii) reaction time, as both factors control the growing of the crystal.

(i) A slow heating rate yielded a crystalline phase without signs of amorphous population, whereas a faster one led to a predominantly amorphous phase. Therefore, it seems that a too fast heating rate prevents the formation of the nuclei necessary for the crystallization of LTL zeolite.

(ii) The required minimum reaction time was about 4 hours. The increase of the reaction time from 4 to 12 h led to bigger (longer diameters, from 600 to 1200 nm), but thinner crystals (lower length, from 180 to130 nm) (Figure 2.4.b). From this point on (12 to 24 h), the crystal stopped growing in diameter, but became thicker (180 nm length).

In consequence, we can obtain thin (coins) or thick (discs) particles by just adjusting the reaction time of the microwave oven. Furthermore, enlarged synthesis times led to smooth crystal surfaces (Figure 2.4.b).

The quality of the crystals is not only reflected into a narrow size distribution and homogeneous morphology but also in their purity and crystallinity. The X-ray fullprofile refinement (Figure 2.5) allowed the comparison between experimental and calculated profiles, and the determination of the unit cell parameters (*a*, *b* = 18.35 Å, *c* = 7.52 Å). It is noticeable the nice agreement of the experimental and calculated profiles (Y_{obs}–Y_{calc} values, blue line) of our homemade LTL zeolite crystals, which indicates the absence of crystalline impurities (Figure 2.5.a). The low line broadening in the XRD pattern confirms their high crystalline grade. Indeed, the crystallite size (calculated by the Scherrerr formula (eq. 2.1)) point out that an unique particle contains few crystalline domains. Compared with commercially available disc shaped LTL zeolite crystals (Lucidot), the herein reported one show improved quality in terms of crystallinity (crystallite size along the c-axis ~120 nm compared to the one calculated for the commercial discs Lucidot ~ 65 nm) (Figure 2.5).

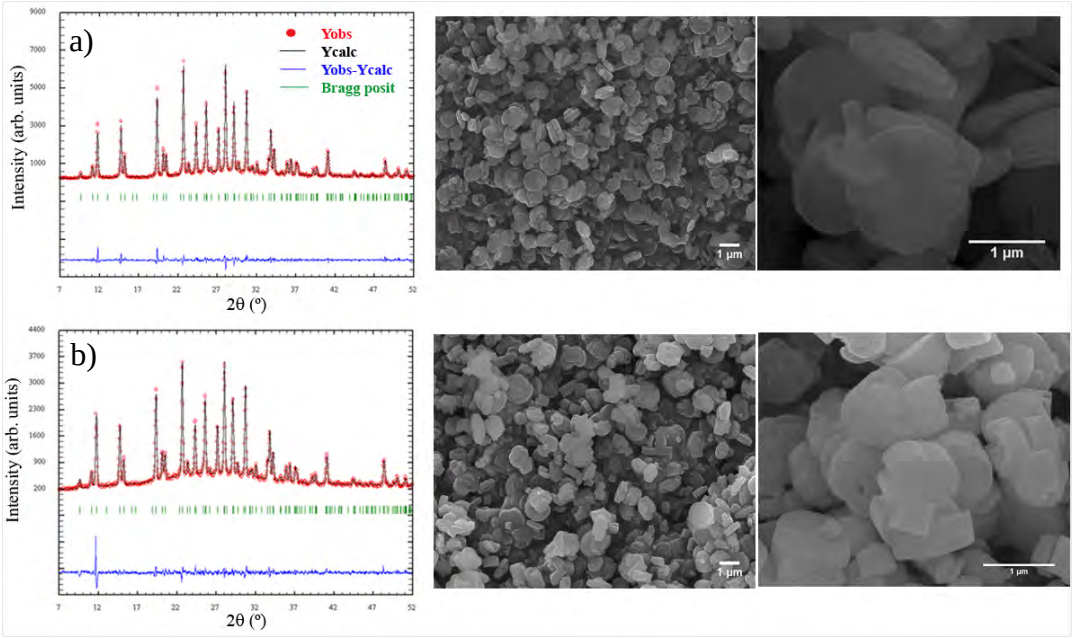

Figure 2.5. XRD Full-profile refinement of a) synthetic vs b) commercial LTL zeolite crystals with its corresponding SEM images.

As a result, disc-shaped crystals with tunable size and thickness can be obtained just adjusting the reaction time and heating rate (Table 2.1 and Figure 2.4.b).

2.1.3. Micrometric LTL zeolite barrels

The synthesis of large LTL zeolite crystals (from 1500 to 3000 nm) with well-defined morphology and high aspect ratio has proven to be useful in the analysis of the distribution, orientation and interaction of guest molecules by time- and space-resolved fluorescence measurements, such as fluorescence confocal microscopy at single-particle level [27].

The LTL zeolite crystallization was confirmed by the X-ray diffraction (XRD) pattern, albeit with small contribution of another crystalline structure, which was identified as zeolite W (Figure 2.6.). This is a synthetic phase with the framework topology of MER (Figure 2.6.b,c). An excess of alkalinity is usually the responsible of the zeolite W crystallization [28] which can be removed by sedimentation.

a)

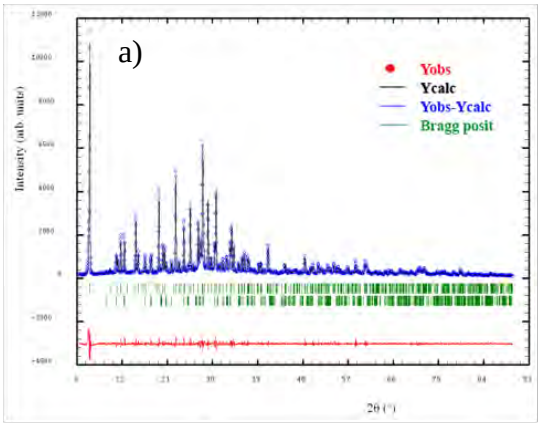

b)

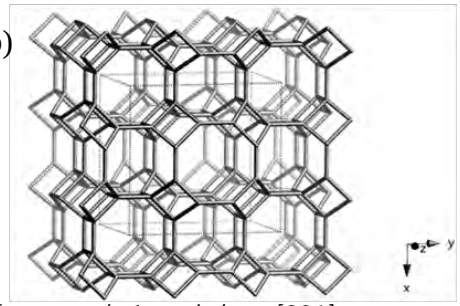

framework viewed along [001]

c)

	Zeolite type	Space Group	Framework type	Unit cell parameters
Phase No. 1	L	P6/mmm hexagonal	LTL	a=b=18.35Å c=7.51 Å
Phase No. 2	W	I mmm orthorhombic	MER	a=14.13 Å b=14.22 Å C=9.92 Å

Figure 2.6. a) X-ray full-profile refinement including both phases LTL zeolite and zeolite W. b) Framework type MER viewed along [001], corresponding to zeolite W. c) Main characteristics of LTL and W zeolites.

The DLS size distribution (Figure 2.4.c) reveal one main population ranging from 1000-3000 nm which comprises both, the length and diameter of the particles, being infeasible to discern between them due to its similar size. Finally, the significantly less intense shoulder at higher sizes (7-10 μm) could be ascribed to the remaining zeolite W particles characterized by bigger sizes compared to those of LTL zeolite, or simply by bigger clusters formed by the agglomeration of LTL zeolite crystals.

Again, the heating rate and reaction time are crucial parameters as both determine the nucleation and growing processes, and therefore the size and morphology of the LTL zeolite crystals. A faster heating rate (from 1 hour to 10 minutes for a fixed reaction time of 12 hours) leads to a higher dispersion of the particle sizes, that means two different particle size populations with unalike aspect ratios (1.4 and 2.0 for a heating rate of 10 min in Table 2.1). Therefore, a too fast heating led to the formation of different types of nuclei, whereas a slower one (1 hour) allow a homogeneous nucleation. On the other hand, an elongation of the reaction time from 12 to 24 hours, with the same heating rate, boosted the elongation of the crystals length and consequently increased their aspect ratio (from 1.8 to 2.2).

As consequence, large cylindrical LTL crystals can be obtained using long reaction times and slow heating rates (Table 2.1 and Figure 2.4.c).

Summing up, LTL zeolite crystals with improved quality and tunable size and morphology are straightforward and successfully achieved by careful control of the microwave heating conditions during the hydrothermal synthesis and with reduced reaction times (just few hours).

These homemade crystals will be the subsequent hosts for the allocation of laser dyes to conform supramolecularly ordered artificial antenna systems, expounded in the following sections (2.2 and 2.3).

More detailed information about the synthesis procedure and characterization of LTL zeolite crystals can be found in the articles published in *Particle* and *Chemical Engineering Journal* attached bellow. In particular, for a deep description of the synthesis route of nanozeolite and disc-shaped LTL zeolite crystals look up the *Particle* report, while for the micrometric LTL zeolite barrels go through the experimental section of *ChemPlumChem* article enclosed in section 2.2.2. Moreover, in these reports the LTL zeolite crystals have been successfully applied as catalytic supports for metals deposition (rhodium and nickel) in biogas reforming processes, a clean, environmental friendly and renewable way to produce hydrogen from biomass.

Particle
& Particle Systems Characterization
www.particle-journal.com
www.MaterialsViews.com

Microwave Synthesis of LTL Zeolites with Tunable Size and Morphology: An Optimal Support for Metal-Catalyzed Hydrogen Production from Biogas Reforming Processes

*Leire Gartzia-Rivero, Jorge Bañuelos, Urko Izquierdo, Victoria Laura Barrio, Kepa Bizkarra, José F. Cambra, and Iñigo López-Arbeloa**

Here, a method is described for the synthesis of Linde type L (LTL) zeolite under microwave-assisted hydrothermal conditions, and its behavior as a support for heterogeneously catalyzed hydrogen production is detailed. Microwave heating reduces the reaction time and improves the quality of the LTL zeolite crystals in comparison to those obtained using conventional ovens. The size and morphology of zeolite can be finely modulated by the composition of the gel and reaction conditions (heating rate, static/dynamic conditions, aging, reaction time, etc). The physicochemical properties of the synthesized LTL zeolites make them appropriate catalyst supports for reforming reactions in which high hydrogen production yields are desired. Therefore, rhodium- and nickel-based bimetallic catalysts are prepared in order to be tested by dry and oxidative biogas reforming processes at 800 °C and atmospheric pressure for hydrogen production. For all the catalysts tested, except for the sodium-exchanged disc-shaped zeolite, hydrogen yields close to the predicted by the equilibrium conversion are reached.

1. Introduction

The term "zeolite" is said to have its origin in the two Greek words *zeo* and *lithos,* meaning "boiling stone."[1] In general, zeolites are microporous crystalline aluminosilicates with well-defined 3D pore structures where water and other types of molecules, such as co-cations and organic molecules, can allocate.[2] Among the wide variety of natural and synthetic zeolites, Linde type L (LTL) zeolite is one of the most interesting and versatile hosts. Its framework is characterized by one-dimensional (1D) channels running along the crystal with hexagonal symmetry. The well-arranged pores of around 7.1 Å in diameter make this kind of framework an excellent candidate for shape-selective catalysis, for hosting of several different type of guests (such as ions, metals, and organic molecules), and for mass transport and/or occlusion.[3] In fact, LTL zeolite has been used in a broad range of fields, including catalytic processes,[4] ion exchange and separation,[5] antenna materials,[6] photosensitizers in solar cells or light-emitting diodes, luminescent solar concentrators,[7] color changing media, and also in bio-medicine, where it is widely used.[8]

For these nanoscale materials to be competitive, it is essential to ensure a good quality of the LTL zeolite crystals, which means achieving homogeneous size distribution of the crystals, defined morphology, and high crystallinity. LTL zeolite is mostly synthesized under hydrothermal conditions using high-pressure vessels and heating with conventional ovens. Gel composition (that is, water content, alkalinity or oxide proportion) as well as the heating conditions (that is, heating rate or temperature) determines crystal size and morphology. LTL zeolite with sizes ranging from nanometers to micrometers and barrel- or disc-shaped morphology have been reported.[9]

Microwave heating has become a valuable tool in modern organic synthesis and in the production of nanoparticles and nanostructures. It provides accurate control of the temperature, ensuring temperature uniformity, preventing gradient formation within the oven and samples. Therefore, the heating process is more efficient, chemical reaction times are reduced, and side reactions are avoided in great extent. This means an improvement in the yield and reproducibility of the process and hence a friendlier environmental methodology.[10]

For this study, we have extrapolated the optimal conditions described in previous reports on LTL zeolite synthesis using conventional ovens to microwave heating.[11] One of the aims of this work is to improve crystal quality and to decrease the reaction time needed for its synthesis, which otherwise takes several days. We have analyzed the effect of the reaction conditions (heating rate, time, temperature and static/dynamic conditions) on the size, morphology, and chemical properties (acidity and ion exchange capacity) of the resulting crystals.

These LTL zeolite crystals were then used as catalyst supports owing to their high surface area and structural stability,

L. Gartzia-Rivero, Dr. J. Bañuelos,
Prof. I. López-Arbeloa
Dpto. Química Física
Universidad del País Vasco (UPV/EHU)
Aptdo 644, 48080 Bilbao, Spain
E-mail: inigo.lopezarbeloa@ehu.es
U. Izquierdo, Dr. V. L. Barrio,
K. Bizkarra, Prof. J. F. Cambra
Dpto. Ingeniería Química y MedioAmbiente
Universidad del País Vasco (UPV/EHU)
C/Alda. Urquijo s/n, 48013 Bilbao, Spain

DOI: 10.1002/ppsc.201300275

combined with their chemical composition.[12,13] Once the catalysts were prepared, the biogas valorization—a renewable resource for hydrogen production through dry and oxidative reforming (DR and OR, respectively)—processes were studied. The DR process is being widely studied because methane and carbon dioxide are consumed in the system, both of which are considered to be the most harmful green house gases. Regarding the active phase of the catalysts, nickel and rhodium metals were used to prepare the corresponding bimetallic catalysts.

The selection of the type of process and the experimental conditions have been carried out on the basis of our previous results; it was reported that a ratio of $O_2/CH_4 = 0.25$ was the most appropriate one to reach the highest hydrogen production yield for OR process,[14] and a H_2/CO ratio around 1 was appropriate for the hydroformylation reaction.[15,16]

With regard to the active metal species incorporated into these supports, nickel was chosen because it is widely used for reforming reaction catalysts, mainly owing to its high activity, availability, and relatively low price. However, it is well known that noble metals, such as rhodium (Rh), ruthenium (Ru) and palladium (Pd), are much more active and stable, and their use decreases the tendency for coke formation in the catalytic surface at high temperatures,[17,18] especially when Rh and Ru are used.[19] Although the noble metals are much more expensive, their use is recommended because the addition of small amount of noble metal to a non-noble metal catalyst leads to an increase in the activity owing to the spill-over effect.[20] Therefore, the synthesized zeolites under microwave heating have been tested as support for the corresponding catalysts. To this end, the parameters to evaluate the methane and carbon dioxide conversion, as well as hydrogen production yield, have been calculated to understand their activity.

2. Results and Discussion

The size and morphology of LTL zeolite crystals can be modulated by changing the source of the reactants, the composition of the gel (alkalinity, water content, SiO_2/Al_2O_3 ratio, etc.), the reaction time, the reaction temperature and the aging time of the gel. We initially used a fixed gel composition (previously optimized)[11a] for each type of zeolite (nanocrystals and disc- or coin-shaped crystals) and analyzed the influence of the reaction conditions and gel pre-treatment in the microwave-assisted hydrothermal synthesis. In all cases, this type of heating reduced the synthesis time up to 90% with regard to conventional ovens (days to hours) and allowed a more precise control of the temperature, preventing gradient formation within the sample. Therefore, zeolites can be produced in few hours, with consequent time and energy savings and improved quality.

2.1. LTL Zeolite Nanocrystals

In these small zeolites, diffusion of the guest molecules (i.e., metals) deeper inside the pores of the host is much easier, and at the same time, they are better supports for adsorption processes because of a larger external surface.

The general hydrothermal synthetic route is detailed in the experimental section. The oxide molar ratio in the gel was fixed at $9.34K_2O{:}1.00Al_2O_3{:}20.20SiO_2{:}412.84H_2O$.[11a] The nanocrystals were successfully obtained after heating at 170 °C for 1 h and straightaway identified by the X-ray diffraction (XRD) pattern. The corresponding dimensions, ranging from 15 to 50 nm were determined using scanning (SEM) and transmission (TEM) electronic microscope images (**Figure 1**). The particles show a general tendency to agglomerate into larger clusters of 80–100 nm, not allowing a size distribution analysis.

The growth of crystals can be controlled by several factors such as static/dynamic conditions during synthesis, previous aging of the gel before heating or with different silica sources. Figure 1 and 1d show the TEM images of the nanocrystals obtained under static and dynamic conditions (stirring during the synthesis). The static crystallization led to crystals with a size of about 40 nm, whereas the dynamic conditions yielded smaller crystals (around 15–20 nm), both keeping the cylindrical morphology (aspect ratio defined as length/diameter, decreased from 3.5 to 2.5). In previous reports using conventional heating, dynamic and static conditions had a negligible impact on the size or morphology of crystals smaller than 1000 nm.[11] The crystallization process is thermally activated, thus the heating method has a crucial role in it, particularly the rate and uniformity of the heat applied to the reaction mixture, which is enhanced when microwave heating is used. Therefore, stirring is recommended for smaller nanoparticles probably because it hampers crystal growing and favors the formation of seeds.

The aging of the gel, before the heating process, also determines the nucleation or growth of the crystals. Figure 1e shows that a 4-h aging process at room temperature allowed crystals to be obtained with a length of around 20 nm and an aspect ratio of about 2.5. Thus, when compared with the nanocrystals synthesized in static conditions, the aging of the gel reduces crystal size, because as with the dynamic conditions, it boosts the formation of more nuclei rather than their growth.

Finally, we also checked the effect of silica source: a water-silica suspension (LUDOX HS-40) or a suspension prepared from silica powder (Aerosil OX-50). Each type of silica contains different impurities exerting different effects on crystal nucleation, thus generating LTL zeolite crystals with characteristic properties in each case. The LTL zeolite nanocrystals obtained using Ludox HS-40 as the silica source and those generated with Aerosil OX-50 are depicted in Figure 1 and **Figure 2**, respectively. The latter crystals, in Figure 2, seem to be slightly larger. To verify the intuitive results from the TEM images, the average crystal size was estimated (defined as average domain size) by the Scherrer equation:

$$\beta_{hkl} = k\lambda / L_{hkl} \cos\theta \quad (1)$$

where k is a dimensionless shape factor ($k = 0.9$), λ is the X-ray wavelength ($\lambda = 1.54$ Å), L_{hkl} the line broadening at half maximum intensity ($\beta_{Inst} = 0.1°$), and θ is the Bragg angle. This equation was applied for two different reflection families, such as (00l) and (hkl), from which information related to the length and diameter of the crystals was respectively extracted.

Results confirmed that the crystals achieved using Aerosil OX-50 were slightly longer. Possibly, the synthesis gel prepared with Aerosil OX-50 needs a much longer crystallization time to yield the same product than when using Ludox HS-40. That

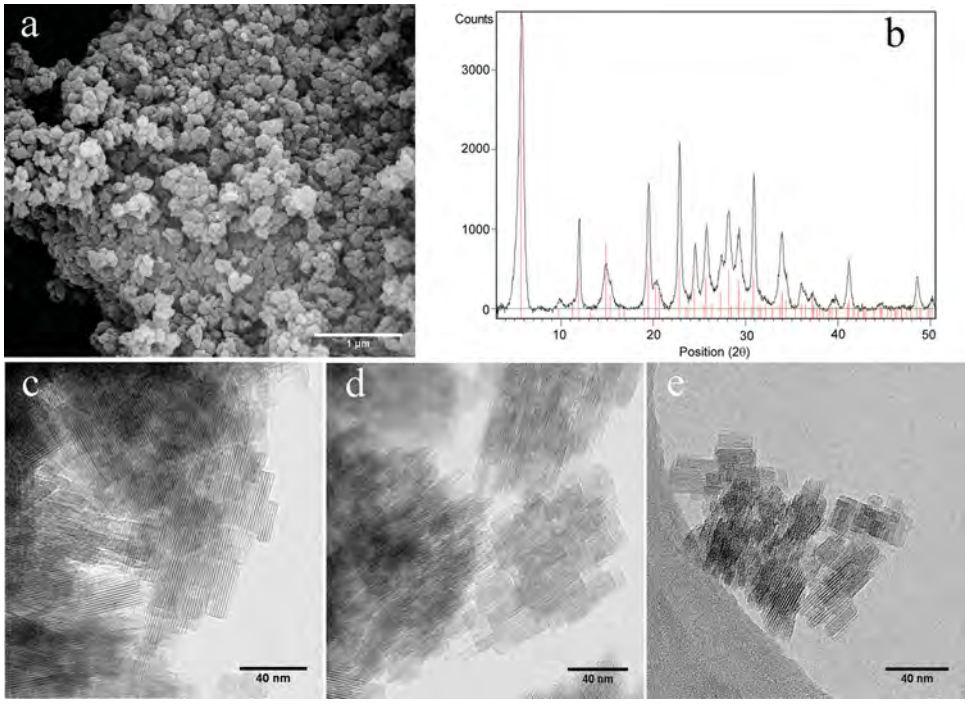

Figure 1. a) Scanning electron microscopy (SEM) image of LTL zeolite nanocrystals, synthesized with Ludox OX-50, and b) the corresponding X-ray diffraction pattern (background extracted) for phase identification (powder diffraction file from database in red is included for comparison). Transmission elelctron microscopy (TEM) images of LTL zeolite nanocrystals obtained under c) static or d) dynamic conditions and e) after aging of the synthesis gel.

is, Ludox HS-40 allows a faster nucleation time and provides more nuclei, which implies a high number of crystals but with a smaller size.

Therefore, smaller nanocrystals are obtained using Ludox as the silica source and dynamic conditions for an aged gel.

2.2. Disc-Shaped LTL Zeolite Crystals

In the previous section, we showed how crystal size can be adjusted by the synthesis conditions. Nonetheless, the morphology of the crystal can also be controlled. Thus, crystals with disc shape are available (low aspect ratio) where their thickness can be also modified in a controlled way. This type of zeolites are desirable to ease their coupling with external devices (i.e., to obtain uniform and well-organized monolayers or membranes),[21] and to have a high number of 1D pores with short diffusion path lengths (around 100 000 channels in a crystal with diameter of 600 nm).[22]

The synthetic procedure is detailed in the experimental section. Gel composition was set at $5.40K_2O$:$5.50Na_2O$:$1.00Al_2O_3$:$30.00SiO_2$:$416.08H_2O$ oxides molar ratio,[11] using Ludox as silica suspension. After heating in a microwave oven at 160 °C, disc-shaped LTL zeolite crystals were achieved. These particles exhibit a homogeneous morphology with an average length of 200 nm, and an average diameter of 1 μm (aspect ratio < 1), which varies upon the heating rate and reaction time, as both factors control the growing of the crystal. Accordingly, the size distribution of these particles studied by dynamic light scattering (DLS) (**Figure 3**) provided two main populations: one assigned to crystal length and the other one to the diameter, depending on the direction the laser passed in the different surfaces of the crystal. The smaller shoulder represents the length of the discs, whereas the higher shoulder shows the data compared against the diameters.

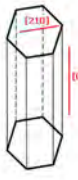

Silica Source	Crystallite Size [nm] (210)	Crystallite Size [nm] (001)
Ludox HS-40	15	50
Aerosil OX-50	9	65

Figure 2. TEM image of LTL zeolite nanocrystals synthesized using Aerosil OX-50 as a silica source. The crystallite sizes (determined by Scherrer formula) are tabulated and classified into the two crystallographic reflections suitable for describing the length (001) and diameter (210), according to the scheme, of LTL zeolite nanocrystals obtained by two different silica sources.

The high quality of the herein reported LTL zeolites obtained by microwave is not only evident by their narrow size distribution and homogeneous morphology but also by their purity and crystallinity. The X-ray full-profile refinement allowed the comparison between experimental and calculated profiles, and the determination of compound unit cell parameters (a,b = 18.35, c = 7.52 Å). **Figure 4** highlights the nice agreement (Y_{obs}–Y_{calc}

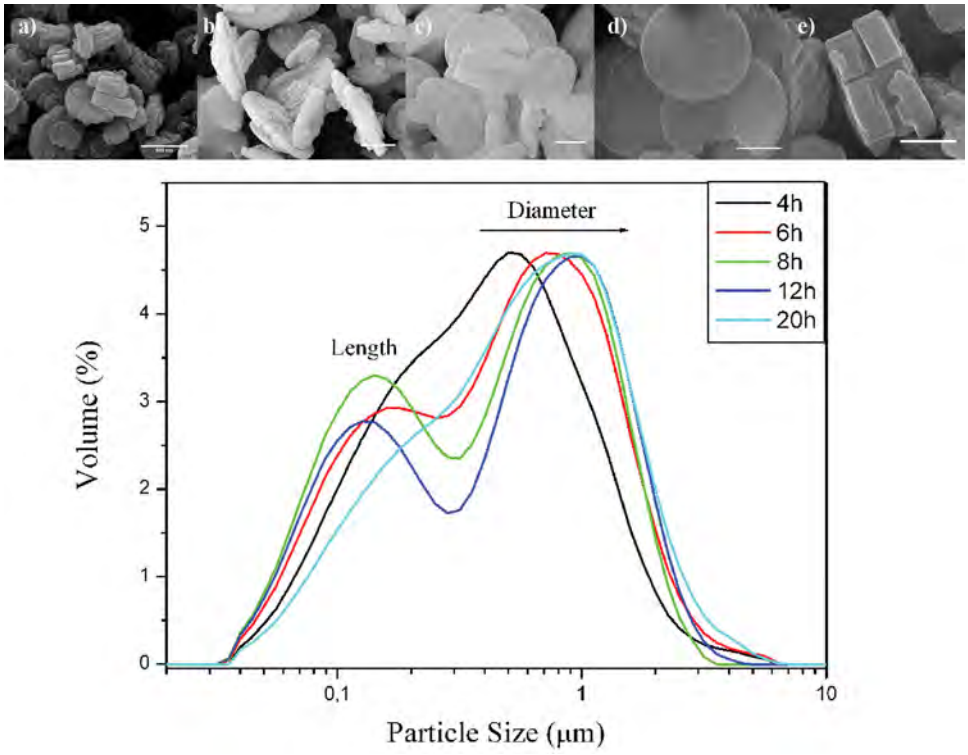

Figure 3. SEM images of disc/coin-shaped LTL zeolite crystals synthesized under a) 4 h, b) 6 h, c) 8 h, d) 12 h, and e) 20 h of reaction time together with the corresponding particle size distribution for each crystal by DLS. All the scale bars indicate the same distance (500 nm).

values, blue line) of our homemade LTL zeolite crystals, without sign of crystalline impurities. The low line broadening in the XRD pattern confirms their high crystalline grade. Indeed, the crystalline size (calculated by the Scherrer formula, Table S1, Supporting Information) reveals that a unique particle contains few crystalline domains, indicating the high quality of the synthesized particles.

The reaction time is a crucial parameter as it determines the nucleation and growing processes, and hence the size and morphology of the LTL zeolite crystals. We have carried out several independent hydrothermal syntheses just changing the reaction time from 4 to 20 h. The increase of the reaction time to 12 h led to bigger (longer diameters, from 0.6 to 1.2 μm), but thinner crystals (lower length, from 180–130 nm), as shown in Figure 3. From this point on, the crystal stopped growing in diameter, only increasing in length, which means thicker discs (180 nm length). Therefore, we can obtain thin (coins) or thick discs by only adjusting the reaction time in the microwave oven. In fact, in cases in which the length of the crystals was similar to the diameter (reaction time of 4 and 20 h), the peak corresponding to the lowest sizes could not be properly distinguished due to the proximity between them. Furthermore, enlarged synthesis times led to smooth crystal surfaces (Figure 3). Therefore, crystals with aspect ratio between 0.3 (discs) and 0.12 (coins) can be generated by only changing the reaction time in few hours. This implies that the number of pore openings per total external surface of the crystals can be controlled, as well as the diffusion path length, which is expected to have an impact on reaction rates.

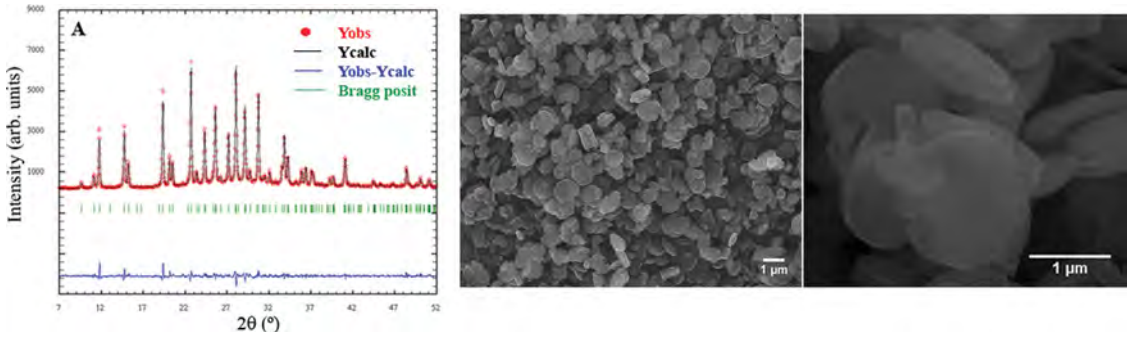

Figure 4. X-ray full-profile refinement of LTL zeolite synthesized by microwave fitted by the FullProf program without structural model. SEM images at different magnifications are also enclosed.

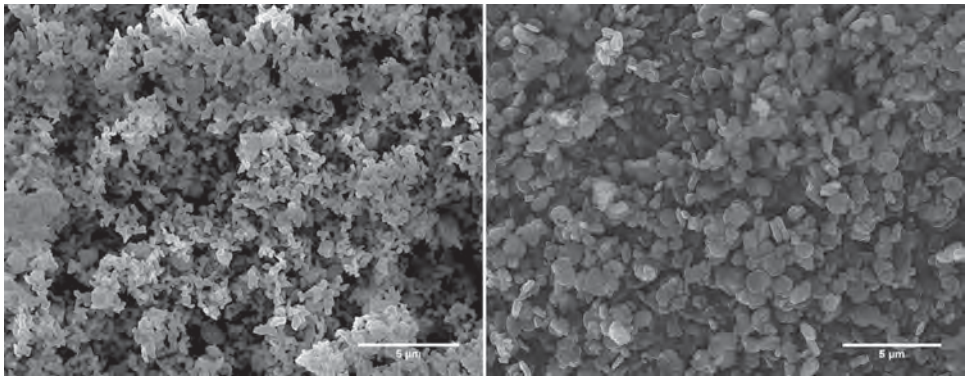

Figure 5. SEM pictures of LTL zeolite crystals after 4 h of crystallization and different heating rates: a) 10 min, b) 1 h.

In contrast to conventional ovens, microwave ovens allow controlling the heating rate, which greatly improves the heat-up speed and prevents temperature gradients. Thus, we analyzed the time needed to reach the synthesis temperature (from 10 min to 1 h) maintaining the same reaction time and temperature. **Figure 5** shows that a faster heating rate led to a predominantly amorphous phase, whereas the slower one yielded a more crystalline phase without signs of amorphous population. It seems that a heating rate that is too fast prevents the formation of the nuclei necessary for the crystallization of LTL zeolite, whereas a slower heating rate promotes the formation of abundant nuclei.

Summarizing, highly crystalline discs with a controlled thickness can be obtained by just fixing the reaction time at a slow enough heating rate.

2.3. Catalysts Characterization and Activity

2.3.1. Textural Properties

Table 1 summarizes the textural properties measured for the calcined zeolites and catalysts in which high surface areas are observed, especially for the nano (N) calcined zeolites. The mentioned calcination process directly affects the LTL zeolite surface area, as reported in our previous work,[23] by decreasing their surface area and the total pore volume. In addition, the micropore region is also significantly affected. However, this process is essential to stabilize the support and remove the salts incorporated during the catalyst preparation process.

Table 1. Textural properties of the calcined supports and catalysts.

	BET [$m^2\ g^{-1}$]	Pore volume [$cm^3\ g^{-1}$]	Micro pore volume [$cm^3\ g^{-1}$]	Pore size [radius, *A*]
D-Na^+	0.4	0.0058	0	263.9
Rh-Ni/D-Na^+	3.1	0.0042	0	250.9
D-Cs^+	12.7	0.0757	0.0020	121.6
Rh-Ni/D-Cs^+	17.1	0.1313	0.0009	155.0
Disc	59.0	0.0690	0.0223	30.48
Rh-Ni/D	38.1	0.1261	0.0115	71.96
N-Na^+	143.5	0.7436	0.0225	105.9
Rh-Ni/N-Na^+	42.9	0.1653	0.0044	77.0
N-Cs^+	96.3	0.6473	0.0097	135.6
Rh-Ni/N-Cs^+	36.5	0.1544	0.0024	84.8
N	210.4	0.7851	0.0493	78.61
Rh-Ni/N	68.4	0.1935	0.0093	58.87

Comparing the disc (D) and nano (N) zeolites, higher areas were obtained for the N zeolites, especially for the pure one (210.4 $m^2\ g^{-1}$). Moreover, as expected, in general, lower areas were measured after metal incorporation.

In the case of D zeolites, for the sodium-exchanged ones (D-Na^+) and its homologous catalyst, a very low surface area was measured. This effect could be a consequence of the calcination process where a strong sintering of this support was observed, while the rest of the catalysts maintained their particle size distribution. This could explain the low Brunauer–Emmett–Teller (BET) area measured. In the case of the other two disc zeolites and catalysts, lower areas were measured for the cesium-exchanged (D-Cs^+) zeolite and catalyst in comparison with the D ones. An unexpected higher are for the catalyst than for the support was measured for the D-Cs^+ zeolite.

Attending to the N zeolites, the Na^+ and Cs^+ incorporation decreased the surface area and pore volume, while the pore size increased. The incorporation of Cs^+ reduced to a greater extent the surface area than for the Na^+.

When metal atoms were incorporated to the N catalysts the pore volume decreased, which may be due to the incorporation of the metal particles into the pores. By contrast, the observed increase of such a parameter for the D catalysts might be due to structural changes in the LTL zeolite framework.

2.3.2. XRD Measurements

XRD analyses were carried out for all the reduced catalysts, as represented in **Figure 6**. The structure of the LTL zeolite was perfectly identified by all the peaks detected at the measured 2θ positions from 5 to 42 (powder diffraction File (PDF): 01–080–1580). However, in the case of the Rh-Ni/Disc-Na^+ catalyst, the LTL zeolite structure disappeared because only NaCl, as an impurity (PDF: 01–077–2064), and Ni crystals were detected. This result is in good agreement with the textural properties, measured by means of N_2 absorption–desorption for this catalyst, and low BET surface area and porosity, which could

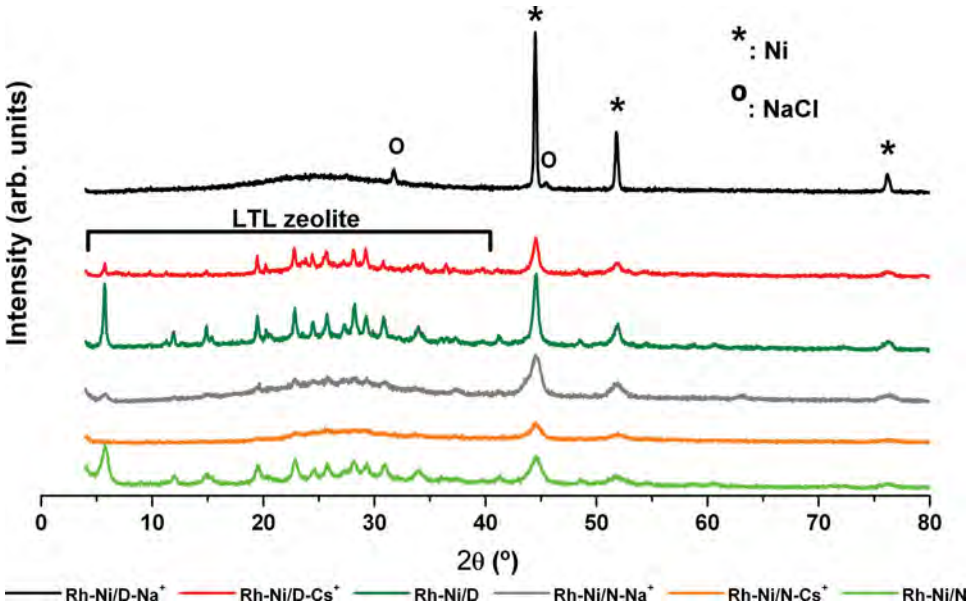

Figure 6. XRD spectra of the freshly reduced catalysts.

Table 2. Ni crystal sizes calculated by Scherrer equation.

Catalyst	Position [°2θ]	Ni crystallite size [nm]
Rh-Ni/D-Na^+	44.48	≈100
Rh-Ni/D–Cs^+	44.48	≈20
Rh-Ni/D	44.49	≈25
Rh-Ni/N-Na^+	44.46	≈10
Rh-Ni/N-Cs^+	44.49	≈10
Rh-Ni/N	44.50	≈10

be associated with the possible sintering process commented above.

The peaks corresponding to the metallic Ni were identified at 2θ values of around 44.5, 53.9, and 76.3° (PDF: 01–087–0712). Taking into account the stronger Ni contribution, 2θ = 44.5°, the crystallite sizes calculated by the Scherrer equation for the catalysts under investigation are summarized in the **Table 2**.

Unfortunately, no Rh contributions were detected by this technique. Thus, this effect can be assigned to the formation of small particles, which could not be detected by this technique (crystal size < 4 nm). Nevertheless, the presence of this metal was confirmed by TEM-EDX, inductively coupled plasma (ICP), and XPS.

2.3.3. TPR Profiles

In the **Figure 7**, the temperature-programmed reduction (TPR) profiles for the fresh calcined catalysts are shown. It is well known that the temperature reduction of particles depends on the location and the type of interaction of the metal with the support.[24] The catalysts supported on the disc-shaped zeolites started the reduction at lower temperature, probably owing to a weaker metal–support interaction.

In addition to the TPR profiles, the deconvolution of the peaks for the Rh-Ni/D and Rh-Ni/N catalysts was carried out in order to explain the contribution to the peaks formed by the different Ni and Rh interactions with the support. For the N catalysts, two main peaks were detected at 470 °C and 565 °C, respectively. According to the literature, the peak at 470 °C is attributed to the reduction of the NiO species.[24] The presence of the peak at higher temperature could suggest a strong interaction between Ni and support. Even more, for these catalysts no Rh species reduction peaks at low temperature were observed. However, for the D catalysts, a rhodium oxide reduction peak at low temperatures, around 185 °C, was detected.[25] For these catalysts, lower temperatures were needed to reduce all of the metal species. In addition, for the D catalysts, the presence of an additional reduction peak was observed, which could be attributed to some other interaction of the metal atoms with the support.

2.3.4. TEM Images

In **Figure 8**, TEM images for the fresh reduced catalysts are depicted. High densities of well-dispersed particles are observed for all the catalysts prepared. Although the dispersion was not measured by this technique, it seems to be high due to the small particle size achieved. However, for the Rh-Ni/D-Na^+ catalyst, larger particles are expected. The obtained images by TEM and the calculated Ni particle sizes by XRD are in good agreement. On the one hand, particles around 100 nm were measured by XRD for the Rh-Ni/D-Na^+ catalyst. However, in general, bigger particles were estimated for the D catalysts than for the N catalysts by XRD, which is also appreciable in the TEM images.

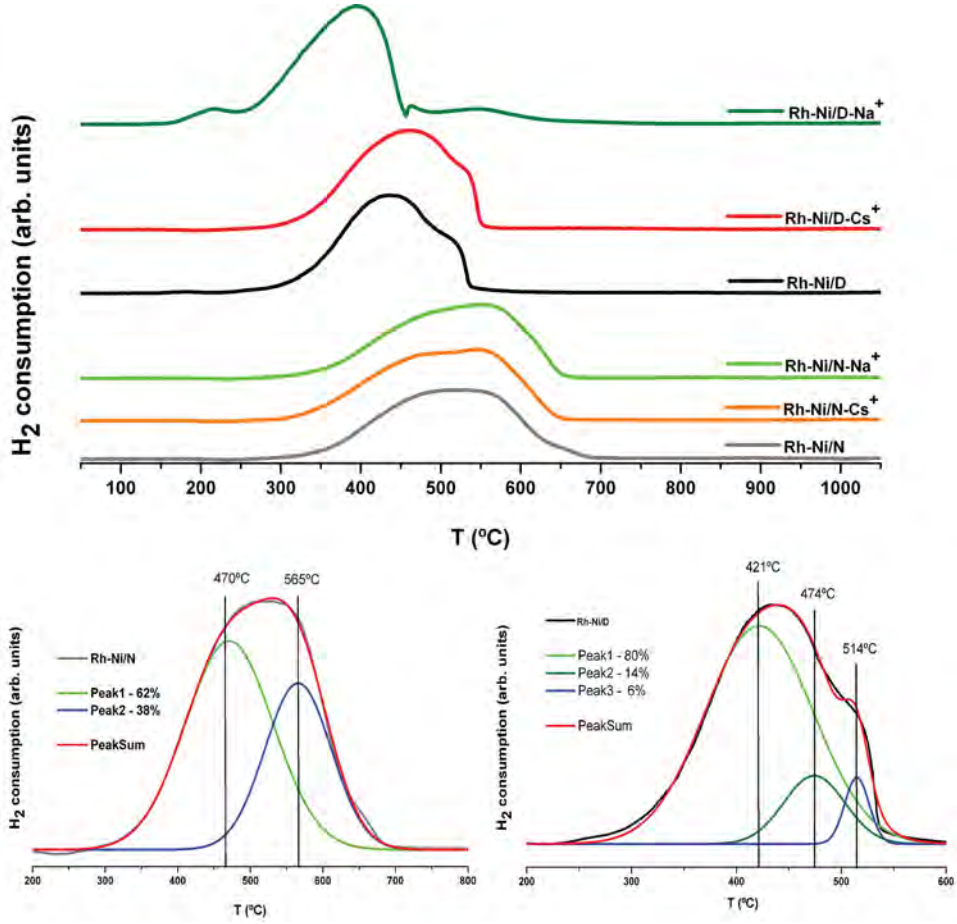

Figure 7. TPR profiles of the freshly calcined catalysts. Deconvolution of the Rh-Ni/N and Rh-Ni/D profiles.

2.3.5. ICP and XPS Characterization Results

Finally, ICP and XPS results are summarized in the **Table 3**. The catalysts chemical composition obtained from ICP revealed Ni and Rh real compositions close to their intended ones (13.0 and 1.0 wt%, respectively). In addition, this technique enables the calculation of a Ni/zeolite atomic ratio to compare it with the ones obtained from XPS analyses. The measured Ni/zeolite atomic ratios by ICP, as the metal and zeolite proportions correspond to the bulk catalysts, are lower than the calculated from the XPS results, because the latter correspond to the external catalyst surface. Thus, higher atomic ratios will be always expected from the XPS measurements.

Among the prepared catalysts, XPS measurements revealed again differences between D and N catalysts. Attending to the Ni atomic concentration, values obtained for the D catalysts are very high compared to the ones for the N catalysts. This is in good agreement with the particle sizes observed in the TEM images and measured by XRD. This high difference could be justified again because the Ni atoms were preferentially located in the outer part of the D catalysts, whereas in the N catalysts, the Ni atoms are located mainly in the inner part of the pores. When N and D catalysts are separately compared, the lower ratios were always calculated for the non-doped supports, and the highest ratios were calculated for the Cs^+-doped supports. Accordingly, it is stated that the presence of Na^+ and Cs^+ hinders the metal incorporation into the pores, in agreement with the BET results commented above. The same behavior was noticed for the Rh atomic ratio. It was not possible to detect it by this technique, due to the presence of Na in the samples.

2.4. Catalytic Activity Results

The previously characterized catalysts were tested in the biogas DR and OR processes. With regard to the results for the DR process (**Figure 9**), high conversion values were obtained by all N catalysts but not for all the D catalysts. Among the N catalysts, no significant differences are observed in their activity. For the three catalysts, carbon dioxide conversion values around 90% and methane conversions around 45% were reached. By contrast, despite the Rh-Ni/D catalyst showed a very similar activity, worse results were measured for the Rh-Ni/D-Cs^+ catalyst. Finally, as expected, no activity was measured by the Rh-Ni/D-Na^+ catalyst in the DR process.

In the case of the biogas OR process, high methane and carbon dioxide conversion values were also reached (**Figure 10**). In addition, the catalysts activity behavior was very similar to the one observed in the DR process. All the N catalysts showed a good catalytic activity, as did the Rh-Ni/D catalyst. The

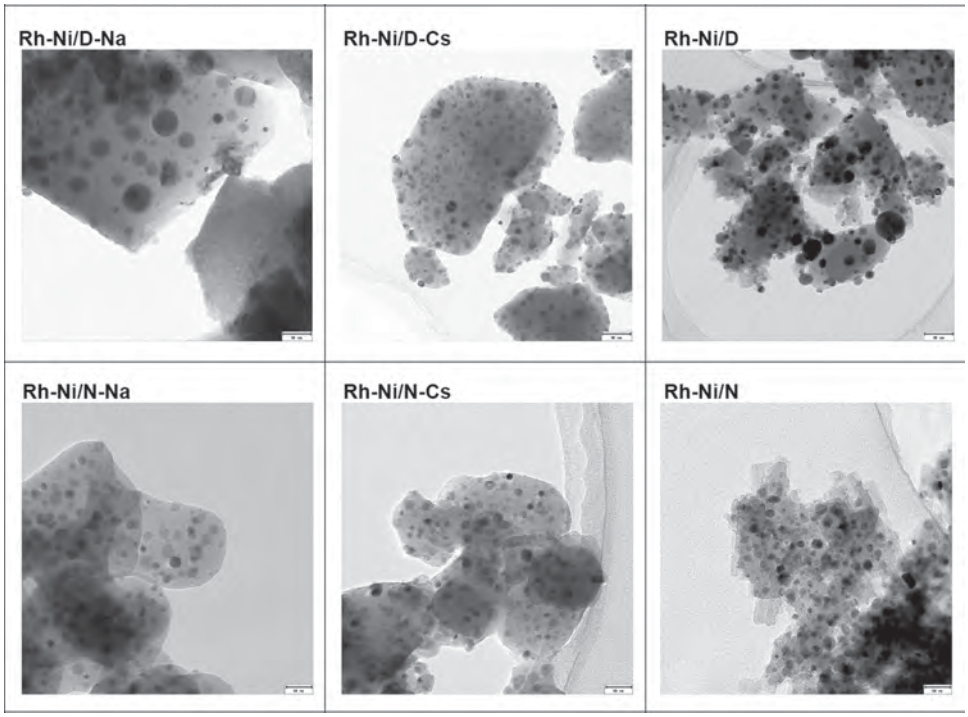

Figure 8. TEM images of the calcined catalysts. Scale size for the disc and nanocatalysts of 80 nm and 30 nm, respectively.

Table 3. ICP measured metal compositions. Ni and Rh atomic ratios calculated for ICP and XPS results.

Catalysts	Composition (ICP, wt%)		Atomic% (ICP)		Atomic% (XPS)	
	Ni	Rh	Ni	Rh	Ni	Rh
Rh-Ni/D-Na^+	11.57	0.84	0.252	0.0083	5.174	–
Rh-Ni/D-Cs^+	12.44	0.78	0.242	0.0076	5.605	1.058
Rh-Ni/D	12.90	0.85	0.223	0.0082	3.098	0.892
Rh-Ni/N-Na^+	11.58	0.86	0.272	0.0091	1.805	–
Rh-Ni/N-Cs^+	13.27	0.82	0.261	0.0079	2.026	0.438
Rh-Ni/N	13.75	0.93	0.223	0.0083	0.470	0.286

Rh-Ni/D-Cs^+ catalyst conversion values were lower and, as a consequence, so too was the obtained hydrogen yield. Finally, the Rh-Ni/D-Na^+ catalyst was also not active for the biogas OR process. For this process, the catalytic activity measured was closer to the calculated equilibrium conversion values.

Regarding the biogas DR and OR catalytic activity, for the fresh calcined LTL zeolites, concordance between catalysts characterization and their catalytic activity is noticed. For the Rh-Ni/D-Na^+ catalyst, low BET areas were measured, and big Ni particles were observed by TEM and measured by XRD. As a consequence, no activity was measured by both DR and OR processes. In addition, for the Rh-Ni/D-Cs^+ catalyst, lower BET areas were measured if they were compared with the more active catalysts. Besides, for this catalyst, the highest Ni atomic concentration was measured by XPS. Focusing on the rest of the prepared catalysts, better characterization results were reported (higher surface areas, better metal surface dispersion, lower atomic concentrations, and lower particle size) and as a consequence, higher hydrogen yields were obtained.

Finally, when comparing the activity between these catalysts and the corresponding ones prepared by conventional techniques presented in a previous work,[23] it can be observed that the relative hydrogen yields obtained depends on the hydrogen production process. Under DR conditions, all the catalysts synthesized under microwave-assisted hydrothermal conditions presented lower hydrogen yields. By contrast, when operating under biogas OR conditions, the cylindrical shaped zeolite catalyst prepared by microwave heating is the most active.

3. Conclusions

High-quality LTL zeolite crystals with tunable size and morphology have been generated by hydrothermal synthesis assisted by microwave heating, simply by adjusting a few reaction conditions (stirring, aging of the gel, time and heating rate) and selecting the appropriate silica source. Thus, crystals of different length (from nanometer to micrometer) and shape (from cylinders to discs with different thickness) can be obtained in a straightforward manner.

The catalytic activities of the catalysts prepared from the not doped LTL zeolites, Rh-Ni/D and Rh-Ni/N, were higher than the corresponding to the Na and Cs exchanged supports, as the differences between them are not significant. In addition, the Na^+ and Cs^+ incorporation affected mainly to the D catalysts, owing to the special morphology of these supports.

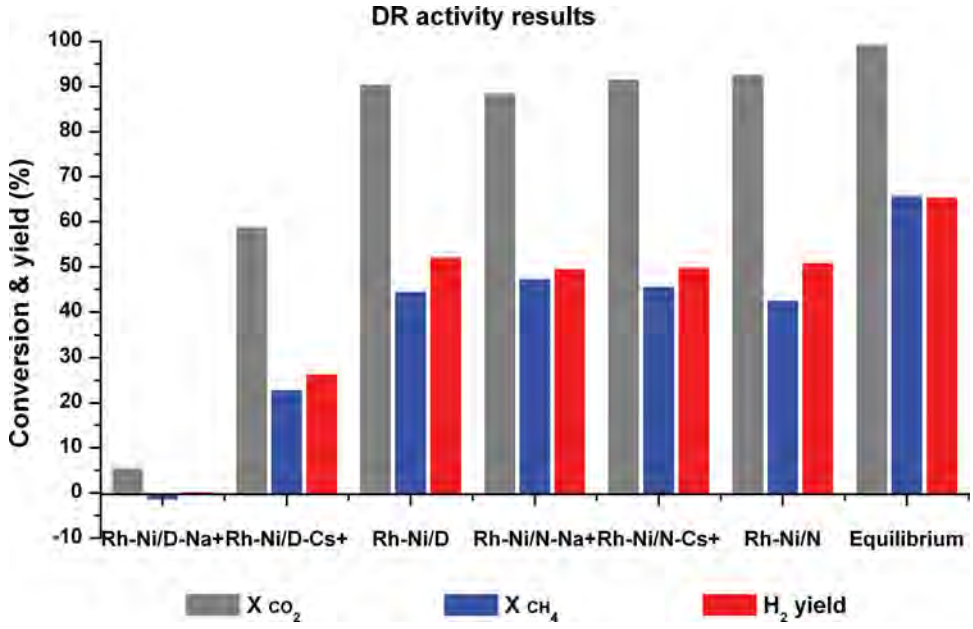

Figure 9. DR catalytic activity results.

4. Experimental Section

Synthesis of LTL Zeolite: The amount of oxide reactants was set to obtain an optimal gel composition for each type of zeolite, either nanosized or disc-shaped. The alumina and silica suspensions required for the gel were prepared separately. The alumina suspension was prepared mixing potassium hydroxide and aluminum hydroxide in bidistilled water, and the solution was refluxed in an oil bath at 120 °C until a clear solution was obtained. On the other hand, potassium hydroxide dissolved in bidistilled water was added to a silica suspension (Ludox HS-40, supplied by Sigma–Aldrich or Aerosil OX-50 by Evonik Industries) and refluxed for 14 h in an oil bath at 120 °C.

After cooling the suspension to room temperature, the potassium aluminate solution was added to the potassium silica suspension under vigorous stirring. The obtained gel was transferred to a polytetrafluoroethylene (PTFE) pressure vessel and heated in a microwave oven (Ethos1, Milestone) at 160 °C or 170 °C for nanosized and disc-shaped zeolites, respectively. Once the crystallization process was finished, the vessel was cooled to room temperature. The obtained product was washed with boiling bidistilled water until the pH of the supernatant was neutral. Finally, the powder was dried at 90 °C for 16 h.

Next, the LTL zeolite was exchanged with Na^+ and Cs^+ to adjust the pH inside the channels. In order to achieve this, the LTL zeolite was suspended in water and exchanged with an excess of NaCl or CsCl under

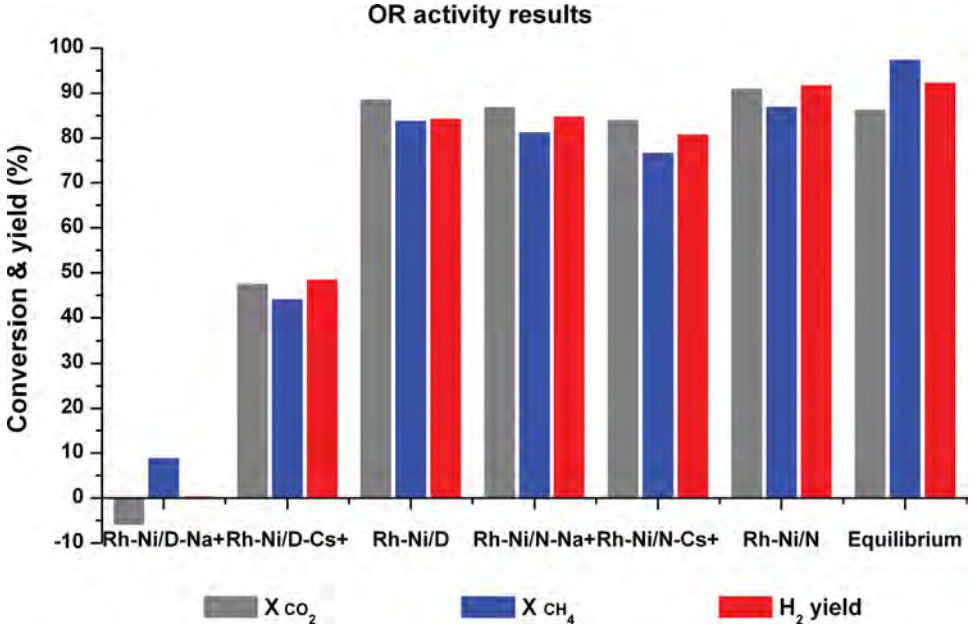

Figure 10. Biogas OR catalytic activity results.

reflux and stirring for 45 min at 80 °C.[26] The cation-exchanged zeolites were then washed and dried in the oven.

Catalyst Preparation: First, the zeolites were calcined at 1073 K for 4 h in order to stabilize the supports. Then, through the wetness impregnation method, the six Rh-Ni bimetallic catalysts were prepared. To this end, an aqueous solution that consisted on nickel (II) nitrate hexahydrate (99.99%; Sigma–Aldrich) and Rh (III) nitrate hydrate (≈36% as Rh; Sigma–Aldrich) was added to reach an intended load of 13 wt% of Ni and 1 wt% of Rh, respectively. The corresponding solutions were stirred for 2 h using a rotatory evaporator and then heated up until all the water was removed. Next, the catalysts were dried and calcined at 1073 K for 4 h in the oven. The calcinations were carried out under an oxidative atmosphere in order to ensure oxidation of the metal species, and remove the salts of the reactants used for their preparation as well as the possible humidity inside the pores.

Characterization Techniques: The synthesized crystals were fully characterized by several techniques. X-ray powder diffraction (PHILIPS X'PERT PRO automatic diffractometer, operating at 40 kV and 40 mA, CuKα radiation, PIXcel solid-state detector) for phase identification and determination of the unit cell parameters (Figure S1, Supporting Information). Preliminary identification of the initial phases was evaluated using the powder diffraction file (PDF) database and XRD data were in line with the LTL zeolite, (S.G.: *P 6*/mmm) (01–080–1580). X-ray fluorescence (XRF) was used for the chemical analysis (PANalytical, AXIOS model, Rh tube) in order to determinate the chemical composition of the synthesized products by means of the percentage weight of the metal oxides (Table S2, Supporting Information). The size and morphology of the nanocrystals were studied by scanning (JEOL JSM-7000F, Schottky FEG) and transmission electron microscopy (Philips SuperTwin CM200, La6B6 filament), where the channel structure of the LTL zeolite crystals was resolved. Finally, the particle size of disc-shaped zeolites was analyzed using a laser dispersion analyzer (Malvern MasterSizerX equipment).

For the catalysts characterization, in addition to the previously mentioned XRD and TEM analyses, an inductively coupled plasma atomic emission spectroscopy (ICP-AES) instrument, model 2000-DV (Perkin Elmer), was used for determining the metallic content in the catalysts. A solution that consisted of $HCl:HNO_3:HF$ = 3:3:2 was prepared to properly disintegrate the amount of 100 mg of catalyst. A digester was used for the total catalysts disaggregation because the presence of some particles could affect the measurements results as well as obstruct the equipment.

The textural properties, BET surface area, pore volume and diameter of the calcined and outgassed (at 573 K for 24 h) zeolites and catalysts were evaluated by means of N_2 adsorption–desorption isotherms obtained at 77 K using an Autosorb 1C-TCD. Regarding the obtained results, pore volume was estimated by the Barrett–Joyner–Halenda (BJH) method for the cumulative desorption pore volume, and in the case of the radius, the BJH desorption Dv(r) method was used.

Finally, a temperature-programmed reduction (TPR) analysis was also performed to determine the reducible species formed during calcination of catalysts and the corresponding reduction temperatures. The measurements were carried out using an Autosorb 1C-TCD apparatus, equipped with a TCD. A continuous flow of 5% H_2/Ar (40 NmL min^{-1}) was passed over 300 mg of calcined catalyst powder. The temperature was increased from room temperature to 1323 K at a rate of 10 K min^{-1}. The sample was previously outgassed at 573 K for 30 min.

Catalytic Activity: The experiments were carried out in a bench-scale Microactivity plant (PID Eng&Tech). The gaseous mixture flows were adjusted by electronic controllers, and an HPLC-Gilson liquid pump was used for the desionizated water injection. A 316-L stainless-steel fixed bed reactor was used for all the experiments carried out. In addition, the catalyst amount used was 340 mg. For all the experiments, a model biogas consisting of 60% CH_4 and 40% CO_2 (vol) was fed.[27–29] Tests were carried out at 1073 K and atmospheric pressure. After the corresponding reactions, the effluent stream was cooled down in a condenser. The condensed water was collected and weighted, and the gas phase was analyzed online by a Micro GC equipped with a thermal conductivity detector (TCD). Three columns, molecular sieve 5 Å PLOT, CP-Sil 5 CB and Poraplot Q, were used in a series arrangement for complete separation of hydrogen, oxygen, nitrogen, methane, carbon monoxide and carbon dioxide, which were calibrated using N_2 as an internal standard. Before running the activity tests, each catalyst was reduced at 1073 K using 350 NmL min^{-1} of a 3:1 N_2:H_2 mixture for 4 h. The activity tests lasted 90 min, and they were stable during this time on stream. The measured parameters were defined as:

$$\text{Methane conversion: } X_{CH_4}(\%) = (V^{in}_{CH4} - V^{out}_{CH4})/V^{in}_{CH4}100 \quad (2)$$

$$\text{Carbon dioxide conversion: } X_{CO_2}(\%) = (V^{in}_{CO_2} - V^{out}_{CO_2})/V^{in}_{CO_2}100 \quad (3)$$

$$\text{Hydrogen yield: } H_2\text{yield}(\%) = V^{out}_{H_2}/(2V^{in}_{CH_4} + V^{in}_{H_2O})100 \quad (4)$$

where: V_i^{in} corresponds to the volumetric flow-rate of reactant i (NmL min^{-1}) and V_i^{out} corresponds to the volumetric flow-rate of product i (NmL min^{-1}).

Supporting Information

Supporting Information is available from the Wiley Online Library or from the author.

Acknowledgements

Gobierno Vasco is gratefully thanked for financial support (projects IT339–10 and S-PE12UN140) and a Ph.D. grant for L. G.-R. UPV/EHU is also thanked for financial support and a Ph.D. grant for U. I. XRD, XPS, and fluorescence measurement, electronic microscope images and dynamic light scattering measurements were carried out in the SGI/IZO-SGIker of the UPV/EHU.

Received: August 9, 2013
Revised: October 17, 2013
Published online: November 29, 2013

[1] a) A. F. Cronsted, *Akad. Hankl. Stockholm* **1756**, *18*, 120; Translation: Ir. G. Sumelius, in *Molecular Sieves*, (Eds: M. L. Occelli, H. Robson), Van Nostrand Reinhold, New York **1992**; b) A. Damour, *Ann. Mines.* **1840**, *17*, 191.
[2] a) H. Manzano, L. Gartzia-Rivero, J. Bañuelos, I. López-Arbeloa, *J. Phys. Chem. C.* **2013**, *117*, 13331; b) M. Veiga-Gutiérrez, M. Woerdemann, E. Prasetyanto, C. Denz, L. De Cola, *Adv. Mater.* **2012**, *24*, 5199.
[3] A. Mech, A. Monguzzi, F. Meinardi, J. Mezyk, G. Macchi, R. Tubino, *J. Am. Chem. Soc.* **2010**, *132*, 4574.
[4] A. Corma, F. Rey, J. Rins, M. J. Sabater, S. Valencia, *Nature* **2004**, *431*, 287.
[5] T. P. Lee, B. Saad, E. P. Ng, B. Salleh, *J. Chromatogr. A.* **2012**, *1237*, 46.
[6] a) L. Gartzia-Rivero, J. Bañuelos-Prieto, V. Martínez-Martínez, I. López-Arbeloa, *ChemPlusChem* **2012**, *77*, 61; b) G. Calzaferri, K. Lutkouskaya, *Photochem. Photobiol. Sci.* **2008**, *7*, 879.
[7] J. S. Batchelder, A. H. Zewail, T. Cole, *Appl. Opt.* **1979**, *18*, 3090.
[8] J. El-Gindi, K. Benson, L. De Cola, H. J. Galla, N. S. Kehr, *Angew. Chem. Int. Ed.* **2012**, *51*, 1.
[9] a) R. Szostak, *Molecular Sieves: Principles of Synthesis and Identification*, Blackie Academic & Professional, London **1998**; b) D. W. Breck, N. A. Acara (Union Carbide Corporation), *US Patent 909264*, **1962**; c) A. I. Lupulescu, M. Kumar, J. D. Rimer, *J. Am. Chem. Soc.* **2013**, *135*, 6608.

[10] a) G. A. Tompsett, W. C. Conner, K. S. Yngvesson, *ChemPhysChem* **2006**, *7*, 296; b) I. Bilecka, M. Niederberger, *Nanoscale* **2010**, *2*, 1358.
[11] a) A. Zabala Ruiz, D. Brühwiler, T. Ban, G. Calzaferri, *Monatshefte Chem./Chem. Monthly* **2005**, *136*, 77; b) G. Schulz-Ekloff, D. Wöhrle, B. van Duffel, R. A. Schoonheydt, *Micropor. Mesopor. Mater.* **2002**, *51*, 91.
[12] P. Frontera, A. Macario, A. Aloise, F. Crea, P. L. Antonucci, J. B. Nagy et al., *Catal. Today* **2012**, *179*, 52.
[13] A. H. Fakeeha, W. U. Khan, A. S. Al-Fatesh, A. E. Abasaeed, *Chin. J. Catal.* **2013**, *34*, 764.
[14] U. Izquierdo, V. L. Barrio, N. Lago, J. Requies, J. F. Cambra, M. B. Güemez, P. L. Arias, *Int. J. Hydrogen Energy* **2012**, *37*, 13829.
[15] U. Izquierdo, V. L. Barrio, J. Requies, J. F. Cambra, M. B. Güemez, P. L. Arias, *Int. J. Hydrogen Energy* **2012**, *38*, 7623.
[16] N. Sudheesh, S. K. Sharma, R. S. Shukla, R. V. Jasra, *J. Mol. Catal. A: Chem.* **2008**, *296*, 61.
[17] M. García-Diéguez, I. S. Pieta, M. C. Herrera, M. A. Larrubia, L. J. Alemany, *J. Catal.* **2010**, *270*, 136.
[18] C. Yang-guang, K. Tomishige, K. Yokoyama, K. Fujimoto, *Appl. Catal. A Gen.* **1997**, *165*, 335.
[19] J. R. Rostrup-Nielsen, *Stud. Surf. Sci. Catal.* **1994**, *81*, 25.
[20] D. San-José-Alonso, J. Juan-Juan, M. J. Illán-Gómez, M. C. Román-Martínez, *Appl. Catal. A Gen.* **2009**, *371*, 54.
[21] A. Zabala Ruiz, H. Li, G. Calzaferri, *Angew. Int. Ed.* **2006**, *45*, 5282.
[22] G. Calzaferri, *Langmuir* **2012**, *28*, 6216.
[23] U. Izquierdo, V. L. Barrio, K. Bizkarra, A. M. Gutierrez, J. R. Arraibi, L. Gartzia, J. Bañuelos, I. Lopez-Arbeloa, J. F. Cambra, under revision.
[24] A. M. Garrido Pedrosa, M. J. B. Souza, A. O. S. Silva, D. M. A. Melo, A. S. Araujo, *Catal. Commun.* **2006**, *7*, 791.
[25] M. Ocsachoque, F. Pompeo, G. Gonzalez, *Catal. Today* **2011**, *172*, 226.
[26] R. Q. Albuquerque, G. Calzaferri, *Chem. Eur. J.* **2007**, *13*, 8939.
[27] S. Rasi, A. Veijanen, J. Rintala, *Energy* **2007**, *32*, 1375.
[28] C. S. Lau, A. Tsolakis, M. L. Wyszynski, *Int. J. Hydrogen Energy* **2011**, *36*, 397.
[29] A. Effendi, Z. G. Zhang, K. Hellgardt, K. Honda, T. Yoshida, *Catal. Today* **2002**, *77*, 181.

Chemical Engineering Journal 238 (2014) 178–188

Contents lists available at ScienceDirect

Chemical Engineering Journal

journal homepage: www.elsevier.com/locate/cej

Ni and Rh—Ni catalysts supported on Zeolites L for hydrogen and syngas production by biogas reforming processes

U. Izquierdo [a], V.L. Barrio [a,*], K. Bizkarra [a], A.M. Gutierrez [b], J.R. Arraibi [b], L. Gartzia [c], J. Bañuelos [c], I. Lopez-Arbeloa [c], J.F. Cambra [a]

[a] Dept. of Chemical and Environmental Engineering, School of Engineering, University of the Basque Country UPV/EHU, c/Alameda Urquijo s/n, 48013 Bilbao, Spain
[b] Edp Naturgas Energía, c/General Concha, 20, 48010 Bilbao, Spain
[c] Dept. of Chemical Physics, University of the Basque Country UPV/EHU Apartado 644, 48080 Bilbao, Spain

HIGHLIGHTS

- Very high conversions were reached by all tested catalysts and operation conditions.
- For biogas SR at S/C = 1.0 and TR, H_2/CO ratios near to 2.0 were obtained.
- The highest hydrogen yield was measured for the biogas OR process at O/C = 0.25.
- DR is the most appropriate process for the conversion of almost all the CO_2.
- The Rh—Ni catalyst based on Zeolite L (30–60 nm) seems to be a promising catalyst.

ARTICLE INFO

Article history:
Available online 4 September 2013

Keywords:
Hydrogen
Biogas valorisation
Catalysis
Zeolite L

ABSTRACT

This study examined the use of three different Zeolites L as catalyst support for biogas valorisation – a renewable resource – through reforming processes. These aluminosilicates are characterised by their high surface areas, affinity for CO_2, and thermal stability, which makes them an interesting and promising support for reforming reactions at high temperature. Three nickel monometallic and their homologous rhodium–nickel bimetallic catalysts were prepared by the incipient wetness impregnation method for each type of Zeolite L. Significant physicochemical differences between the Zeolites L and catalysts were noticed by the characterisation using scanning electron microscope (SEM), transmission electron microscope (TEM), inductively coupled plasma atomic emission spectrometry (ICP-AES), H_2 chemisorption, N_2 physisorption, temperature programmed reduction (TPR) X-ray diffraction (XRD) and X-ray photoelectron spectroscopy (XPS) techniques. The catalysts were tested in dry reforming (DR), steam reforming (SR) with steam to carbon (S/C) ratio of 1.0 and 2.0; oxidative reforming (OR) at O_2/CH_4 = 0.25; and tri-reforming (TR) with S/C ratio of 1.0 and O_2/CH_4 = 0.25. For all the experiments, a synthetic biogas, which consisted of 60% CH_4 and 40% CO_2 (vol.), was fed to a fixed bed reactor system at 1073 K and atmospheric pressure. The same experimental conditions and reactions were studied in previous works of the authors, in which γ-Al_2O_3 was used as a catalyst support. Thus, this work allows comparing the achieved activities by the tested catalysts supported on those different supports. Among the processes studied, for the biogas SR at S/C = 1.0 and TR processes, H_2/CO ratios near to 2.0 were obtained, which is an appropriate ratio for the Fischer–Tropsch synthesis (FTS). In the case of the catalysts tested, the Rhodium (Rh) incorporation improved their activity. Rh—Ni catalyst based on Zeolite L (30–60 nm) is the most active catalyst for hydrogen generation.

1. Introduction

Hydrogen has come to be considered as "the fuel of the future" and this opportunity should be exploited by improving the existing technologies and processes as well as innovating new ones. The main challenges of catalytic hydrogen and/or syngas production involves the selected process, the processed feed, and the yield of the catalysts used, which is normally measured by the activity, selectivity, and stability. In the present study, biogas was selected as a raw material because it is considered to be a green and renewable feed [1–4]. Using a synthetic biogas without contaminants, four different reforming processes were studied: dry reforming (DR), the most conventional; steam reforming (SR), very well

* Corresponding author. Tel.: +34 946017242.
E-mail address: laura.barrio@ehu.es (V.L. Barrio).

1385-8947/$ - see front matter © 2013 Elsevier B.V. All rights reserved.
http://dx.doi.org/10.1016/j.cej.2013.08.093

known for natural gas; oxidative reforming (OR), and tri-reforming (TR), suitable process for biogas valorization [5]. For the study of these processes, reversible Water Gas-Shift reaction must also be taken into account due to the high temperatures and conversions. Therefore, the following reactions were the most important ones studied:

$$\text{DR}: \quad CH_4 + CO_2 \leftrightarrow 2CO + 2H_2 \quad (\Delta H^0 = 247\ \text{kJ/mol}) \tag{1}$$

$$\text{SR}: \quad CH_4 + H_2O \leftrightarrow CO + 3H_2 \quad (\Delta H^0 = 206\ \text{kJ/mol}) \tag{2}$$

$$\text{OR}: \quad CH_4 + 1/2O_2 \rightarrow CO + 2H_2 \quad (\Delta H^0 = -36\ \text{kJ/mol}) \tag{3}$$

TR: Combination of (1), (2) and (3).

$$\text{r}-\text{WGS}: \quad CO_2 + H_2 \leftrightarrow CO + H_2O \ (\Delta H^0 = 41\ \text{kJ/mol}) \tag{4}$$

Based on previous studies in which γ-Al_2O_3 was used as a support for nickel and rhodium–nickel based catalysts [6,7], the following operating conditions were chosen: steam to carbon (S/C) ratio of 1.0 and 2.0 for biogas SR, O_2/CH_4 of 0.25 and 0.50 for biogas OR, and S/C of 1.0 and O_2/CH_4 of 0.25 for TR reactions. In this work, the catalyst support was also tested with the aim to study its influence in the activity of the catalysts for the described processes.

Catalyst support plays an important role because properties like thermal stability, surface area, capacity of maintaining the metal dispersion during the reaction or acidity can be key factors that stand out from the existing ones [8]. For the reactions of the present study, alumina support is most commonly used due to its thermal stability and in the case of γ-Al_2O_3, the high surface area [8–11]. However, considering the previous mentioned properties, Zeolites also offer higher surface areas, specific micropore structure, and affinity to CO_2 [8,12]. Some types of Zeolites were tested as active metal support in the dry reforming of methane, and it was observed that the nature of Zeolite support has a significant influence on the overall performance of the catalyst [13,14]. The Zeolite L prepared in this study is a crystalline aluminosilicate with a hexagonal symmetry and one-dimensional channels (pore aperture around 7.1 Å) running along the crystal. Its morphology and size can be modulated by the synthesis conditions [15]. These three Zeolites were synthesised by Gartzia-Rivero et al. [15] who described all its structural and morphological properties in previous reference. Zeolite L has been experimentally used as a catalyst not only in the hydrodesulfurisation of fluid catalytic cracking (FCC) gasoline [16], dehydrogenation of propane [17] or isobutane [18,19], but also in selective chlorination of toluene [20]. In general, different types of zeolites are being used as catalyst supports in reforming processes, and commonly studied as potential candidates for dry reforming processes [8,12,13,21–27].

Regarding the active phase, among the existing non-noble metals, Nickel (Ni) is most widely used for reforming reactions because of its availability and relatively low price. However, it is well known that noble metals like Rhodium (Rh), Ruthenium (Ru), Palladium (Pd), etc. are much more active, stable and their use decreases the tendency of coke formation in the catalytic surface at high temperatures [28–30], especially when Rh and Ru are used [31]. Although the noble metals are much more expensive, it has been reported that adding a small amount of noble metal to a non-noble metal catalyst increases the activity and dispersion of the non-noble metal due to the spill-over effect [32]. We found that the addition of 1 wt.% of Rh to Ni/Al_2O_3 catalyst has a strong influence on the catalytic performance towards the biogas reforming processes under investigation. On this basis, in this study, the effect of Ni and Rh addition to three different Zeolite L's is reported.

2. Experimental procedure

2.1. Catalyst preparation

The Zeolite L's herein used were prepared by microwave-assisted hydrothermal synthesis, which provides a good control over the temperature and ensures homogeneous and efficient heating. Crystals of different morphology (from disc to cylinders) and size (from nm to μm) were obtained starting from a fixed gel composition (9.34 K_2O–1.00 Al_2O_3–20.20 SiO_2–412.84 H_2O for the nanosize cylinders and 5.40 K_2O–5.50 Na_2O–1.00 Al_2O_3–30.00 SiO_2–416.08 H_2O for the microsize discs) [33], which was optimised to yield each kind of zeolites.

The experimental procedure for each type of zeolite was quite similar, and it has been previously mentioned about the micrometer crystals [15]. Overall, the alumina and silica suspensions were prepared separately under reflux and heating at 120 °C. Once a clear solution is achieved, the alumina was added to the silica suspension under vigorous mechanical stirring. The obtained gel was transferred to a polytetrafluoroethylene (PTFE) pressure vessel and heated in a microwave oven at 170 °C for 1 h (nanosize cylinders) and 160 °C for 8 h (micrometer size discs). Afterwards, the vessel was cooled down to room temperature and the obtained crystals were washed with boiling doubly distilled water and dried at 90 °C for 16 h.

The alumina suspension was prepared by mixing potassium hydroxide (KOH) and metallic aluminium powder in doubly distilled water under argon flow, and the mixture was stirred at low temperature (0 °C) for 15 min. After letting the solution warm up to room temperature, stirring was continued for 1.5 h under the inert atmosphere. This solution was added to a silica suspension (Ludox, supplied by Sigma–Aldrich) with vigorous mechanical stirring. After aging the gel for 3–6 min, it was transferred to a PTFE pressure vessel and heated in a microwave oven at 175 °C for 12 h. Once the crystallisation process was finished, the vessel was cooled down to room temperature. The obtained solid was washed with boiling doubly distilled water until the pH of the supernatant became neutral. Finally, the crystals were dried at 90 °C for 16 h.

Regarding catalyst preparation, first, the Zeolites were calcined at 1073 K for 4 h in order to stabilize de supports. Then, six different catalysts were prepared by incipient wetness impregnation method: three Ni monometallic catalysts and their three homologous Rh—Ni bimetallic catalysts. In case of monometallic catalysts, an aqueous solution of Nickel (II) nitrate hexahydrate (99.99%; Sigma Aldrich) was added to reach an intended load of 13 wt.% of Ni [6]. The corresponding solutions were stirred for 2 h using a rotatory evaporator and then heated up until all the water was removed. Next, the catalysts were dried and calcined at 1073 K for 4 h in the oven. For the bimetallic catalysts, the same Ni proportion used for monometallic catalysts was incorporated, and after the calcination step, a Rh (III) nitrate hydrate (~36% as Rh; Sigma Aldrich) aqueous solution was added to achieve nominal loading of 1 wt.% of Rh. Once the Rh was incorporated, the bimetallic catalysts were calcined again under the conditions described previously. The calcinations were carried out under an oxidative atmosphere in order to ensure oxidation of the metal species, and remove the salts of the reactants used for their preparation as well as the possible humidity inside the pores. In addition, it has been reported that dispersion increases in the samples that are previously calcined and then activated with hydrogen [22].

2.2. Reactor preparation

A 316-L stainless-steel fixed bed reactor was used for all the experiments carried out. In addition, the catalyst amount used

was 340 mg, as in previous works, in order to compare the obtained results. With this catalyst amount, the following weight hourly space velocities (WHSV, calculated taking into account all the reactants fed) were calculated for the test and are compiled in Table 1.

2.3. Activity measurements

A bench-scale Microactivity plant (PID Eng&Tech) was used for the activity tests. The gaseous mixture flows were adjusted by electronic controllers, and a HPLC-Gilson liquid pump was used for the desionisated water injection. The reactor was electrically heated in a furnace and the thermocouple located in the reactor.

For all the experiments, a model biogas consisting of 60% CH_4 and 40% CO_2 (vol.) was fed [2,34,35]. Tests were carried out at 1073 K and atmospheric pressure. These experimental conditions were decided due to the endothermic nature of the reforming reactions, which are favoured at high temperature and low pressure. However, at high temperatures, coke formation and its deposition on the catalytic surface can inhibit the activity of the catalysts [28,32,36–38]. As in the previous works of the authors, a temperature of 1073 K was used without apparent catalyst deactivation due to the coke formation during the time on stream [6,7]. After the corresponding reactions, the effluent stream was cooled down in a condenser. The condensed water was collected and weighted, and the gas phase was analysed online by a Micro GC equipped with a thermal conductivity detector (TCD). Three columns, Molecular Sieve 5 Å PLOT, CP-Sil 5 CB, and Poraplot Q, were used in a series arrangement for complete separation of hydrogen, oxygen, nitrogen, methane, carbon monoxide, and carbon dioxide, which were calibrated using N_2 as an internal standard. Before running the activity tests, each catalyst was reduced at 1073 K using 350 N mL/min of a 3:1 N_2:H_2 mixture for 4 h. The activity tests lasted 90 min, and they were stable during this time on stream. The measured parameters were defined as:

$$\text{Methane conversion}: \; X_{CH4}\,(\%) = \left(V^{in}_{CH4} - V^{out}_{CH4}\right)/V^{in}_{CH4} \times 100 \quad (5)$$

$$\text{Carbon dioxide conversion}: X_{CO2}\,(\%) = \left(V^{in}_{CO2} - V^{out}_{CO2}\right)/V^{in}_{CO2} \times 100 \quad (6)$$

$$\text{Hydrogen yield}: \; H_2 \text{ yield}\,(\%) = V^{out}_{H2}/\left(2 \cdot V^{in}_{CH4} + V^{in}_{H2O}\right) \times 100 \quad (7)$$

$$(H_2/CO)^{out} \text{ molar ratio } (H_2/CO)^{out} = (V_{H2}/V_{CO})^{out} \quad (8)$$

where V^{in}_i is the corresponds to the volumetric flow-rate of reactant i (N mL/min), V^{out}_i is the corresponds to the volumetric flow-rate of product i (N mL/min).

2.4. Catalyst characterization

Fresh catalysts were characterised by different techniques. An inductively coupled plasma atomic emission spectroscopy (ICP-AES) instrument, model 2000-DV (Perkin Elmer), was used for determining the metallic elements in the catalysts. A solution that consisted of HCl:HNO_3:HF = 3:3:2 was prepared to properly disintegrate the amount of 100 mg of catalyst. In addition, a digester was used for the total catalysts disaggregation because the presence of some particles could affect the measurements results as well as obstruct the equipment.

Table 1
WHSV values obtained in the studied processes.

Process	Conditions	WHSV (h^{-1})
DR		75.0
Biogas SR	S/C = 1.0	104.8
	S/C = 2.0	134.6
Biogas OR	O/C = 0.25	131.8
	O/C = 0.50	188.6
Biogas TR	S/C = 1.0, O/C = 0.25	161.5

The textural properties, Brunauer–Emmett–Teller (BET) surface area, pore volume and diameter of the calcined and outgassed (at 573 K for 24 h) catalysts were evaluated by means of N_2 adsorption–desorption isotherms obtained at 77 K using an Autosorb 1C-TCD. Amounts of around 100 mg for Zeolite L supports, and around 400 mg for the catalysts were used in the measurements to ensure the minimum surface area required by the equipment, 10 m^2. With regard to the obtained results, pore volume was estimated by the Barrett–Joyner–Halenda (BJH) method for the Cumulative Desorption Pore Volume, and in the case of the radius, the BJH Desorption Dv(r) method was used.

The structure of the disc and cylindrical Zeolite L (1–3 μm) was characterised by a JEOL JSM-7000-F scanning electron microscope (SEM), equipped with a Schottky field emission cathode. In the case of cylindrical Zeolite L (30–60 nm), transmission electron microscopes (TEM) were acquired on a Philips CM 200 transmission electron microscope at an acceleration voltage of 200 kV with a LaB_6 filament. Typically, a small amount of sample was suspended in pure ethanol, sonicated and dispersed over a Cu grid with a carbon-coated cellulose acetate–butyrate holey film. TEM images were recorded using a 4 k × 4 k TVIPS CCD camera at different magnifications.

Ni dispersion was measured by H_2-pulse chemisorption at 313 K in the Autosorb 1C-TCD unit. Prior to the pulse chemisorption experiment, all samples were reduced under pure H_2 flow (40 N mL/min) for 2 h at 1073 K. To calculate the metal dispersion of the catalysts, an adsorption stoichiometry of H/Ni = 2 was assumed.

A temperature programmed reduction (TPR) analysis was performed to determine the reducible species formed during calcination of catalysts and the corresponding reduction temperatures. The measurements were carried out using an Autosorb 1C-TCD apparatus, equipped with a TCD. A continuous flow of 5% H_2/Ar (40 N mL/min) was passed over 500 mg of calcined catalyst powder. The temperature was increased from room temperature to 1273 K at a rate of 10 K/min. The sample was previously outgassed at 573 K for 30 min.

X-ray powder diffraction (XRD) patterns were also collected using a PHILIPS X'PERT PRO automatic diffractometer operating at 40 kV and 40 mA, in theta–theta configuration, secondary monochromator with Cu Kα radiation (λ = 1.5418 Å) and a PIXcel solid state detector. The samples were mounted on a zero background silicon wafer fixed in a generic sample holder. Data were collected from 10 to 80° 2θ (step size = 0.026 and time per step = 625 s) at retention time. A fixed divergence and an anti-scattering slit giving a constant volume of sample illumination were used.

Finally, XPS technique was used to evaluate the surface characteristics of the samples. The measurements were carried out with a VG Escalab 200R spectrometer equipped with a hemispherical electron analyser and an Al Ka1 (hv = 1486.6 eV) 120 W X-ray source. The powdered samples were deposited on a stainless steel sample holder, placed in the pre-treatment chamber and degassed at 573 K. The base pressure of the spectrometer was typically 10^{-9} torr. The spectra were collected at pass energy of 20 eV, which is typical of high resolution conditions. Used catalysts were analysed with this technique.

3. Results and discussion

3.1. Fresh catalysts characterisation results

3.1.1. Chemical composition, ICP-AES, and H_2 pulse chemisorption

The catalysts chemical compositions, which were determined by ICP-AES, are shown in Table 2. The metal contents of most of

Table 2
Calcined catalysts chemical composition and H_2 chemisorption results.

	Disc catalyst		Cylindrical (1–3 μm) catalyst		Cylindrical (30–60 nm) catalyst	
	Ni	Rh—Ni	Ni	Rh—Ni	Ni	Rh—Ni
Composition (wt.%)	11.14	0.88–12.36	12.66	1.02–14.07	11.92	1.09–13.17
Active metal surface area (m^2/g)	3.12	3.51	3.44	3.25	3.75	**9.56**
Metal dispersion (%)	4.21	4.13	3.97	3.36	4.72	**10.48**
Crystallite size (nm)	24.05	24.79	25.49	30.50	21.45	**9.79**

the catalysts are very similar to their nominal ones (1.0 wt.% Rh and 13.0 wt.% Ni).

The H_2 pulse chemisorption results for the reduced catalysts are also outlined in Table 2. The active metal proportions used for calculating the parameters were the ones obtained by the ICP technique. Among the obtained results, the measured parameters were quite similar in the case of monometallic catalysts, but not for the bimetallic ones. For the catalysts supported on the Disc Zeolite L, small differences between the monometallic and bimetallic catalysts were detected. In case of Cylindrical (1–3 μm) catalysts, significant differences regarding the crystal sizes were observed, which was similar to the rest of the measured parameters. However, the expected increase of metal dispersion due to the spill-over effect was not noticed for those two catalysts.

For the Cylindrical (30–60 nm) catalysts, the biggest differences were detected; both monometallic and bimetallic catalysts supported on this Zeolite L presented the highest active metal surface area and metal dispersion, these catalysts being the ones with the smallest particle size. Moreover, the bimetallic catalyst experienced increased dispersion when Rh was incorporated. The previously prepared catalysts did not experience the spill-over effect, which could be explained due to the obtained lowest crystal particle size that could incorporate inside the porous structure of this support.

3.1.2. Textural properties, BET, of the Zeolites L and the corresponding catalysts

The textural properties of the fresh and calcined Zeolites and calcined catalysts are outlined in Table 3. The measured BET surface area was estimated according to the obtained N_2 absorption–desorption isotherm.

First, the textural properties of all Zeolite L's were measured. After calcination, a significant change of these properties was noticed in terms of the surface area diminution, which can be attributed to the high temperature (1073 K) that was used. The pore volume and the pore radius remained without significant differences. Finally, the fresh and calcined Cylindrical (30–60 nm) samples presented the highest values of total pore volume and pore size. After metal incorporation, as it could be expected, much lower surface areas were measured when catalysts and Zeolites L were compared. Both the monometallic and bimetallic catalyst surface areas decreased, although the catalysts supported on the Cylindrical (30–60 nm) remained with the higher areas.

Attending to the total pore volume, the value of this parameter decreased when Ni and Rh was incorporated. The values of Table 3 correspond to the pore volume measured for the mesopores (calculated through BJH method) and the parentheses values correspond to the micropores (using DR method). For the mono and bimetallic samples the micropores contribution was negligible. For Cylindrical (30–60 nm) catalyst, after metal impregnation the pore volume decreased and the pore size increased for both samples. Indeed taking into account the results obtained by the H_2 pulse chemisorptions, in the case of the monometallic catalyst, small pores could be blocked by metal atoms, and for the bimetallic catalyst, the particles could incorporate in the internal porous structure.

In the case of Disc and Cylindrical (1–3 μm) catalysts, the increase in pore size is five times higher than for the Cylindrical (30–60 nm) catalysts, which is between two to three times higher. However, as the initial pore size value for the Cylindrical (30–60 nm) Zeolite L is bigger than for the Disc and Cylindrical (1–3 μm), they presented higher pore size values. Therefore, for the Cylindrical (30–60 nm) bimetallic catalyst, the characteristics of the support, with a higher pore volume and size, enabled that metal incorporation (with smaller particles as it was measured by H_2 chemisorption) in the internal structure.

3.1.3. SEM and TEM results

Fig. 1 illustrates the morphology and size distribution of the synthesised Zeolites L. The smallest Zeolites were characterised by TEM, which reveals crystals with a size of about 30–60 nm, and even resolves the channel structure. Particle-size distribution was unreliable in this case since the nanoparticles tend to agglomerate and self-associate into larger clusters of 80–100 nm. The morphology of the other supports was analysed by SEM. The larger crystals were up to 2 μm in length and around 1 μm in diameter, keeping the same cylindrical morphology. Indeed, Dynamic Light Scattering (DLS) provided just a population centred at 1.5 μm, owing to their similar length and diameter (high aspect ratio). Finally, the disc/coin-shape Zeolites were characterised by a low aspect ratio (thin crystals). In fact, the DLS suggested two main domains; one placed at 0.7–1.0 μm, assigned to the disc diameter, and the other at 0.1–0.2 μm, attributed to the thickness.

3.1.4. Temperature-programmed reduction, TPR

Fig. 2 shows all TPR profiles of calcined catalysts. In the case of catalysts based on Cylindrical Zeolite L (1–3 μm), the profiles are very similar. The main peak at around 730 K is attributed to the

Table 3
Fresh and calcined support and fresh catalysts textural properties, BET (parentheses values: micropores volume contribution).

	Disc				Cylindrical (1–3 μm)				Cylindrical (30–60 nm)			
	Zeolite L		Catalyst		Zeolite L		Catalyst		Zeolite L		Catalyst	
	Fresh	Calcined	Ni	Rh—Ni	Fresh	Calcined	Ni	Rh—Ni	Fresh	Calcined	Ni	Rh—Ni
Surface area (m^2/g)	258.1	134.4	40.4	41.74	159.9	152.0	22.62	26.18	418.7	335.0	95.32	64.12
Pore volume (cm^3/g)	0.043	0.061	0.095	0.117	0.048	0.043	0.054	0.067	0.905	0.933	0.449	0.625
	(0.123)	(0.064)	–	–	(0.077)	(0.072)	–	–	(0.174)	(0.130)	–	–
Pore size (Å)	13.8	17.1	54.0	62.5	13.3	13.3	55.0	57.8	54.3	66.8	95.5	198.0

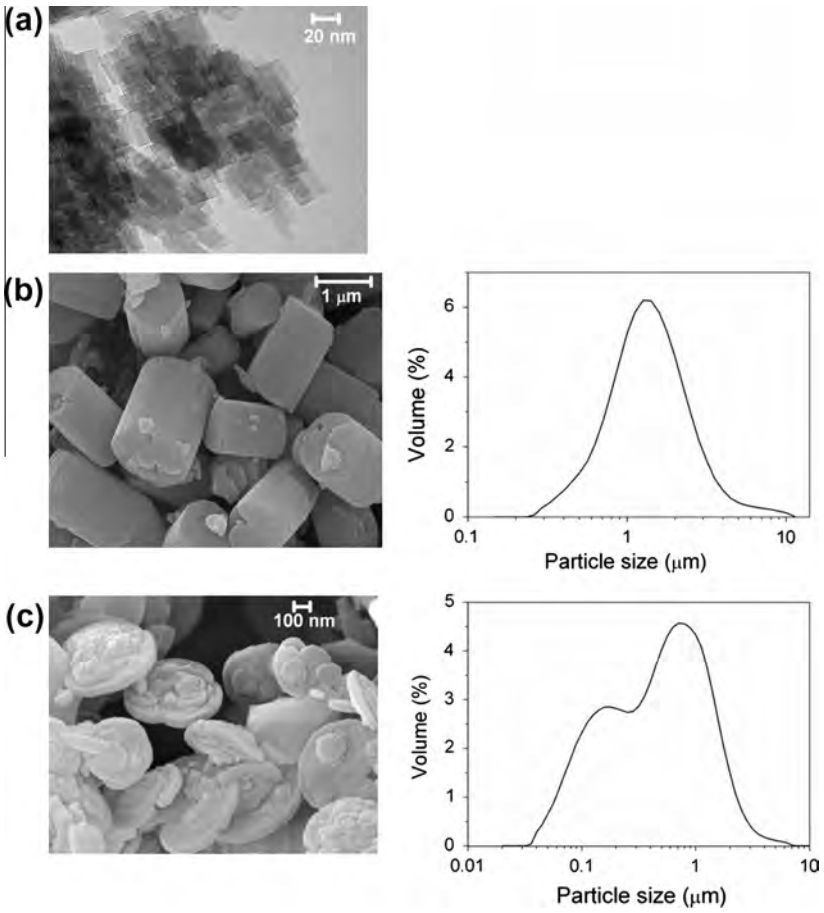

Fig. 1. (a) TEM image of Zeolite L nanocrystals, (b) SEM image and DLS size-distribution analysis of the micrometer cylindrical Zeolite L and (c) the same for disc-shape crystals.

reduction of NiO with very low interaction with the support [39]. The presence of two other small peaks can be observed at 820 and 1000 K assigned to the reduction of NiO particles with high interaction with the support and to Ni species located on the hexagonal prism, respectively [40]. When Rh was incorporated, the profiles differed in: (i) peak at around 450 K attributed to the Rh—Al interaction [41], (ii) higher hydrogen consumption measured for the bimetallic catalyst at 730 K, and (iii) lower reduction temperature required for the Ni species (spill-over effect).

For Disc Zeolite L catalyst profiles, as for the Cylindrical (1–3 μm) Zeolite L, the presence of the three peaks is not very clear due to the proximity between them. After Rh incorporation the reduction peak of NiO gradually shifted to lower temperatures, contributing mainly to the first one.

For the Cylindrical (30–60 nm) Zeolite L catalysts, in the case of Ni monometallic catalyst, the main peak appeared at the highest temperature (1150 K). For the bimetallic catalyst, the addition of Rh might contribute to the formation of Rh—Al species at lower temperatures instead of the non-stoichiometric and stoichiometric Ni-spinels formed at high temperatures [42].

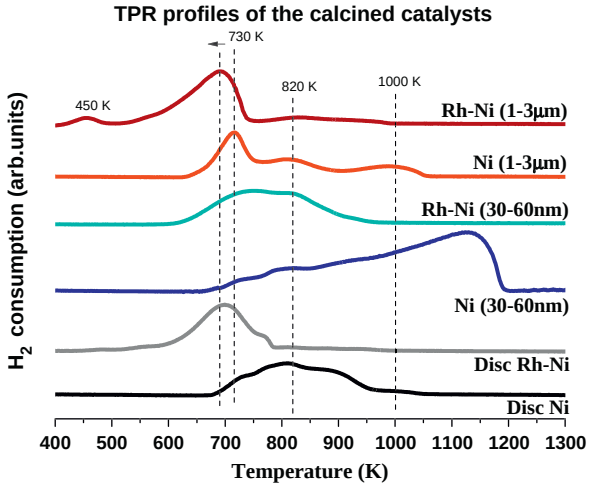

Fig. 2. TPR profiles of calcined catalysts.

3.1.5. XRD of the Zeolites L and catalysts

XRD analyses were carried out for all the Zeolites L and catalysts. Fig. 3 presents the obtained XRD profiles for Disc Zeolite L and the consequent two catalysts. Disc Zeolite L was perfectly identified by the detected peaks at all the measured 2θ positions (Powder Diffraction File (PDF): 01-080-1580). This profile was used as a reference to compare and identify the contributions of different Ni and Rh species. In the case of Ni catalysts, and comparing its profile to the one obtained for Disc Zeolite L, the peaks that correspond to NiO can be clearly observed (PDF: 00-044-1159) at $2\theta = 43.46$. Taking into account the NiO contribution, the calculated crystallite size (calculated by Scherrer equation) is around 30 nm. Lastly, a very similar profile to the one obtained by Ni catalyst was measured for Rh—Ni catalysts. Thus, no peaks coming from any Rh interaction (PDF: 00-005-0685) were detected and

additionally, the crystallinity of NiO was maintained constant as proved by the same crystal size. In addition, the calculated crystal sizes are very similar to the ones measured by the H_2 chemisorption technique (24.05 nm for monometallic; 24.79 nm for bimetallic catalyst). Besides, no Rh contributions were detected by this technique even after more accurate measurements in the range of 2θ where these peaks should appear (2θ = 80.5 or 89.1). However, the presence of this metal was detected by doing semi-quantitative X-ray fluorescence analyses to Rh containing catalysts (see Fig. 5) in addition to the analysis done by ICP-AES. As a result, Rh species must be too small (<4 nm) as it was not possible to be detected by XRD.

The same analyses were carried out for the Cylindrical (1–3 μm) Zeolite L and corresponding catalysts. The XRD spectra are shown in Fig. 4. From the analysis performed on Zeolite L (1–3 μm), the presence of two different types of structures was detected. One of them corresponds to Zeolite L and the other to Merlinoite zeolite (PDF: 01-083-1533) as can be seen in the diffractogram of Fig. 4. The contribution of each type of zeolite to the sample was semi-quantitatively calculated, the sample being composed by approximately 75% of Zeolite L and 25% of Merlinoite. Focussing on the spectra of the catalysts, NiO crystals of around 60 nm were detected for the Ni catalyst. In the case of Rh—Ni catalyst, the NiO particles suffered some dispersion as crystals of about 30 nm were found. Moreover, for this catalyst no contribution of any Rh species was measured by this technique, although this metal was detected again by X-ray Fluorescence and in the previously presented ICP-AES analyses.

Lastly, in Fig. 5, XRD spectra for Cylindrical (30–60 nm) Zeolite L and the resulting catalysts are shown. In this case, approximately 20 nm NiO crystals were detected for Ni catalysts. In the case of Rh—Ni catalyst, due to the dispersion effect again, NiO crystals of around 5 nm were found. In this case, the measured crystal sizes are very similar to the ones measured by the H_2 chemisorption technique (21.45 nm for monometallic; 9.79 nm for bimetallic catalyst). For this catalyst, no Rh interactions were noticed using this technique, but their presence, as for the rest of Rh containing catalysts, was confirmed by the X-ray Fluorescence and ICP-AES analyses.

3.1.6. XPS results of the used samples

Information on the Ni state and the surface composition of the used catalysts was obtained by XPS analysis. For all catalysts, the binding energy of Ni $3p_{3/2}$ core level was measured at 856.6 eV and it was attributed to the Ni^{2+} species. The presence of metallic Ni was not observed in none of the samples. In the case of Rh, it was only detected for the Disc sample, suggesting that for the Cylindrical (30–60 nm) and Cylindrical (1–3 μm) the Rh should be incorporated into the porous structure. Deconvolution of the C 1s signal gives a peak at 284.5 eV with a small contribution at 286.6 eV that would be related to graphitic carbon and C=O [43], respectively. The C=O can be assigned to the interaction of CO_2 on the metallic and/or zeolite surface [44]. The presence of carbon species with a strong charge effect at around 282.7 eV was also observed.

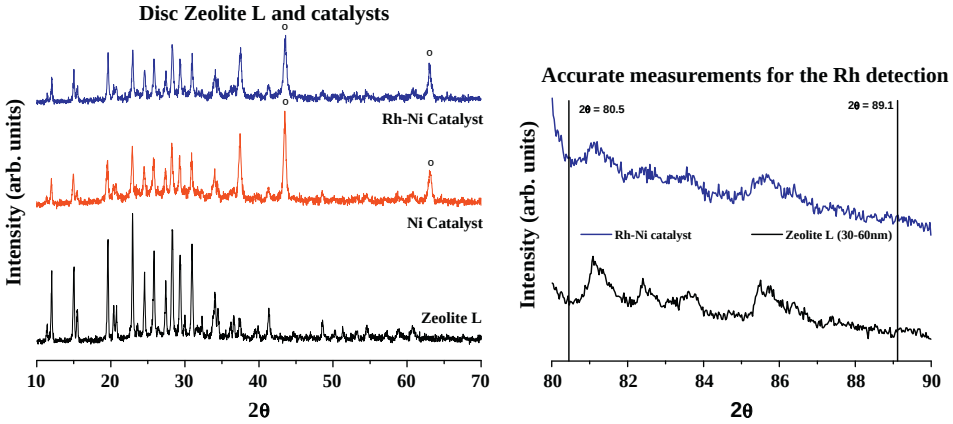

Fig. 3. Different XRD spectra for the disc Zeolite L and the corresponding catalysts.

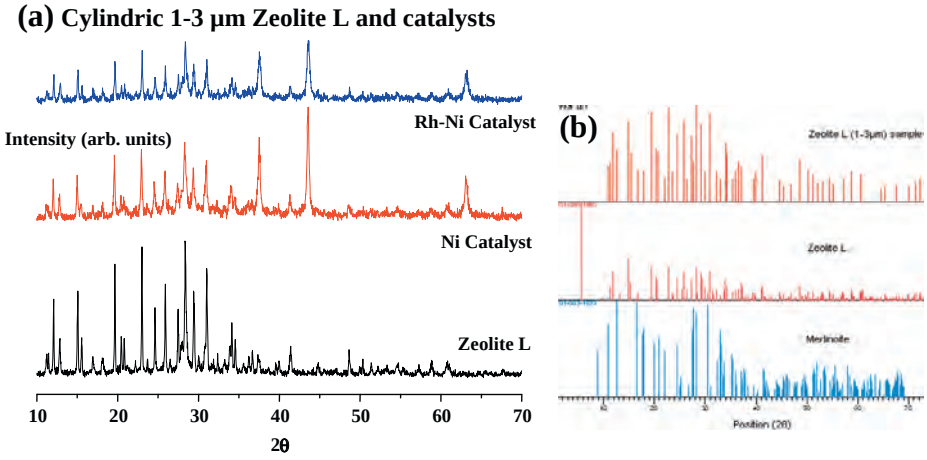

Fig. 4. (a) XRD spectra for the Cylindrical (1–3 μm) Zeolite L and catalysts. NiO peaks are marked by "°" symbol. (b) XRD diffractogram for the Zeolite L (1–3 μm).

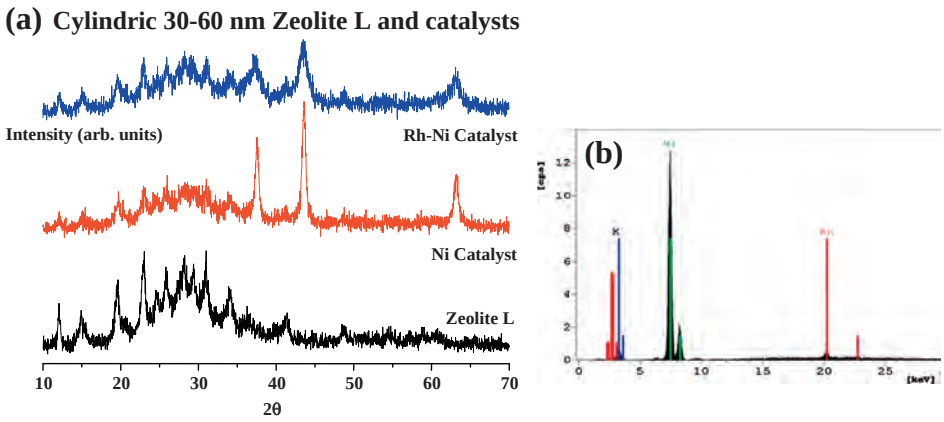

Fig. 5. (a) XRD spectra for the Cylindrical (30–60 nm) Zeolite L and catalysts. NiO peaks are marked by "°" symbol. (b) X-ray fluorescence analysis results for the Rh—Ni catalyst.

Table 4 compiles the relative intensities of the total carbon with respect to the Rh—Ni and Ni catalysts used. The percentage of the C (1s) area coverage for the bimetallic samples is lower ranging from 30.9% to 39.4%. Thus, a higher percentage was measured for the Ni catalysts. Only the Ni catalysts obtained a low percentage that could due to the low activity achieved for this catalyst.

3.2. Activity results

All the prepared catalysts were tested for biogas DR, SR, OR and TR reactions. The activity results presented in Figs. 6 and 7 correspond to the measured parameter for each tested catalyst and studied process. Fig. 6 presents the methane conversion results for the tested catalysts and studied processes.

Attending the results obtained for the different processes, in the DR process, the methane conversion reached almost the equilibrium values for the catalysts apart from the Ni and Rh—Ni (1–3 μm) catalysts, which did not reach that value. In the case of Ni Disc catalyst, the value reached was higher than the equilibrium due to the possible presence of hot spots inside the fixed bed reactor. For the SR process, the effect of water addition by increasing the S/C ratio was not positive as the methane conversion measured did not change or slightly decreased. On the contrary, in the OR process, the increase of oxygen content was positive for all the catalysts except for Ni and Rh—Ni (1–3 μm) catalysts, which was probably due to the heat being released by the methane oxidation reaction onto the particle surface. For the TR process, in the case of bimetallic catalysts, the methane conversion reached high values similar to the ones for OR process at $O_2/CH_4 = 0.25$.

Focussing on the tested catalysts, the Ni and Rh—Ni (1–3 μm) catalysts presented lower values for methane conversion compared to other catalysts. Moreover, when the monometallic Ni (1–3 μm) catalyst was tested for SR at S/C = 2.0 and TR processes, the measured methane conversion was negative. This fact might be due to the low affinity to water addition of this type of Zeolite L, which could inhibit these processes. The small amount of methane produced (4.9% in SR and 6.1% in TR process) could be explained through the contribution of the methanation reaction [45], and could be due to the presence of Ni species in the hexagonal prism of Zeolite L.

Both, the Ni and Rh—Ni Disc and Cylindrical (30–60 nm) catalysts achieved higher methane conversions. For these catalysts, Rh incorporation improved the methane conversion reaching values higher than 80% in all the studied processes except DR. Therefore, the Zeolite L catalysts that were made showed that the presence of Rh evidenced a better catalytic activity. Indeed, for these bimetallic systems, for OR at $O_2/CH_4 = 0.50$, and the TR processes, similar methane conversion values were achieved; thus, the water addition did not seem to clearly improve methane conversion.

Focussing on the obtained results, for the OR process at $O_2/CH_4 = 0.50$, the methane conversion for Rh—Ni Disc catalyst was 97.53% and 95.10% for Cylindrical (30–60 nm) catalysts. In the TR process, the methane conversion for Rh—Ni Disc catalyst was 97.04% and 96.42% for Cylindrical (30–60 nm) catalysts. Therefore, the OR at $O_2/CH_4 = 0.50$ and the TR processes using bimetallic Rh—Ni Disc and Cylindrical (30–60 nm) catalysts seemed to be the most appropriate conditions and catalysts to convert almost all the methane fed.

In Fig. 7, carbon dioxide conversion activity results are shown for all the tested catalysts and studied processes. Regarding the processes studied, as it happened for the methane conversion, the CO_2 reforming capacity decreased when the S/C ratio was increased from 1.0 to 2.0. On the contrary, the high values for the methane conversion reached in the OR at $O_2/CH_4 = 0.50$ and the TR processes, were not reached for the CO_2 conversion. For the OR processes, the contrary tendency was followed, higher CO_2 conversions were reached when lower oxygen was introduced in the system. This could be due to the presence of more methane that could react with the CO_2 through the DR reforming reaction. And finally, for the CO_2 conversion, the DR and the OR at $O_2/CH_4 = 0.25$ processes reached the maximum values – very closed to the equilibrium conversion-except for the Ni (1–3 μm) catalyst.

Taking into account all the processes studied, for the bimetallic Rh—Ni Disc and Cylindrical (30–60 nm) catalysts CO_2 equilibrium conversions were almost achieved in all the tested processes. For

Table 4
Tested catalysts surface composition obtained by XPS.

Used samples of catalyst	Disc		Cylindrical (30–60 nm)		Cylindrical (1–3 μm)	
	Rh—Ni	Ni	Rh—Ni	Ni	Rh—Ni	Ni
Sample relative intensities (%) of C(1s)	39.4	40.8	32.4	47.9	30.9	36.1

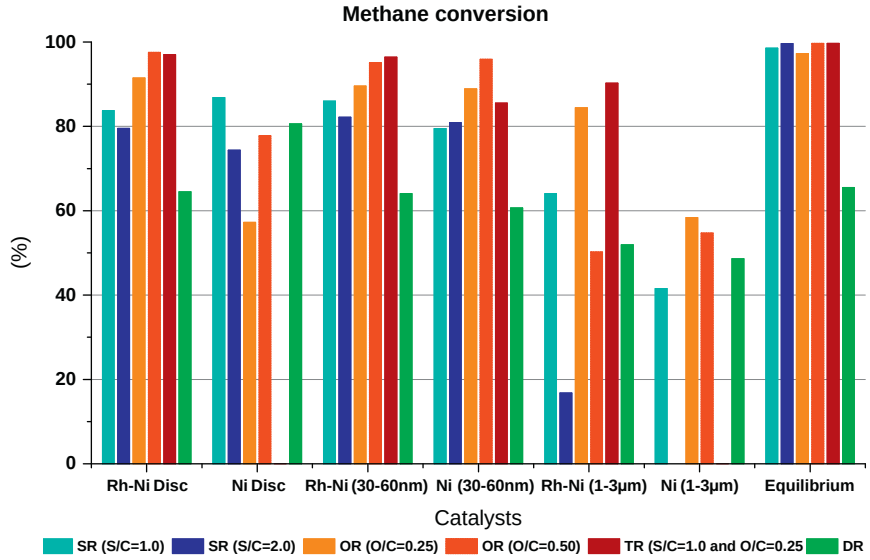

Fig. 6. Methane conversion results of the tested catalysts and studied processes.

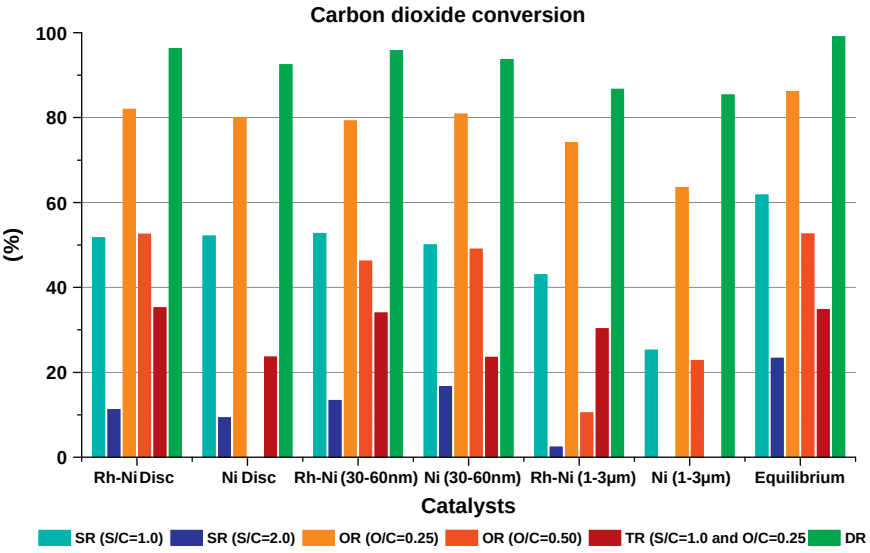

Fig. 7. Carbon dioxide conversion results of the tested catalysts and studied processes.

those two catalysts is evidenced that the presence of Rh metal again increased the obtained CO_2 conversion values in all the tested processes and conditions (except to the SR process at S/C = 1.0).

Focusing in the results, for Ni Disc catalyst, this catalyst did not show apparent activity when it was tested in the TR process as the CO_2 and CH_4 conversion values demonstrate with a minus 9.2% of CO_2 conversion and minus 11.9% of CH_4 conversion which could be associated to the methanation reaction [45].

Regarding the Ni and Rh—Ni (1–3 μm) catalyst, they showed lower CO_2 conversion capacity if they are compared with the rest of the catalysts, nevertheless the measured values were specially high for the OR at O/C = 0.25 and DR processes. For the Ni (1–3 μm) catalyst, the CO_2 conversion was minus 10.5% at S/C = 2.0 and minus 7.5% for the TR process.

3.3. Discussion

In Fig. 8 hydrogen production yield results of the tested catalysts and processes are represented. This parameter depends on the hydrogen produced and the methane and water fed to the system (see Section 2.3 Activity measurements). Thus, the hydrogen production flow-rate depends on the catalysts activity, the methane volumetric flow-rate- that was kept constant in all the studied processes- but in the case of the water content, it was different in the tested processes and for the OR and DR processes, no water was added to the system. This means that comparisons should be made in a certain process between the tested catalysts.

Attending to the previous considerations, the bimetallic Disc and Cylindrical (30–60 nm) catalysts seemed to be the most appropriate ones for the different studied SR and OR processes obtaining the highest hydrogen yield for the OR process at the O/C ratio of 0.25.

As a consequence of the poor methane and carbon dioxide conversions reached by the Ni and Rh—Ni (1–3 μm) catalysts, the lowest hydrogen production yields were achieved by these catalysts.

Finally, in Fig. 9, the last calculated parameter results are shown, which corresponds to the synthesis gas ratio, H_2/CO. The desired ratio for liquid hydrocarbons production through Fischer–Tropsch synthesis and for the methanol synthesis is close

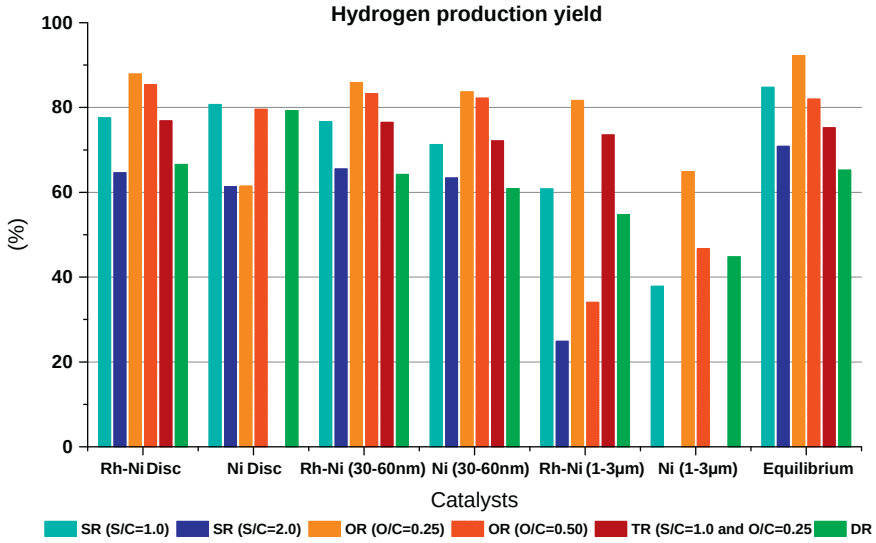

Fig. 8. Hydrogen production yield results of the tested catalysts and studied processes.

to 2 [36,46,47]. Moreover, a synthesis gas ratio of 1 is needed for the Oxo (also known as hydroformylation), which can be obtained through DR and OR processes.

Focussing on the equilibrium calculations results, SR at S/C = 2.0 is the unique process that overcomes this ratio. For the SR at S/C = 1.0 and TR processes, ratios near to this value can be obtained so that a subsequent step (apart from the purification) should be considered to achieve the desired syngas ratio of 2. Operating in OR or DR processes conditions, syngas ratios of 1 can be reached. In any case, the most active catalysts would be selected in order to achieve the highest conversion values and the most selective ones in order to facilitate the subsequent purification steps.

With regard to the catalysts' results, for H_2/CO ratio, close values to 2 for were reached for almost all the catalysts as it should be expected for the equilibrium ones. Only Ni (1–3 μm) catalysts did not reach those values.

In Fig. 10, the H_2 yield, metal dispersion and ICP results (as metal content) are represented for Zeolite L studied catalysts and for the γ-Al_2O_3 catalysts [6] in order to compare them. For the Disc and Cylindrical (30–60 nm) catalysts higher H_2 yields were reached for similar metals content. This higher production of hydrogen can be attributed to the higher dispersion of the metals incorporated into the Zeolite L measured by H_2 chemisorption. As

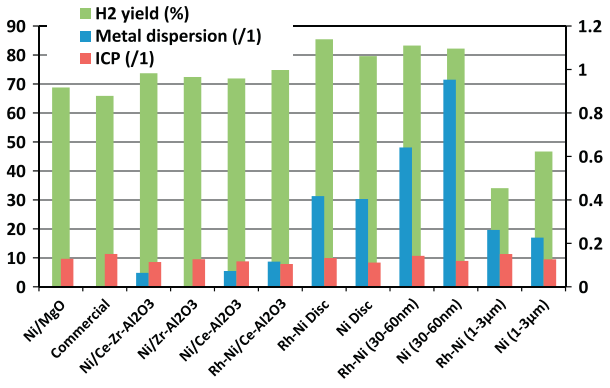

Fig. 10. H_2 yield, metal dispersion and ICP results for the tested catalysts.

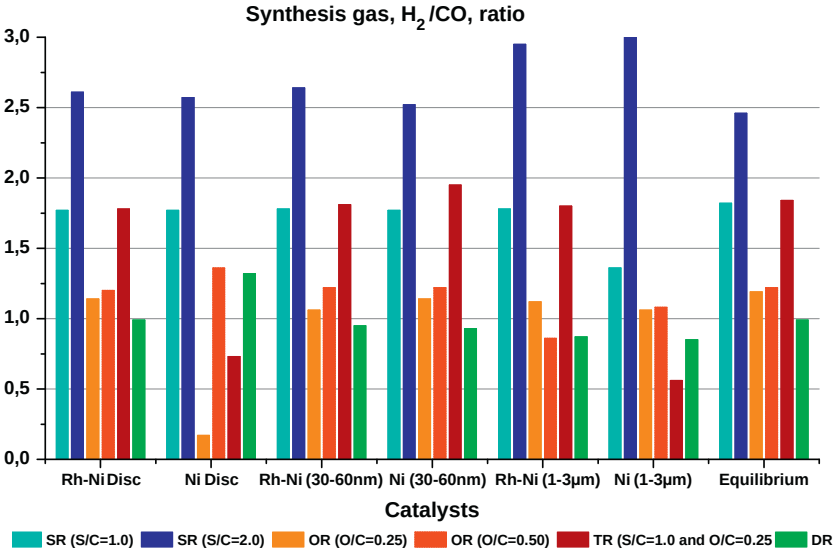

Fig. 9. Synthesis gas, H_2/CO ratio results of the tested catalysts and studied processes.

it was commented before, in Section 3.1.1., in the case of the Cylindrical Zeolite L the metal dispersion achieved for both samples was very high with a very small particles size. Nevertheless, the anchorage of NiO species for the bimetallic sample (as TPR analysis shown) enhanced a higher performance for this catalytic sample. For the Ni Cylindrical (30–60 nm) and bimetallic Rh—Ni Disc and Cylindrical (30–60 nm) catalysts, hydrogen yield higher than 80% was reached. In the case of the bimetallic samples lower carbon was measured by XPS covering the external surface.

Comparing the results with the ones obtained for γ-Al_2O_3 catalysts higher hydrogen yields, for γ-Al_2O_3 catalysts, the maximum hydrogen yield achieved was around 70% while for the Zeolite L catalysts was higher than 80%. Thus, the support had a clear effect improving the hydrogen obtained.

4. Conclusions

The main objective of this work was to use Zeolite L as a catalyst support based on Ni and Rh—Ni metals for the study of several biogas reforming processes in order to generate renewable energy. In this sense, the hydrogen and/or syngas generated and their possible uses were also analysed.

Taking into account the catalysts' activity and according to the morphological difference between the Disc and Cylindrical (30–60 nm) Zeolites L, different activities were measured. For the SR processes, the Disc catalysts were more active at the lowest S/C ratio, and the activity decreased when the S/C ratio increased to 2.0. On the contrary, the Cylindrical (30–60 nm) catalysts were more active in OR at O/C = 0.50 and decreased when the S/C ratio increased to 0.5.

In all the tested processes, Ni and Rh—Ni catalysts based on Cylindrical (1–3 μm) Zeolite L achieved the lowest activity values. This could be associated to: (i) the presence of Merlinoite zeolite – detected by XRD – which contributes around 25% of the sample, and (ii) the presence of NiO species with low interaction with the support – measured by TPR – that were not active.

With the exception of Ni Disc catalysts for SR at S/C = 1.0 and DR processes, the bimetallic catalysts showed much better reforming capacities in the tested processes and conditions. Thus, Rh incorporation increased catalytic activity in all the reforming processes tested and obtaining a low carbon deactivation (measured by XPS). The Rh—Ni catalysts based on Disc and specially the Cylindrical (30–60 nm) Zeolite L seemed to be a very promising catalyst due to its very high metallic dispersion (measured by H_2 chemisorption), the presence of NiO species with strong interaction with the support (measured by TPR), and excellent activities. Therefore, the nano Zeolite L, prepared with the lowest size of particle incorporated into Zeolite L, was most active for the biogas reforming reaction.

Acknowledgments

This work has been supported by the Basque Government EJ/GV (VALMICRO. S-PE12UN140), and the University of the Basque Country UPV/EHU (US11/04) and the Ministry of Science and Innovation (OIL2H2. ENE2011-23950). SEM and TEM images and DLS analysis were provided by the SGI/IZO-SGIker of the UPV/EHU. L.G. acknowledges the phD Grant from the Basque Country Department of Education, Research, and Universities.

References

[1] W. Qiao, X. Yan, J. Ye, Y. Sun, W. Wang, Z. Zhang, Evaluation of biogas production from different biomass wastes with/without hydrothermal pretreatment, Renew Energ. 36 (2011) 3313–3318.
[2] S. Rasi, A. Veijanen, J. Rintala, Trace compounds of biogas from different biogas production plants, Energy 32 (2007) 1375–1380.
[3] P. Börjesson, M. Berglund, Environmental systems analysis of biogas systems – Part I: fuel-cycle emissions, Biomass Bioenergy 30 (2006) 469–485.
[4] P. Kolbitsch, C. Pfeifer, H. Hofbauer, Catalytic steam reforming of model biogas, Fuel 87 (2007) 701–706.
[5] H.J. Alves, C.B. Junior, R.R. Niklevicz, E.P. Frigo, M.S. Frigo, C.H. Coimbra-Araujo, Overview of hydrogen production technologies from biogas and the applications in fuel cells, Int. J. Hydrogen Energy 38 (2013) 5215–5225.
[6] U. Izquierdo, V.L. Barrio, J. Requies, J.F. Cambra, M.B. Güemez, P.L. Arias, Tri-reforming: a new biogas process for synthesis gas and hydrogen production, Int. J. Hydrogen Energy, 2012 <http://dx.doi.org/10.1016/j.ijhydene.2012.09.107>.
[7] U. Izquierdo, V.L. Barrio, N. Lago, J. Requies, J.F. Cambra, M.B. Güemez, P.L. Arias, Biogas steam and oxidative reforming processes for hydrogen production in conventional and microreactor reaction systems, Int. J. Hydrogen Energy 37 (2012) 13829–13842.
[8] P. Frontera, A. Macario, A. Aloise, F. Crea, P.L. Antonucci, J.B. Nagy, et al., Catalytic dry-reforming on Ni-zeolite supported catalyst, Catal. Today 179 (2012) 52–60.
[9] O.A. Bereketidou, M.A. Goula, Biogas reforming for syngas production over nickel supported on ceria–alumina catalysts, Catal. Today 195 (2012) 93–100.
[10] S. Damyanova, B. Pawelec, K. Arishtirova, J.L.G. Fierro, Biogas reforming over bimetallic PdNi catalysts supported on phosphorus-modified alumina, Int. J. Hydrogen Energy 36 (2011) 10635–10647.
[11] X. Junke, Z. Wei, L. Zhaojing, W. Jihui, M. Jianxin, Biogas reforming for hydrogen production over a Ni–Co bimetallic catalyst: effect of operating conditions, Int. J. Hydrogen Energy 35 (2010) 13013–13020.
[12] A.H. Fakeeha, W.U. Khan, A.S. Al-Fatesh, A.E. Abasaeed, Stabilities of zeolite-supported Ni catalysts for dry reforming of methane, Chin. J. Catal. 34 (2013) 764–768.
[13] A. Kaengsilalai, A. Luengnaruemitchai, S. Jitkarnka, S. Wongkasemjit, Potential of Ni supported on KH zeolite catalysts for carbon dioxide reforming of methane, J. Power Sources 165 (2007) 347–352.
[14] W. Nimwattanakul, A. Luengnaruemitchai, S. Jitkarnka, Potential of Ni supported on clinoptilolite catalysts for carbon dioxide reforming of methane, Int. J. Hydrogen Energy 31 (2006) 93–100.
[15] L. Gartzia-Rivero, J. Bañuelos-Prieto, V. Martínez-Martínez, I. López Arbeloa, Versatile photoactive materials based on zeolite L doped with laser dyes, Chem. Plus Chem. 77 (2012) 61–70.
[16] Q. Huo, T. Dou, Z. Zhao, H. Pan, Synthesis and application of a novel mesoporous zeolite L in the catalyst for the HDS of FCC gasoline, Appl. Catal. A Gen. 381 (2010) 101–108.
[17] K.G. Azzam, G. Jacobs, W.D. Shafer, B.H. Davis, Dehydrogenation of propane over Pt/KL catalyst: investigating the role of L-zeolite structure on catalyst performance using isotope labeling, Appl. Catal. A Gen. 20 (2010) 264–270.
[18] J.M. Hill, R.D. Cortright, J.A. Dumesic, Silica- and L-zeolite-supported Pt, Pt/Sn and Pt/Sn/K catalysts for isobutane dehydrogenation, Appl. Catal. A Gen. 168 (1998) 9–21.
[19] R.D. Cortright, J.A. Dumesic, L-zeolite-supported platinum and platinum/tin catalysts for isobutane dehydrogenation, Appl. Catal. A Gen. 129 (1995) 101–115.
[20] A.P. Singh, S.B. Kumar, Para selective chlorination of toluene with an L-zeolite catalyst, Appl. Catal. A Gen. 126 (1995) 27–38.
[21] J.S. Chang, S.E. Park, H. Chon, Catalytic activity and coke resistance in the carbon dioxide reforming of methane to synthesis gas over zeolite-supported Ni catalysts, Appl. Catal. A Gen. 145 (1996) 111–124.
[22] U.L. Portugal, A.C.S.F. Santos, S. Damyanova, C.M.P. Marques, J.M.C. Bueno, CO_2 reforming of CH_4 over Rh-containing catalysts, J. Mol. Catal. A – Chem. 184 (2002) 311–322.
[23] U.L. Portugal, C.M.P. Marques, E.C.C. Araujo, E.V. Morales, M.V. Giotto, J.M.C. Bueno, CO_2 reforming of methane over zeolite-Y supported ruthenium catalysts, Appl. Catal. A – Gen. 193 (2000) 173–183.
[24] C. Crisafulli, S. Scirè, S. Minicò, L. Solarino, Ni–Ru bimetallic catalysts for the CO_2 reforming of methane, Appl. Catal. A – Gen. 225 (2002) 1–9.
[25] D. Halliche, O. Cherifi, A. Auroux, Microcalorimetric studies and methane reforming by CO_2 on Ni-based zeolite catalysts, Thermochim. Acta 434 (2005) 125–131.
[26] S.M. Gheno, S. Damyanova, B.A. Riguetto, C.M.P. Marques, C.A.P. Leite, J.M.C. Bueno, CO_2 reforming of CH_4 over Ru/zeolite catalysts modified with Ti, J. Mol. Catal. A – Chem. 198 (2003) 263–275.
[27] A.N. Pinheiro, A. Valentini, J.M. Sasaki, A.C. Oliveira, Highly stable dealuminated zeolite support for the production of hydrogen by dry reforming of methane, Appl. Catal. A Gen. 355 (2009) 156–168.
[28] M. García-Diéguez, I.S. Pieta, M.C. Herrera, M.A. Larrubia, L.J. Alemany, Nanostructured Pt- and Ni-based catalysts for CO_2-reforming of methane, J. Catal. 270 (2010) 136–145.
[29] V.A. Tsipouriari, A.M. Efstathiou, Z.L. Zhang, X.E. Verykios, Reforming of methane with carbon dioxide to synthesis gas over supported Rh catalysts, Catal. Today 21 (1994) 579–587.
[30] C. Yang-guang, K. Tomishige, K. Yokoyama, K. Fujimoto, Promoting effect of Pt, Pd and Rh noble metals to the $Ni_{0.03}Mg_{0.97}O$ solid solution catalysts for the reforming of CH_4 with CO_2, Appl. Catal. A – Gen. 165 (1997) 335–347.
[31] J.R. Rostrup-Nielsen, Aspects of CO_2-reforming of methane, Stud. Surf. Sci. Catal. 81 (1994) 25–41.
[32] D. San-José-Alonso, J. Juan-Juan, M.J. Illán-Gómez, M.C. Román-Martínez, Ni, Co and bimetallic Ni–Co catalysts for the dry reforming of methane, Appl. Catal. A – Gen. 371 (2009) 54–59.

[33] A. Zabala Ruiz, D. Bruhwiler, T. Bau, G. Calzaferri, Synthesis of zeolite L. Tuning size and morphology, Monatsh. Chem. 136 (2005) 77–89.
[34] C.S. Lau, A. Tsolakis, M.L. Wyszynski, Biogas upgrade to syn-gas (H_2–CO) via dry and oxidative reforming, Int. J. Hydrogen Energy 36 (2011) 397–404.
[35] A. Effendi, Z.G. Zhang, K. Hellgardt, K. Honda, T. Yoshida, Steam reforming of a clean model biogas over Ni/Al_2O_3 in fluidized- and fixed-bed reactors, Catal. Today 77 (2002) 181–189.
[36] A.E. Castro Luna, M.E. Iriarte, Carbon dioxide reforming of methane over a metal modified Ni–Al_2O_3 catalyst, Appl. Catal. A 343 (2008) 10–15.
[37] M. Wisniewski, A. Boréave, P. Gélin, Catalytic CO_2 reforming of methane over Ir/$Ce_{0.9}Gd_{0.1}O_{2-x}$, Catal. Commun. 6 (2005) 596–600.
[38] E.X. Verykios, Mechanistic aspects of the reaction of CO_2 reforming of methane over Rh/Al_2O_3 catalyst, Appl. Catal. A 255 (2003) 101–111.
[39] A.M. Diskin, R.H. Cunningham, R.M. Ormerod, The oxidative chemistry of methane over supported nickel catalysts, Catal. Today 46 (1998) 147–154.
[40] A. Luengnaruemitchai, A. Kaengsilalai, Activity of different zeolite-supported Ni catalysts for methane reforming with carbon dioxide, Chem. Eng. J. 144 (1) (2008) 96–102.
[41] J.J. Strohm, J. Zheng, C. Song, Low-temperature steam reforming of jet fuel in the absence and presence of sulfur over Rh and Rh–Ni catalysts for fuel cells, J. Catal. 238 (2006) 309–320.
[42] M. El Doukkali, A. Iriondo, J.F. Cambra, L. Jalowiecki-Duhamel, A.S. Mamede, F. Dumeignil, P.L. Arias, Pt monometallic and bimetallic catalysts prepared by acid sol–gel method for liquid phase reforming of bioglycerol, J. Mol. Catal. A: Chem. 368–369 (2013) 125–136.
[43] S. Rakass, H. Oudghiri-Hassani, P. Rowntree, N. Abatzoglou, Steam reforming of methane over unsupported nickel catalysts, J. Power Sources 158 (2006) 485–496.
[44] B. Pawelec, S. Damyanova, K. Arishtirova, J.L.G. Fierro, L. Petrov, Structural and surface features of PtNi catalysts for reforming of methane with CO_2, Appl. Catal. A 323 (2007) 188–201.
[45] M.P. Lai, W.H. Lai, R.F. Horng, C.Y. Chen, W.C. Chiu, S.S. Su, Y.M. Chang, Experimental study on the performance of oxidative dry reforming from simulated biogas, Energy Proc. 29 (2012) 225–233.
[46] D.P. Antonio, P. Nathaniel, Estudios de viabilidad de sistemas de purificación y aprovechamiento de biogas. Capítulo 5: Nuevos usos del biogas. Ministerio de ciencia e Innovación, 2010. PS120000-2007-6.
[47] S.T. Sie, R. Krishna, Fundamentals and selection of advanced Fischer–Tropsch reactors, Appl. Catal., A 55 (1999) 70–186.

2.2. Dye-Doped LTL Zeolites

The inner space of LTL zeolite can be filled with one or more kinds of dyes with suitable sizes (pore aperture of 7.1 Å). For dyes fitting the channels like a glove, the geometrical constraints imposed by the solid framework avoids the formation of aggregates (H-type or excimers, which usually efficiently quench the fluorescence emission from the monomers), improves the chemical, thermal and photochemical stability of the guest molecule and forces it to align in a preferred orientation, crafting highly organized photoactive materials. Thus, the unidimensional (1D) channels of LTL zeolite are ideal candidates to host high amount of fluorophores in an ordered disposition.

2.2.1. BODIPY laser dyes in LTL zeolite

Currently, there is a wide variety of commercially available laser dye families, which cover the ultraviolet, visible and near infrared regions of the electromagnetic spectrum. Among them, Boron DiPyrromethenes (BODIPY) outstand as versatile and attractive fluorophores not only as lasers but also as biological markers and probes in bioimaging, or photosensitizers in photovoltaic devices and singlet oxygen generation, just for highlighting some of the several applications of these organic molecules [29,30]. This is due to their high chemical, thermal and photo-stability, strong absorption and fluorescence bands and a core susceptible to several synthetic routes, which allow tailor-made functionalization and a fine tuning of the photophysical properties [31,32]. In view of these excellent properties we decided to incorporate commercial BODIPYs (PM546 and 567) with small enough size into the 1D channels of LTL zeolite looking for hybrid photoactive materials (Figure 2.7).

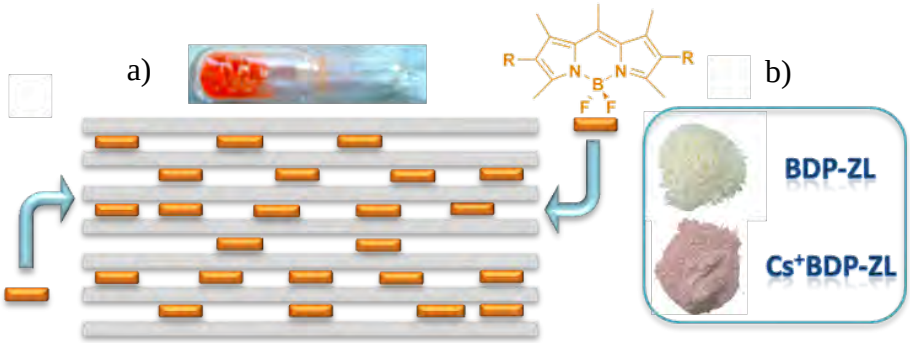

Figure 2.7. BDP-doped LTL zeolite. a) The fluorophore dye is embedded in the unidimensional channels of the zeolite by adsorption at gas phase in a sealed glass ampoule under vacuum. b) Colourless powder of non-treated BODIPY-doped LTL zeolite (top) and orange-brown powder of Cs^+-exchanged LTL zeolite (bottom) doped with BODIPY dye.

Owing to the neutral character of the BODIPY, its incorporation and diffusion into the channels takes place by adsorption at the gas phase at high temperatures. To this aim, the dye was sealed together with untreated and cesium-exchanged LTL zeolite in an ampoule at vacuum, and sublimated in a rotating oven, respectively (Figure 2.7).

The incorporation of BODIPY into untreated nanometer size LTL zeolite leads to colourless powder and no spectral bands are detected in the visible region (Figure 2.7.b). These findings suggest that the dye successfully diffuses into the pores because it is known that BODIPY is completely bleached in acid media (pH ‹ 2) [33] and confirms the key role of the pH conditions inside the pores in the photophysics of the dye. This discovery is another demonstration to evidence that the inner space of the synthesized LTL zeolite is characterized by a high acidity. That is the reason why the untreated LTL zeolite channels damages the dye and consequently its colour is totally bleached. Thus, in order to avoid undesirable acid-base equilibrium, the pH was adjusted by cation (cesium, pka = 3.7) exchange. Nonetheless, the allocation of the same dye into Cs^{+}-exchanged LTL zeolite provides an orange-brown powder (Figure 2.7.b), which absorption and fluorescence profiles match those recorded in diluted solutions (Figure 2.8.a). Besides, it is mainly adsorbed as monomer, although at very high loadings (around 90%, determined by thermogravimetry) a new red-shifted absorption band appears, indicative of J-type aggregation (nearly collinear disposition of the electronic transition dipole moments of the monomers). The presence of such intermolecular entities should be avoided because damages the fluorescence response of the material, thus loadings ≤ 40% were used to ensure the presence of monomers exclusively.

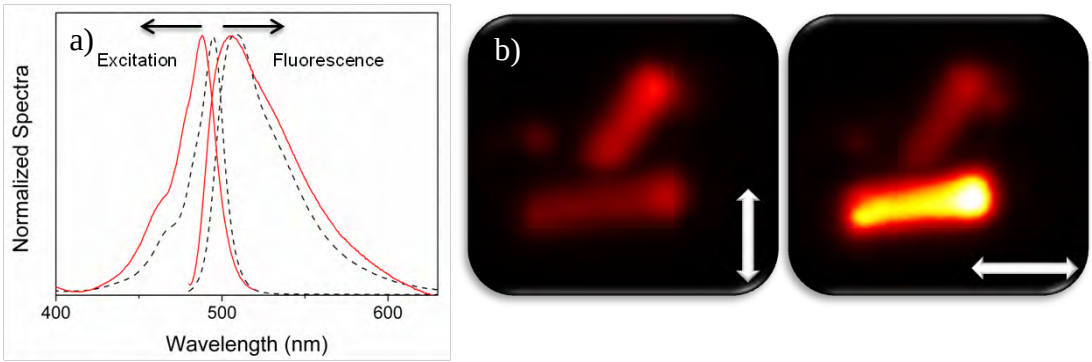

Figure 2.8. a) Normalized emission and excitation spectra of cesium-exchanged LTL zeolite doped with BDP (40%) in toluene (red solid line) and of the free dye in diluted solutions (black dashed line). b) Fluorescence images using vertical or horizontal polarized light (arrows indicate the direction of polarized light).

So as to analyze the orientation and distribution of the dye into the LTL zeolite crystals, the above BODIPYs were also occluded into large crystals (around 2 μm length), which enable the study by fluorescence confocal microscopy (standard resolution of λ/2, being λ the excitation wavelength). The corresponding fluorescence image of a single particle reveals uniform emission intensity along the crystal, which confirms the homogeneous and deep diffusion of the dye into the channels (Figure 2.8.b). Moreover, the material showed a high anisotropy response to the vertically and horizontally polarized light; no emission was observed when the fluorescence was monitored perpendicular to the main axis of the crystal, whereas a bright emission signal was switched on when the light was polarized along the main axis (Figure 2.8.b). This anisotropy response of the material proves the dye inclusion into the channels in a preferred orientation with its transition dipole moment parallel to the main axis of the crystal.

The fluorescence decay data of the BODIPY-doped material is quite complex and a multiexponential fit (up to three exponentials) is required to reproduce it. While the longest lifetime (5-6 ns) reminds to the usual lifetime of the BODIPY dye in solution, the other two faster ones (around 1.5 ns and 0.5 ns) could be produced by microheterogeneities in the zeolitic channel [34], which consequently result in specific interactions with the guest molecules. Such complex excited state dynamics motivates us to get a deeper inside in the nature of the specific interactions between the dye and the framework adsorption sites within the pores. To this aim, we accomplished a theoretical study (molecular dynamics and *ab initio* methods) of the BODIPY dyes into the LTL framework with the help of Dr. H. Manzano, which belongs also to the Molecular Spectroscopy research group.

Theoretical calculations reveal a specific interaction of the BF_2 bridge of the BODIPY with the remaining protons in the adsorption sites, which result in a loss of a fluorine atom $(BODIPY\text{-}F)^+$(Figure 2.9.a). Indeed a closer inspection of the absorption spectrum in the ultraviolet region points out the presence of a new band (centred at 315 nm), apart from the typical one placed in the green-yellow part of the visible (485 nm) (Figure 2.9.b). Thus, we should differentiate two adsorption sites, one in which the identity of the BODIPY is kept and responsible of the main Vis absorption band (HOMO → LUMO transition), and the other one in which a chemical reaction takes place between the BODIPY and the acidic protons from the zeolite, which leads to a loss of a fluorine from the dye (Figure 2.9.a). Moreover, such interaction promotes a

rearrangement of the electronic distribution of the π-system and as consequence the HOMO-2 → LUMO transition becomes allowed, explaining theoretically the appearance of the new hypsocromic UV absorption band (Figure 2.9.b and c). These specific interactions explain the multiexponential behaviour of the excited state deactivation in BODIPY-doped LTL zeolites and postulate the formation of the BODIPY-F^+ entity as one of the main responsibles of the fast lifetimes derived from the decay curve deconvolution.

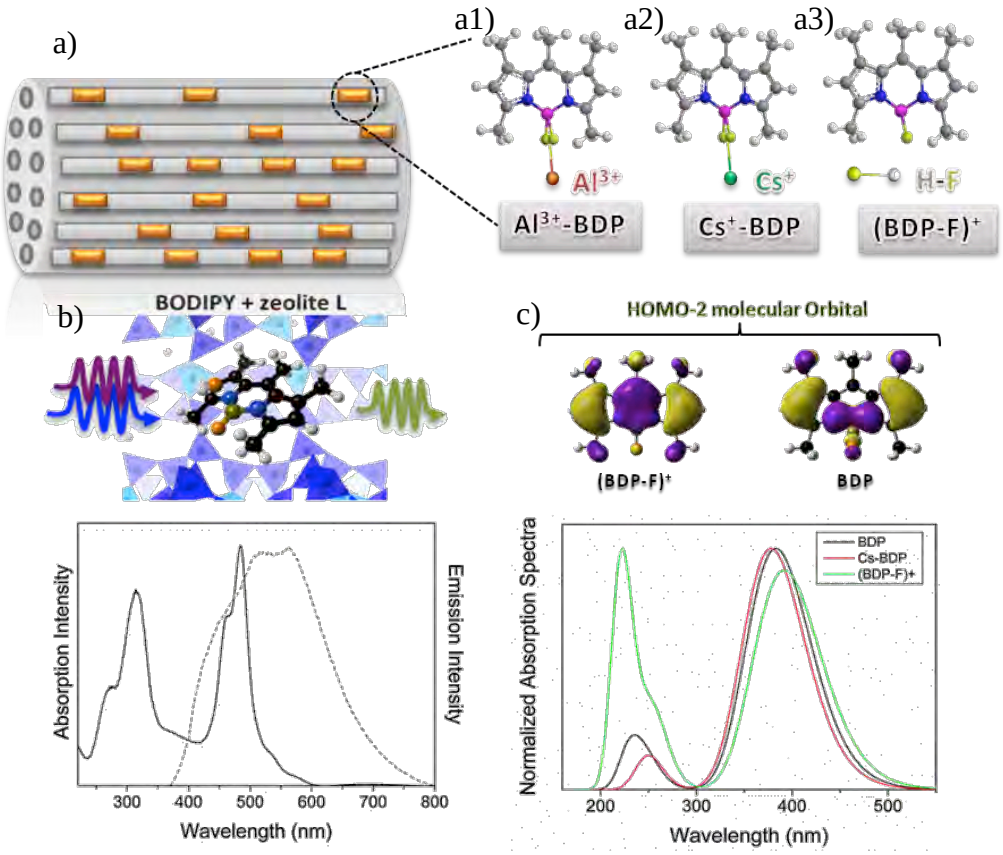

Figure 2.9. a) Schematic view of BDP-doped LTL zeolite with the representation of different absorption sites present in the inner part of the zeolitic channels: a1) Al-coordinated absorption site, a2) Cs^+-BDP complex and a3) monofluorated BODIPY (BODIPY-F)$^+$ together with the produced HF molecule. b) Experimentally recorded UV-Vis absorption (solid line) and emission spectra (dashed line) and schematic illustration of the dual absorption but single emission c) HOMO-2 molecular orbital representation for the molecules (BDP-F)$^+$ and BDP and simulated absorption spectra of BDP dye, Cs^+-BDP complex and (BODIPY-F)$^+$ molecule.

Therefore, albeit the cesium replacement reduces the acidity, the high reactivity of the BODIPY with the protons supports the coexistence of both species; the Cs^+-BODIPY and the (BODIPY-F)$^+$. Nevertheless, regardless of the excited one (UV or Vis excitation), a single emission is recorded at 545 nm (Figure 2.9.b). Consequently, under UV excitation an energy transfer process from one entity to another is efficiently achieved. As result, the confinement of a sole BDP dye into LTL zeolite channels leads

to a hybrid photoactive material behaving itself as an antenna system. It presents light absorption expanded to the UV and broad fluorescence emission is achieved regardless of the excited absorption band (Figure2.9.b).

In the following section we will take this system as reference to prepare antenna systems, in which we will try to reinforce the absorption in the UV and span it to the red-edge of the visible by its combination with carefully selected dyes.

Additional information regarding the theoretical calculations and photophysical properties of the BODIPY-doped LTL zeolite hybrid material can be found in the *Journal of Physical Chemistry C* report attached bellow.

THE JOURNAL OF PHYSICAL CHEMISTRY C

Article

pubs.acs.org/JPCC

Ultraviolet–Visible Dual Absorption by Single BODIPY Dye Confined in LTL Zeolite Nanochannels

Hegoi Manzano,* Leire Gartzia-Rivero, Jorge Bañuelos, and Iñigo López-Arbeloa

Molecular Spectroscopy Laboratory, Department of Physical Chemistry, University of the Basque Country UPV/EHU, Aptdo. 644, 48080-BILBAO, Spain

Supporting Information

ABSTRACT: A new hybrid material with dual UV/vis light-harvesting ability has been prepared based on PM546 dye confined in zeolite L nanochannels. Besides the characteristic vis green-yellow absorption of the dye in solution, a new band arises due to specific host–guest interactions, spanning the UV and blue edge of the vis. A chemical reaction takes place between the PM546 and acid protons from the zeolite, removing a fluorine atom from the BODIPY and giving rise to the new hypsochromic absorption. As result, a single dye presents light absorption at two different wavelengths, as well as a broad fluorescence emission, which covers a wide part of the vis region through a FRET process.

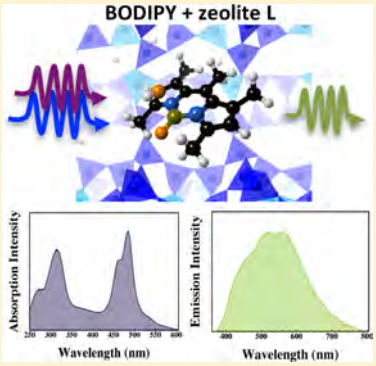

INTRODUCTION

Hybrid organic inorganic photoelectronic devices are promising alternatives to conventional silicon-based solar cells. They are generally built of cheap and environmentally friendly materials, easily adaptable to operate over a large variety of wavelengths, and can be tailored with versatile designs.[1] The encapsulation of organic fluorophores into a nanostructured host can avoid the formation of aggregates, improve the chemical, thermal, and photochemical stability of the dye, and force it to align in a preferred orientation, crafting highly organized photoactive hybrid materials.[2] Not only the properties of the fluorophores are ameliorated by such a cage effect but also the guest itself may behave as a fluorescent sensor to monitor the properties of the host adsorption sites.[3] Furthermore, the combination of complementary dyes could lead to efficient synergistic effects through an energy transfer process, creating highly adaptable systems. For instance, antenna devices and white-light-emitting systems have been fabricated by the encapsulation inside nanoporous materials of carefully chosen dyes with efficient and tunable Föster resonance energy transfer (FRET).[4]

In this work, we aim to build a hybrid photoactive material for energetic applications, formed by insertion of PM546 into the zeolite L framework (Figure 1). We have chosen such a guest dye, from the boron-dipyrromethene (BODIPY) family, due to its unique photophysical properties.[5,6] Pyrromethenes are characterized by their high fluorescent efficiency, which can be modulated over a wide range of absorption and emission wavelengths, changing the substitution pattern, making them versatile for a wide range of applications.[7] Among the available molecular sieves, zeolite L is a matchless choice.[8−10] Its framework structure results in a series of parallel one-dimensional nanochannels, with a pore aperture of 7 Å.[11] It is ideal to allocate inside fluorophores homogeneously distributed along the zeolite, and strongly oriented in a preferential direction.

We found that the specific interaction between the BODIPY and the zeolite L originates a radical change in the spectral signature of the dye, with the apparition of a new band in the UV-blue region, while conserving the characteristic vis green-yellow absorption. Such an interesting change might be relevant for the application of the system as a light-harvesting material: the nanoconfinement of a single dye in the zeolite can absorb light from two spectral regions far away, increasing the light collection efficiency of the system. Herein, we describe the BODIPY–zeolite L system, characterize its photophysical properties, and investigate the cause of the new spectral band using experimental techniques and atomic-scale simulations.

EXPERIMENTAL AND THEORETICAL METHODS

Experimental Methods. We produced nanosized LTL zeolites with an average size in the largest direction of 45 ± 15 nm via hydrothermal synthesis, using microwave heating to obtain a homogeneous morphology and a narrow size distribution of the crystals. In acidic solutions, the structural integrity of BODIPY is affected, since the protonation of the amine lone pairs lead to the corresponding dipyrromethene by removal of the BF_2 bridge.[12−14] To avoid this, we exchanged the zeolitic protons by Cs^+ cations,[15] suspending the zeolite L in a saturated solution of CsCl under reflux and stirring during 3 h at 80 °C. The PM546 (laser grade, purchased from

Received: May 25, 2013
Revised: May 31, 2013
Published: June 4, 2013

   dx.doi.org/10.1021/jp4051676 | J. Phys. Chem. C 2013, 117, 13331−13336

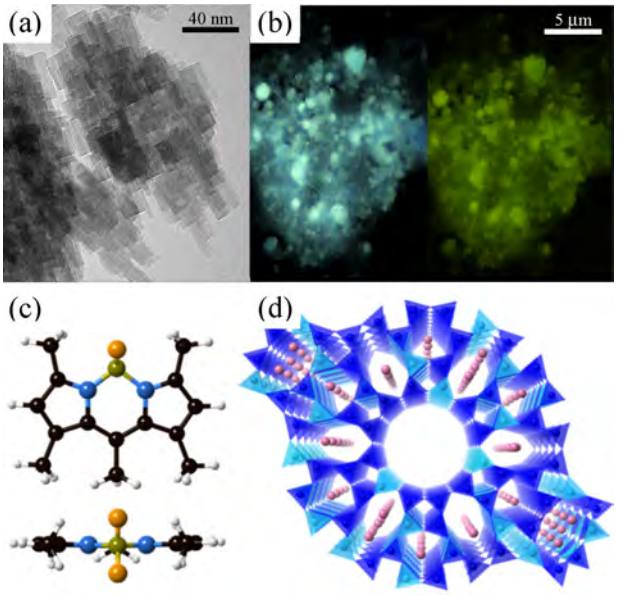

Figure 1. (a) TEM image of the nanometric zeolites synthesized using a microwave-assisted hydrothermal method. (b) Fluorescence images of the hybrid zeolite−dye system, under 350/50 and 470/40 nm band-pass excitation and recording the emission with 400 and 515 nm long passes, respectively (from left to right) (c) Atomic representation of the PM546 dye perpendicular and parallel to the molecular plane. The atoms are represented as spheres of several colors: C in black, H in white, N in blue, B in green, and F in orange. (d) Zeolite L supercell representation in the *z* crystallographic direction, perpendicular to the 1D nanochannels. The silicate and aluminate units are represented as dark and light blue tetrahedral omitting the framework oxygen atoms for a better view, and the Cs ions are shown as pink spheres.

Exciton) was then hosted inside the Cs^+-exchanged nanozeolite channels by gas-phase adsorption at high temperatures (180° during 2 days). We had previously confirmed the dye stability at the operation temperature, proving that its photophysics did not change after sublimation. Dye-doped zeolite was rinsed with butanol several times.

TEM images were recorded with a Philips CM200 microscope to assign the crystal size (around 45 nm), whereas the crystalinity of the sample was verified by XRD spectra taken in a Bruker D8 Advance Vario.[27] Al-NMR spectra were also recorded before and after dye insertion into the zeolite. The absorption spectra were registered in a Varian spectrophotometer (model Cary 4E) detecting the transmitted light for diluted liquid solutions and the reflected light, by means of an integrating sphere, for the solid samples. The fluorescence steady-state spectra and the CIE 1931 chromaticity diagram were recorded in an Edinburgh Instruments spectrofluorimeter (model FLSP920). The emission measurements were carried out in a right-angle configuration for dye solutions, and in the front-face configuration for dye-doped zeolites (solid state). Fluorescence images were recorded with an optical inverted microscope with an epi configuration (Olympus BX51) equipped with a color CCD (DP72). The excitation was set by Chroma band-pass filters (350/50 and 470/40), and emission was collected with Chroma cutoff filters (E400LPv2 and E515LPv2, from 400 and 515 nm, respectively).

Computational Methods. The Monte Carlo code Towhee[16,17] was used to determine the equilibrium position of the cesium ions inside the zeolite in the canonical ensemble.[18] The Cs atoms were initially located close to aluminum. The Monte Carlo movements were then done with a 0.2 Å maximum length for the atomic displacements and an acceptance threshold of 0.5, using the DX-1597-2-7 pseudorandom number generator method.[19] Thermodynamic equilibrium was reached after 10^6 steps. The potential energy was computed employing the ClayFF force field,[20] using the Edwald summation method account for the long-range electrostatic interactions.[21]

Ab initio molecular dynamics simulations have been carried out within the density functional theory framework[22] with the SIESTA code.[23] A double-ζ polarized basis set was used to represent valence orbitals, with Troullier−Martins pseudopotentials[24] factorized in the Kleiman−Bilander form to mimic the effect of nuclei and core electrons. The calculations were done at the Γ point with a mesh cutoff of 300 Ry. The Born−Oppenheimer dynamics were done in the canonical ensemble, allowing the movement of the guest dye molecule and the host zeolitic framework atoms. We used a 0.1 fs time step to integrate the equation of motion using a Verlet algorithm,[25] and a Nose thermostat[26] coupling constant of 100 Ry fs^2. The temperature was increased from 10 to 450 K during 2.5 ps, and then a 25 ps trajectory was simulated: initially 15 ps of the BODIPY inside the Cs-zeolite, and then 10 ps inside the H-zeolite. The structural quantities and energies at the absorption sites were integrated from 5 ps time blocks. Additional MD simulations of the isolated dye were carried out for 10 ps to compare the free and confined conformations of the molecule.

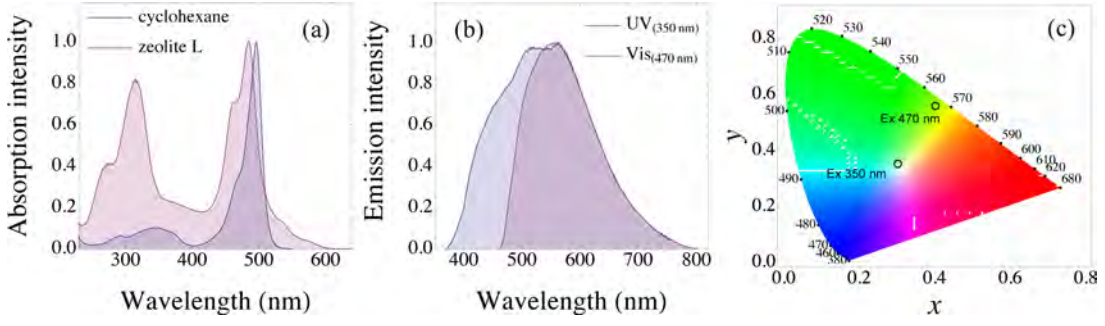

Figure 2. (a) Normalized absorption spectra of the PM546 in cyclohexane solution (blue) and confined in the zeolite L nanopores recorded in the solid state (red). The hybrid system preserves the band around 490 nm, and a new signal in the UV region arises. (b) Normalized emission spectra of the BODIPY hosted inside the zeolite collected after excitation at 350 (blue) and 450 nm (red). (c) Representation of the emission colors in the CIE 1931 chromaticity diagram[31] calculated from the fluorescence spectra under 350 and 450 nm irradiation, showing up the white-light emission of the dye-doped material.

dx.doi.org/10.1021/jp4051676 | J. Phys. Chem. C 2013, 117, 13331−13336

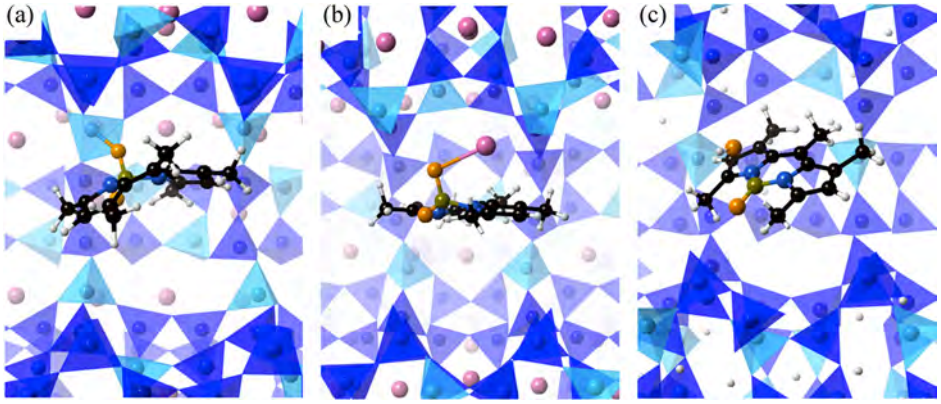

Figure 3. Configuration of the dye in the three identified absorption states. The snapshots are taken directly from the MD simulation, and the representation shows the inner part of the zeolitic channels with its longitudinal axis lying horizontally. The color code is the same as that in Figure 1. (a) Al-coordinated absorption site: a fluorine atom from the BODIPY is coordinated to an Al atom from the zeolite. (b) Cs^+−BODIPY complex in the zeolite nanochannel. (c) Monofluorated BODIPY $(PM546\text{-}F)^+$ and HF molecules situated in the zeolite channel. The fluorine atom that remains in the dye situates in a planar configuration with the molecule rings.

The electronic structure and absorption spectra were investigated with Gaussian.[27] The molecules obtained from the MD simulations were optimized within the Hartree−Fock theoretical framework, using a LanL2DZ basis set.[28] The absorption spectra were computed considering a Franck−Condon transition in a single-point single-excitation configuration interaction (CIS) calculation,[29] using the same basis set as before.

RESULTS AND DISCUSSION

The absorption spectrum of the BODIPY confined in the zeolite shows the expected main absorption band at 485 nm, in the middle energetic zone of the visible spectra, which maximum absorption wavelength and shape match with the registered in diluted solutions[5] (Figure 2). Surprisingly, a new band appears at much higher energies and is centered at 315 nm. Such a band has not been previously reported for BODIPY in a wide range of conditions, so we can conclude that the photophysic signature of the dye has changed due to specific interactions with the surrounding environment in the zeolite L channels. The formation of dye aggregates is nevertheless excluded, since the loading was set low enough to avoid it, and the aggregations would lead to absorption bands shifted toward lower energies.

Both absorption processes lead to fluorescent emission. The excitation at 350 nm results in a broad band with a maximum at 545 nm, similar to that recorded after excitation at 450 nm, with the only difference of a hypsochromic shoulder (Figure 2). It is very likely that the new blue fluorescence emission overlaps with the visible absorption band typical of the BODIPY, a Förster resonance energy transfer (FRET) taking place, which explains the single emission. The strong response to polarized light confirms that the dyes are located in the zeolitic channel, most probably as monomers, and indicates that the transition dipole moment (longitudinal molecular axis) of the dyes is disposed coplanar to each other and parallel to the 1D zeolitic channel,[30] factors that enable and maximize FRET processes. The dual light absorption by a single dye over a wide part of the visible and the UV is a very interesting feature for technological applications, such as sensors working in the UV/vis regions. In addition, the broad emission band (white light) enables the emission wavelength modulation (Figure 2), leading to the antenna effect and creating a versatile photoactive system for solar energy harvesting applications.

It is important to understand the origin of the new photophysical process for a future applicability of the developed material. To that end, we carried out an ab initio molecular dynamics simulation of PM546 absorbed in the LTL zeolite with the SIESTA code.[23] We built a 1 × 1 × 3 supercell of all-siliceous LTL zeolite, and substituted randomly Si atoms by Al to achieve the experimental Al/Si ratio of ∼1/3. The charge was balanced by adding Cs ions, optimizing their positions by a Monte Carlo energy minimization process. At equilibrium, the cations are located in the cancrinite and the 8/8-ring intersection cages, but not in the main channels, in agreement with the positions determined by X-ray diffraction.[32] Since our experiments indicate that there is no dye aggregation, a single PM546 molecule was introduced in the main channel, with the larger molecular axis running parallel to the channel direction. We increased the temperature from 10 to 450 K during 2.5 ps, the highest temperature achieved during the incorporation of the dye into the zeolite. Because of the thermal contribution, any chemical process that might affect the BODIPY structural integrity will be more likely in this temperature regime.

During the 25 ps of MD trajectory, we identified two absorption sites (Figure 3a,b). Initially, a fluorine atom from the BODIPY coordinates to an aluminum atom from the zeolitic framework. The chromophore is bonded to the zeolite, and the aluminum coordination changes from tetrahedral to trigonal-bipyramidal. After 5 ps, a cesium cation leaves the cancrinite cages and reaches the main channel. The fluorine atoms of the BODIPY then strongly interact with the electropositive Cs^+, leaving the aluminum absorption site. The adsorption energy of the BODIPY forming a Cs^+−PM546 complex is 50.9 kcal/mol, 18.1 kcal/mol higher than the Al-coordinated configuration. Therefore, the most favorable thermodynamic configuration of PM546 inside the LTL zeolite corresponds to the dye located in the main channel forming a complex with a cesium counterion. The lower distortion of the dye planarity is the probable reason for the higher stability of this configuration. Furthermore, the identical[27] Al-NMR signal measured for the zeolite before and after the dye insertion indicates that the aluminate units do not change their tetrahedral shape, confirming the absence of this adsorption configuration (see the Supporting Information).

dx.doi.org/10.1021/jp4051676 | J. Phys. Chem. C 2013, 117, 13331−13336

The Cs^+−BODIPY complex formation may be the cause of the new absorption band. To address this assumption, we investigated the electronic structure and excitation energies and oscillator strengths of the isolated dye and the cation−dye complex using the Gaussian code.[27] The HOMO−LUMO gap of the Cs^+−BODIPY complex is similar to that of the PM546 dye, just 0.001 eV larger. Furthermore, we did not observe any change in the HOMO−LUMO orbitals' spatial representations. Because the electronic structure of both systems is nearly identical, it is not surprising then that they present similar absorption spectra. The shape of the simulated spectra matches qualitatively with the experimental result, yet it is shifted toward higher energies with respect to the experiment due to the CIS overestimation of the energy gap.[33] We can conclude then that the formation of the Cs^+−BODIPY complex is not the origin of the new spectral signal in the UV region.

We seek another reason for the new UV absorption band. As mentioned before, the BODIPY dyes are very sensitive to acidic conditions. Although we exchanged the protons with cesium atoms to decrease the acidity of the zeolite, the cationic-exchange efficiency is not 100%.[34] Therefore, we explored the possibility that nonexchanged residual protons of the zeolite cause changes in the dye that explain the new spectral signature. For that end, we replaced the cesium atoms with hydrogen atoms in the final step of the MD trajectory and continued the dynamics. The zeolitic protons migrate from the center of the cancrinite and 8 × 8 intersection cages and coordinate to Si−O−Al bridging oxygen atoms. Regarding the Cs^+−dye complex, the substitution of Cs by H entails important structural changes. The strong H−F interaction has a more covalent character than the Cs−F, and the fluorine atom leaves the BODIPY to form hydrogen fluoride, leaving a monofluorated charged dye $(PM546\text{-}F)^+$ (Figure 3c). This reaction is thermodynamically favorable (ΔH_{react} = −206.7 kcal/mol), and barrier-less since it also takes place during a simple energy minimization process. The simulated absorption spectrum of the $(PM546\text{-}F)^+$ molecule shows the normal band of the BODIPY, together with a new one at higher energies (Figure 4). The shape of the computed spectrum utterly agrees with the experimentally recorded one, so we can conclude that the monofluorated BODIPY is responsible for the UV absorption. From the spatial representation of the molecular orbitals, presented in the Supporting Information, it can be seen that the HOMO and LUMO do not change appreciably after losing a fluorine atom in PM546, and consequently the vis absorption signal is not altered. However, there is a change in the HOMO-2 orbital, responsible for the new UV absorption band. The absence of a fluorine atom changes the spatial distribution of the electrons, increasing the extension of the π-electron system, and the HOMO-2 to LUMO transition becomes strongly allowed.

The $(PM546\text{-}F)^+$ species explains the experimentally recorded absorption bands. However, the presence of a considerable amount of exchanged Cs^+ makes it likely that some dye molecules do not react with protons, and are stabilized in the form of the Cs^+−PM546 complex. It is reasonable that both species, the Cs^+−PM546 complex and the $(PM546\text{-}F)^+$ molecules, could coexist. Their co-occurrence does not modify the discussed origin of the UV band, and is fully compatible with the experimental spectra. On the one hand, the absorption spectra could be formed by the combination of the UV band that originated from the monofluorated HOMO-2 to LUMO transition and the vis band due to the HOMO to LUMO transition of both species. On the other hand, the emission spectra are similar regardless of the excited band, a fact that we attributed to a Förster resonance energy transfer (FRET) process. In such an energy transfer, the $(PM546\text{-}F)^+$ molecules act as a donor when the UV region is excited, and neighboring $(PM546\text{-}F)^+$ species or Cs^+−PM546 complexes could be the acceptor, since both of them present the vis absorption band. It is worth mentioning that the collinear disposition of the molecules in the 1D zeolitic channel maximizes the orientation factor in the Förster formalism.

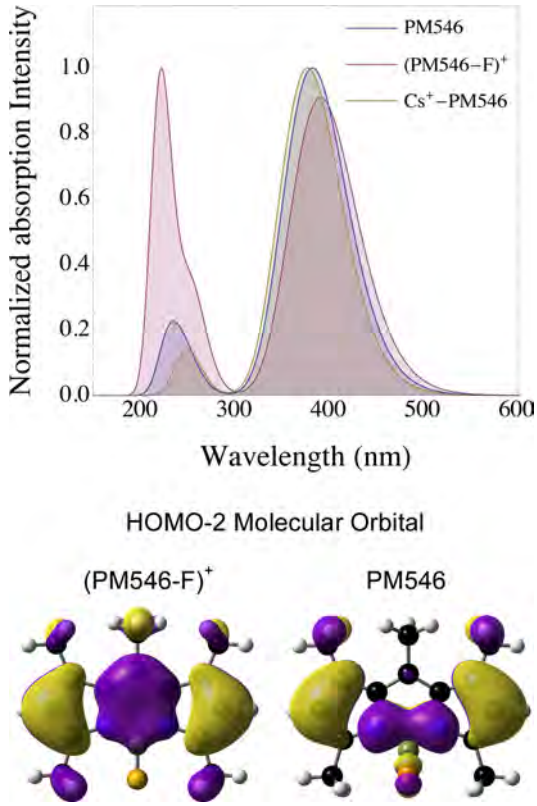

Figure 4. (a) Simulated absorption spectra of the P546 dye (blue), the Cs^+−PM546 complex (yellow), and the $(PM546\text{-}F)^+$ molecule (red) using the CIS method. There is a clear disparity when a fluorine atom is removed from PM546, since a new band at higher energies that matches the experimental data appears, due to an allowed HOMO-2 to LUMO transition. (b) HOMO-2 molecular orbital representation of the $(PM546\text{-}F)^+$ molecule and the PM546. The higher energy occupied frontier orbitals HOMO and HOMO-1 present the same spatial localization in both systems, as it can be seen in the Supporting Information.

Finally, we investigated another factor that may influence the electronic structure and, therefore, the absorption spectra of the confined BODIPY. According to our simulations, the most stable configuration of PM546 in vacuum is planar, although it can bend considerably due to thermal motion, with a maximum deviation from the planarity of ±21°. When the dye is confined in the zeolitic channel, there is a geometrical constrain that forces the BODIPY to bend, and the equilibrium angle departs considerably from the planarity. In section 2 of the Supporting Information, we present the equilibrium angles of the dye averaged over 5 ps of the molecular dynamics trajectory. It can be seen that the $(PM546\text{-}F)^+$ and Cs^+−PM546 species have equilibrium angles of 19.9° and 13.7°, respectively. In addition,

dx.doi.org/10.1021/jp4051676 | J. Phys. Chem. C 2013, 117, 13331−13336

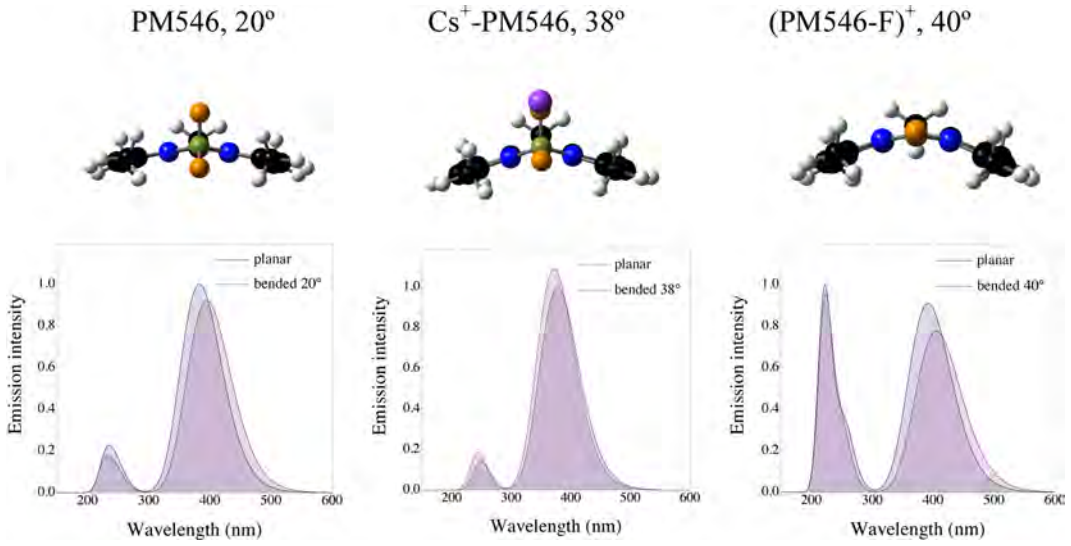

Figure 5. Simulated absorption spectra of the PM546, Cs^+−PM546, and $(PM546\text{-}F)^+$ species in their planar equilibrium configurations and at the maximum bending angle recorded during the molecular dynamics trajectory.

the thermal motion induces further bending, with a maximum deviation of ±20°, similar to that of the free dye.

Such a distortion from planarity might reduce the delocalization of the orbitals across the dye, decreasing their absorption intensity or inducing spectral shifts. To study this possibility, we computed the absorption spectra of the three species, PM546, $(PM546\text{-}F)^+$, and Cs^+−PM546, at the maximum recorded deviation from planarity (21, 40, and 38°, respectively). First, we fixed the dihedral angle at the desired value, and relaxed the remaining atomic positions. A single-point CIS calculation was then performed to the optimized structure. The results are presented in Figure 5. The spectra of the bent configurations have been normalized with respect to the maxima of the planar configurations to have an indication of the changes in the oscillator strength. The results reveal that the distortion does not affect substantially the absorption spectra. There are small changes in the oscillator strength and small displacement of the absorption maxima, although none of the changes are important.

CONCLUSIONS

In this work, we have presented a new hybrid photoactive material, based on the confinement of PM546 dyes into nanometric channels of the LTL zeolite. The hybrid system presents light absorption covering a wide part of the UV−vis regions. Such a spectral signature makes the material very versatile, since a single material could harvest light from two spectral regions far from each other. The new UV absorption band originated from a chemical change of the BODIPY. Fluorine atoms from the dye react with protons of the zeolitic framework, and one F atom leaves the dye. The newly found molecule preserves the HOMO−LUMO structure of the PM546, while the electronic structure of the HOMO-2 changes, making the HOMO-2 to LUMO transition strongly allowed. This fact is remarkable, since other dyes hosted in zeolites do not preserve the band characteristic of basic pH after protonation.[35]

Regardless of the excited band, a fluorescent emission with a similar wavelength is achieved via FRET-type energy transfer. This simplifies and enhances the light-harvesting process, collecting energy at different wavelengths simultaneously with just one fluorophore, and makes the system appealing for the development of antenna devices. Further effort is being carried out to tune the absorption and emission of the presented hybrid system, modifying the substitution pattern of the BODIPY. It is worth mentioning that the high sensitivity of PM546 to protons makes it a possible candidate as acidity site sensors in zeolites.

ASSOCIATED CONTENT

Supporting Information

X-ray diffraction pattern of the synthesized nanozeolite; structural data of the PM546 in vacuum, the PM546 coordinated to zeolitic Al, the Cs^+−PM546 complex inside the zeolite, and the $(PM546\text{-}F)^+$ species inside the zeolite; ^{27}Al-NMR of the zeolite with and without dye loading, and structural data of the aluminum coordinated to the PM546; spatial representation of the HOMO-2, HOMO-1, HOMO, and LUMO orbitals of all the molecules; and wavelengths and oscillator strengths of the HOMO-2 to LUMO, HOMO-1 to LUMO, and HOMO to LUMO transitions. This material is available free of charge via the Internet at http://pubs.acs.org.

AUTHOR INFORMATION

Corresponding Author

*E-mail: hegoi.manzano@ehu.es.

Notes

The authors declare no competing financial interest.

ACKNOWLEDGMENTS

This work was supported by the Spanish Government through the MAT2010-20646-204-04 project. H.M. and L.G.-R. acknowledge, respectively, the IT339-10 contract and the Ph.D. grant from the Basque Country Department of Education, Research, and Universities. The computing resources, transmission electron microscopy (TEM), X-ray diffraction (XRD), and aluminum nuclear magnetic resonance (^{27}Al-NMR) measurements of the SGIker (UPV/EHU) are gratefully acknowledged, as well as the computing resources of the i2Basque project.

REFERENCES

(1) Mech, A.; Monguzzi, A.; Meinardi, F.; Mezyk, J.; Macchi, G.; Tubino, R. Sensitized NIR Erbium(III) Emission in Confined Geometries: A New Strategy for Light Emitters in Telecom Applications. *J. Am. Chem. Soc.* **2010**, *132* (13), 4574−4576.

(2) Calzaferri, G. Nanochannels: Hosts for the Supramolecular Organization of Molecules and Complexes. *Langmuir* **2012**, *28* (15), 6216−6231.

(3) Corma, A.; Díaz, U.; García, T.; Sastre, G.; Velty, A. Multifunctional Hybrid Organic−Inorganic Catalytic Materials with a Hierarchical System of Well-Defined Micro- and Mesopores. *J. Am. Chem. Soc.* **2010**, *132* (42), 15011−15021.

(4) Ramachandra, S.; Schuermann, K. C.; Cucinotta, F.; Calzaferri, G.; De Cola, L. Förster Resonance Energy Transfer in Quantum Dot Dye Loaded Zeolite L Nanoassemblies. *Small* **2011**, *7* (10), 1488−1494.

(5) López-Arbeloa, F.; Bañuelos, J.; Martinez, V.; Arbeloa, T.; López-Arbeloa, I. Structural, Photophysical and Lasing Properties of Pyrromethene Dyes. *Int. Rev. Phys. Chem.* **2005**, *24* (2), 339−374.

(6) Ulrich, G.; Ziessel, R.; Harriman, A. The Chemistry of Fluorescent Bodipy Dyes: Versatility Unsurpassed. *Angew. Chem., Int. Ed.* **2008**, *47* (7), 1184−1201.

(7) Loudet, A.; Burgess, K. BODIPY Dyes and Their Derivatives: Syntheses and Spectroscopic Properties. *Chem. Rev.* **2007**, *107* (11), 4891−4932.

(8) Cheetham, A. K.; Férey, G.; Loiseau, T. Open-Framework Inorganic Materials. *Angew. Chem., Int. Ed.* **1999**, *38* (22), 3268−3292.

(9) Tao, Y.; Kanoh, H.; Abrams, L.; Kaneko, K. Mesopore-Modified Zeolites: Preparation, Characterization, and Applications. *Chem. Rev.* **2006**, *106* (3), 896−910.

(10) Schulz-Ekloff, G.; Wohrle, D.; van Duffel, B.; Schoonheydt, R. A. Chromophores in Porous Silicas and Minerals: Preparation and Optical Properties. *Microporous Mesoporous Mater.* **2002**, *51* (2), 91−138.

(11) Barrer, R.; Villiger, H. The Crystal Structure of the Synthetic Zeolite L. *Z. Kristallogr.* **1969**, *128* (3−6), 352−370.

(12) Reisfeld, R.; Yariv, E.; Minti, H. New Developments in Solid State Lasers. *Opt. Mater.* **1997**, *8* (1), 31−36.

(13) Bañuelos, J.; López Arbeloa, F.; Arbeloa, T.; Salleres, S.; Vilas, J.; Amat-Guerri, F.; Liras, M.; López Arbeloa, I. Photophysical Characterization of New 3-Amino and 3-Acetamido BODIPY Dyes with Solvent Sensitive Properties. *J. Fluoresc.* **2008**, *18* (5), 899−907.

(14) Li, J.; Hu, B.; Hu, G.; Li, X.; Lu, P.; Wang, Y. An Efficient Synthesis of Heptaaryldipyrromethenes from Tetraarylcyclopentadienones and Ammonium Acetate and Their Extension to the Corresponding BODIPYs. *Org. Biomol. Chem.* **2012**, *10* (44), 8848−8859.

(15) Albuquerque, R. Q.; Calzaferri, G. Proton Activity inside the Channels of Zeolite L. *Chem.—Eur. J.* **2007**, *13* (32), 8939−8952.

(16) Martin, M. G. *MCCS Towhee 7.0.2*; 2012. http://towhee.sourceforge.net.

(17) Martin, M. G.; Thompson, A. P. Industrial Property Prediction Using Towhee and Lammps. *Fluid Phase Equilib.* **2004**, *217* (1), 105−110.

(18) Metropolis, N.; Rosenbluth, A. W.; Rosenbluth, M. N.; Teller, A. H.; Teller, E. Equations of State Calculations by Fast Computing Machines. *J. Chem. Phys.* **1953**, *21* (6), 1087−1092.

(19) Deng, L.-Y. Efficient and Portable Multiple Recursive Generators of Large Order. *ACM Trans. Model. Comput. Simul. (TOMACS)* **2005**, *15* (1), 1−13.

(20) Cygan, R. T.; Liang, J. J.; Kalinichev, A. G. Molecular Models of Hydroxide, Oxyhydroxide, and Clay Phases and the Development of a General Force Field. *J. Phys. Chem. B* **2004**, *108* (4), 1255−1266.

(21) Ewald, P. P. The Calculation of Optical and Electrostatic Grid Potential. *Ann. Phys.* **1921**, *64* (3), 253−287.

(22) Parr, R. G.; Yang, W. *Density-Functional Theory of Atoms and Molecules*; Oxford University Press: Oxford, England, 1989.

(23) Artacho, E.; Anglada, E.; Dieguez, O.; Gale, J. D.; Garcia, A.; Junquera, J.; Martin, R. M.; Ordejon, P.; Pruneda, J. M.; Sanchez-Portal, D.; Soler, J. M. The Siesta Method; Developments and Applicability. *J. Phys.: Condens. Matter* **2008**, *20* (6), 064208.

(24) Troullier, N.; Martins, J. L. Efficient Pseudopotentials for Plane-Wave Calculations. *Phys. Rev. B* **1991**, *43* (3), 1993−2006.

(25) Verlet, L. Computer Experiments on Classical Fluids. I. Thermodynamical Properties of Lennard-Jones Molecules. *Phys. Rev.* **1967**, *159* (1), 98.

(26) Nose, S. A Molecular Dynamics Method for Simulations in the Canonical Ensemble. *Mol. Phys.* **1984**, *52* (2), 255−268.

(27) Frisch, M. J.; Trucks, G. W.; Schlegel, H. B.; Scuseria, G. E.; Robb, M. A.; Cheeseman, J. R.; Montgomery, J. A., Jr.; Vreven, J. T.; Kudin, K. N.; Burant, J. C.; Millam, J. M.; Iyengar, S. S.; Tomasi, J.; Barone, V.; Mennucci, B.; Cossi, M.; Scalmani, G.; Rega, N.; Petersson, G. A.; Nakatsuji, H.; Hada, M.; Ehara, M.; Toyota, K.; Fukuda, R.; Hasegawa, J.; Ishida, M.; Nakajima, T.; Honda, Y.; Kitao, O.; Nakai, H. M. X.; Hratchian, E. P.; Cross, J. B.; Adamo, C.; Jaramillo, J.; Gomperts, R.; Stratmann, R. E.; Yazyev, O.; Austin, A. J.; Cammi, R.; Pomelli, C.; Ochterski, J. W.; Ayala, P. Y.; Morokuma, K.; Voth, G. A.; Salvador, P.; Dannenberg, J. J.; Zakrzewski, V. G.; Dapprich, S.; Daniels, A. D.; Strain, M. C.; Farkas, O.; Malick, D. K.; Rabuck, A. D.; Raghavachari, K.; Foresman, J. B.; Ortiz, J. V.; Cui, Q.; Baboul, A. G.; Clifford, S.; Cioslowski, J.; Stefanov, B. B.; Liu, G.; Liashenko, A.; Piskorz, P.; Komaromi, I.; Martin, R. L.; Fox, D. J.; Keith, T.; Al-Laham, M. A.; Peng, C. Y.; Nanayakkara, A.; Challacombe, M.; Gill, P. M. W.; Johnson, B.; Chen, W.; Wong, M. W.; Gonzalez, C.; Pople, J. A. *Gaussian 03*, Revision B.04; Gaussian Inc.: Pittsburgh, PA, 2003.

(28) Wadt, W. R.; Hay, P. J. Ab Initio Effective Core Potentials for Molecular Calculations. Potentials for Main Group Elements Na to Bi. *J. Chem. Phys.* **1985**, *82* (1), 284.

(29) Foresman, J. B.; Head-Gordon, M.; Pople, J. A.; Frisch, M. J. Toward a Systematic Molecular Orbital Theory for Excited States. *J. Phys. Chem.* **1992**, *96* (1), 135−149.

(30) Gartzia-Rivero, L.; Bañuelos-Prieto, J.; Martínez-Martínez, V.; López-Arbeloa, I. Versatile Photoactive Materials Based on Zeolite L Doped with Laser Dyes. *ChemPlusChem* **2012**, *77* (1), 61−70.

(31) Smith, T.; Guild, J. The C.I.E. Colorimetric Standards and Their Use. *Trans. Opt. Soc.* **1931**, *33* (3), 73.

(32) Seoung, D.; Lee, Y.; Kim, S. J.; Lee, H.-H.; Ahn, D.; Shin, N.-S.; Vogt, T.; Lee, Y. Pressure-Induced Hydration and Cation Migration in a Cs^+ Exchanged Gallosilicate Zeolite LTL: Synchrotron X-Ray Powder Diffraction Study at Ambient and High Pressures. *Microporous Mesoporous Mater.* **2010**, *136* (1−3), 75−82.

(33) Cramer, C. J. *Essentials of Computational Chemistry: Theories and Models*; John Wiley & Sons: Chichester, England, 2002.

(34) Calzaferri, G.; Leiggener, C.; Glaus, S.; Schurch, D.; Kuge, K. i. The Electronic Structure of Cu^+, Ag^+, and Au^+ Zeolites. *Chem. Soc. Rev.* **2003**, *32* (1), 29−37.

(35) Bussemer, B.; Dreiling, I.; Grummt, U.-W.; Mohr, G. J. Spectroscopic and Quantum Chemical Study of the Brønsted Acid Sites in Zeolite L Channels with Acidochromic Cyanine Dyes. *J. Photochem. Photobiol., A* **2009**, *204* (2), 90−96.

2.2.2. Energy transfer in dye-doped LTL zeolite

Once the BODIPY dye has been successfully inserted into the LTL zeolite nanochannels, we combine this guest with suitable dyes working in the blue- and red-edge of the visible to span the light absorption range to the whole UV-Vis region and develop hybrid host-guest antenna systems. The chosen dyes should be small enough to diffuse into the channels and must have a proper spectral overlap with the bands of the BODIPY to enable the excitation energy transfer via Förster mechanism (dipole-dipole coupling, see chapter 1 about EET), also known as through-space energy transfer. To reinforce the UV-blue absorption and cover the red region, an oxazole (DMPOPOP) dye and oxazine laser dyes have been selected, respectively. Both kinds of fluorophores fulfill the above described requirements. The guest molecules will be sequentially inserted at low enough loadings to avoid aggregation. Thus, and taking into account the geometrical restrictions imposed by the framework, which avoids the guests sliding over each other, a well organized system is feasible; energy donors will be located at the center of the crystals, whereas energy acceptors will be in the pore entrances. The final goal would be the achievement of a system capable of harvesting the light from the UV/Vis/NearIR and transfer it to the crystal ends so as to retrieve red emission via successive FRET processes within the LTL zeolite channels.

Before building the whole hybrid system we should firstly check if the energy transfer between the flurophore pairs, blue-green (DMPOPOP-PM546) and yellow-red (PM567-Ox1), takes place inside the channels of disc-shaped LTL zeolite. To this aim, we first inserted the energy donors (DMPOPOP and PM567, respectively, via sublimation) and then the acceptors (PM546 and oxazine, respectively, the last one via cationic exchange) (Figure 2.10). In both cases the excitation at the donor absorption region led to its emission following by the acceptor emission band, albeit this last does not absorb light at the excitation region (Figure 2.10). These results indicate that the excitation energy is transferred through-space from the donors placed at the center of the crystals to the flanking acceptors. In fact, the Time Resolved Emission Spectra (TRES) show that the acceptor emission after donor excitation becomes progressively enhanced as the delay time after excitation increases. Moreover, the fluorescence lifetime of the donor decreases by the presence of the acceptor. Such trends clearly and undoubtedly confirm that the acceptor excited state is being populated from the donor excited state via a non-radiative mechanism (FRET), which deactivates the donor emission.

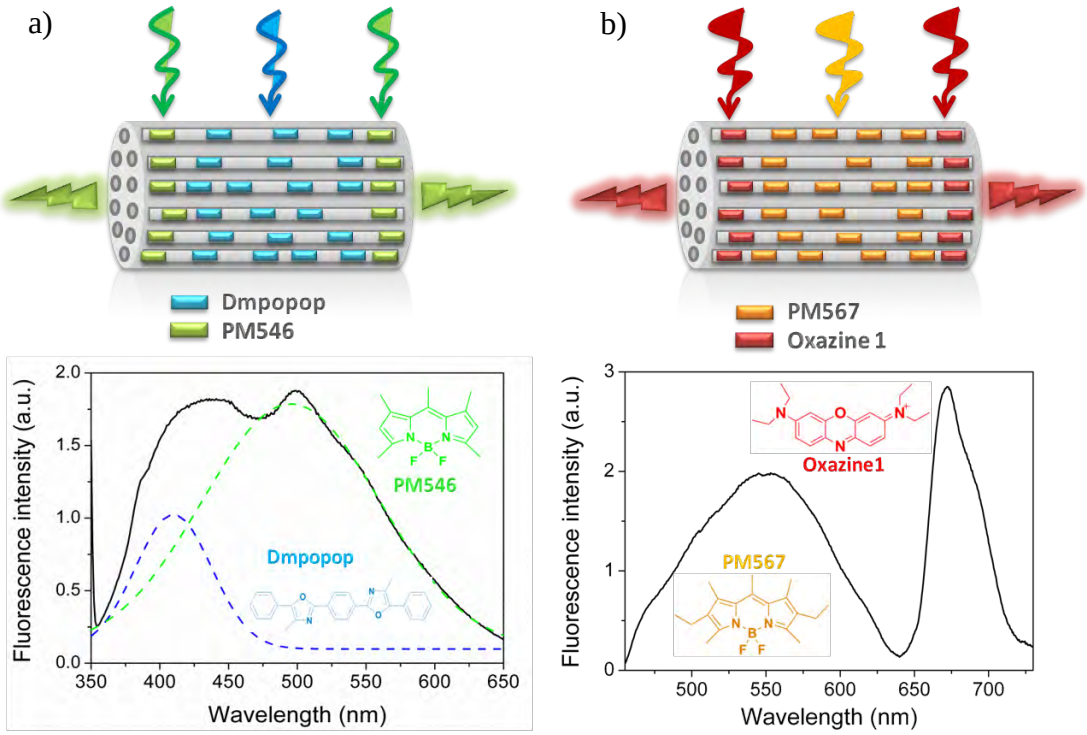

Figure 2.10. Schematic representations of supramolecularly organized dye-zeolite LTL antenna materials by sequential insertion of different dyes. a) Emission spectrum after excitation at 340 nm for the DMPOPOP-PM546 pair. b) Emission spectrum after excitation at 440 nm for the PM567-Ox1 pair.

Once checked that the chosen pairs of dyes undergo FRET processes, we now focus on the broaden antenna system where three dyes are combined and sequentially inserted in the zeolitic channels; first the donor DMOPOP, then the BODIPY and finally the oxazine (Figure 2.11). The fluorescence spectrum recorded after first donor excitation, where other two dyes do not absorb, shows its emission followed by that of PM567 and finally the acceptor Ox1 fluorescence band (Figure 2.11.b). Moreover, regardless of the excitation wavelength the red emission from the oxazine is detected. The TRES (Figure 2.11.d) exhibits a progressive increase of the oxazine emission signal with the delay time after excitation, while the average lifetime of the donor decreases. All these trends, confirm that FRET is taking place and as consequence light over a wide spectral region is efficiently harvested and straightway transported to the edges of the zeolites via successive FRET hopes, and finally converted into red emission. Nonetheless, the FRET is partial and the emission of each chromophore is simultaneously detected. The sum of these emissions spanning the whole visible leads to white-light emission (Figure 2.11.b, top). That is, the excitation at the UV edge give rise to a white-light emitting material where the emission can be finely tuned in the blue, green and red regions by using the proper filters (Figure 2.11.b, bottom).

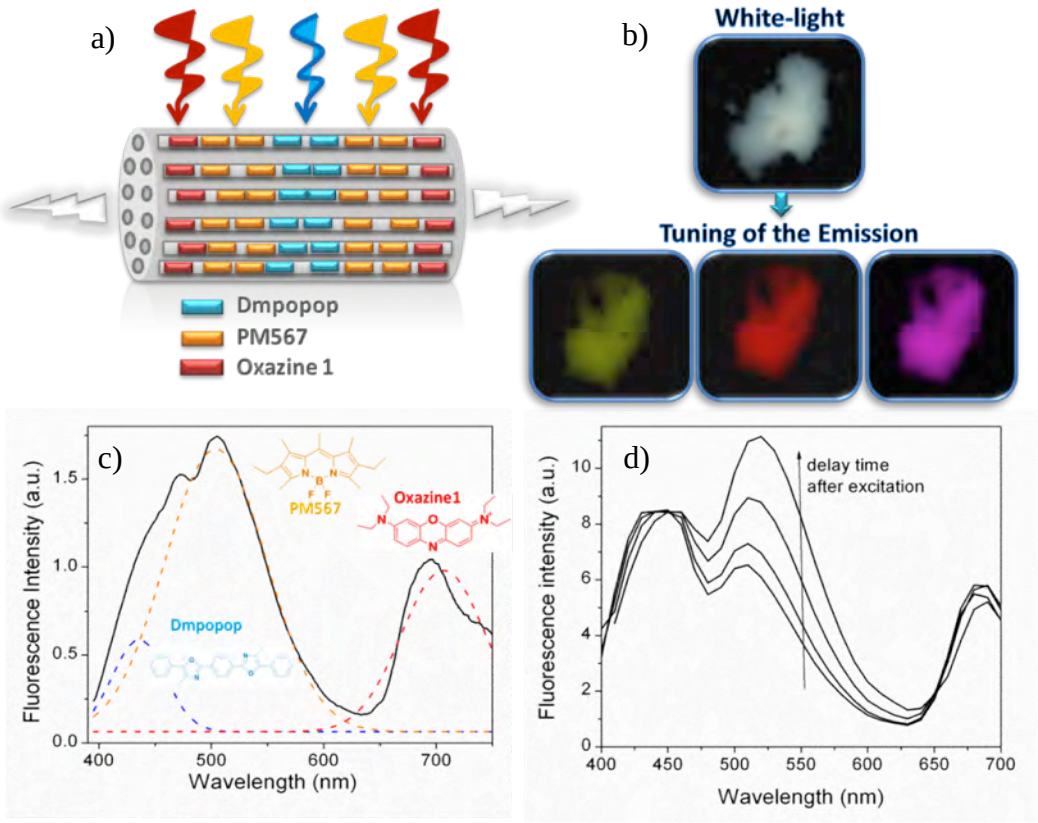

Figure 2.11. a) Schematic representation of the antenna material prepared by the sequential insertion of three different dyes into the LTL zeolite channels. b) Fluorescence images of LTL zeolite doped with DMPOPOP-PM567-Ox1 under 350/50 nm excitation and recording the emission with the corresponding long-pass filters: 400 nm (top), 515 nm (bottom left), 580 nm (bottom middle), and 665 nm (bottom right). c) Fluorescence spectrum recorded upon selective excitation of the first donor at 385 nm. d) Normalized Time-Resolved Emission Spectra (TRES) recorded at different times after excitation.

The FRET efficiency can be modulated by several parameters, such as dye concentration, donor-acceptor ratio and distance, relative orientations and spectral overlap [35]. As the first ones have been exhaustively analyzed in the literature for systems based of dye-doped LTL zeolite, we focused our attention in the last one (spectral overlap). To test it we built another antenna system maintaining constant the above mentioned parameters, but using a carbostyril (C165) as blue emitting energy donor and other oxazine (Ox4) as the final acceptor. This dye combination is characterized by a higher spectral overlap and accordingly should prompt a more efficient FRET process (Figure 2.12.b).

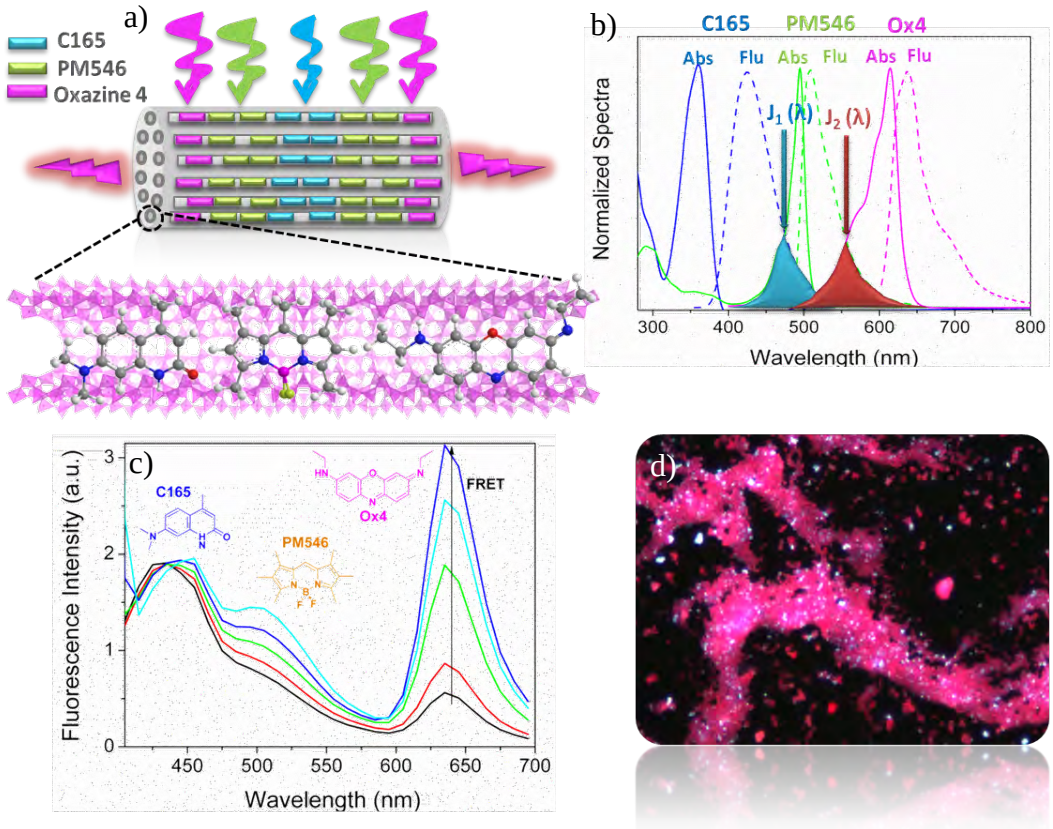

Figure 2.12. a) Schematic representation of the antenna material b) Normalized absorption and fluorescence spectra of dyes forming the system and the corresponding integrated spectral overlap. c) Normalized Time-Resolved Emission Spectra (TRES) recorded at different times after excitation. d) Fluorescence image of dye-zeolite hyrbrid system under 350/50 nm excitation and recording the emission with a long-pass filters of 400 nm.

As expected, the fluorescence spectra after UV donor excitation (Figure 2.12.c) shows the emission of each chromophore as a result of successive FRET processes from the carbostyryl to the adjacent BODIPY and from here to the neighboring oxazine. Nonetheless if we compare this antenna with the aforementioned one (Figure 2.11), the red emission is more prominent (Figure 2.12.c and d) and the emission of the first donors is more strongly quenched due to an increase on the FRET process. Therefore, a fine tuning of the spectral overlap (Figure 2.12.b) between the involved dyes in the antenna system is a good strategy to modulate the FRET efficiency and enhance the red emission or alternatively favor the white-light emission.

For a deeper understanding of the above studied antenna systems extended information about the material confection and photophysical characterization is available in the attached *ChemPlusChem* publication.

DOI: 10.1002/cplu.201100020

Versatile Photoactive Materials Based on Zeolite L Doped with Laser Dyes

Leire Gartzia-Rivero, Jorge Bañuelos-Prieto,* Virginia Martínez-Martínez, and Iñigo López Arbeloa[a]

Different laser dyes (with special interest in boron dipyrromethene) are incorporated as guests into the channels of zeolite L. The resulting doped material is fully characterized by steady-state and time-resolved photophysical techniques. The pores of zeolite L are filled with high amounts of dyes, which are exclusively present in their monomeric form and aligned in a preferential orientation, thus generating an organized photoactive material. The ordered disposition of the dye, mostly along the direction of the zeolite L nanochannels, was confirmed by confocal fluorescence microscopy. A careful selection of fluorophores along with controlled loading allows the harvest of light from the entire ultraviolet/visible region for conversion into white light, or alternatively, tuning of the emission in the blue, green, and red regions, owing to the presence of energy-transfer processes in the antenna systems built up in this work.

Introduction

The incorporation of an organic photoactive guest (i.e. fluorescent dyes) into a nanostructured solid host is a booming area of research, and is reflected by the increasing number of related publications.[1–5] Among other applications, these multifunctional dye-doped materials are being used successfully to develop new optoelectronic devices. The aim is to take advantage of the benefits provided by the organic (guest molecule) and the inorganic (solid matrix) entities, that is, the optical, spectroscopic, electronic, and chemical properties of the organic fluorophores combined with the structural, mechanical, and thermal characteristics of the solid inorganic framework. The rigid environment of the surrounding solid host protects the fluorophore, thus improving its chemical, thermal, and photochemical stability.[6,7] Rigidity may also affect (in a controlled manner) the electronic, magnetic, and optic properties of the enclosed molecules. Nonetheless, not only the properties of the fluorophore are ameliorated by their encapsulation, but also the organic molecule could be used as a fluorescent sensor to monitor the physicochemical properties of the solid framework.[8,9] All these features reveal the high versatility of the hybrid materials resulting from the combination between the solid host and the dye molecule.

There is a large variety of solid hosts which can be classified in terms of their nature; organic (i.e. polymers) and inorganic (i.e. silicon-based materials), or on the basis of the architecture of the solid framework; one-dimensional (nanotubes or channels), two-dimensional (layered materials, i.e. clays) or three-dimensional (cavities or cross-linking pores).[10–12] In this sense, zeolites offer a wide variety of frameworks (cavities or channels).[13] These aluminosilicate molecular sieves can host different molecules depending of their size. Among the wide variety of natural and synthetic zeolites, zeolite L is one of the most interesting and versatile hosts because of its one-dimensional channels running along the crystal (Scheme 1).[14] These cylindrical pores have a diameter of around 7.1 Å and fluorophores of the appropriate size can be located inside (Scheme 1). The geometrical restrictions of the channels impose a specific orientation of the dye and protect it against temperature as well as chemical or photochemical damages.

Currently, there is a wide variety of commercially available laser dye families, which cover the ultraviolet, visible, and near-infrared regions of the electromagnetic spectrum.[15–18] To the best of our knowledge this is the first time that BODIPY dyes have been incorporated into the nanochannels of zeolite L. Lately, boron dipyrromethene (abbreviated as BODIPY or BDP; Scheme 1) laser dyes have become the most commonly used active media in tunable dye lasers[19–21] owing to their strong absorption and fluorescence bands usually located in the green-yellow part of the visible spectrum.[22–24]

Herein, we thoroughly characterize the BODIPY-doped zeolite L and afterwards demonstrate the intramolecular energy-transfer processes between BODIPY and other chosen dyes (DMPOPOP and oxazine 1, Scheme 1) acting as donors and acceptors, respectively, within the zeolite channels. The presence of an efficient energy-transfer process in solid frameworks and its understanding is one of the key factors in the development of new photonic devices.

This phenomenon is applied in antenna systems where light of different energies is harvested and transferred by successive efficient energy hops to the reaction center and with the desired energy (mimicking the natural photosynthesis pro-

[a] L. Gartzia-Rivero, Dr. J. Bañuelos-Prieto, Dr. V. Martínez-Martínez, Prof. Dr. I. López Arbeloa
Departamento de Química Física
Universidad del País Vasco, (UPV-EHU)
Apartemento 664, 48080 Bilbao (Spain)
Fax: (+34) 94 601 3500
E-mail: jorge.banuelos@ehu.es

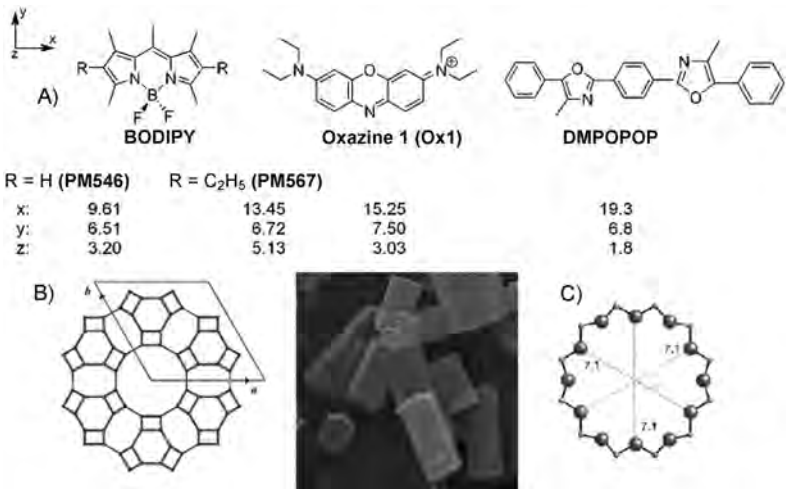

Scheme 1. A) Molecular structure and dimensions (Å) of the dyes. B) View of the hexagonal framework of zeolite L. C) The main channel entrance.

cess).[25–27] Alternatively, the partial energy transfer allows emission bands in the whole visible spectrum: blue, green, and red regions. The sum of these emissions results in a white-light-emitting device.[28–31] There is a growing interest by the scientific community in materials where the emission energy can be modulated in the whole visible region with just one system. Therefore, the resulting dye-doped solid materials are very versatile and allow the design of tailor-made devices for multiple applications.

Results and Discussion

Zeolite L doped with BODIPY

We first assessed if dyes can efficiently penetrate into the channels of zeolite L. To this aim, we chose nanometer size zeolite L because it gives less light scattering, thus making it easier to record the photophysical properties. The commercial zeolite L used is of good quality, as revealed by its narrow size distribution and uniform morphology in the TEM image (Figure 1).

BODIPY dyes, PM567 and PM546, were introduced into untreated and cesium-exchanged zeolite L. In the first case (non-exchanged zeolite L), the dye was completely bleached and a colorless powder was obtained with no absorption bands in the visible region, meanwhile in the latter case (cesium-exchanged), an orange-brown powder was obtained. These results confirm that the BODIPY is absorbed into the zeolite channels and the key role of the pH conditions inside the pores in the photophysics of the dye is highlighted. It is known that BODIPY dye is unstable at pH < 2 (probably, because it losses the BF_2 bridge), thus the very acidic environment of the untreated zeolite channels damages the dye, and, consequently its color disappears.[32–34] Nevertheless, the previous exchange of zeolite with Cs^+ modifies the acidity to a pH range where BODIPY is stable, thus showing the absorption band characteristic of this dye (Figure 2). The photophysical measurements were carried out in toluene because its refraction index matches that of the zeolite L and the dye did not leak out during the measurement. Therefore, all the zeolite L samples were exchanged with Cs^+ previous to incorporation of the dye.

The real content of BODIPY in the zeolite was determined by thermogravimetic analysis. Figure 3 compares the thermo-

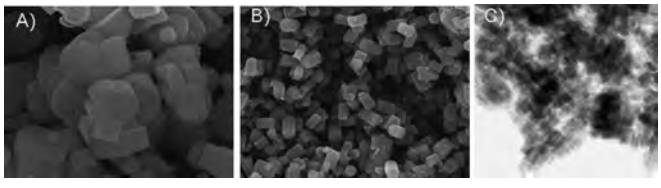

Figure 1. SEM images of A) zeolite L crystals Lucidot DISC, B) synthesized large crystals of 1–2 μm, and C) TEM image of Lucidot NZL40.

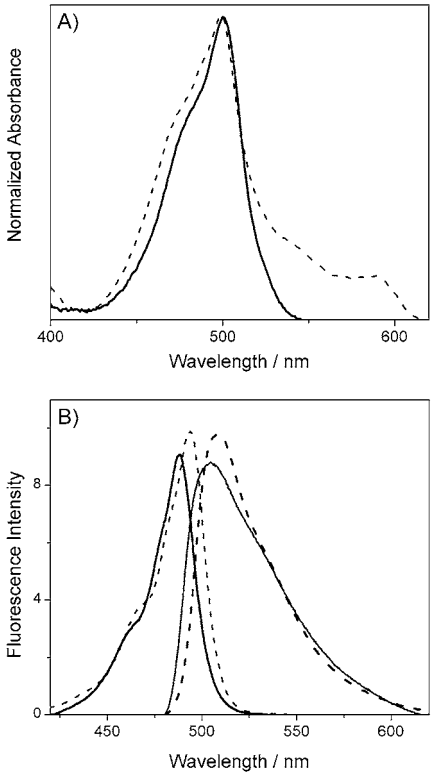

Figure 2. A) Normalized absorption spectrum in toluene of cesium-exchanged zeolite L doped with PM546, 40% (solid line) and 90% (dashed line). B) Normalized emission and excitation spectra of zeolite L doped with PM546 (40%) in toluene (solid line) and of the free dye in diluted solutions (dashed line).

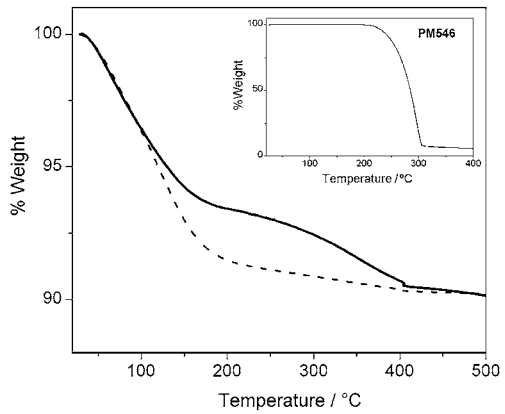

Figure 3. Thermogravimetric analysis of zeolite L (dashed) and zeolite L doped with PM546 (40%; solid line). The corresponding curve for the free PM546 is also included in the inset.

grams of the free dye, the zeolite L, and the BODIPY-doped zeolite L. The first drop in the thermogram of zeolite L from 25–150 °C corresponds to water desorption from inside the pores. From this point the zeolite L was stable up to at least 600 °C, as was expected for an inorganic material. When the BODIPY dye was incorporated in the inner space of the zeolite, the fall previously assigned to the water desorption was not so pronounced. The presence of dye molecules inside the channels has replaced part of the water previously trapped within the zeolite. The new weight drop from 200–400 °C (around 5% of weight loss) is attributed to the degradation of dye molecules inside the channels corresponding to 40% of the loading. This result is in relatively good agreement with the theoretical estimation (described in the experimental section), that is, the real loading by thermogravimetic analysis was 40% for the theoretical dye loading of 60%. It should be kept in mind that during washing of the doped zeolite, some dye molecules may be removed from the outer surface. Furthermore, the BODIPY in the zeolite was not fully degraded even at 400 °C, meanwhile the free BODIPY was degraded at 300 °C. Therefore the thermal stability of BODIPY was improved as a result of the cage protecting effect of the surrounding zeolite host.

The corresponding absorption spectra of BODIPY-doped zeolite L, for moderate to high loadings (up to 40%) were characterized by a single band, which reminds us of that observed in diluted solutions (Figure 2). Furthermore, the fluorescence band was very narrow and intense and thus very similar to that measured in diluted solutions of the dye (Figure 2), therefore new light emitting entities were not detected. Also, the excitation spectrum perfectly matched the absorption spectrum (Figure 2), thus suggesting that the emission came exclusively from the monomer. These results point out that the BODIPY is absorbed into the zeolite channels exclusively as a monomer, because no evidence of dye aggregation was observed in spite of the high number of molecules close to each others in the channels. The size of the pore aperture prevented the penetration of aggregates, while the geometrical restrictions imposed inside the zeolite channels made it difficult for the molecules to self associate.

Nonetheless, for very high loadings (around 90%) the corresponding absorption spectrum showed a new weak band at lower energies with respect to monomers in the nanometer-size zeolites (Figure 2). The detection of such a band appeared even at lower loadings in larger crystals. H-type aggregates, π–π stacking interaction, or excimer formation can be ruled out because the geometrical restrictions imposed by the zeolite L framework and the size of the BODIPY dye (similar to the pore diameter) prevents a parallel disposition of the electronic transition dipole of the monomers. Furthermore, typically an H-type aggregate is characterized by a shoulder observed at high energies in the absorption spectrum and this is not seen here. Reabsorption and reemission phenomena could also be present and will be more important at high loading, however, such phenomena cannot explain the presence of a new absorption band. According to the exciton coupling theory the presence of such red-shifted absorption bands are typical of a head to tail (J-type) aggregate with a collinear disposition of the electronic transition dipole moments of the monomers.[35,36] Typically, BODIPY dyes show a very low tendency to self-associate even in concentrated media. Only a few reports have claimed the presence of aggregation of BODIPY in confined systems (in general, biological systems) where the chromophores are forced to be in close contact.[37–39] Recently, Calzaferri, De Cola, and coworkers have reported the presence of J-type aggregates for high amounts of dyes (i.e. pyronine and perylene, which have a similar or larger size than BODIPY) in large zeolite L crystals (around 2–3 μm length).[26,40–42] They also detected new red-shifted absorption band and its corresponding fluorescence, and attributed such new entity to a J-aggregate coupling in terms of a Davydov splitting in confined systems when two chromophores are close enough. Thus, by increasing the dye loading and controlling the spatial separation between them they nicely showed the presence of this new entity mainly located at the entrances of the channels and in big crystals, where the molecule diffusion is hindered. These findings also explain the photophysical behavior observed for high BODIPY loadings. In fact, taking into account its molecular size, which nearly fits the pore size, it is very likely that BODIPY is aligned parallel to the channel and that at high loadings its electronic transition dipole moments can be aligned, thus giving rise to a J-aggregate coupling caused by intermolecular interactions. Unfortunately, we were not able to detect the corresponding emission of this new entity. The excitation at the new red-shifted absorption did not give rise to any emission.

Nevertheless, the presence of such kinds of electronic couplings that lead to aggregations should be avoided for the scope of this study. As will be detailed later, this dye will be combined with other fluorophores looking for energy transfer between them inside the zeolite channel. To this aim, it is essential to ensure that only monomers are presents because aggregates will compete for the light absorption in the energy transfer. Furthermore, aggregates quench the fluorescence emission of the monomer and usually show a weaker emission if they fluorescence.[35] Thus, BODIPY dye successfully diffuses into the channels of zeolite L and a high content of monomers

can be reached (around $\leq$40% of loading, where the above-described J-aggregate coupling is avoided).

The lifetimes of the dye-doped zeolites recorded by the confocal fluorescence microscope are shown in Table 1. The recording and processing of the fluorescence decay curves should be considered with caution owing to the difficulty of working with sub- and micrometer particles, which act as scatter centers hampering the proper recording of the decay curve. Also, there are other intrinsic problems when working with solid inclusion complexes that further complicate the analysis. Thus the fluorescence decay data have been measured for sample prepared in different ways—in suspension, thin films (spin-coated), powder (0.1 and 0.01 mm thickness), and in small aggregates of disc-shaped zeolite L doped with dyes (spin-coated samples) by using a confocal fluorescence microscopy in this last case. In all cases multiexponential decays were achieved for the dye-doped zeolites. The only difference was that a very short lifetime, $\leq$0.2 ns, usually appeared in powder samples measured by the conventional single-photon counter technique but not by time-resolved confocal microscopy. This lifetime was attributed to the high scattering (Rayleigh dispersion) which is further decrease in single crystals as compared to the bulk sample (data not shown). In this way the decay curves provided by the confocal fluorescence microscope are more realistic and easier to handle (Table 1). The decay curves were measured for different crystals in the same sample. The curves were nearly the same, which confirms the homogeneity of the dye doping process.

Dyes in the adsorbed state usually have multiexponential behavior owing to the heterogeneity of the matrix and its microenvironments.[43–45] For the case of zeolite L doped with both BODIPY dyes (for loadings around $\leq$40%) the decay curve is described by three lifetimes. The longest lifetime resembles a typical lifetime recorded for BODIPY in moderately polar solutions (5–6 ns), whereas the second lifetime (1.5–2 ns) could be ascribed to the different microenvironments in the zeolite channels.[40] Finally, the fastest lifetime of around 0.5 ns could be due to specific interactions between the dye in the excited state (probably with the BF_2 unit of the BODIPY) and the surrounding silanol groups of the zeolite channels.

To analyze the dye distribution and orientation in the zeolite crystal we synthesized cylindrical crystals of 1–2 μm length, by using the hydrothermal synthetic route described in the experimental section. These crystals are appropriate for study by fluorescence confocal microscopy at the single-particle level.[41] Figure 4 shows the fluorescence emission of a single zeolite L particle doped with BODIPY. The fluorescence intensity was uniform along the crystal, without sign of emission of other entities (i.e. J-aggregate coupling), thus indicating that the dye was homogeneously adsorbed and distributed into the channels.

In addition, the use of polarized light provides valuable information about the dye orientation in the pores. The doped crystals showed an anisotropy response to vertically and horizontally polarized light; a bright emission signal was detected when the light was polarized along the crystal main axis, whereas nearly no emission was observed when the fluorescence was monitored perpendicular to the crystal main axis. Thus, BODIPY molecules are oriented with their transition moment aligned parallel to the crystal's longitudinal axis. As a consequence, it is confirmed that the dye is exclusively located inside the zeolite channels; if the molecules were adsorbed in the outer surface, the random distribution of the transition moments of the dye would give rise to a non-anisotropy response to the polarized light.

Table 1. Fluorescence lifetimes of the dye-doped zeolite L at different excitation and emission wavelength measured by confocal fluorescence microscopy in spin-coated samples.

	λ_{exc} [nm]	λ_{em} [nm]	Multiexponential τ [ns] (contribution [%])	$<\tau>$ [ns][a]
Dyes in solution				
DMPOPOP	370	430	0.25(9), 1.39(91)	1.37
PM546	470	510	5.58	–
PM567	470	530	6.09	–
Ox1	575	620	0.71	–
Dyes in zeolite L				
DMPOPOP	370	440	1.18(62), 3.16(38)	2.41
PM546	470	510	0.5(60), 1.7(30), 5.26(10)	2.82
PM567	470	550	0.6(58), 2.1(28), 6.8(10)	3.74
Ox1	530	700	0.90(47), 2.75(53)	2.33
DMPOPOP-PM546	370	430	0.29(78), 1.2 (20), 3.50(2)	1.11
	370	550	0.24(66), 1.18(4), 4.55(30)	4.02
PM567-Ox1	470	550	0.22(63), 1.57(30), 5.71(7)	3.05
	470	680	1.60 (36), 3.66(64)	3.29
DMPOPOP-PM567-Ox1	370	440	0.23(55), 1.57(30), 3.70(7)	2.03
	370	550	0.29(49), 1.73(42), 5.76(9)	3.08
	370	680	1.42(70), 3.42(30)	2.43

[a] $<\tau>$ is the mean lifetime of the averaged amplitudes.

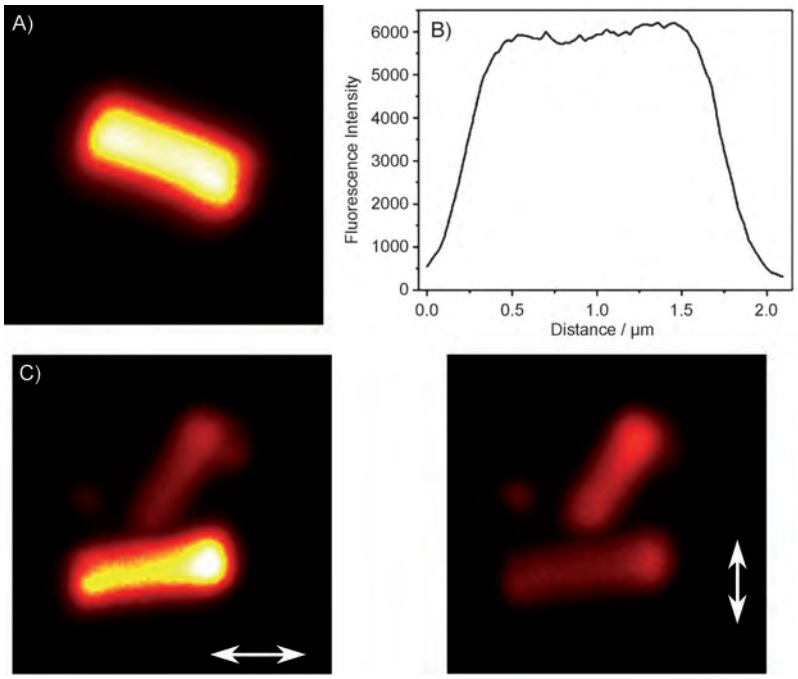

Figure 4. A) Fluorescence intensity image of PM567-doped zeolite L particles (2 μm length). B) Fluorescence intensity profile along the crystal. C) Fluorescence images using vertical or horizontal polarized light (arrows indicate the direction of polarized light).

Energy transfer in dye-doped zeolite L

To elaborate antenna systems and white-light-emitting devices it is necessary to combine different dyes to achieve efficient intermolecular energy-transfer processes within the zeolite L channels. The energy transfer should take place via a through-space Förster mechanism (dipole–dipole coupling), where the essential requirement is a spectroscopic overlap between the fluorescence spectrum of the donor and the absorption spectrum of the acceptor.[46,47] Taking into account that the BODIPY spectroscopic bands are located in the middle part of the visible (green-yellow), we chose a blue-emitting (DMPOPOP) and a red-emitting (Ox1) dye. Similar trends to those obtained for BODIPY were achieved for these fluorophores (DMPOPOP and Ox1) in the polarization experiments because they have the adequate size to penetrate inside the channels almost exclusively in monomeric form and with the molecular longitudinal axis parallel to the channels main axis.[48] These fluorophores fulfill the spectroscopic overlap requisites and efficiently penetrate inside the channels with the transition dipole moments oriented along the channel main axis, as described above. Such collinear disposition of the dyes should favor the energy transfer since it maximizes the orientational κ^2 term in the Förster formalism.[49,50] The antenna systems were built using disc-shaped zeolite L crystals. This morphology is characterized by a large basal surface with regard to the coat of the crystal and is appropriate for building a fully organized device.

Before inserting the three dyes in zeolite L we checked if the energy transfer between the fluorophore pairs could efficiently take place. To this aim, we studied systems with two dyes sequentially incorporated in the zeolite channels. Thus, the zeolite L was first doped with DMPOPOP (loading of 25%) and afterwards with PM546 (20%), leaving the DMPOPOP at the middle of the crystal, whereas the PM546 remained at the pore entrances. The dye loadings were not too high to ensure that only monomers were present in the channels to avoid the formation of aggregates. These entities compete in the light absorption with the monomers, are usually nonfluorescent, and induce an extra nonradiative pathway for the monomers through an energy-transfer process to the aggregate. In the multidye-doped zeolites the photophysical characterization was carried out in the solid state (powder) because the acceptor at the entrances of the pore leak out in suspensions. Figure 5 shows that after excitation at 370 nm, where DMPOPOP absorbed, its fluorescence band was detected (440 nm) but was followed by another emission band characteristic of PM546 (520 nm). It should be mentioned that both emission bands were better resolved in time-resolved emission spectra (TRES) experiments than in the steady-state. TRES spectra show that the emission of the PM546 came from the DMPOPOP because the fluorescence of the former grew progressively with the delay time after excitation. Furthermore, the excitation spectrum fixing the emission at the PM546 (560 nm) provided both bands, which correspond to DMPOPOP and PM546 itself. These results highlight the presence of an intermolecular energy-transfer process from donor DMPOPOP to acceptor PM546. In this way ultraviolet, blue, and green light was collected and yellow emission from the BODIPY was achieved.

The deconvolution of fluorescence decay of DMPOPOP in zeolite L is biexponential: 1.18 ns (62%) and is similar to that obtained in solution. Meanwhile, a longer value of 3.16 ns (38%) is likely due to the increased rigidity imposed by the host. For simplicity, average lifetimes are also considered (Table 1). In fact, after direct excitation of DMPOPOP, its average lifetime at $\lambda_{em} = 430$ nm decreased (from 2.41 ns to 1.11 ns) through the presence of PM546 with respect to the sample only doped with the DMPOPOP (Table 1). These results confirm that the fluorescence emission of the donor DMPOPOP was quenched by the intermolecular energy-transfer process to the acceptor PM546 (Figure 5). Thus, the decay curve registered in the DMPOPOP region for the DMPOPOP-PM546-doped zeolite L was analyzed with three-exponentials. The long lifetime of approximately 3.5 ns with the lower contribution to the global decay, could be due to the emission from DMPO-

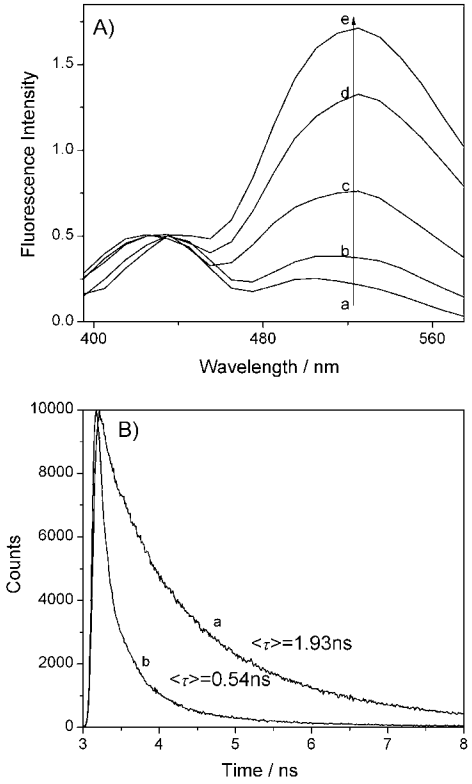

Figure 5. A) Normalized time-resolved emission spectra recorded at different times after excitation at 370 nm: a) 0.07 ns; b) 0.37 ns; c) 2.38 ns; d) 5.13 ns; e) 10.99 ns for zeolite L doped with DMPOPOP and PM546. B) Fluorescence decay curves of a) DMPOPOP- and b) DMPOPOP-PM546-doped zeolite L recorded upon selective excitation of DMPOPOP at 370 nm. All the measurements were performed in the solid state.

POP, which is probably located at the center of the crystal and too far away from the acceptor, and as a consequence has more difficulty to transfer the energy to it. The shorter and predominant lifetime around 0.3 ns is attributed to the DMPOPOP molecules being in closer proximity to the acceptor molecules, with their fluorescence quenched by the intermolecular energy-transfer process. Indeed, if the emission was monitored in the PM546 emission region ($\lambda_{em}=550$ nm), keeping the excitation at 370 nm, at which DMPOPOP absorbs then the characteristic lifetime of BODIPY appeared. In addition, the average lifetime is similar to that observed with only BODIPY in zeolite L, thus indicating that it behaves as an energy acceptor. Therefore, the energy transfer into the zeolite channel is successful and a fully organized system is achieved. Owing to the molecule size of the dye and the geometrical restriction imposed by the channel rigidity, the molecules cannot slide over to avoid donor–acceptor intercalation and, hence, the donor is located at the center, whereas the acceptor is placed at the ends of the channel.

The second antenna system was built by doping zeolite first with PM567 (loading 10%) and then with Ox1 (loading of 2%). Again, the above donor–acceptor disposition should be expected (i.e. donors flanked by acceptors). The corresponding absorption spectrum, shown in Figure 6, was the sum of the bands corresponding to each chromophore, thus confirming that both dyes were present in the zeolite channels and without signs of aggregation. The excitation of PM567 at 470 nm gave rise to its emission followed by a strong red emission assigned to Ox1 (Figure 6). Thus, the intermolecular energy transfer took place and, consequently, yellow light was mostly converted into red light. The time-evolution of the fluorescence spectrum showed an enhancement of the emission from the acceptor, in detriment of the donor, thus increasing the delay time after excitation. Notably, the red-shift of the oxazine 1 in the zeolite environment, with respect to that in solution, could be assigned to specific interactions between the lone pair of electron of the xantene aromatic amino group and the silanol groups of the channel framework. In general, the photophysics of amino-substituted xanthene derivatives (i.e. rhodamine, coumarins) are governed by such interactions because they control the hybridization of the amino group and hence the delocalization of the lone pair of electrons through the xanthene ring.[51]

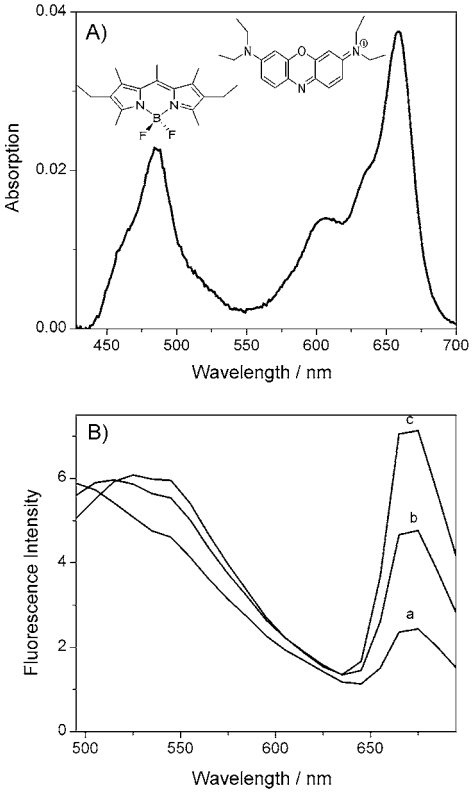

Figure 6. A) Absorption (by reflectance) and B) normalized time-resolved emission spectra ($\lambda_{em}=470$ nm) of zeolite L doped with PM567 and Ox1 in the solid state recorded at different times after excitation at 470 nm: a) 0.18 ns; b) 1.46 ns; c) 5.86 ns. The spectra were recorded from the bulk powder.

As expected, the lifetime analysis shows similar trends to those previously described for the DMPOPOP-PM546 system. The average lifetime of the donor PM567 ($\lambda_{em}=550$ nm) decreased in the presence of Ox1 as a result of the energy-transfer process. With regard to the lifetimes obtained when only Ox1 was included in zeolite L, an extra longer lifetime compo-

nent of approximately 2.75 ns is observed, whereas in diluted dye-solution just a single lifetime of around 0.7 ns is recorded. This mismatch should be due to the constrained space of the channels or the above-mentioned specific interaction of the amino group with the surrounding silanol groups. The longest lifetime in the antenna is increased even more in the presence of PM567, thus confirming that PM567 acts as an energy acceptor (Table 1).

Finally, we built the antenna system to harvest of light from the entire UV/Vis region by combining the above three dyes. The donor DMPOPOP (loading 10%) was inserted first, then the PM567 (10%), and finally the last acceptor Ox1 (10%). In this way a fully organized system was achieved where the DMPOPOP donor was located at the center, flanked by the PM567 fluorophore and with the Ox1 acceptors at the entrances of the zeolite crystal. The excitation of the donor DMPOPOP led to its emission followed by that of PM567 and finally the acceptor Ox1 fluorescence band (Figure 7). The fluorescence spectra, which were measured at different times after excitation, show that the emission from the PM567 comes from the DMPOPOP and afterwards the emission from the Ox1 appears as a result of successive energy-transfer processes. The longer lifetime of BODIPY produces a progressive increase of its emission band time after the pulse. Again, the TRES provides a better resolution of the bands corresponding to each chromophore as compared to the steady-state spectrum (Figure 7). The average lifetime evolution with the excitation and emission wavelengths confirms the energy-transfer process. Accordingly, the average lifetimes of the donors decrease as a result of the extra nonradiative pathway, which provides the energy transfer. The PM567 behaves as a donor and acceptor at the same time. Finally, the decay curve in the emission region of Ox1 ($\lambda_{em} = 680$ nm) is characterized by an average lifetime close to that without the donor fluorophores, thus confirming that the energy arrives from the DMPOPOP, through the PM567, and then to the Ox1 (Table 1).

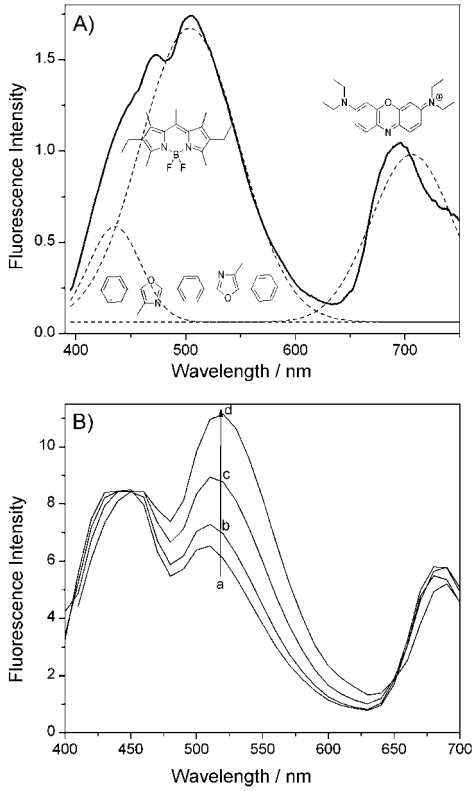

Figure 7. A) Fluorescence spectrum recorded upon selective excitation of the donor at 385 nm in zeolite L doped with DMPOPOP, PM567, and Ox1. The spectrum was fitted to three Gaussians (dashed line). B) Normalized time-resolved emission spectra recorded at different times after excitation at 370 nm: a) 0.24 ns; b) 1.22 ns; c) 3.05 ns; d) 3.72 ns. The spectra were recorded from the bulk powder.

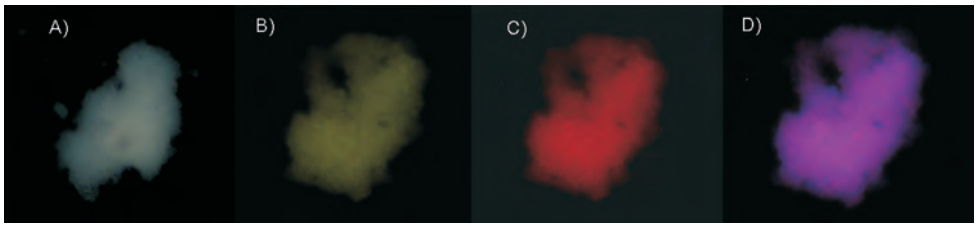

Figure 8. Fluorescence images of zeolite L doped with DMPOPOP-PM567-Ox1 under 350/50 nm excitation and recording the emission with several band passes: A) 400 nm, B) 515 nm, C) 580 nm, and D) 665 nm.

Furthermore, Figure 7 shows that by exciting the donor three emission bands were simultaneously obtained; blue from DMPOPOP, green from BODIPY and red from oxazine 1, thereby emitting white light. Indeed, the microscope images of an aggregate of zeolite L disc particles doped with the three dyes clearly show a bright white emission upon excitation in the UV region (Figure 8A). In addition, by using the appropriate emission filters in the fluorescence microscope green and red light could be observed (Figure 8B, C, and D), thus suggesting that the desired emission region can be selected with the present hybrid systems.

The design of this kind of antenna or white-light device consisting of dye guests allocated into a nanostructured host is not only limited to zeolite L, as other channeled framework can be used. For example $AlPO_4$-5, an aluminophosphate analogous to zeolite L and characterized by one-dimensional parallel channels with a similar pore size, could be used.[52]

Conclusion

Therefore, the zeolite L doped with more than one dye is a very versatile system with promising and interesting future prospects. Further work is in progress in our laboratory to optimize the dye loading proportions in order to control the energy-transfer process, that is, to enhance the energy transfer efficiency for antenna systems (where the emission from the

red dye prevails) or modulate its efficiency for white-light-emitting devices (simultaneous emission of all the fluorophores).

To the best of our knowledge, this is the first time that BODIPY laser dyes have been incorporated into zeolite L channels. As a result, high fluorescent and ordered materials have been achieved. The geometrical restrictions imposed by the rigid zeolite L framework led to a high dye loading in monomeric form and with the molecules oriented along the channels. Very high loadings should be avoided to avoid the formation of aggregates.

The combination of the appropriate dyes into the channels of zeolite L gave rise to energy-transfer processes. Modulating the energy-transfer efficiency (i.e. adjusting the relative proportions of the dyes into the zeolite L channels or using zeolite L of different size) could lead to highly organized devices with entirely different applications. Doping zeolite L with several dyes (with different spectroscopic characteristics) at similar loadings results in a partial energy transfer, thus leading to white-light emission or even the tuning of the emission in the blue, green and red regions with the proper filters.

The dye-doped materials obtained here are well organized and highly fluorescent, which are both essential requirements for the development of competitive optoelectronic devices.

Experimental Section

Materials

Laser grade BODIPY dyes, (PM546[53] and PM567[54], Exciton), oxazine 1, and DMPOPOP (Sigma–Aldrich) were purchased and used as received without further purification. The corresponding dimensions of each molecule were calculated by the semiempirical AM1 method using in the MOPAC package.

Nanometer size and disc-shape zeolite L were acquired from Clariant (Lucidot NZL 40 and Lucidot DISC, respectively). The nanometer crystals size is around 30–60 nm, whereas the discs are characterized by a low aspect ratio (length around 0.2–0.4 μm and diameter of approximately 0.5–2 μm), as shown in Figure 1. In addition, we synthesized bigger crystals (length 1–2 μm) with cylindrical morphology and these were also considered for the optical microscopic analysis (Figure 8). These zeolites were produced by a hydrothermal process assisted by microwave energy. The synthetic process was carried out as follows: the amount of reactants used was set to achieve a molar gel composition of K_2O (2.21)/Al_2O_3 (1.00)/SiO_2 (9.00)/H_2O (164.60).[55] The alumina suspension was prepared by mixing KOH and metallic aluminum powder in doubly distilled water under a flow of argon, and the mixture was stirred at low temperature (0 °C) for 15 min. After allowing the solution to warm to RT, stirring was continued for 1.5 h under the inert atmosphere. This solution was added to a silica suspension (Ludox, supplied by Sigma–Aldrich) under vigorous mechanical stirring. After aging the gel for 3–6 min it was transferred to a polytetrafluoroethylene (PTFE) pressure vessel and heated in a microwave oven at 175 °C for 12 h. Once the crystallization process was finished, the vessel was cooled to RT. The thus obtained gel was washed with boiling doubly distilled water until the pH of the supernatant was neutral. Finally, the crystals were dried at 90 °C for 16 h. The zeolite crystals were characterized by scanning electron microscopy (SEM) and X-ray diffraction techniques.

Dye loadings

The amount of dye incorporated in the zeolite L channels for a certain loading was estimated using the theoretically calculated (AM1) molecular dimensions of the molecule and the unit cell parameters provided by X-ray diffraction.[56] The dimension of the unit cell along the channel is 7.5 Å. Considering the length of the long axis of the molecule, the adsorption site filled for each dye can be estimated, that is, the number of unit cells occupied by a dye molecule. Indeed, the adsorption site for BODIPY (long axis 9–14 Å) and Ox1 (12 Å) should be extended to two unit cells, whereas DMPOPOP (19 Å) occupies three cells. Thus, knowing the number of unit cells in the zeolite sample, the dye loading is calculated according to the desired occupancy of the adsorption sites. Then, the actual dye loading was determined by thermogravimetry.

Dye incorporation

Before dye incorporation, the zeolite L was treated with Cs^+ to adjust the pH. This cation was chosen because to its high pK_a value. To this aim, zeolite L was suspended in water and exchanged with an excess amount of CsCl under reflux and stirring during 45 min at 80 °C. Cationic dyes (Ox1) were incorporated into the cesium-exchanged zeolite L through cationic exchange by means of addition of an aqueous solution of Ox1 to a suspension of zeolite L in water at 50 °C. The resulting mixture was stirred and heated under reflux over 6 h.[57,58] Neutral dyes (BODIPY and DMPOPOP) were incorporated into cesium-exchanged zeolite L by using gas-phase insertion at high temperatures.[59] After vacuum dry of the zeolite, it was sealed together with the adequate quantity of the dye under vacuum in an ampoule. Then, the dye was sublimated in a rotary oven over 2 days at 170 °C and 200 °C for BODIPY and DMPOPOP, respectively. All the dye-doped zeolite was rinsed with butanol several times to remove the molecules adsorbed onto the external surface of the crystal.

Instrumental techniques

The photophysical properties of the dye-doped zeolites were measured in suspensions and in the solid state (powder). The absorption spectra were recorded by using a Varian spectrophotometer (model Cary 4E) by detecting the transmitted light for the suspensions or by detecting the reflected light, by means of an integrating sphere, for the solid samples. The fluorescence and excitation spectra were recorded by using a SPEX spectrofluorimeter (model Fluorolog 3-22). The spectra were corrected for the wavelength dependence of the monochromator, the lamp profile, and the photomultiplier sensitivity. Time-resolved emission spectra (TRES) and fluorescence decay curves were recorded by using a time-correlated single-photon counter (Edinburgh Instruments, model FL 920, equipped with a MultiChannelPlate detector Hamamatsu C4878) with picosecond resolution (20–30 ps). The decay curves were recorded after excitation with an appropriate diode laser (PicoQuant 370, 470, and 530 nm), and the emission at the fluorescence maxima was monitored. The curves were fitted to exponentials and the lifetimes were determined from their slopes. The goodness of the fit was assessed by the chi-square statistical parameter and the distribution of the residuals. The fluorescence emission measurements were carried out in suspensions (using the right-angle configuration), in thin films (spin-coated), and in the solid state (powder between two quartz slide conforming a sample thickness of 0.1 and 0.01 mm) using the front-face configuration.

Time-resolved fluorescence microscopy measurements were recorded by using a confocal microscope (model MicroTime 200, PicoQuant) using an inverted microscope (Olympus IX71) with epi configuration and with an oil-immersed objective (Olympus model UPLFL). The excitation was performed with picosecond pulsed diode lasers (410, 470, and 640 nm) using 70 ps pulses at a 20 MHz repetition rate. The fluorescence signal was collected by the same objective and focused (through a 50 μm pinhole) onto single-photon avalanche photodiode detectors (Micro Photon Devices, MPD-APD). Unpolarized excitation light was obtained by means of a $\lambda/4$ filter (Thorlabs WPQ05M-488) and used for polarization measurements. The emission signal collected was divided by a polarizer beam splitter into two mutually perpendicular polarization orientation beams, which are simultaneously detected by two detector channels. The decay curves were also recorded with the confocal fluorescent microscope using similar methodology as described above for the photon-counter (decay curve deconvolution into exponentials), but onto a single particle.

Acknowledgements

Scanning (SEM) and transmission (TEM) electron microscopy, X-ray diffraction, and thermogravimetry measurements were provided by the SGI/IZO-SGIker of the UPV/EHU. We thank the Basque Government for financial support (project nos. SA09UN61 and SA2010/96), for a predoctoral scholarship (L.G.), and a postdoctoral contract (V.M.).

Keywords: antenna systems · energy transfer · laser dyes · photoactive materials · zeolites

[1] M. Busby, H. Kerschbaumer, G. Calzaferri, L. De Cola, *Adv. Mater.* **2008**, *20*, 1614 – 1618.
[2] A. Guerrero-Martínez, S. Fibikar, I. Pastoriza-Santos, L. M. Liz-Marzan, L. De Cola, *Angew. Chem.* **2009**, *121*, 1292 – 1296; *Angew. Chem. Int. Ed.* **2009**, *48*, 1266 – 1270.
[3] Y. Wang, Y. Yue, H. Li, Q. Zhao, Q. Fang, P. Cao, *Photochem. Photobiol. Sci.* **2011**, *10*, 128 – 132.
[4] I. López-Duarte, D. Le-Quyenh, I. Dolamic, M. V. Martinez-Diaz, T. Torres, G. Calzaferri, D. Bruehwiler, *Chem. Eur. J.* **2011**, *17*, 1855 – 1862.
[5] O. Matthias, C. A. Strassert, L. De Cola, *G.I.T. Lab. J. Eur.* **2010**, *14*, 24 – 25.
[6] G. Schulz-Ekloff, D. Wöhrle, B. Duffel, R. A. Schoonheydt, *Microporous Mesoporous Mater.* **2002**, *51*, 91 – 138.
[7] M. Owaga, K. Kuroda, *Chem. Rev.* **1995**, *95*, 399 – 438.
[8] V. Ramamurthy, D. F. Eaton, *Chem. Mater.* **1994**, *6*, 1128 – 1136.
[9] M. C. Jiménez, M. A. Miranda, I. J. Vaya, *J. Am. Soc.* **2005**, *127*, 10134 – 10135.
[10] M. E. Davis, *Nature* **2002**, *417*, 813 – 821.
[11] Y. Tao, H. Kanoh, L. Abrams, K. Kaneko, *Chem. Rev.* **2006**, *106*, 896 – 910.
[12] H. Fischer and J. Kunen in *Recent Advances in Polymer Nanocomposites*, (Eds.: S. Thomas, G. E. Zaikov, and S. V. Valsaraj), Brill, Leiden, The Netherlands, **2010**, pp. 47 – 118.
[13] Ch. Baerlocher, W. M. Meier, D. H. Olson, *Atlas of Zeolite Framework Types*, 5th Ed, Elsevier, Amsterdam, **2001**.
[14] T. Ohsuna, B. Slater, F. Gao, J. Yu, Y. Sakamoto, G. Zhu, O. Terasaki, D. E. W. Vaughan, S. Qiu, C. R. A. Catlow, *Chem. Eur. J.* **2004**, *10*, 5031 – 5040.
[15] P. Vounisiou, A. Selimis, G. J. Tserevelakis, K. Melessanaki, P. Pouli, G. Filippidis, C. Beltsios, S. Georgiou, C. Fotakis, *Appl. Phys. A* **2010**, *100*, 647 – 652.
[16] N. Tanaka, W. N. Sisk, *J. Photochem. Photobiol. A* **2005**, *172*, 109 – 114.
[17] D. Y. Chen, Y. G. Jiang, R. W. Fan, E. B. Jia, Y. Q. Xia, Y. Yao, *Laser Phys.* **2009**, *19*, 1877 – 1881.
[18] A. Ghanadzadeh, A. Zeini, A. Kashef, M. Moghadam, *J. Mol. Liq.* **2008**, *138*, 100 – 106.
[19] M. J. Ortiz, I. Garcia-Moreno, A. R. Agarrabeitia, G. Duran-Sampedro, A. Costela, R. Sastre, F. López Arbeloa, J. Bañuelos-Prieto, I. López Arbeloa, *Phys. Chem. Chem. Phys.* **2010**, *12*, 7804 – 7811.
[20] E. Yariv, S. Schultheiss, T. Saraidarov, R. Reisfeld, *Optical Materials* **2001**, *16*, 29 – 38.
[21] A. Costela, I. García-Moreno, R. Sastre, *Phys. Chem. Chem. Phys.* **2003**, *5*, 4745 – 4763.
[22] F. López Arbeloa, J. Bañuelos-Prieto, V. Martínez, T. Arbeloa, I. López Arbeloa, *Int. Rev. Phys. Chem.* **2005**, *24*, 339 – 374.
[23] A. Loudet, K. Burgess, *Chem. Rev.* **2007**, *107*, 4891 – 4932.
[24] G. Ulrich, R. Ziessel, A. Harriman, *Angew. Chem.* **2008**, *120*, 1202 – 1219; *Angew. Chem. Int. Ed.* **2008**, *47*, 1184 – 1201.
[25] G. Calzaferri, *Top. Catal.* **2010**, *53*, 130 – 140.
[26] G. Calzaferri, R. Meallet-Renault, D. Bruehwiler, R. Pansu, I. Dolamic, T. Dienel, P. Adler, H. Li, A. Kunzmann, *ChemPhysChem* **2011**, *12*, 580 – 594.
[27] V. Vohra, A. Devaux, L. Dieu, G. Scavia, M. Catellani, G. Calzaferri, C. Botta, *Adv. Mater.* **2009**, *21*, 1146 – 1150.
[28] W. Ki, J. Li, G. Eda, M. Chhowalla, *J. Mater. Chem.* **2010**, *20*, 10676 – 10679.
[29] J. Kido, M. Kimura, K. Nagai, *Science* **1995**, *267*, 1332 – 1334.
[30] S. Park, J. E. Kwon, S. H. Kim, J. Seo, K. Chung, S-Y. Park, D.-J. Jang, B. M. Medina, J. Gierschner, S. Y. Park, *J. Am. Chem. Soc.* **2009**, *131*, 14043 – 14049.
[31] T. Rosenow, M. Furno, S. Reineke, S. Olthof, B. Luessem, K. J. Leo, *Appl. Phys.* **2010**, *108*, 113113/1 – 113113/5.
[32] T. Gareis, C. Huber, O. S. Wolfbeis, J. Daub, *Chem. Commun.* **1997**, *18*, 1717 – 1718.
[33] M. Kollmannsberger, T. Gareis, S. Heinl, *Angew. Chem.* **1997**, *109*, 1391 – 1393; *Angew. Chem. Int. Ed. Engl.* **1997**, *36*, 1333 – 1335.
[34] T. Werner, C. Huber, S. Heinl, M. Kollmannsberger, J. Daub, O. S. Wolfbeis, *Fresenius J. Anal. Chem.* **1997**, *359*, 150 – 154.
[35] F. López Arbeloa, V. Martínez, T. Arbeloa, I. López Arbeloa, *Reviews in Fluorescence, Vol. 5*, (Ed.: C. D. Geddes), Springer, New York, Dordrecht, Heidelberg, London, **2008**, pp. 1 – 35.
[36] V. Martinez Martinez, F. López Arbeloa, J. Bañuelos-Prieto, I. López Arbeloa, *J. Chem. Phys. B* **2005**, *109*, 7443 – 7450.
[37] D. Tleugabulova, Z. Zhang, J. D. Brennan, *J. Phys. Chem. B* **2002**, *106*, 13133 – 13138.
[38] B. Ventura, G. Marconi, M. Bröring, R. Krüger, L. Flamigni, *New J. Chem.* **2009**, *33*, 428 – 438.
[39] I. Mikhalyov, N. Gretskaya, F. Bergström, L. B.-A. Johansson, *Phys. Chem. Chem. Phys.* **2002**, *4*, 5663 – 5670.
[40] M. Busby, A. Devaux, C. Blum, V. Subramaniam, G. Calzaferri, L. De Cola, *J. Phys. Chem. C* **2011**, *115*, 5974 – 5988.
[41] M. Busby, C. Blum, M. Tibben, S. Fibikar, G. Calzaferri, V. Subramaniam, L. De Cola, *J. Am. Chem. Soc.* **2008**, *130*, 10970 – 10976.
[42] G. Calzaferri, D. Brühwiler, T. Meng, L.-Q. Dieu, V. L. Malinovskii, R. Häner, *Chem. Eur. J.* **2010**, *16*, 11289 – 11299.
[43] K. Rurack, K. Hoffman, W. Al-Soufi, U. Resch-Genger, *J. Phys. Chem. B* **2002**, *106*, 9744 – 9725.
[44] D. Pevenage, M. Van der Auweraer, F. C. De Schryver, *Langmuir* **1999**, *15*, 8465 – 8473.
[45] G. P. Wiederrecht, G. Sandi, K. A. Carrado, S. Seifert, *Chem. Mater.* **2001**, *13*, 4233 – 4238.
[46] J. R. Lakowicz, *Principles of Fluorescence Spectroscopy,* 2nd Ed, Kluwer Academic/Plenum, New York, **1999**.
[47] G. Calzaferri, S. Huber, H. Maas, C. Minkowski, *Angew. Chem.* **2003**, *115*, 3860 – 3888; *Angew. Chem. Int. Ed.* **2003**, *42*, 3732 – 3758.
[48] A. Gasecka, L.-Q. Dieu, D. Bruehwiler, S. Braseelet, *J. Phys. Chem. B* **2010**, *114*, 4192 – 4198.
[49] J. R. Lakowicz, G. Piszczek, J. S. Kang, *Anal. Biochem.* **2001**, *288*, 62 – 75.
[50] M. P. Singh, G. F. Strouse, *J. Am. Chem. Soc.* **2010**, *132*, 9383 – 9391.
[51] F. López Arbeloa, T. López Arbeloa, I. López Arbeloa, *Trends Photochem. Photobiol.* **1994**, *3*, 145 – 155.
[52] M. Ganschow, C. Hellriegel, E. Kneuper, M. Wark, C. Thiel, G. Schulz-Ekloff, C. Bräuchle, D. Wörhrle, *Adv. Funct. Mater.* **2004**, *14*, 269 – 276.
[53] F. López Arbeloa, T. López Arbeloa, I. López Arbeloa, *J. Photochem. Photobiol. A* **1999**, *121*, 177 – 182.

[54] T. López Arbeloa, F. López Arbeloa, I. López Arbeloa, I. García-Moreno, A. Costela, F. Amat-Guerri, *Chem. Phys. Lett.* **1999**, *299*, 315 – 321.
[55] A. Zabala Ruiz, D. Brühwiler, T. Bau, G. Calzaferri, *Monatsh. Chem.* **2005**, *136*, 77 – 89.
[56] G. Calzaferri, S. Huber, H. Maas, C. Minkowski, *Angew. Chem.* **2003**, *115*, 3860 – 3888; *Angew. Chem. Int. Ed.* **2003**, *42*, 3732 – 3758.
[57] R. Q. Albuquerque, G. Calzaferri, *Chem. Eur. J.* **2007**, *13*, 8939 – 8952.
[58] H. Maas, A. Khatyr, G. Calzaferri, *Microporous Mesoporous Mater.* **2003**, *65*, 233 – 242.
[59] B. Bussemer, D. Munsel, H. Wünscher, G. J. Mohr, U. Grummt, *J. Phys. Chem. B* **2007**, *111*, 8 – 15.

Received: October 10, 2011
Revised: November 21, 2011
Published online on December 16, 2011

2.3. EXTERNAL FUNCTIONALIZATION OF LTL ZEOLITE

Finally, a further degree of organization can be achieved by functionalizing the channel entrances of LTL zeolite with specific tailor-made molecules (stopcock) via covalent linkage (Figure 2.13) [11,36]. Such molecules grafted at the pores, plug the channels to avoid the leakage of the guest molecules adsorbed inside the channels and connect the inner space of the zeolite with the outside thanks to FRET processes, in which the stopcock molecule would act as the final acceptor, making easier the coupling of the material with other external devices.

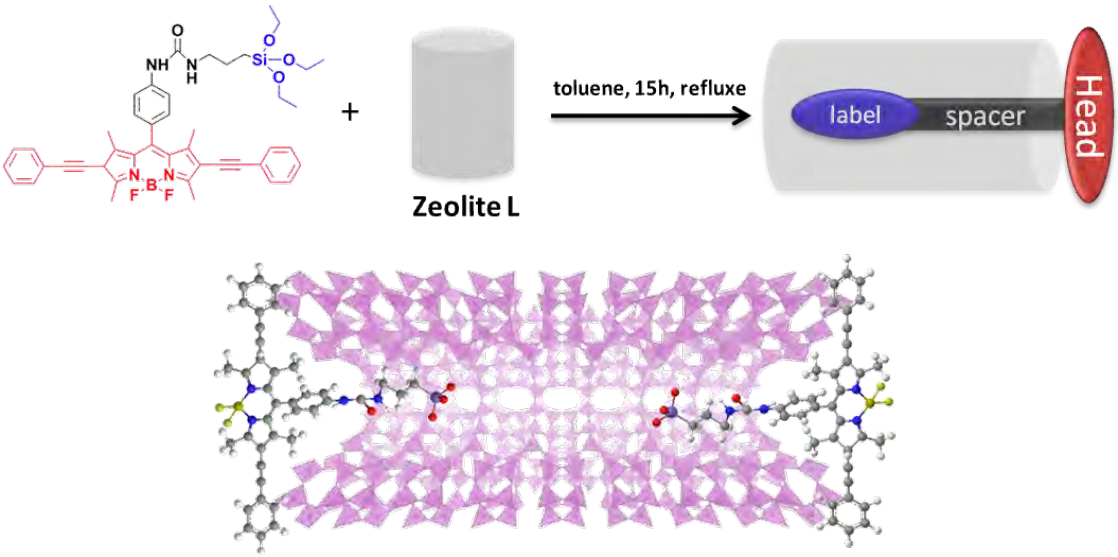

Figure 2.13. Molecular structure of the stopcock and the reaction principle to attach it to the LTL zeolite channel entrances. The spacer and label are located inside the channel, the head is too big to enter.

The chemical and physical properties of the base of the cylindrically shaped LTL crystals bearing the channel entrances and those of the coat are quite different and this divergence can be used for a selective modification of mainly the channel entrances of the zeolite. This selective modification can be done by adjusting the equivalent ratio between the channel entrances and the reactive stopcock to 1:1.

The adequate design of these stopcock molecules plays a key role because firstly it should be able to be adsorbed into the pores and subsequently covalently anchored by reaction with free silanol (Si-OH) groups located at the channel entrances, while keeping intact the photophysical properties of the chromophore; at the same time the emission should be modulated by appropriate functionalization so as to shift it to the red-edge of the visible [37]. Keeping all this requirements in mind, we have designed a molecule consisting in a label, a spacer and a head moiety, which has been synthesized by Prof. Y. Xiao from Dalian University in China. The head consists in a large enough

BODIPY core to avoid its diffusion into the channels, and with extended conjugation to shift its emission towards the red (Figure 2.13). The label is an organosilane moiety, which reacts with the zeolitic silanols after hydrolysis and policondensation reactions. The spacer (a long enough polymethylene chain) is used to avoid interferences of the label with the photophysical signatures of the chromophore and also to ensure the suitable penetration of the label into the channels (Figure 2.13).

In fact, fluorescence microscopy image (Figure 2.14.b) reveals that the stopcock molecules are successfully grafted to the microsized LTL zeolite and this takes place preferentially in the channels entrances because the silanol group's density is higher than in the coat. Besides, the photophysical properties of the stopcock are unaltered after the covalent binding (Figure 2.14.a).

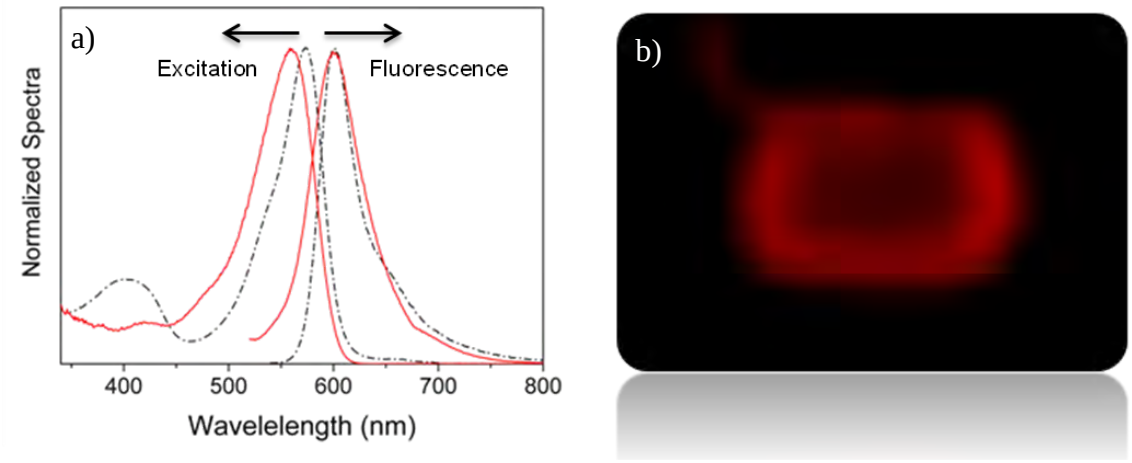

Figure 2.14. a) Normalized excitation and emission spectra of the BODIPY stopcock grafted to LTL zeolite crystals (solid) and free in toluene (dash dotted). b) Fluorescence microscopy image of a single LTL crystal functionalized with the BODIPY stopcock.

Once checked that the designed closure molecule is valid we proceeded to build the antenna system by its combination with a suitable energy donor. In this sense, DMPOPOP has been again chosen because it has a broad absorption band and its emission band overlaps well with the absorption band of the stopcock. Thus, the DMPOPOP donor will be placed inside the channels and the stopcock acceptor at the entrances. Disc-shaped zeolite has been selected owing to its morphology, characterized by a basal surface much higher than the coat (low aspect ratio), which ensures that the stopcock molecules are placed mainly in the channel entrances and the ongoing FRET process occurs along the direction of the channels. Selective excitation of DMPOPOP led to an important red fluorescence from the stopcock at around 607 nm (Figure 2.15), of course, owing to FRET process taking place, which is

effective albeit the donor-acceptor distance should be longer than when both are inside the channels.

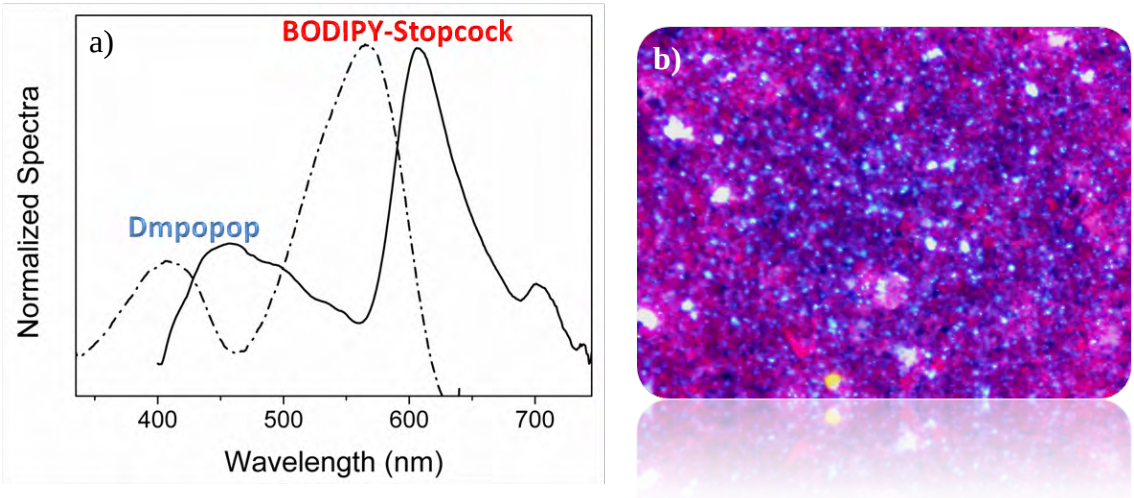

Figure 2.15. a) Normalized excitation (emission measured at 660 nm, dashed line) and emission (excited at 350 nm, solid line) spectra of DMPOPOP enclose into the channel and BODIPY stopcock grafted in the LTL zeolite entrances. b) Fluorescence microscopy image of the hybrid zeolite-dye system under 350/50 nm band-pass excitation and recording the emission with 400 nm long pass filter.

In conclusion, the coupling of an external acceptor stopcock fluorophore at the ends of the LTL zeolite channels allows a second stage of organization, in which the excitation energy is radiationless transported by donor molecules placed in the inner space of the channels and finally injected to the acceptor molecules placed at the entrances. Thus, the stopcock molecules enable the communication between the guest molecules on the inside with materials or molecules outside and also prevent small molecules like H_2O or O_2 (fluorescence quenchers) from diffusing into the interior of the crystals.

Bibliography

[1] P. Gómez-Romero and C. Sanchez, *Porous Inorganic-Organic Hybrid Materials, in Functional Hybrid Materials,* Wiley-VCH, Weinheim, **2003**, p. 86-121.

[2] F. Liebau, *Micropor. Mesopor. Mater.,* **2003**, 58, 15-72.

[3] W. M. Meier, D. H. Olson and C. Bärlocher, *Atlas of Zeolite Framework Types,* Elsevier, London, **2001**.

[4] R. M. Barrer and H. Villiger, *Z. Kristallogr.,* **1969**, 128, 352-370.

[5] A. Corma, *Nature,* **2009**, 461, 182-183.

[6] M. B. J. Roeffaers, B. F. Sels, H. Uji-i, B. Blanpain, P. L'hoest, P. A. Jacobs, F. C. De Schryver, J. Hofkens and D. E. De Vos, *Angew. Chem. Int. Ed.,* **2007**, 46, 1706-1709.

[7] F. Cucinotta, A. Guenet, C. Bizzarri, W. Mroz, C. Botta, B. Milian-Medina, J. Gierschner and L. De Cola, *ChemPlusChem,* **2014**, 79, 45-57.

[8] V. Vohra, A. Devaux, L. Dieu, G. Scavia, M. Catellani, G. Calzaferri and C. Botta, *Adv. Mater.,* **2009**, 21, 1146-1150.

[9] S. Huber and G. Calzaferri, *ChemPhysChem,* **2004**, 5, 239-242.

[10] A. Mech, A. Monguzzi, F. Cucinotta, F. Meinardi, J. Mezyk, L. De Cola and R. Tubino, *Phys. Chem. Chem. Phys.,* **2011**, 13, 5605-5609.

[11] N. S. Kehr, B. Ergün, H. Lülf and L. De Cola, *Adv. Mater.,* **2014**, 26, 3248-3252.

[12] C. S. Cundy and P. A. Cox, *Micropor. Mesopor. Mater.,* **2005**, 82, 1-78.

[13] A. G. Gomez, G. de Silveira, H. Doan and C. Cheng, *Chem. Commun.,* **2011**, 47, 5876-5878.

[14] L. Itani, K. N. Bozhilov, G. Clet, L. Delmotte and V. Valtchev, *Chem. Eur. J.,* **2011**, 17, 2199-2210.

[15] O. Larlus and V. P. Valtchev, *Chem. Mater.,* **2004**, 16, 3381-3389.

[16] I. Bilecka and M. Niederberger, *Nanoscale,* **2010**, 2, 1358-1374.

[17] S. A. Galema, *Chem. Soc. Rev.,* **1997**, 26, 233-238.

[18] Y. Li and W. Yang, *J. Membr. Sci.,* **2008**, 316, 3-17.

[19] G. A. Tompsett, W. C. Conner and K. S. Yngvesson, *ChemPhysChem,* **2006**, 7, 296-319.

[20] A. Z. Ruiz, D. Brühwiler, T. Ban and G. Calzaferri, *Monatshefte Chem. /Chem. Monthly,* **2005**, 136, 77-89.

[21] S. Hashimoto and J. Kiuchi, *J. Phys. Chem. B,* **2003**, 107, 9763-9773.

[22] A. Jawor, B. Jeong and E. M. V. Hoek, *J. Nanopart. Res.,* **2009**, 11, 1795-1803.

[23] G. Schulz-Ekloff, D. Wöhrle, B. van Duffel and R. A. Schoonheydt, *Micropor. Mesopor. Mater.,* **2002**, 51, 91-138.

[24] R. Szostak, *Molecular Sieves,* Blackie academic & Professional, London, **1992**.
[25] P. Cao, H. Li, P. Zhang and G. A. Calzaferri, *Langmuir,* **2011**, 27, 12614-12620.
[26] A. I. Lupulescu, M. Kumar and J. D. Rimer, *J. Am. Chem. Soc.,* **2013**, 135, 6608-6617.
[27] V. Martínez-Martínez, R. García, L. Gómez-Hortigüela, R. Sola Llano, J. Pérez-Pariente and I. López-Arbeloa, *ACS Photonics,* **2014**, 1, 205-211.
[28] A. Bieniok, K. Bornholdt, U. Brendel and W. H. Baur, *J. Mater. Chem.,* **1996**, 6, 271-275.
[29] A. Bessette and G. S. Hanan, *Chem. Soc. Rev.,* **2014**, 43, 3342-3405.
[30] J. M. Dubach, C. Vinegoni, R. Mazitschek, P. Fumene Feruglio, L. A. Cameron and R. Weissleder, *Nat. Commun.,* **2014**, 5, 3946-3955.
[31] G. Ulrich, R. Ziessel and A. Harriman, *Angew. Chem. Int. Ed.,* **2008**, 47, 1184-1201.
[32] J. Banuelos, F. L. Arbeloa, V. Martinez, M. Liras, A. Costela, I. G. Moreno and I. L. Arbeloa, *Phys. Chem. Chem. Phys.,* **2011**, 13, 3437-3445.
[33] T. Gareis, C. Huber, O. Wolfbeis S. and J. Daub, *Chem. Commun.,* **1997**, 1717-1718.
[34] M. Busby, A. Devaux, C. Blum, V. Subramaniam, G. Calzaferri and L. De Cola, *J. Phys. Chem. C,* **2011**, 115, 5974-5988.
[35] J. R. Lakowicz, *Principles of Fluorescence Spectroscopy,* Springer, Singapore, **2006**.
[36] I. Lopez-Duarte, D. Le-Quyenh, I. Dolamic, M. V. Martinez-Diaz, T. Torres, G. Calzaferri and D. Bruehwiler, *Chem. Eur. J.,* **2011**, 17, 1855-1862.
[37] H. Lu, J. Mack, Y. Yang and Z. Shen, *Chem. Soc. Rev.,* **2014**, 43, 4778-4823.

CHAPTER 3

Energy Transfer in Dye-Doped Latex Nanoparticles

One of the most widespread alternatives to the constrained inorganic framework described in the previous section are the organic polymers. These kind of hosts protect the guest molecules but also ensure a better compatibility with the organic fluorophore, albeit usually provide a less rigid environment. Besides, owing to the current vast knowledge in organic chemistry, it is possible to modulate the physicochemical properties of the surrounding host providing it with controllable chemical composition and viscoelastic properties [1-3].

The encapsulation of fluorophores (e.g., into cyclodextrines, calixarenes or cucurbiturils) is a common strategy to: (i) protect and isolate the molecules avoiding specific interactions with the surrounding media (especially important for bioimaging) and (ii) to enhance the photophysical properties of the enclosed fluorophores by reducing molecular motions and aggregation, phenomena which usually causes intense and undesirable fluorescence quenching [4,5]. Besides, dye aggregation is one of the most important limiting factors in the laser performance because aggregates compete with the monomers in the absorption of the pump irradiation [6].

Nowadays, many efforts are conducted to the development of bright fluorophores emitting in the red-edge of the visible [7,8]. Overall, one of the major drawbacks of red-emitting laser dyes resides in their poor photostability and/or low absorption at the standard pump wavelength 532 nm [9]. In order to overcome these detriments we developed a strategy based on: 1) the encapsulation of laser dyes in latex nanoparticles (NP), consisting of a terpolymeric mixture of P-MMA-HEMA-GMA (methyl methacrylate; 2-hydroxylethyl methacrylate and glycidyl methacrylate), with tailored size and composition, and 2) the use of a mixture of suitable dyes, in which a photostable donor molecule with good absorption at 532 nm, i.e., Rhodamine 6G (Rh6G), would be the responsible of absorbing the pump radiation and transfer it via

FRET hops to a proximal long-wavelength emitting acceptor dye, such as Nile Blue (NB) [10].

The simultaneous encapsulation of both dyes into latexes should provide an efficient FRET process owing to the close contact of donor and acceptor molecules, giving rise to long-wavelength fluorescent materials (Figure 3.1). This red spectral window is of special interest for biomedicine and bioimaging due to the capability of this wavelength to penetrate deeper into tissues and reduce the interferences with the autofluorescence background of biological samples [11,12].

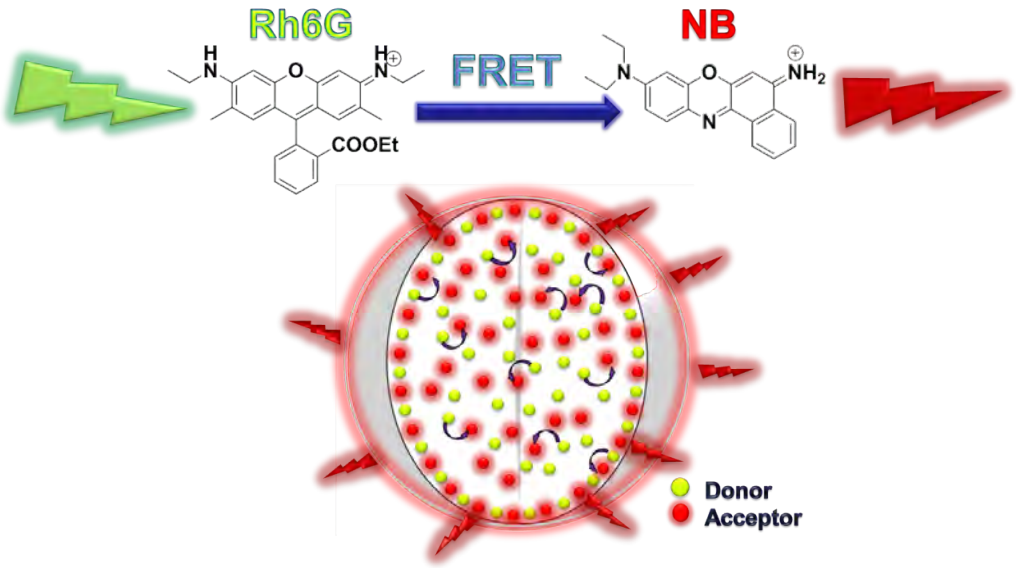

Figure 3.1. Sketch of dyes encapsulated into the latex NP with the corresponding molecular structures of donor Rh6G and acceptor NB molecules undergoing FRET. The arrows indicate the energy transfer process via FRET mechanism.

Against this background, in this chapter we will deeply analyze the influence of the dye-confinement on the photohysical signatures of Rh6G and NB together with the FRET process between them. Firstly, the photophysical properties of Rh6G in NPs with different dye-content, size, composition and surface charge will be analyzed, all of them tuneable in a controlled way by the synthesis conditions. Afterwards, the additional presence of NB will be considered and the corresponding factors controlling the FRET efficiency will be studied.

The aqueous colloidal suspensions of dye-doped latex NPs were synthesized by Prof. E. Enciso (Universidad Complutense de Madrid, UCM) whereas the evaluation of their lasing properties was carried out by Prof. I. García-Moreno, Prof. A. Costela and

Dr. L. Cerdán (Instituto Rocasolano, CSIC, Madrid) which also accomplished the theoretical modelization of the FRET process and dye distribution within the NP.

It is an important fact to remark that the herein reported results are presented mainly from a phenomenological point of view. More detailed information about the synthesis (Prof. E. Enciso) and modelling (Dr. L. Cerdán) methods as well as for the photophysical and lasing characterization is available in the respective articles attached to the corresponding sections.

3.1. Rh6G-Doped Anionic and Cationic NPs

Firstly, it is essential to study the role of the confinement in the photophysical signatures of the encapsulated dye. To this aim, we compare the spectroscopic properties of the Rh6G confined in latexes dispersed in water with those of the dye dissolved in the mixture of monomers MMA, HEMA and GMA, which mimics the latex environment, with the same molar ratio of the monomer feed mixture utilized in the NP preparation (Figure 3.2). The shape of the absorption and emission spectra in the colloidal suspensions matched with that registered in the mimetic liquid solution (Figure 3.2). Just a slight bathocromic shift (4-5 nm) of the spectral bands was detected upon dye confinement. Therefore, no aggregates were present even at the high amounts of dye occluded into the NPs (up to 10^{-2} M). Thus, the encapsulation of Rh6G in latex NPs enables to record the laser action at higher dye concentrations without the negative interference of aggregates, which is one of the most relevant limiting factors for the competitive laser performance of rhodamines. Moreover, the obtained fluorescence quantum yields were similar (around 0.75) in both environments, inside the NP and in the mimetic mixture. The fluorescence decay curves were analyzed as monoexponentials, with a slightly higher lifetime in the latex (~4.4 ns) with respect to the solution (3.6 ns) probably due to a decrease of the internal conversion processes constant (mainly by rotational deactivation) imposed by the confinement in the latex framework. As a result, high lasing efficiencies from Rh6G are recorded in these colloidal suspensions, reinforced by the elongation of the optical pathway in the resonator cavity due to the presence of NPs which act as nanoscatter centres [13].

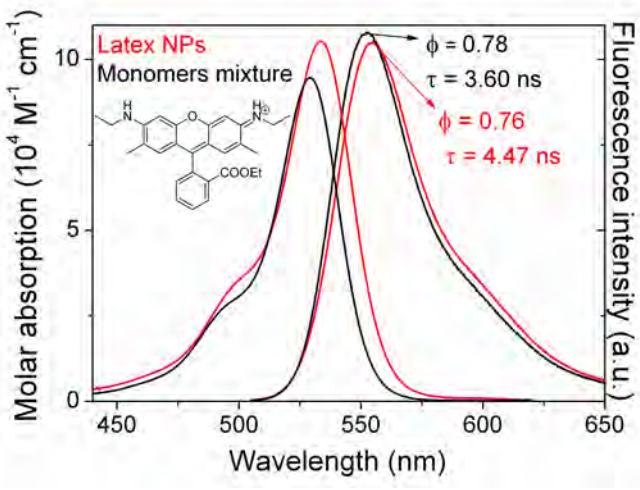

Figure 3.2. Absorption and fluorescence spectra of Rh6G-doped NPs in aqueous suspension (red line) and in the mimetic monomer mixture (black line).

Once checked that the photophysical and laser properties of Rh6G are noticeably enhanced by its encapsulation in latex NPs, we proceeded to analyze different parameters: such as anionic or cationic character of the surface, concentration of the encapsulated dye, size of the nanoparticles and polymeric composition of the latexes [14,15] (Table 3.1). The charged nature of the particle surface will be crucial as it rules the final dye distribution within the NP, which in turn highly influences the photophysical properties (Table 3.1). Thus for a proper discussion of the influence of the rest of variables, anionic and cationic NPs will be described separately.

3.1.1. Rh6G in Anionic NPs

Rh6G is characterized by a low sensitivity to the organic solvent nature [16]. Hence, whereas the latex composition has minor effect on its photophysical properties, the rest of the aforementioned variables (size and dye amount) exert a deep impact on its photophysical features. Table 3.1. summarizes size and dye amount dependent representative photophysic parameters measured in diluted solutions, while more concentrated solutions were required for the registration of laser properties.

The size of the anionic NPs was varied from 22 to 166 nm, keeping the rest of parameters nearly constant. Whereas no changes were observed in the photophysical parameters up to diameters around 70 nm, a further increase in the size was deleterious (decrease of the fluorescence quantum yield from 0.75 to 0.50).

Table 3.1. Photophysical and lasing properties of Rh6G encapsulated in anionic (A) and cationic (C) nanoparticles as a function of a) NPs diameter (dye concentration inside NP ~ 7 mM and fixed latex concentration in solution) and b) Dye content within the NP (particle diameters around 45-55 nm).

a) As a function of NPs Diameter

D (nm)	20		40		55	
NP surface	A	C	A	C	A	C
λ_{ab} (nm)	533.0	528.0	533.5	529.0	533.5	528.0
λ_{fl} (nm)	559.0	554.0	559.5	556.0	559.5	556.0
Φ	0.75	0.84	0.77	0.78	0.74	0.81
τ (ns)	2.75 (15%) 4.54 (85%)	4.36	2.74 (17%) 4.54 (83%)	4.41	2.70 (19%) 4.50 (81%)	4.36
Eff (%)	33	54	10	39	6	29

b) As a function of Dye Content

C_{NP} (mM)	1.4-1.6		5.5-6.2		9.9-12.1	
NP surface	A	C	A	C	A	C
λ_{ab} (nm)	533.5	529.0	533.5	529.0	533.5	528.0
λ_{fl} (nm)	555.5	553.0	558.5	553.0	559.5	556.0
Φ	0.76	0.73	0.71	0.72	0.74	0.70
τ (ns)	4.47	4.37	4.52	4.53	2.40 (20%) 4.41 (80%)	4.41
Eff (%)	-	34	2	38	4	34

D: NP mean diameter; C_{NP}: dye concentration inside NP; λ_{ab}: absorption wavelength; λ_{fl}: fluorescence wavelength; Φ: fluorescence quantum yield; τ : fluorescence lifetime; Eff (%): laser energy conversion efficiency.

However, the influence of the NPs diameter becomes even stronger in the laser action. A laser efficiency of 33% was obtained for 20 nm size particles but no laser emission was detected for the bigger ones (Figure 3.3). The reason of this behavior is ascribed to the strong light scattering from the latexes, which promotes an overall loss of emission capability, especially in the laser media where high amount of latexes are present due to the required high optical densities.

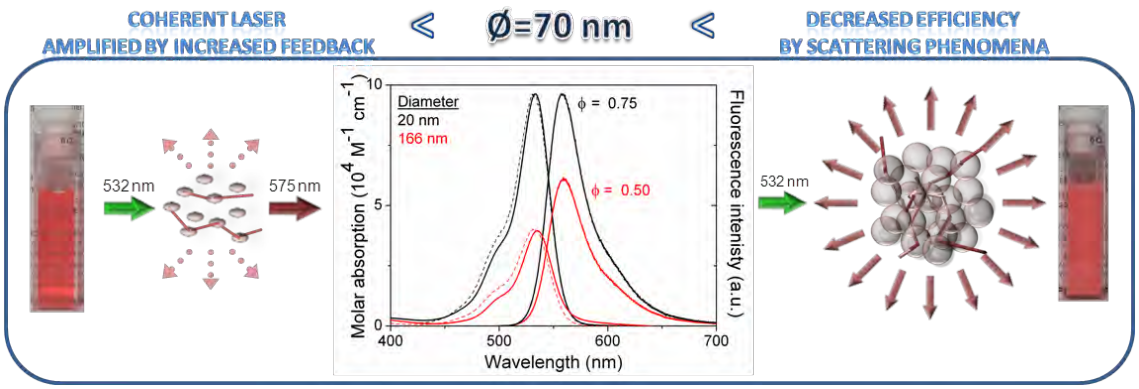

Figure 3.3. Illustration of Rh6G-doped NPs optical properties highly dependent on the particle size.

On the other hand, the dye content in the latex anionic NP was increased from around 1 mM to 10 mM, keeping constant both NP size and latex contents (Table 3.1). In spite of the huge dye loading of the NP the shape of the absorption spectra did not change, indicating the lack of aggregation even the high tendency of Rh6G to self-associate in moderately concentrated solutions. In water solution aggregation appears at concentrations beyond 10^{-5} M [17], whereas in polar organic solvents such tendency is much lower (› 10^{-3}M) [18]. Accordingly, the polar organic environment afforded by the latex nanoparticles makes feasible to work at such high concentrations (up to 10 mM), unattainable in solution without signs of aggregation. Though an increase of the dye content in the latex did not alter the position of the absorption spectra, the fluorescence spectra showed a slight bathochromic displacement, which is ascribed to re-absorption/re-emission processes [19]. Indeed, a decrease of the optical pathway (1 mm cell using front-face configuration) countervails the bathochromic shift. Anyway, the re-absorption/re-emission phenomena are quite faint because the fluorescence quantum yield (obtained in diluted solutions) remained basically constant while increasing the Rh6G content. Nonetheless, the deconvolution of the fluorescence decay curves slightly changes with the dye content in the NP. Thus, while monoexponential decay curves were achieved for the lower dye loadings inside the NP (1-5·10^{-3}M), a further increase of the dye concentration leads to a biexponential fit characterized by the presence of an additional short lifetime (2.5-3 ns) (Figure 3.4 and Table 3.1). Such behaviour could be assigned to the presence of two different environments into the latex nanoparticles: the core and the shell (interphase). The rhodamine would tend to locate in the middle of the particle, due to its hydrophobic character, far away from the water interphase. Nonetheless, an increase of the dye content into the latex NPs should tend to force some of the dye molecules to migrate

to the periphery (latex/water interphase). Such distribution is favoured by the electrostatic attractive interaction of the negatively charged surface of the NP and the cationic dye. As a result, two environments can be distinguished in the anionic NP, each one with an associated lifetime, the core favoured by hydrophobic interaction, and the shell, owing to electrostatic forces. The following study of the cationic NPs will allow us to gain deeper insight into the final dye distribution.

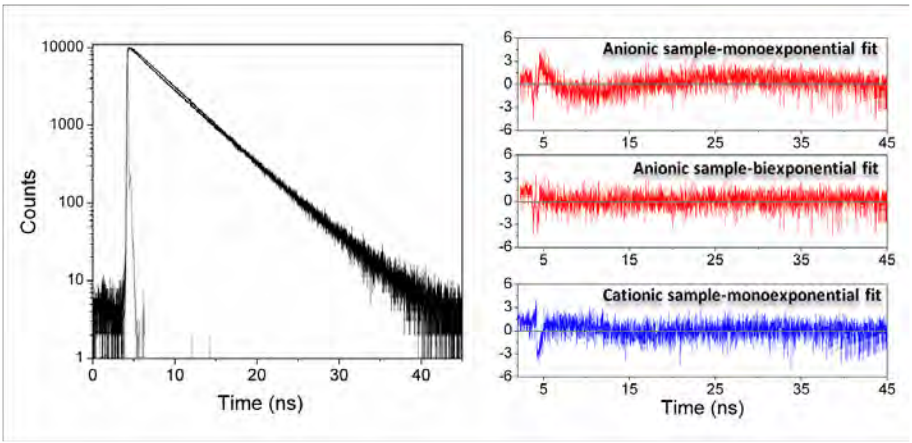

Figure 3.4. Fluorescence decay curves of Rh6G embedded in anionic and cationic NPs respectively, and the residuals of the corresponding mono- and biexponential fits.

3.1.2. Rh6G in Cationic NPs

In order to study the influence that the charge of the NPs has in the optical properties of the encapsulated Rh6G we now consider samples with positively charged surfaces. A direct comparison with anionic NPs of similar size, composition and dye loadings (Table 3.1) also revealed absorption and fluorescence bands similar to those registered in solution even at high concentrations, indicating again the lack of aggregation. In turn, the fluorescence quantum yield mostly increased from ≈ 0.75, in anionic NPs, to ≈ 0.85 when the Rh6G dye is encapsulated in cationic NPs, which is reflected in the increase of the laser efficiency (Table 3.1). Moreover, the fluorescence decay curves in cationic NPs are always analyzed as monoexponential (≈4.4 ns) regardless of the dye content. That is, the required second exponential in anionic NPs for a proper fit is no longer needed in cationic NPs (Figure 3.4). This means that the dye distribution inside the NPs is mainly ruled by the surface charge of the latex NPs due to electrostatic forces (Figure 3.5). Accordingly, in cationic NPs the strong electrostatic repulsion with the enclosed cationic Rh6G prevent them from allocating near the water/latex interphase, placing them preferentially in the core (monoexponetial fit with a lifetime of around 4-5 ns), while in anionic NPs the electrostatic attractions push

molecules from the core to the interphase, leading to two different environments with the corresponding biexponential fit (the longer lifetime assigned to the core and the shorter one to the latex/water interphase) (Figure 3.5). It is likely that the improvement of the fluorescent capacity in cationic NPs could be assigned to the decrease of the dye content in the latex/water intherphase, since the fluorescence quantum yield of Rh6G dye in water is lower (0.59) compared to that shown in monomer solutions mimicking the latex environment (0.78). These results demonstrate the important role played by the sign and strength of the electrostatic shell of the NP in the development of competitive nanosized photonic materials.

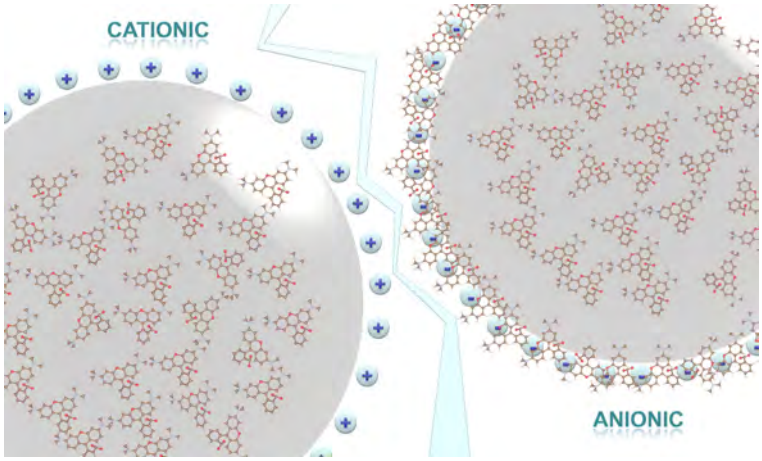

Figure 3.5. Sketch of Rh6G distribution inside anionic and cationic NPs.

To get more insights of the dye distribution dependence on the surface charge of the NPs (anionic vs cationic) we felt prompted to synthesize micrometer-size particles (MP) to analyze them under the confocal fluorescence microscopy, likely the best technique to elucidate the molecules distribution at the single-particle level, using the Fluorescence Lifetime Imaging (FLIM) technique [20]. Unfortunately, the above synthetic routes to achieve anionic or cationic NPs did not allow attaining large enough particles as to be seen properly under the microscope. To circumvent this problem, the synthetic method was changed to obtain microsized (around 2 μm in diameter) latex particles with a polymeric composition of P-MMA-DVB (polimetil methacrylate-divynilbenzene). Nevertheless, one should keep in mind that the peripheral structure of the MPs is completely different with regard to the NPs. The last ones have a negatively (anionic) or a positively (cationic) charged surface, whereas the former ones are expected to be slightly negative due to the presence of carboxylic groups coming from the specific composition. As consequence, the results attained in

MPs cannot be directly extrapolated to NPs but will provide a clear picture of the dye distribution along a single particle.

The fluorescence decay curves registered in single MPs were analyzed as biexponential functions, indicating the presence of two main lifetime populations. The FLIM image (where each pixel corresponds to a fitted lifetime) showed a heterogeneous distribution with the longer lifetimes (ranging from 3-3.5 ns and 50-60% contribution) located in the periphery (red) while the shorter ones (comprising 1.5-1.8 ns with 30-40% contribution) placed in the core (blue) of the particle (Figure 3.6). The fluorescence lifetime profile supports such distribution since the outskirts of the MP showed longer lifetimes than the inner space (Figure 3.6.e). In turn, the fluorescence intensity image together with its profile along the MP demonstrates that even if the dye distribution is quite homogeneous along the MP, the lower intensities were detected in the center of the particles, leading to a ring-shaped intensity profile (Figure 3.6). The regions of higher fluorescence intensity could be assigned to a higher density of dye molecules or alternatively to a change in the fluorescence capacity with the microenvironment.

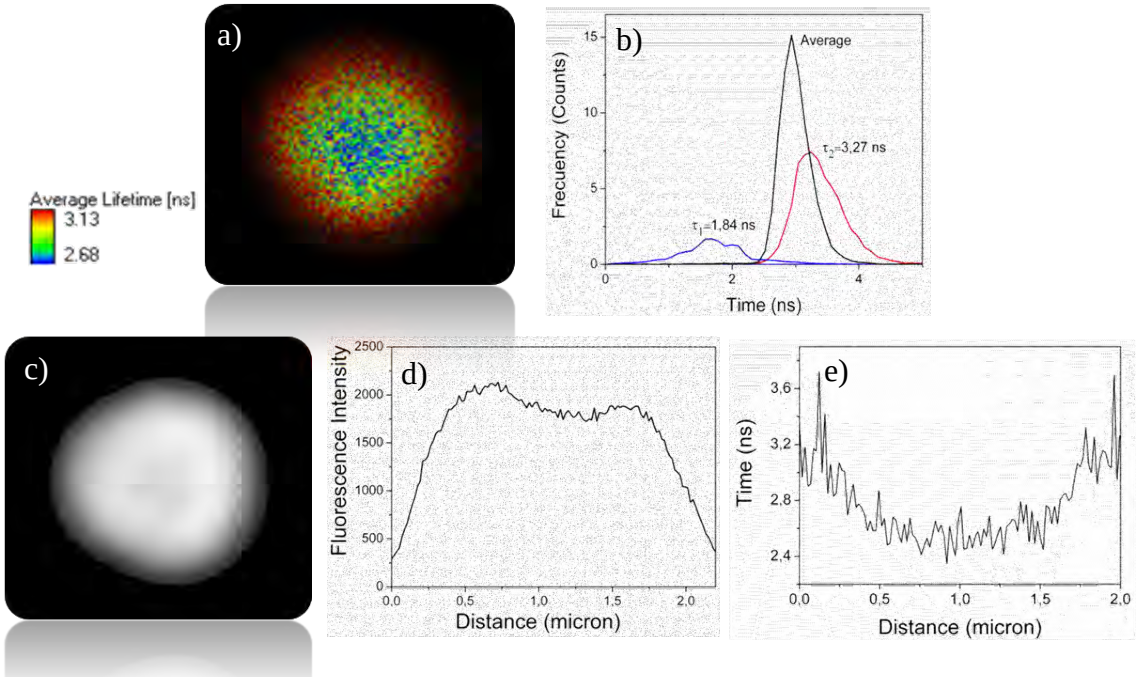

Figure 3.6. (a) FLIM image and (b) histogram representing the average lifetime of a single MP doped with Rh6G (black line in the center) and the two fitted lifetimes 1.84 ns and 3.27 ns (blue and red curves, respectively). (c) Fluorescence intensity image and (d) profile along the MP. (e) Fluorescence lifetime profile across the MP.

At a first sight the presence of two or more lifetimes in Rh6G-doped MPs could be ascribed to the coexistence of two species (i.e., monomer and aggregate) or also to different microenvironments (inner space and periphery) within the particle, in analogy to anionic NPs, where the longer lifetime was assigned to the hydrophobic environment (center of the particle) and the shorter one to the latex/water interphase. However, in the herein analyzed MPs the longer lifetime is preferentially located in the outskirts. We should remark again that the NP and MP cannot be compared due to the divergent surface charge induced by the latex monomeric composition employed for each case. Alternatively, the presence of different lifetimes along the MP could also be assigned to a physic phenomenon with a photonic origin (Purcell effect). This phenomenon is ascribed to the spontaneous emission inhibition experienced by emitters confined in subwavelength cavities [21,22]. The recording of the fluorescence spectra at different regions of the MP (center and periphery) clarifies the situation (Figure 3.7). The fluorescence band position and shape is very similar regardless of the irradiated region and also matches that recorded for diluted Rh6G solution. Therefore, the formation of new fluorescent species is discarded and the presence of two different lifetimes should be ascribed to different microenvironments within the MP (likely assisted by the Purcell effect), in line with the picture predicted in anionic NPs with high dye loadings.

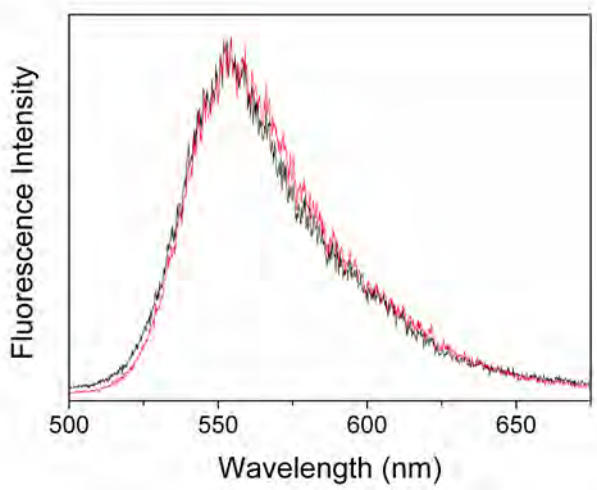

Figure 3.7. Emission spectra of Rh6G recorded in different regions of the MP, the core (black) and the shell (red).

After studding in-depth the distribution of Rh6G dye inside particles of different sizes and compositions, we will continue now with the discussion of the photophysical properties of the Rh6G encapsulated in cationic NPs with the aim of further analyze some possible variables affecting the photophysics of the material. As in anionic NPs,

several parameters were systematically changed in the positively charged-surface NPs to analyze their impact in the photophysics of Rh6G, such as NP size, dye concentration, monomeric composition, dielectric constant and even surfactant structure (Table 3.2). Although the photophysical properties are not strongly affected by most of the above mentioned factors, there are some structural and compositional parameters that should be stressed.

Table 3.2. Most important photophysical parameters of Rh6G-doped cationic NPs as a function of NP size, monomeric composition, dye content, and surfactant composition. Samples with similar characteristics but without the corresponding variations of each series have been added at the bottom of the table for comparison.

	Dye concentration inside NP (mM)			**Dielectric constant R-OH (%)**			**Monomer composition MMA/HEMA/X**			**Surfactant [Surfactant]~2mM**		
	Low 1.0	Interm 7.9	High 23.2	MeOH (10%)	EtOH (12.5%)	PrOH (12%)	X=GMA 37.5/25/37.5	X=AA 57/25/18	X=GMA 37.5/25/37.5	TTAB	DTAB	TOAB
D (nm)	36	31	37	26	87	311	28	43	26	30	93	186
λ_{ab} (nm)	529.0	529.0	529.0	529.0	530.0	530.0	529.0	527.0	525.0	29.0	532.0	528.0
λ_{fl} (nm)	552.0	555	557.0	556.0	557.0	557.0	556.0	556.0	553.0	555.0	559.0	556.0
Φ	0.74	0.71	0.66	0.75	0.73	0.69	0.78	0.76	0.71	0.72	0.73	0.64
τ (ns)	4.22	4.53	4.38	4.50	4.53	4.35	4.66	4.37	4.10	4.46	4.42	4.23
Eff (%)	15	37	18	48	4	-	55	42	52	53	4	-
				No alcohol: d=21 nm; λ_{ab}=528.0; λ_{fl}=554.0; Φ=0.80; τ=4.35; Eff(%)=49			X=0 (72/25/0): d=32 nm; λ_{ab}=527.0; λ_{fl}=555.0; Φ=0.75; τ=4.35 Eff(%)=45			CTAB: d=21 nm; λ_{ab}=528.0; λ_{fl}=554.0; Φ=0.75; τ=4.36; Eff(%)=21		

It is noticeable that in cationic NPs the addition of increased volumetric proportions of alcohols (methanol, ethanol or propyl-alcohol) to water during the synthesis leads to particles with larger sizes (up to 310 nm). In line with the results of anionic NPs, an increase of the diameter in this case beyond 55 nm causes a progressive decrease of the fluorescence capacity (from 0.75 to 0.65) (Table 3.2). This decline might be attributed to the light scattering that should reduce, as in anionic NPs, the number of emitted photons reaching the detector. Besides, a dye leakage from the NPs is observed, probably assisted by the repulsive interactions between the cationic NP and Rh6G as well as by the presence of alcohols, causing that part of the

encapsulated Rh6G is now surrounded by water, a medium in which shows a reduced quantum yield and a higher tendency for aggregation. Moreover, for high amounts of Rh6G the reabsorption/reemission phenomena influence the photophysical properties of the system, leading to an overall diminution of the emission capability (around 10%).

In contrast to anionic NPs, the change in the monomeric composition or surfactant of the cationic latexes alters the photophysical properties of the Rh6G (Table 3.2). Thus, the replacement of MMA by either GMA or AA (acrylic acid) renders improved quantum yields and slightly bathochromically shifted absorption and emission bands, whereas the copolymerization with BA (butyl acrylate) decreases the fluorescence emission efficiency of Rh6G ($\Phi_{GMA} \approx \Phi_{AA} > \Phi_{BA}$) and shifts the bands to higher energies. Moreover, the nature of the surfactant not only affects the morphological properties of the particle but also influences the photophysical characteristics (Table 3.2). While the reduction in the aliphatic chain for single-chain surfactants lead to a slight decrease of the fluorescence quantum yield accompanied by little shifts in absorption and fluorescence spectra, the use of quadruple-chain surfactants such as TOAB (tetraoctylammonium bromide) favours the formation of NPs with bigger sizes and has a negative influence on the emission capability since the fluorescence quantum yield decreases to 0.64 (Table 3.2). In fact, one should take with care the conclusions about monomeric and surfactant composition effects because the change of these parameters also renders NPs with different morphology, for instance, bigger NPs which directly affects negatively the fluorescence emission capability. Therefore, the above pointed reduction of the fluorescence efficiency could be mainly attributed to size effects rather than composition ones.

Summing up, the confinement of Rh6G in latex NPs is highly profitable for the photophysical signatures of the dye and greatly enhances the photostability and laser efficiency of the Rh6G as compared with the performance of the same dye in solution. The bright fluorescence emission of the dye is kept upon encapsulation, while aggregation is avoided even at high dye concentrations (upon 10^{-2}M). Besides, the electronic characteristic of the surface determines the dye distribution inside the NP. Thus, the electrostatic attraction in anionic latexes pushes the dye from the inside to the latex/water intherphase, whereas the electrostatic repulsions in cationic nanospheres locate the molecules in the core of the NP, leading to improved fluorescence response. The amount of dye (re-absorption/re-emission effects) and the NP size (scatter) are highlighted as the key parameters ruling the emission properties

of the colloid. It should be emphasized the proper correlation of the photophysical properties with the lasing efficiency, although the last one is more sensitive to the modification of the structural and chemical properties of the NPs.

The article reported in *Laser Physics Letter* Journal asses the critical dependence on the charged-surface interfacial effect of both the photophysics and the laser behaviour in dye-doped latexes.

IOP Publishing | Astro Ltd Laser Physics Letters

Laser Phys. Lett. **11** (2014) 015901 (6pp) doi:10.1088/1612-2011/11/1/015901

Letter

Focusing on charge-surface interfacial effects to enhance the laser properties of dye-doped nanoparticles

Luis Cerdán[1], Leire Gartzia-Rivero[2], Eduardo Enciso[3], Jorge Bañuelos[2], Iñigo López Arbeloa[2], Angel Costela[1] and Inmaculada García-Moreno[1]

[1] Instituto de Química-Física 'Rocasolano', CSIC, Serrano 119, E-28006 Madrid, Spain
[2] Departamento de Química Física, Universidad del País Vasco-EHU, Apartado 644, 48080 Bilbao, Spain
[3] Departamento de Química Física I, Facultad de Ciencias Químicas, Universidad Complutense de Madrid, Ciudad Universitaria, E-28040 Madrid, Spain

E-mail: lcerdan@iqfr.csic.es

Received 8 October 2013, revised 12 November 2013
Accepted for publication 14 November 2013
Published 6 December 2013

Abstract

The synthesis of nanoparticles (NPs) for which only a single property is modified in a controlled manner is a challenge due to the fact that several physicochemical parameters are entangled. This letter assesses, from both experimental and theoretical points of view, the critical dependence on the charged-surface interfacial effect of the laser behavior in photonic nanomaterials based on dye-doped latexes without interference from other physicochemical parameters. When the dye and the NPs have similar charge nature, strong electrostatic repulsion prevents the dye molecules from being directly adsorbed in the surface and maintains the dye homogeneously distributed inside the NP, thus reducing deleterious interfacial effects. The highly homogeneous inner morphology leads to at least two-fold laser behavior enhancement of Rh6G in cationic NPs as compared with their anionic counterparts, and at least three-fold enhancement over Rh6G behavior in water solution.

Keywords: dye laser, latex nanoparticles, simulation, interfacial effects, optical materials

1. Introduction

Colloids based on latex nanoparticles (NPs) in aqueous suspensions display unique and interesting properties as a result of their small size and large interfacial area. Because the interfacial area dominates, major efforts have been undertaken to tailor the latex properties/performance issues, focusing on surface modifications by means of chemical groups and/or by varying the total particle charge [1–7]. In this context, ionic surfactant molecules become a key parameter in the NP morphology, as they are known to delimit an electrostatic shell, whose sign and strength are of special relevance in determining the behavior of bio-inspired materials [8–10]. In the same way, charge-dependent interfacial effects, which up to date have not been paid much attention, could be critical in improving some useful properties of nano-sized photonic materials based on active optical latexes doped with ionic dyes. In this context, and taking into account that most of the fluorescent dyed particles commercially available are based on ionic polymeric spheres internally doped with ionic fluorophores[4], an in-depth analysis of those effects acquires special relevance. Thus, the present work is focused on controlling charge-surface interfacial effects in dye-doped NPs to enhance their laser action, which is an operation requiring more demanding conditions than those needed for

[4] See, for example, catalogs from Molecular Probes, Thermo Scientific and Bangs Laboratories Inc.

Table 1. Photophysical and lasing properties of Rh6G encapsulated into cationic NPs. For comparison purposes the corresponding data from similar dye-doped anionic latexes [13] are included. (Note: definition of variables: D: NP diameter; W_{Dye}: dye concentration (with respect to polymer mixture); W_{NP}: content of latex NPs in aqueous suspensions; λ_{abs}: absorption wavelength; ε_{max}: absorption coefficient; λ_{flu}: fluorescence wavelength; ϕ: fluorescence quantum yield; τ: fluorescence lifetime; Eff: laser energy conversion efficiency; λ_{la}: laser wavelength.)

Sample	D (nm)	W_{Dye} (wt%)	W_{NP} (wt%)	λ_{abs} (nm)	ε_{max} (10^4 M^{-1} cm^{-1})	λ_{flu} (nm)	ϕ	τ (ns)	Eff (%)	λ_{la} (nm)
C1	21	0.35	4	528.0	6.9	554.0	0.84	4.36	54	575
C2	42	0.32	3.8	529.0	7.0	556.0	0.78	4.41	39	574
C3	53	0.33	3.8	528.0	6.9	556.0	0.81	4.36	29	574
A1	20	0.33	3.4	533.0	9.6	559.0	0.75	2.75 (15%) 4.54 (85%)	33	578
A2	44	0.33	6	533.5	9.7	559.5	0.77	2.74 (17%) 4.54 (83%)	10	575
A3	55	0.33	6	533.5	9.9	559.5	0.74	2.70 (19%) 4.50 (81%)	6	573

merely inducing fluorescence. To this aim, we have designed a strategy that enables one to solely assess the influence of the charge on the interactions of the NPs with dyes, without interference from other physicochemical parameters.

In a recent work, we demonstrated, for the first time, Förster resonance energy transfer (FRET) assisted laser emission in colloidal suspensions of dye-doped latexes based on mixtures of Rhodamine 6G (Rh6G) with Nile blue (NB), acting as donor and acceptor, respectively [11]. A thorough photophysical study revealed that these latexes possessed an unexpected core/thin shell morphology: (a) the core is a homogeneous polymer particle in which both donors and acceptors are homogeneously and uniformly dissolved and (b) the surface (or very thin shell) is formed by the so-called NP 'hairy layer' (surface roughness or fuzziness [12]), in which both donors and acceptors would be adsorbed with a concentration different to that in the core. Since we used an anionic surfactant in the synthesis, the 'hairy layer', formed by the polymer/surfactant/water interfacial layer, had a certain negative charge distribution, inducing electrostatic attraction forces toward cationic dyes such as Rh6G and NB. This unexpected morphological inhomogeneity, which was verified by the bi-exponential decay of the fluorescence lifetime of Rh6G even in the absence of acceptor molecules [13], could be limiting an efficient photonic behavior from the final system. Trying to avoid such interfacial effects, herein we have synthesized and characterized dye-doped cationic NPs where the sign of the surfactant charge is changed but otherwise the size, shape and composition of the new latex is kept unaltered with respect to those previously analyzed [13, 14]. The findings herein obtained provide straightforward and facile strategies for designing dyed NPs able to sustain improved photostable and efficient fluorescence and laser operation, dealing with some of the actual pressing challenges in the field from an applied point of view.

2. Experiment

2.1. Materials

Laser dye Rhodamine 6G (Rh6G) (Fluka, >95% purity) was used as received. Methyl methacrylate (MMA) (Aldrich, 99%) was purified with a 0.1 M sodium hydroxide solution to remove the inhibitor. 2-Hydroxyethyl methacrylate (HEMA) (Aldrich, 97%), glycidyl methacrylate (GMA) (Fluka, 97%), 2,2-azobis(2-methyl propionamidine) hydrochloride (AIBA) (Sigma, 99%) and cetyl trimethyl ammonium bromide (CTAB) (Sigma 99%) were used without further purification. Deionized water was obtained from a Direct QTM 5 Millipore.

2.2. NPs synthesis

It is analogous to the one corresponding to anionic NPs [13], but changing only the surfactant and initiator. Rh6G was dissolved in a monomer mixture MMA/HEMA/GMA in a 70/20/10 weight proportion. CTAB (2.5×10^{-3} M) was added into the aqueous polymerization medium as a cationic colloidal stabilizer. After oxygen degassing with a nitrogen flux, the reactor was heated to 65 °C and the free radical polymerization was started by addition of the cationic initiator AIBA. The optimized ratio of Rh6G to polymer was kept constant at ∼0.30 wt%, being the NP concentration in the colloidal suspension of ∼4 wt% (table 1). The size distribution by volume of the sensitized nanospheres (table 1) was measured by quasielastic laser light scattering with a Brookhaven Zetasizer (Brookhaven Instruments Ltd) at 25 °C.

2.3. Laser characterization

Original suspensions, without dilution, were contained in 1 cm optical path quartz cells carefully sealed to avoid solvent evaporation. The samples were transversely pumped

at 532 nm with 5.5 mJ, 6 ns FWHM pulses from a frequency-doubled *Q*-switched Nd:YAG laser (Monocrom STR-2+) at a 10 Hz repetition rate. The excitation pulses were line-focused onto the front face of the cell, providing pump fluences on the active medium of 180 J cm^{-2}. The oscillation cavity (2 cm length) consisted of a 90% reflectivity aluminum mirror, with the end lateral face of the cell as output coupler. The laser emission was monitored perpendicular to the excitation beam, collected by an optical fiber, imaged onto the input slit of a monochromator (Acton Research Corp.) and detected with a charge-coupled device (CCD) (SpectruMM:GS128B). The estimated error of the energy measurements was 10%. Details of the experimental setup can be found elsewhere [11, 13].

2.4. Photophysical properties

The photophysical properties were registered in diluted aqueous suspensions of latex NPs doped with Rh6G to avoid reabsorption/reemission phenomena. These suspensions are obtained by diluting the original ones to a latex content of 0.03–0.04 wt%, with the Rh6G concentration in the suspension thus being reduced from 3×10^{-4} to 2×10^{-6} M. UV–vis absorption and fluorescence spectra were recorded on a Cary 4E spectrophotometer and on a SPEX Fluorolog 3–22 spectrofluorimeter, respectively. The absorption spectra were recorded using a blank suspension of latex in water as a reference. However, in most cases the baseline was subsequently corrected manually to appropriately adjust the zero of absorbance. Fluorescence quantum yields (ϕ) were evaluated from corrected spectra using a diluted solution (10^{-6} M) of Rh6G dye in water ($\varphi = 0.59$) as a reference. Radiative decay curves were registered by the time correlated single-photon-counting technique (Edinburgh Instruments, model FL920). Fluorescence emission was monitored at the maximum emission wavelength after excitation at 470 nm by means of a diode laser (PicoQuant, model LDH470) with 150 ps fwhm (full width at half-maximum) pulses. The fluorescence lifetime (τ) was obtained from the slope after the deconvolution of the instrumental response signal from the recorded decay curves by means of an iterative method. The goodness of the exponential fit was controlled by statistical parameters (χ^2, Durbin–Watson, and analysis of the residuals).

3. Results and discussion

Under the described experimental conditions, Rh6G doped cationic latexes led to improved laser efficiency and photostability with respect to that exhibited by this same dye into anionic NPs of similar size and composition (sample C1 versus A1 in table 1) and pumped under otherwise identical experimental conditions [13]. Although both samples emitted broad-line-width laser light close to 575 nm (figure 1 and table 1), the laser efficiency of Rh6G increased from 33% (Sample A1) up to 54% (Sample C1), with the emission threshold decreasing from 0.22 mJ to 0.15 mJ, respectively. These efficiencies and thresholds are higher and lower, respectively, than those reported before in analogous systems (30 nm polymeric NPs doped with PM567) [15]. Nevertheless, this comparison is not very appropriate, since experimental parameters affecting the laser properties—dye loading, NP content in the solution, cavity properties—are not the same in both systems, and must be taken with care.

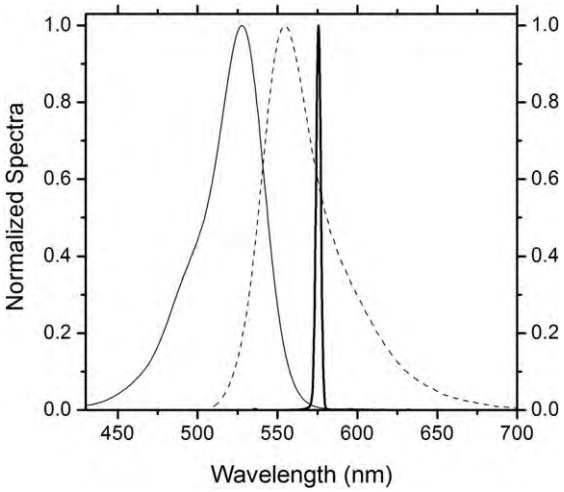

Figure 1. Normalized absorption (solid line), fluorescence (dashed line) and laser (thick solid line) spectra of sample C1.

The photostability (evolution of the emission with the number of pump pulses at a controlled repetition rate) of the dye-sensitized NPs was evaluated by irradiating under lasing conditions 10 μl of water dispersion contained in capillary tubes [13]. The cationic system resulted to be highly photostable since the emission remained at its initial value after 100 000 pump pulses at a 10 Hz repetition rate. To better assess the laser photostability of the Rh6G doped cationic NPs, the colloidal suspension was pumped under more drastic conditions by increasing the repetition rate up to 30 Hz. The cationic system still exhibited high photostability, since the emission dropped by less than 5% from its initial value after 100 000 pump pulses, as compared with a drop to a 50% of the anionic system after the same number of pulses (figure 2). In addition, the lasing efficiency of the Rh6G doped cationic latexes was three-fold higher than that recorded from a water solution of dye with no latexes, indicating the relevance of the laser enhancement reached with the new system herein synthesized.

The influence of the inner morphology of the dye-doped latex NP on its laser behavior was properly assessed by analyzing the photophysical properties of these cationic colloids with respect to those previously registered in similar anionic systems [13]. The confinement of Rh6G into cationic NPs leads to a homogeneously dispersed suspension characterized by absorption and emission spectra (figure 1) analogous to those registered for the same dye in solution and in anionic NPs [13], presenting only slight shifts in the absorption and emission peak wavelengths (table 1). This, together with the absence of new spectral features, rules out the presence of aggregates or new species after NP synthesis. The fluorescence quantum yields (up to 0.85) are slightly

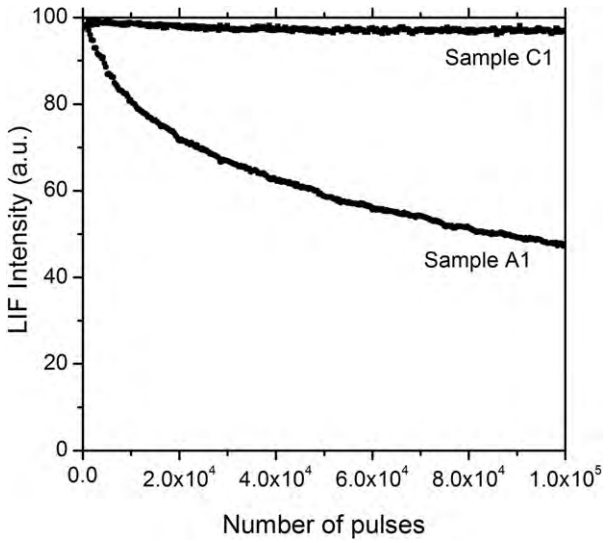

Figure 2. Normalized laser-induced fluorescence (LIF) emission as a function of the number of pump pulses for Rh6G confined into cationic and anionic NPs pumped with 5.5 mJ/pulse at a 30 Hz repetition rate.

higher than those registered in similar dye-doped anionic NPs (≈0.75) (table 1). The increase in the fluorescence ability of Rh6G could be related to a decrease of the dye content in the NP–water interphase, since the fluorescence quantum yield of Rh6G increases from 0.59 when dissolved in water [16] up to the value 0.78 registered in a monomer solution mimicking the latex environment [13]. From the photophysics viewpoint, the most important feature in cationic latexes arises through the analysis of the fluorescence lifetime of Rh6G, which is strongly affected by the ionic charge of the surfactant, since it no longer exhibits the above-mentioned bi-exponential character. On the contrary, in the present case the decay curve is properly adjusted to a mono-exponential (≈4.4 ns) (table 1). The mono-exponential character of the fluorescence lifetime provides further support to our initial hypothesis: in the case of two components having similar charge nature (cationic), strong electrostatic repulsion prevents them from being adsorbed and maintains Rh6G molecules preferably homogeneously distributed inside the NP, thus reducing deleterious interfacial effects.

It is worth noticing that the improved laser efficiency observed in the cationic NPs with respect to those of the anionic ones is also evidenced for larger NPs. Although both systems follow the same tendency; the larger the NP is, the lower the laser efficiency becomes, an increase of the diameter from 20 nm to 55 nm drastically reduces the lasing efficiency in anionic colloids (from 33% in sample A1 to just 6% in sample A3, table 1) while the cationic latex with the largest diameter still lases with high efficiency (29%) (samples C1–C3 in table 1).

In order to back up the above hypothesis, we made use of a numerical model based on laser rate equations to gather information on the laser efficiencies simulated from the known photophysical parameters, NP size, and pumping conditions. The model, which was successfully applied to evaluate the effect of optical scattering on the laser performance of dye solutions, is fully described in [17].

Table 2. Computed and experimental laser efficiencies of Rh6G encapsulated into cationic and anionic NPs. (Note: definition of variables: n_d: average volume density of dye molecules; Eff^{th}: Computed laser energy conversion efficiency (values in parentheses correspond to calculation assuming two species); Eff^{exp}: experimental laser energy conversion efficiency.)

Sample	n_d ($\times 10^{17}$ cm^{-3})	Eff^{th} (%)	Eff^{exp} (%)
C1	1.8	56	54
C2	1.5	44	39
C3	1.6	32	29
A1	1.4	48 (43)	33
A2	2.5	16 (9)	10
A3	2.5	10 (5)	6

Unlike the samples evaluated in [17], the colloidal solutions are discontinuous gain media in which the amplification processes take place only within the NPs; the surrounding media acting as a passive region. To model these systems a space discretization smaller than the NP size would be needed ($\Delta x \ll 20$ nm), but this would imply an unaffordable computation power and time. Therefore, we made use of a mean field theory in which the discrete nanoscopic properties of the colloidal dispersion (dye concentration and refractive index) were averaged to assume an effectively continuous active medium with scattering losses due to the discontinuous nature of the refractive index. Hence, the averaged volume density of dye molecules in the solution n_d was calculated according to:

$$n_d = W_{Dye} W_{NP} \frac{\rho_W \rho_{NP}}{\rho_{NP} - W_{NP}(\rho_{NP} - \rho_W)} \frac{N_A}{M_W} \qquad (1)$$

where $\rho_W = 1$ g cm^{-3} and $\rho_{NP} = 1.15$ g cm^{-3} are the densities of water and NPs, respectively, W_{Dye} and W_{NP} are the weight percents of dye (with respect to polymer content) and polymer in the solution, respectively, N_A is Avogadro's number and $M_W = 479.02$ g mol^{-1} is the dye molecular weight. The values of n_d corresponding to each sample numerically evaluated are presented in table 2. The photophysical properties used were those in table 1, while the remaining computational parameters were assumed to be: active medium length $L = 1$ cm and width $b = 300$ μm, rear mirror reflectivity $R_1 = 0.99$, output coupler (cuvette facet) reflectivity $R_2 = 0.04$, pump pulse duration 6 ns FWHM, and pump energy $E_p = 5$ mJ.

Table 2 lists the computed laser efficiencies Eff^{th} for both the cationic and the anionic samples. The predicted values for the cationic NPs (C1–C3 in table 2) show a very good agreement with the experimental values (Eff^{exp}) for all the NP diameters evaluated. The reduction in the laser efficiencies with the size is due to the deleterious effects of optical scattering, which gain weight as the diameter increases. On the other hand, the predicted values for the anionic NPs (A1–A3 in table 2) do not present such a good agreement with the experimental values, since the former overestimate the latter, with differences of up to 50%. This discrepancy has its origin in the deleterious effects of the interfacial layer

present in the anionic particles, which is not taken into account in the model.

To take this effect into account, we have to assume that the dye molecules in the core and the surface are independent and present different photophysical parameters (lifetime and quantum yield), as explained before. This means that we have to assume in the model that there are two species contributing to the total emission. The weight of each exponential in the fluorescence lifetime measurements (table 1) is indicative of the population (n_d) corresponding to each species. In other words, the population in the core, with a lifetime of ∼4.5 ns, is around 80–85%, while the population in the surface, whose lifetime is around 2.7 ns, reaches 15–20%. On the other hand, each population must present a different quantum yield due to the different surrounding environment. To estimate the value corresponding to each region, we must assume that the measured quantum yields (table 1) are weighted averages of the quantum yields in the core and surface. Since the monomer compositions of the anionic and cationic NPs are exactly the same, we can assume that the quantum yield of the dyes in the core of the anionic NPs is the same as that measured for the cationic dyes, i.e., $\phi_C \sim 0.8$. Hence, the quantum yield of the dyes in the surface (ϕ_S) can be calculated as:

$$\phi_S = \frac{\phi - p_C\phi_C}{1 - p_C} \quad (2)$$

where ϕ is the experimentally measured quantum yield, and p_C is the relative amount of dyes in the core (∼0.8). Equation (2) renders quantum yields in the surface of $\phi_S \sim 0.4$. This implies that the dyes in the surface present a fluorescence capability significantly reduced as compared with that of the dyes in the core, a fact that can explain the differences observed in the laser efficiencies. This reduction in the quantum yield could have an origin in both the chemical and electrostatic environment 'felt' by the dyes at the surface. As explained before, Rh6G molecules at the surface of the NP are in close proximity to water molecules, a medium in which this dye shows a reduced quantum yield of 0.59. On the other hand, the dye molecules in the surface are more exposed to the electric field generated by the charges in the surface (due to surfactant head and polymer end groups), which is known to affect the oscillator strength of the dye and, in turn, its quantum yield [18]. To know the extent of each of these effects would require a study which is beyond the scope of the present work, but which will be taken into account for future works.

Table 2 lists in parentheses the computed laser efficiencies Eff^{th} for the anionic NPs samples when taking into account the previous assumptions. The predicted values now show a much better agreement with the experimental values (Eff^{exp}) (excepting the one for sample A1, which will be discussed later). The above results confirm that the origin of the differences in the laser efficiencies when comparing cationic and anionic NPs is in the deleterious effects of the interfacial layer present in the latter. It could be argued that the differences in the laser efficiencies could result from the different polymer content W_{NP} in A2 and A3 with respect to C2 and C3 (table 1). Nevertheless, the laser efficiencies of samples A2 and A3 were recalculated assuming $W_{NP} = 3.8\%$, and values of 19% and 12%, respectively, were obtained, which, in spite of having been improved, are still significantly lower than those of samples C2 and C3.

Finally, the results obtained with sample A1 have to be taken with care since, due to the inherent difficulty synthesizing anionic latexes sized below 25 nm, its synthesis protocol was slightly modified toward a two-step mechanism [13]. Under these conditions, some of the input parameters required to model its behavior could be uncertain, explaining the discrepancy between the theoretical and experimental results observed solely in the analysis of this sample.

4. Conclusions

In summary, we have demonstrated, from both experimental and theoretical points of view, the critical dependence on the charged-surface interfacial effect of the laser behavior in photonic nanomaterials based on dye-doped latexes. Although synthesizing NPs for which only a single property is modified in a controlled manner is a challenge due to the fact that several physicochemical parameters are entangled, this letter demonstrates that it is possible to assess the influence of the charge on the dye–NP interactions without interference from other physicochemical parameters. When the dye and the NPs have similar charge nature, strong electrostatic repulsion prevents the dye molecules from being directly adsorbed in the surface and maintains the dye homogeneously distributed inside the NP, thus reducing deleterious interfacial effects. The highly homogeneous inner morphology leads to at least two-fold enhancement in the laser efficiency of Rh6G in cationic NPs as compared with their anionic counterparts, and at least three-fold enhancement over Rh6G behavior in water solution. The results here reported show that the sign and strength of the electrostatic shell delimited by the surfactant play key roles in the development of nano-sized photonic materials with enhanced optical properties.

Acknowledgments

This work was supported by Projects MAT2010-20646-C04-01, MAT2010-20646-C04-04 and MAT2012-39199-C02-02 of the Spanish Ministerio de Economia y Competitividad (MINECO). Also, Gobierno Vasco (IT339-10) is gratefully acknowledged for financial support and a PhD grant for LGR.

References

[1] Faul C F J 2003 *Adv. Mater.* **15** 673–83
[2] Jeon S and Granick S 2004 *Macromolecules* **37** 2919–23
[3] Gao J, Lee D, Yang Y, Holdcroft S and Frisken B J 2005 *Macromolecules* **38** 5854–6
[4] Udayana R J K, Nguten C T, Wilson B A, Shinoda W and Nielsen S O 2011 *Soft Matter* **7** 6942–52
[5] Kumar S, Aswal V K and Kohlbrecher J 2012 *Langmuir* **28** 9288–97
[6] Krovi S A, Swindell E P, O'Halloran T V and Nguyen S T 2012 *J. Mater. Chem.* **22** 25463–70

[7] Sinha P, Szilagyi I, Montes Ruiz-Cabello F J, Maroni P and Borkovec M 2013 *J. Phys. Chem. Lett.* **4** 648–52
[8] Verma A and Stellacci F 2010 *Small* **6** 12–21
[9] Asati A, Santra S, Kaittanis C and Perez J M 2010 *ACS Nano* **4** 5321–31
[10] Hünn D *et al* 2013 *ACS Nano* **7** 3253–63
[11] Cerdán L, Enciso E, Martin V, Bañuelos J, Lopez Arbeloa I, Costela A and Garcia-Moreno I 2012 *Nature Photon.* **6** 621–6
[12] Farinha J P S, Charreyre M T, Martinho J M G, Winnik M A and Pichot C 2001 *Langmuir* **17** 2617–23
[13] Martin V, Bañuelos J, Enciso E, Lopez Arbeloa I, Costela A and Garcia-Moreno I 2011 *J. Phys. Chem.* C **115** 3926–33
[14] Enciso E, Costela A, Garcia-Moreno I, Martin V and Sastre R 2010 *Langmuir* **26** 6154–7
[15] Monguzzi A, Frigoli M, Larpent C and Meinardi F 2012 *RSC Adv.* **2** 11731–6
[16] López Arbeloa F, López Arbeloa T and López Arbeloa I 2001 *Handbook of Advanced Electronic and Photonic Materials and Devices* vol 7, ed H S Nalwa (New York: Academic) pp 209–45
[17] Cerdán L, Costela A, García-Moreno I, Martín V and Pérez-Ojeda M E 2011 *J. Quantum Electron.* **47** 907–19
[18] Kalinowski J, Mezyk J, Meinardi F, Tubino R, Cocchi M and Virgili D 2008 *Chem. Phys. Lett.* **453** 82–6

3.2. Energy Transfer in Dye-doped Anionic NPs

The encapsulation of donor-acceptor mixtures into nanometric latex particles is a straightforward strategy to place dyes closer and enable efficient FRET processes [23,24]. Once checked that the confinement of Rh6G was beneficial for the fluorophore properties we proceeded to the co-encapsulation of a suitable acceptor pair. The oxazine NB was selected as the ideal candidate since its absorption band in solution shows a suitable spectral overlap with the emission band of Rh6G, and its emission is placed towards the red region (Figure 3.8). The main objective is to overcome the poor photostability and low absorption capability of red laser dyes at the standard pump wavelength (i.e., low absorption of NB at 532 nm) by exciting a photostable dye (Rh6G) which should transfer the excitation energy efficiently via FRET to the NB, the emitting red dye, consequently reducing the photobleaching and leading to an efficient red laser signal.

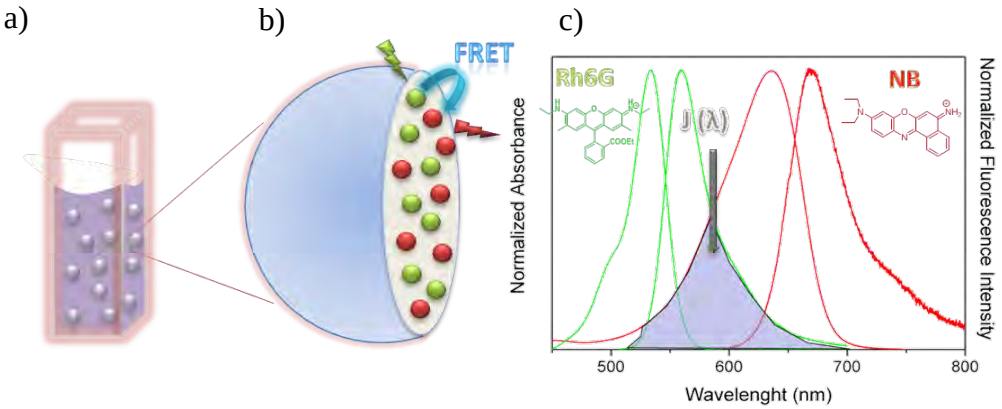

Figure 3.8. a) Colloidal suspension of Rh6G/NB mixture embedded in latex NPs. b) Sketch of FRET process between dyes (Rh6G in green dots and NB in red dots) within the NP. c) Normalized absorption and fluorescence spectra of colloidal suspensions of NPs doped with Rh6G (green line) and NB alone (red line). The region in grey accounts for the spectral overlap (J(λ)) between donor emission and acceptor absorption. Inset: Chemical structures of Rh6G and NB.

Before analyzing confined donor-acceptor colloidal suspensions we first should asses the photophysics of the encapsulated NB in the absence of donor. As previously observed for the Rh6G, the photophysical properties of the NB once enclosed into anionic NPs (Φ=0.47, τ=2.53 ns) did not varied significantly respect to that obtained in solution (Φ=0.43, τ=2.07 ns in ethanol) and without signs of aggregation. However, and in analogy to Rh6G, at high dye concentrations (above ~ $6 \cdot 10^{-3}$ M inside the particle) the fluorescence decay curve requires the use of biexponential functions. Indeed, NB is a cationic dye (as Rh6G) and its distribution inside the anionic NP should be ruled also by

the attractive electrostatic interactions at the interphase, explaining the biexponential behavior.

To get more knowledge about the distribution of the NB within the latex particles we characterized microsized particles by fluorescence confocal microscopy, as we made before for Rh6G. Again, it should be stressed that the surface charge is not exactly the same in NPs and MPs, so they cannot be directly compared. The time-resolved fluorescence analysis of a single MP (Figure 3.9) leads to biexponential decay curves described with a long lifetime (2.1-2.3 ns with 35-45% contribution), placed on the outskirts of the particle, and a short one (1.2-1.5 ns with 40-55%), situated in the core of it. This behavior reminds that observed for the Rh6G-doped MPs, where the presence of two distinguished lifetimes was assigned to the existence of different environments; the centre or core, and the periphery or interphase, with the likely contribution of the aforementioned Purcell's effect. Such similar trend is logic since both Rh6G and NB are cationic dyes. However, there are slight differences in the dye distribution within the MP.

The NB is characterized by a more homogeneous dye distribution within the MP suggesting a more favoured diffusion to the centre of the MP (Figure 3.9). In fact, the intensity profile shows the tendency of the dye to locate preferably in the core of the particle (Figure 3.9.d), whereas in the case of Rh6G the profile was ring-shaped (Figure 3.9). Such behaviour should be related to the higher hydrophobicity of the NB which places the molecules in the MP core preferentially.

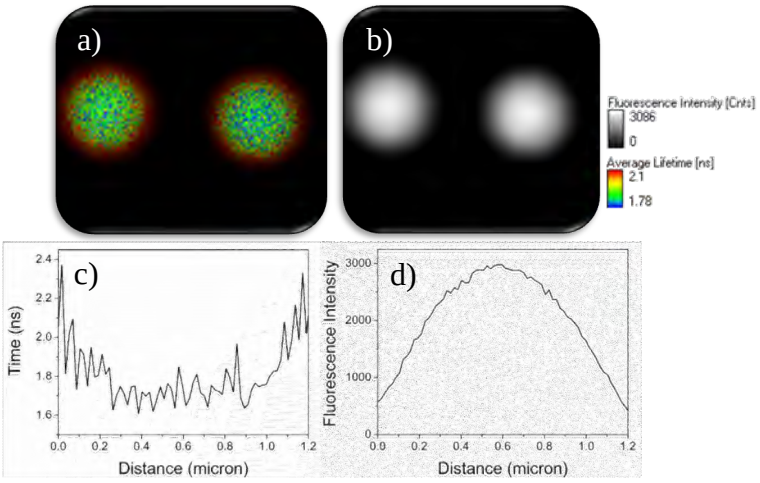

Figure 3.9. a) FLIM image. b) Fluorescence image intensity. c) Fluorescence lifetime profile and d) Fluorescence intensity profile along the MP doped with NB.

Once checked that the spectroscopic properties of each dye (Rh6G and NB) confined in NPs are kept and even improved with respect to liquid solution, we now consider NPs in which both dyes are encapsulated to promote FRET processes. Unfortunately, the NB is unstable in cationic NPs and the dye is oxidized to yield Nile Red. For that reason, only anionic NPs were considered as susceptible to provide efficient FRET processes.

The absorption spectrum confirms the presence of both dyes and that the identity of each chromophore is kept upon encapsulation into anionic NPs (Figure 3.10). The selective excitation of the Rh6G at a wavelength where the NB does not absorb led to its fluorescence signal followed by a strong and dominating red emission from the NB. Moreover, the excitation spectra monitored at long wavelengths where only the NB emits matches perfectly the absorption spectrum (Figure 3.10). This is due to a FRET process which occurs even in diluted colloidal suspensions (total amount of dye in solution around 2×10^{-6} M) due to the confinement effect which arranges donors and acceptors in close contact. This contrast with the very high optical densities (~10^{-3} M) required in liquid solutions to force short donor-acceptor distances (10-100Å) and consequently to detect FRET process. The herein developed system based on dye-doped latex NPs allows the achievement of high FRET efficiencies even in diluted suspensions and at concentrations (inside the NP) beyond the solubility limit in liquid solutions.

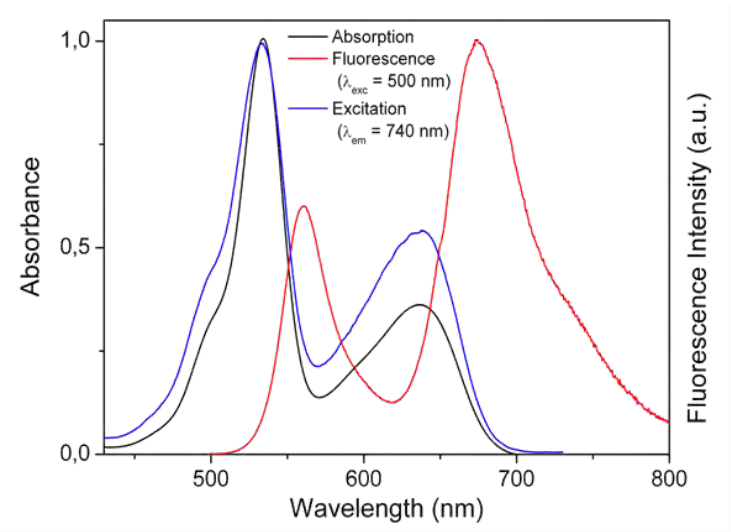

Figure 3.10. Normalized absorption (black), fluorescence (red) and excitation (blue) spectra of a colloidal suspension of anionic NPs with a Rh6G/NB proportion 1.5/1.

The fluorescence decay curve of the donor was also affected by such FRET process (Figure 3.11). Thus, lifetimes monitored at the Rh6G emission region become much faster by the presence of the acceptor NB with regard to NPs doped only with Rh6G. This is a consequence of the Rh6G excited state quenching caused by the energy transfer process towards the acceptor NB. Such reduction of the donor lifetime is an adequate tool to evaluate the energy transfer efficiency of the system. Therefore, the FRET efficiency was calculated from a comparison of the fluorescence decay curves of the donor in the absence ($I_f^D(t)$) and presence of the acceptor ($I_f^{D+A}(t)$) with the equation: [25]

$$\phi_{EET} = 1 - \frac{\int_0^\infty I_f{}^{D+A}(t)dt}{\int_0^\infty I_f{}^{D}(t)dt} \qquad \text{(eq. 3.1)}$$

reaching values as high as $\Phi_{FRET} = 0.88$ when [Rh6G]=5.5 mM and [NB]=11 mM.

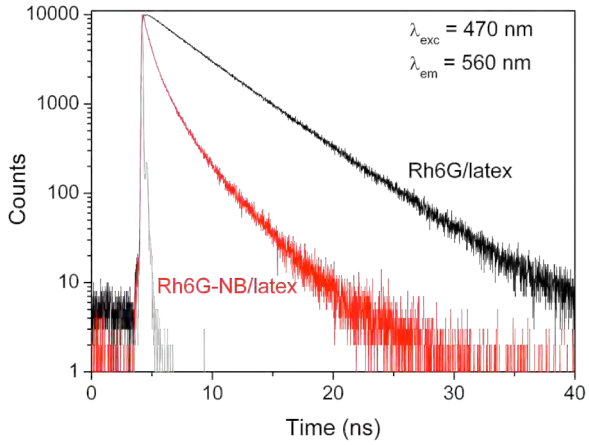

Figure 3.11. Fluorescence decay curve of Rh6G in latex in the absence (black) and presence (red) of NB, exciting at 470 nm and monitoring the emission at 560 nm.

The donor fluorescence decay curve is not only a practical tool to determine the FRET efficiency, but also can be nicely applied to know the dye distribution into the nanoparticle [26]. That is why a theoretical model has been adapted by Dr. L. Cerdán to predict the location of the dyes in confined anionic spherical NPs [27]. This model presages the donor decay curve considering different dye distributions and checks its suitability with the ones recorded experimentally. In such a way, firstly the NP was considered as a homogeneous polymer mixture (MMA/HEMA/GMA) where dyes were also uniformly distributed. However so as to reproduce the registered experimental

trends a core/shell morphology was needed to be assumed. In this regime a satisfactory agreement was achieved. That is, the results provided by the model point out a picture in which the dye distribution in anionic NPs is described as a core/thin shell morphology with a smooth transition from the core to the shell as follows: (i) the core consisting of a homogeneous polymer mixture of MMA/HEMA/GMA where both dyes are homogeneously solved; (ii) a thin shell formed of negatively charged surface (hairy layer), induced by the anionic surfactant (SDS) used in the synthesis, in which both cationic dyes are attracted.

Nevertheless, one should take into account that the non-radiative donor-acceptor energy transfer (hetero-FRET) is not the only viable process taking place in this system, and other competitive phenomena can happen at the same time (Figure 3.12). For instance, the non-radiative energy transfer process is also feasible between molecules of the same type (i.e., energy migration through donors)[28]. Such homo-FRET should reinforce the hetero-energy transfer because the excitation energy can reach acceptor traps which are far away from the first absorbing donor via successive energy migration hops. However, the emission of a Rh6G molecule can be absorbed by other molecule giving rise to an energy transfer process feasible via radiative mechanism (RET). Thus, photons emitted by a Rh6G molecule surviving the FRET process into a NP could also be absorbed via radiative process by a Rh6G molecule (homo-RET) or a NB acceptor (hetero-RET) in a distant nanoparticle (Figure 3.12).

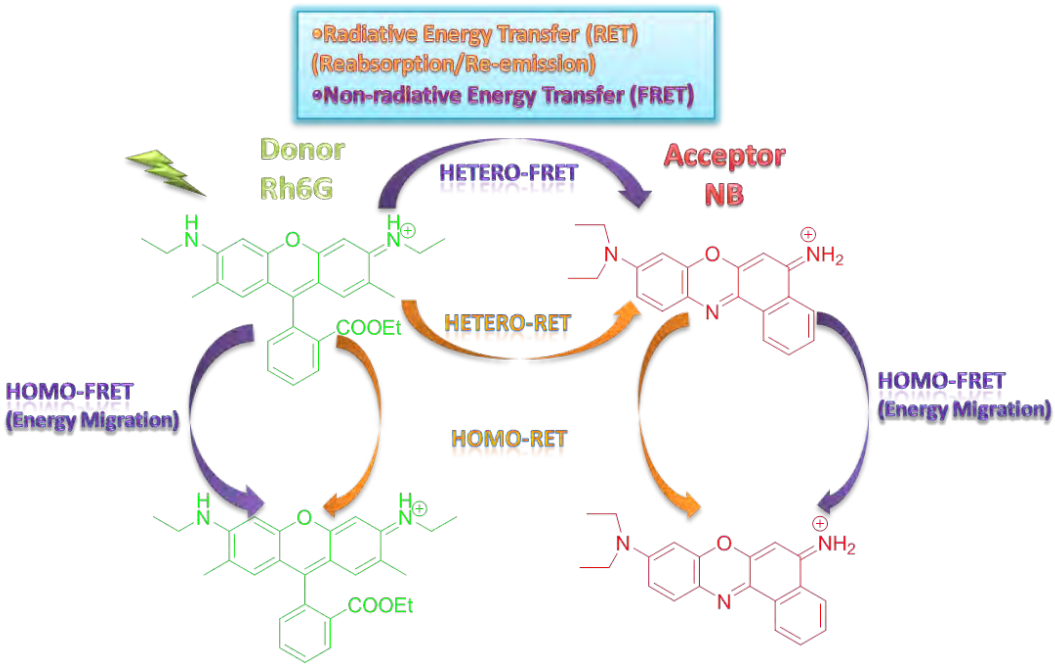

Figure 3.12. Sketch of energy transfer mechanisms present in the colloidal suspensions.

The influence of such radiative processes can be minimized in the recording of the photophysical propeties by a simple dilution, but are unavoidable and very significant in the laser performance due to the high optical densities required. In this conditions the probability of RET processes is largely enhanced and contributes noticeably to the whole energy transfer process. Indeed, the total energy transfer determined by the laser spectra was always higher than the one calculated in diluted colloidal suspensions by fluorescence decay curves. Such RET contribution, always present in high optical density media, can be minimized in diluted enough samples, using front-face configuration with short optical pathlength cuvettes or by mathematical correction methods to achieve the acceptor emission from the donor via pure FRET process (Figure 3.13) [29]. In fact, the recorded emission spectrum of the concentrated solution shown in Figure 3.13 (red line) is very similar to the more diluted one (black line) due to the shortening of the optical pathway (0.1 cm) and the front-face configuration.

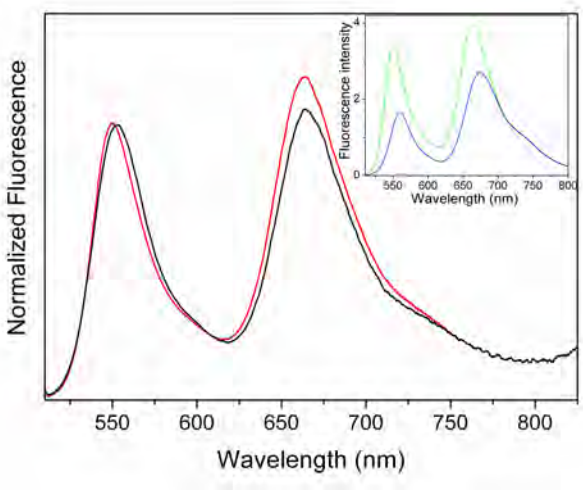

Figure 3.13. Effect of radiative energy transfer processes on fluorescence emission. Normalized fluorescence (to the donor emission) of the latex suspension of Rh6G and NB at low ($3{\cdot}10^{-6}$ M, black line) and high ($3{\cdot}10^{-4}$ M, red line) dye concentration, recorded with a 0.1 cm optical pathway cuvette and corrected from re-absorption/re-emission phenomena. Inset: fluorescence spectra of the concentrated sample before (blue line) and after (green line) mathematical correction.

3.2.1. Donor/Acceptor concentration effects in energy transfer

The balance between radiative and non-radiative pathways in the overall detected energy transfer prompted us to perform a detailed study of the dye concentration (donor/acceptor ratio and total amount of dye) effect on the FRET efficiency in anionic NPs of around 40 nm (diameter which ensures optimal

photophysics and laser action) doped with Rh6G and NB. In the following sections we pretend to know which factors alter the RET-FRET balance and how.

Acceptor concentration effects

We first analyzed a series of anionic NPs doped with a nearly fixed donor concentration ([Rh6G] ≈ 5.5 mM) and a variable acceptor concentration ([NB] = 0.5-11 mM). An increase in the amount of the acceptor led to an enhanced emission from the NB with respect to that of the donor upon excitation at the last one (Figure 3.14.b). At the same time, the emission deactivation of the donor was stronger (faster lifetimes) indicating a clear improvement in the FRET efficiency (Figure 3.14.a).

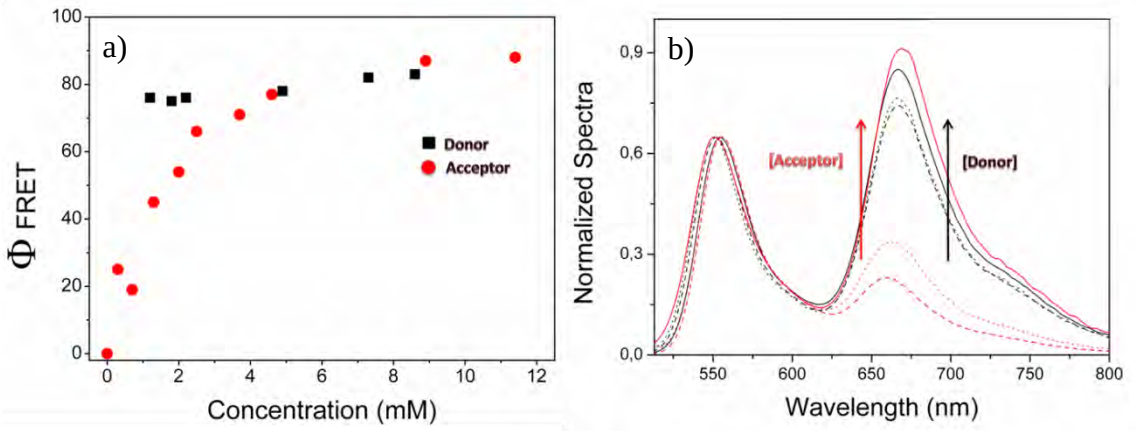

Figure 3.14. a) FRET efficiency as a function of donor (black square) and acceptor (red dot) concentration for a fixed acceptor and donor concentration (~ 5 mM), respectively. b) Evolution of the fluorescence spectra normalized to the donor emission under excitation at 470 nm as a function of acceptor (red) and donor (black) concentration.

Moreover, the time evolution of the acceptor emission (monitored at 670 nm upon donor excitation) is characterized by an initial growth –which confirms that the excited state of the NB is populated by means of FRET process from the Rh6G excited molecules– and a posterior decay related to a fluorescent deactivation which becomes faster as the NB concentration increases. The acceptor excited state dynamics also provide information about the FRET process. At low acceptor concentrations the growing component is slow (around 1.5 ns), reflecting the low probability of the energy transfer process and lengthening the NB lifetime (around 4.2 ns). At higher acceptor concentrations the transfer rate becomes faster as it is evident from the fast growing (around 0.15 ns) and the intrinsic lifetime of the NB is now detected (around 3 ns). Finally, at the highest acceptor concentrations the lifetime is slightly shortened. This last behaviour can be ascribed to the variation in the NB molecules distribution within

the NP when increasing its concentration. As it happens with Rh6G, the increase of the amount of NB molecules within the NP carry some of them to the periphery nearer to the water/latex interphase, an environment which favours lifetimes shortening, as explained previously.

The enhancement of the energy transfer probability when increasing the acceptor concentration (Figure 3.14 and Table 3.3) should be assigned to reduced average donor/acceptor distances and mainly to the more available energy traps ready to catch the excitation energy from the donors, as a result of the encapsulation of the dyes in the latex NPs.

Table 3.3. Average fluorescence lifetimes (recorded at the donor emission region upon donor excitation) and calculated energy transfer efficiencies in colloidal Rh6G-NB anionic NPs with variable donor and acceptor concentrations.

Donor concentration effects				**Acceptor concentration effects**			
[Rh6G] (mM)	**[NB] (mM)**	**‹τ›** **(ns)**	**Φ_{FRET} (%)**	**[Rh6G] (mM)**	**[NB] (mM)**	**‹τ›** **(ns)**	**Φ_{FRET} (%)**
1.2	5.9	1.10	76	5.5	1.3	2.50	45
2.2	4.3	1.10	76	5.6	2.2	2.18	54
4.9	4.6	1.04	78	4.9	4.6	1.04	78
8.6	4.9	0.78	82	5.4	8.9	0.53	88

With the aim of undoubtedly establishing the influence of the dye confinement in the FRET efficiency, we compared one of the above studied colloidal NP suspensions with a liquid solution of both dyes adjusting the dye concentration to that achieved in latex ([Rh6G]=5.5 mM, [NB]=1 mM) (Figure 3.15). The estimated FRET capability of the dye mixture doped in latex NPs was 4 times higher than the same donor/acceptor concentration in solution (Φ_{FRET} =10% in ethanolic solution vs 45% in NP environment) (Figure 3.15), even though Förster radius was higher in solution (R_0=55 Å in ethanol *vs* R_0=47 Å into the NP). This unusual behaviour could be due to the re-absorption and re-emission effects present at such high concentrations in solution, which directly affect the donor lifetime measurements (lengthening it from 4.05 ns in diluted solution to 6.08 ns in concentrated solutions) and hinder the correct estimation of the FRET

efficiency. These results prompted us to prepare a solution reducing the Rh6G concentration to 0.5 mM with the aim of decreasing the re-absorption/re-emission effects, while the concentration of NB was kept as above. As a result, the FRET efficiency increased up to 57%, much higher than that of the more concentrated solution and even than in the NP. This result fits better with the aforementioned Förster radius, which inferred a higher FRET efficiency in solution and highlight the key role which play RET processes in energy transfer for concentrated systems. So as to evaluate the results obtained by the encapsulation of Rh6G and NB dyes into latex NPs in a proper context, it should be considered that NPs allowed the confinement of high concentrations of Rh6G (up to 11 mM) without signs of aggregation and solubility problems, whereas the highest NB concentration in ethanolic solution was much lower (1 mM).

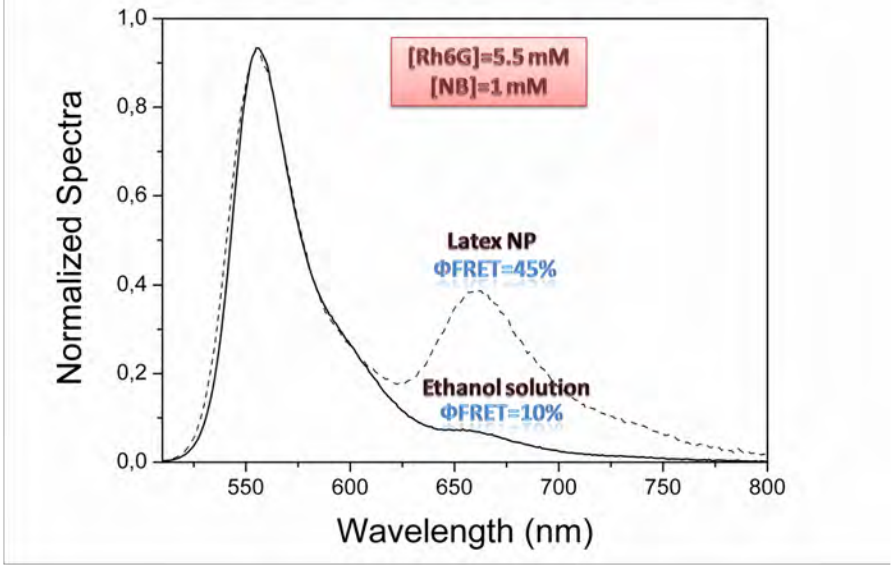

Figure 3.15. Normalized fluorescence spectra under donor excitation at 500 nm of a mixture of [Rh6G]=5.5 mM and [NB]= 1 mM in ethanol solution (solid) and within the NP (dashed).

Donor concentration effects

As showed above the acceptor concentration has a deep impact in the FRET efficiency. However, the donor concentration is also a parameter to be considered carefully. To analyze the influence of the donor concentration in the FRET efficiency we selected samples with a fixed acceptor concentration ([NB]~5.5 mM) and a variable donor one ([Rh6G]=1-9 mM).

For donor concentrations bellow ≤ 2 mM the FRET efficiency was nearly constant with a value around 76%. Beyond this point, the FRET efficiency resulted

slightly improved, reaching values up to 84% (Table 3.3 and Figure 3.14). Such increase appears to be somehow surprising because we have already checked a clear reduction of the FRET efficiency in highly concentrated samples in solution. The small increase of the energy-transfer efficiencies detected at higher donor concentrations in NPs should be ascribed to energy migration (homo-FRET) among neighboring donor molecules which allows the access to distant acceptor molecules. The energy migration is feasible due to the broad spectral overlap between the emission and absorption bands of the Rh6G and a Förster radius (R_0 = 47 Å) as high to that of the hetero-FRET among Rh6G and NB (R_0 = 47 Å). As consequence, at high donor concentrations, RET processes will gain importance and would influence the overall FRET efficiency.

Total dye amount effects

From the results herein obtained it is concluded that there are several pathways contributing to the whole energy transfer process especially in highly concentrated samples. To clarify this issue we evaluate a series of samples with a fixed donor-acceptor molar ratio (~0.9) while increasing the total dye concentration in the NP (from 3-11 mM) (Figure 3.16).

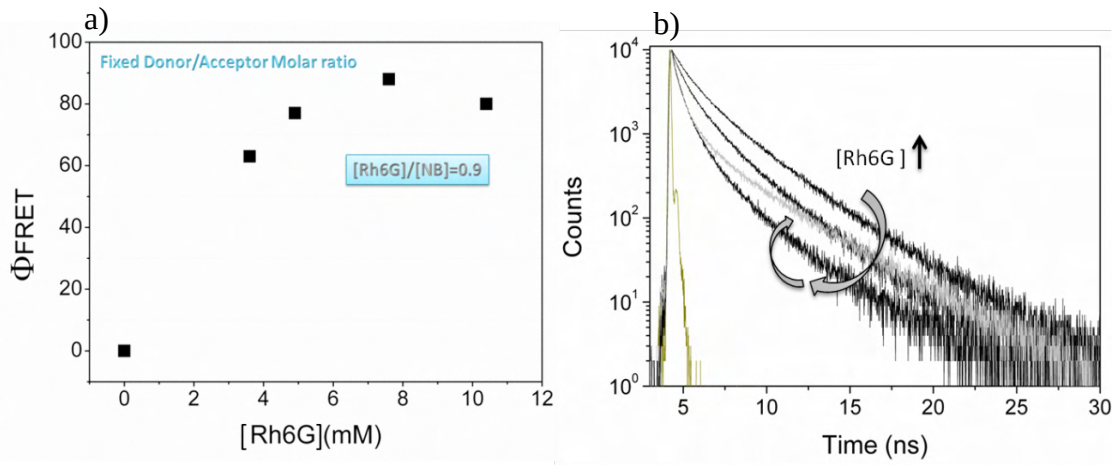

Figure 3.16. a) FRET efficiency as a function of dye concentration for a fixed donor/acceptor ratio. b) Fluorescence decay curves after 470 nm excitation and recording the emission at 560 nm, where the donor emits. As the total amount of dye content increases the decay rate becomes faster (black) until a certain concentration, beyond this point the decay rate becomes slower (grey) indicating a decrease of the energy transfer efficiency.

As the amount of dye is increased the FRET process becomes more efficient, reaching values as high as 88% for dye concentrations around 8 mM (Figure 3.16.a), due to the reduction of donor-acceptor distances which in turn increases the probability for hetero-FRET processes also assisted by the homo-FRET. Nevertheless, beyond this dye concentration the FRET efficiency reaches a plateau and even decreases (Figure

3.16.a) probably due to an intensification of other non-radiative bimolecular competing processes -such as collisional deactivation, aggregation, static quenching [25,30]- which compete with the energy transfer processes. Summing up, the donor and acceptor concentrations determine the contribution of the different pathways in the energy transfer and hence rule the FRET efficiency. Overall, the FRET efficiency is greatly ameliorated with the acceptor concentration due to the more available energy traps and a reduction in the average donor/acceptor distances. Furthermore, the increase of the donor amount also leads to an improvement of the energy transfer capability mostly via energy migration between donors, which allow reaching acceptor molecules located far away. Nonetheless, an increase of the total dye concentration beyond a given optimal value worsens the FRET efficiency. In any case, the probability of RET processes increases with the concentration of dyes. It is noteworthy to emphasize the possibility of studying FRET dynamics in NPs at concentrations beyond the solubility limit in liquid solutions, reaching FRET efficiencies much higher than those obtained in solution.

Donor and acceptor concentration effects on FRET and laser properties of latex NPs doped with mixtures of Rh6G and NB are further analyzed in the enclosed article published in the *Journal of Physical Chemistry C*.

THE JOURNAL OF PHYSICAL CHEMISTRY C

Article

pubs.acs.org/JPCC

Förster Resonance Energy Transfer and Laser Efficiency in Colloidal Suspensions of Dye-Doped Nanoparticles: Concentration Effects

Leire Gartzia-Rivero,[†] Luis Cerdán,*[,‡] Jorge Bañuelos,[†] Eduardo Enciso,[§] Íñigo López Arbeloa,[†] Ángel Costela,[‡] and Inmaculada García-Moreno[‡]

[†]Departamento de Química Física, Universidad del País Vasco-EHU, Aptdo. 644, 48080 Bilbao, Spain

[‡]Departamento de Sistemas de Baja Dimensionalidad, Superficies y Materia Condensada, Instituto de Química-Física "Rocasolano" (CSIC), Serrano 119, 28006 Madrid, Spain

[§]Departamento de Química Física I, Facultad de Ciencias Químicas, Universidad Complutense de Madrid, Ciudad Universitaria, 28040 Madrid, Spain

Supporting Information

ABSTRACT: The donor and acceptor concentration effects on Förster resonance energy transfer (FRET) and laser properties of polymer nanoparticles (NPs) highly doped with two dyes are comprehensively analyzed. Rhodamine 6G (Rh6G, donor) and Nile Blue (NB, acceptor) are incorporated into anionic methacrylic NPs ~40 nm in size, in concentrations [Rh6G] = 1−9 mM and [NB] = 0.5−11 mM. The FRET efficiency is mostly influenced by the acceptor concentration due to the presence of more available energy traps and a reduction in the average donor/acceptor distances. We show that the presence of homo-FRET among donors may give rise to an enhancement on the net hetero-FRET efficiency mainly when the concentration of donors exceeds that of the acceptors. When the concentration of both dyes is raised beyond a given value, the FRET efficiency is reduced due to the influence of competing quenching processes. Carefully selected mixtures of Rh6G/NB allow achieving FRET efficiencies as high as 88% and efficient laser emission in which the excitation/pumping light has been fully transferred from Rh6G (~575 nm) to NB (~700 nm). Finally, it is shown that, although a higher FRET efficiency does not guarantee higher acceptor laser efficiencies, both are mostly affected by the acceptor concentration and the total amount of dye molecules inside the NPs. This study acquires special relevance since the use of NPs not only allows achieving FRET efficiencies much higher than those attainable in liquid solution (88% vs 57%) but also opens the door to the study of FRET dynamics at concentrations beyond the solubility limit in liquid solutions and without the undesirable effects of reabsorption/re-emission processes (at least for the Rh6G/NB pair).

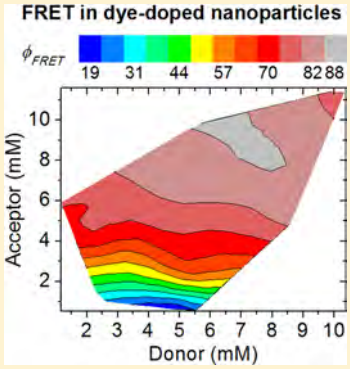

1. INTRODUCTION

The incorporation of fluorophores (either organic dyes,[1−6] quantum dots,[7−13] conjugated polymers,[14−20] or lanthanide complexes[21−26]) into nano- and micrometer-sized organic and inorganic particles has become a strategy of increasing importance for optoelectronic, bioimaging, and sensing applications.[27−32] For bioimaging applications this procedure serves to circumvent the often undesired sensitivity and interactivity of most chromophores to their local environment and, at the same time, allow increasing their fluorescence quantum yields and photostabilities.[33−38] In this regard, polymeric nanoparticles (NPs) offer a unique access as scaffold to develop smart multichromophoric systems allowing collective optical processes such as Förster resonance energy transfer (FRET), with important and extensive applications as wavelength converters,[39,40] self-assembled light-harvesting networks,[41] sensing tools,[42−44] or photoswitchable devices.[45]

It is common knowledge that the FRET efficiency is mostly influenced by the acceptor concentration,[46] provided that both donors and acceptors are homogeneously distributed. This is true at very low donor concentrations, where particular donor/donor interactions are negligible. However, at high donor concentrations, excitation energy migration among donors may be effective,[47] whereupon it may have a relevant influence on the overall FRET efficiency. For this reason, most of the existing theoretical work deals with very low donor concentrations to overcome this influence.[48−50] Nevertheless, if FRET is used to obtain laser emission at the acceptor wavelength, then very high concentrations of both donor and acceptor are needed to achieve sufficient population inversion and gain. In this regard, we reported recently FRET-assisted laser emission in colloidal suspensions of dye-doped NPs,[51] showing that the confinement of laser dyes (Rhodamine 6G as donor and Nile Blue as acceptor) undergoing energy transfer into subwavelength latex NPs enhanced significantly the laser efficiency and photostability of red-emitting laser dyes under

Received: April 1, 2014
Revised: May 8, 2014
Published: May 27, 2014

Table 1. Structural and Photophysical Properties of Samples under Study Doped with Only One Dye

sample	NP[a] wt %	d[b] (nm)	[Rh6G][c] (mM)	[NB][c] (mM)	λ_{em}[d] (nm)	$\tau_i[A_i]$[e] (ns)	$\langle\tau\rangle$[f] (ns)
D	6.1	39	6.3	-	560	3.11 [0.21]; 4.70 [0.79]	4.37
A	6.5	38	-	6.2	670	1.43 [0.17]; 2.65 [0.83]	2.44

[a]Weight proportion of nanoparticles (NPs) in the suspension. [b]NP diameter. [c]NP dye concentration. [d]Wavelength used for fluorescence lifetime (τ_i) measurement. [e]Fluorescence lifetimes (τ_i) and weights (A_i, $\Sigma A_i = 1$) obtained from a multiexponential fit of the decay curve. [f]Amplitude average lifetime.

532 nm pumping. The same line of reasoning applies when FRET is to be used in bioimaging applications, where a bright signal at the desired wavelength is imperative.[52−54]

At the present time, there remains a major need for a comprehensive characterization of these two-dye-doped NPs exploiting FRET processes, as well as a better understanding of the relationship between the composition of the NPs and their optical behavior as fluorophores and laser active media. To this aim, herein we carry out a systematic study on the FRET and laser properties of colloidal suspensions of latex NPs ∼40 nm in size doped with high concentrations of dyes. We study their dependencies on the donor and acceptor dye concentrations to determine the conditions that optimize the efficiency of the emission process and result in improved lasing performance. This study acquires special relevance since the NPs allow studying the efficiency and dynamics of the FRET process at dye concentrations up to 10 times higher than those that can be achieved in the liquid phase, without the common problems of dye solubility and aggregation.

2. EXPERIMENTAL SECTION

Materials. The laser dyes Rh6G from Fluka and NB from Exciton (>99% purity and laser grade) were used as received; their purity was confirmed by spectroscopic and chromatographic methods. Methyl methacrylate (MMA) (Aldrich, 99%) was purified with a 0.1 M sodium hydroxide solution to remove inhibitor. 2-Hydroxyethyl methacrylate (HEMA) (Aldrich, 97%), glycidyl methacrylate (GMA) (Fluka, 97%), potassium persulfate (KPS) (Sigma, 99%), and sodium dodecyl sulfate (SDS) (Sigma 99%) were used without further purification. Deionized water was obtained from a Direct QTM 5 Millipore.

Synthesis of Nanoparticles. The particles were prepared from a batch emulsion polymerization according the procedure previously reported.[37] Different amounts of Rh6G and NB dyes were dissolved in a monomer mixture of MMA:HEMA:GMA with weight ratios of 70:20:10. SDS was added into the aqueous polymerization medium as a surfactant stabilizer. After degassing, the reactor was heated to 65 °C and the polymerization started by adding a KPS aqueous solution and performed during 3 h. The particle sizes and size distribution were determined by quasielastic laser light scattering with a Brookhaven Zetasizer (Brookhaven Instruments Ltd.) at 25 °C. About 0.1 mL of each suspension was diluted with 2.9 mL of water immediately after polymerization. The solid content of the suspension was determined by drying 2.5 mL of suspension in an oven at 45 °C up to constant weight.

Photophysical Properties. The FRET processes were characterized in diluted samples (dye concentration around 2 μM and optical pathway 1 cm) of the original aqueous NP suspensions with the aim to avoid at maximum reabsorption/re-emission effects that would compromise the interpretation of the FRET properties.[51] Concentrated dye solutions were registered with cuvettes of 0.01 mm. UV−vis absorption and fluorescence spectra were recorded on a Cary 4E spectrophotometer and on a SPEX Fluorolog 3−22 spectrofluorimeter, respectively, using front-face configuration in the last technique for concentrated samples. Radiative decay curves were registered by the time-correlated single-photon technique (Edinburgh Instruments, model FL920), provided with a Multi Channel Plate (Hamamatsu C4878). Fluorescence decay rates were monitored at the peak emission wavelengths corresponding to Rh6G (donor) and NB (acceptor) after excitation at 470 nm with a diode laser (PicoQuant, model LDH470). For the sample without a donor, a LED exciting at 600 nm was used. The fluorescence lifetime (τ) was obtained from the slope after the deconvolution of the instrumental response signal from the recorded decay curves by means of an iterative method. The goodness of the multiexponential fit ($I_F(t) = A_0 - \Sigma A_i \exp(-t/\tau_i)$) was controlled by statistical parameters (χ^2, Durbin−Watson and the analysis of the residuals). The decay curves monitored at the acceptor region upon excitation of the donor were more accurately described as a growth (acceptor population through FRET, $A_i < 0$) and a decay (fluorescence deactivation, $A_i > 0$), this being deconvoluted in multiexponentials. Molecular dipole moments were calculated using the Gaussian 09 software from the optimized ground state geometries by means of the B3LYP hybrid method (density functional theory, DFT) and the double-valence basis set (6-31g) with a polarization function.

Lasing Properties. Original suspensions, without dilution, were contained in 1 cm optical path quartz cells carefully sealed to avoid solvent evaporation. The samples were transversely pumped at 532 nm with 5.5 mJ, 6 ns fwhm pulses from a frequency-doubled Q-switched Nd:YAG laser (Monocrom STR-2+) at 10 Hz repetition rate. The exciting pulses were line-focused onto the front face of the cell, providing pump fluences on the active medium of 180 J/cm^2. The oscillation cavity (2 cm length) consisted of a 90% reflectivity aluminum mirror, with the end lateral face of the cell as the output coupler. The laser emission was monitored perpendicular to the exciting beam, collected by an optical fiber, imaged onto the input slit of a monochromator (Acton Research Corp.), and detected with a charge-coupled device (CCD) (SpectruMM:GS128B). The estimated error of the energy measurements was 10%. Details of the experimental setup can be found elsewhere.[51]

3. RESULTS AND DISCUSSION

To study the influence of the relative donor/acceptor proportions on the photophysics of the FRET process and on the laser performance, a thorough evaluation of both aspects was performed as a function of both the donor and acceptor concentrations. The diameter of the NPs and the amount of latex in the suspension were kept as similar as possible to avoid the FRET efficiency dependence on NP size and to allow a proper comparison.

3.1. Photophysical Properties. We began by evaluating the emission properties of NPs incorporating only Rh6G or NB

dx.doi.org/10.1021/jp503218z | J. Phys. Chem. C 2014, 118, 13107−13117

(samples D and A, respectively, Table 1). The absorption and fluorescence spectra of both samples are very similar to those of dilute solutions of the same dyes (Figure 1), indicating the absence of dye aggregation, despite the high dye loadings inside the NP (~6 × 10^{-3} M). Interestingly, the analysis of the fluorescence decay curves of both dyes requires the use of biexponential functions to be properly fitted (Table 1).

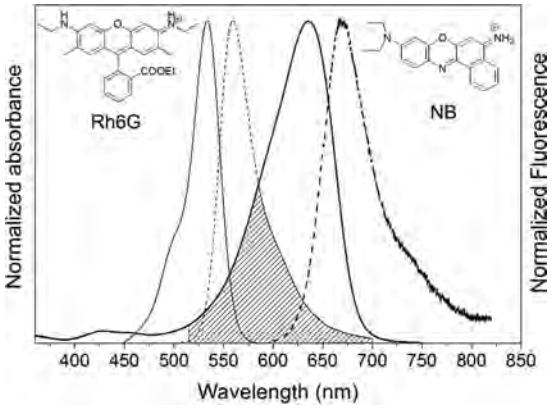

Figure 1. Normalized absorption (solid lines) and fluorescence (dashed lines) spectra of colloidal suspensions of NPs doped with Rh6G alone (thin lines) and NB alone (thick lines). The striped region accounts for the spectral overlap between the Rh6G emission and the NB absorption. Inset: Chemical structures of Rh6G and NB.

The two contributions to the lifetime might be assigned to two different environments within the latex NP:[51] a core consisting of a homogeneous terpolymer of MMA/HEMA/GMA, in which the dye is homogeneously solved, and a thin shell formed by the so-called NP "hairy layer" (polymer/surfactant/water interface), in which the dye would be adsorbed with a concentration differing that of the core. Both cationic dyes tend to locate at the center of the NP due to their hydrophobicity (DFT-calculated molecular dipole moments are μ_{NB} = 3.97 D and μ_{Rh6G} = 4.45 D). However, as we used an anionic surfactant, this "hairy layer" could have a certain negative charge distribution, which would electrostatically attract cationic dyes such as Rh6G and NB. Taking into account that the fluorescence lifetimes are shorter in water solution,[55−58] the core of the NP could contribute to the longest and main component of the lifetime, whereas the shortest and residual component could be ascribed to the hairy layer, which is swelled with water.

Once the photophysical properties of both donor and acceptor alone were evaluated to serve as a reference, we proceeded to study the photophysics of NPs containing mixtures of dyes undergoing FRET. The efficiency of the FRET process in the latex NPs can be obtained from the comparison of the fluorescence decay curves of the donor in the absence ($I_F^D(t)$) and presence ($I_F^{D+A}(t)$) of acceptors as[46]

$$\phi_{FRET} = 100\%\left(1 - \frac{\int I_F^{D+A}(t)\,dt}{\int I_F^{D}(t)\,dt}\right) \quad (1)$$

The fluorescence decay curve of a donor (Rh6G) in the presence of acceptors (NB) confined in systems with spherical symmetry undergoing FRET follows a complex dynamics which depends on the donor and acceptor radial distributions inside the NP,[48] but it can be phenomenologically treated and fitted as a multiexponential decay $I_F(t) = A_0 - \Sigma A_i \exp(-t/\tau_i)$. Within this approximation, ϕ_{FRET} can be estimated according to the equation

$$\phi_{FRET} = 100\%\left(1 - \frac{\langle\tau\rangle}{\langle\tau_0\rangle}\right) \quad (2)$$

where $\langle\tau_0\rangle$ and $\langle\tau\rangle$ are the amplitude average lifetimes of the donor alone and donor subjected to FRET, respectively, being defined as

Table 2. Structural and Photophysical Properties of Samples under Study with a Fixed Donor Concentration ([Rh6G] ~ 5.5 mM)

sample	NP[a] wt %	d^b (nm)	[Rh6G][c] (mM)	[NB][c] (mM)	$\lambda_{em}{}^d$ (nm)	$\tau_i[A_i]^e$ (ns)	$\langle\tau\rangle^f$ (ns)	$\phi_{FRET}{}^g$ (%)
AC1	6.9	43	5.5	0.3	560	2.61 [0.43]; 4.22 [0.57]	3.53	25
					670	0.27 [<0]; 1.58 [<0]; 4.25 [>0]	-	
AC2	7.3	42	5.2	0.7	560	3.25 [0.61]; 4.62 [0.39]	3.78	19
					670	0.28 [<0]; 1.66 [<0]; 4.37 [>0]	-	
AC3	6.9	45.9	5.5	1.3	560	1.55 [0.52]; 3.52 [0.48]	2.50	45
					670	0.24 [<0]; 1.26 [<0]; 3.71 [>0]	-	
AC4	7.1	44	5.6	2	560	1.29 [0.54]; 3.22 [0.46]	2.18	54
					670	0.73 [<0]; 1.92 [<0]; 3.50 [>0]	-	
AC5	6.9	48	5.2	2.5	560	0.45 [0.34]; 1.54 [0.45]; 3.51 [0.21]	1.58	66
					670	0.63 [<0]; 3.22 [>0]	-	
AC6	6.9	44	5.6	3.7	560	0.41 [0.35]; 1.34 [0.46]; 3.13 [0.19]	1.33	71
					670	0.60 [<0]; 3.06 [>0]	-	
AC7	6.0	34	4.9	4.6	560	0.31 [0.44]; 1.17 [0.42]; 2.95 [0.14]	1.04	77
					670	0.38 [<0]; 2.82 [>0]	-	
AC8	6.8	42	5.4	8.9	560	0.20 [0.63]; 0.86 [0.31]; 3.23 [0.06]	0.59	87
					670	0.16 [<0]; 2.13 [>0]	-	
AC9	5.3	41	5.5	11.4	560	0.16 [0.62]; 0.79 [0.31]; 2.73 [0.07]	0.53	88
					670	0.13 [<0]; 1.94 [>0]	-	

[a]Weight proportion of nanoparticles (NPs) in the suspension. [b]NP diameter. [c]NP dye concentration. [d]Wavelength used for fluorescence lifetime (τ_i) measurement. [e]Fluorescence lifetimes (τ_i) and weights (A_i, ΣA_i = 1) obtained from multiexponential fit of decay curve. [f]Amplitude average lifetime. [g]FRET quantum yield.

dx.doi.org/10.1021/jp503218z | J. Phys. Chem. C 2014, 118, 13107−13117

$$\langle \tau \rangle = \sum A_i \tau_i \tag{3}$$

where the coefficients A_i are the weight of each contribution to the lifetime in the multiexponential.

The FRET rate from an electronically excited donor (D*) to an acceptor (A) separated by a distance r is given by[46]

$$w(r) = \frac{1}{\tau_D}\left(\frac{R_0}{r}\right)^6 \tag{4}$$

where τ_D is the donor lifetime in the absence of acceptors and R_0 is the most characteristic FRET parameter, known as Förster radius, which is defined as the donor−acceptor separation for which the donor emits and transfers (to the acceptor) its energy with the same probability. R_0 depends on the photophysical properties of the donor and acceptor and is given by[46]

$$R_0^{\,6} = \frac{9000(\ln 10)\kappa^2\phi_f}{128\pi^5 N_A n^4}\int_0^\infty F_D(\lambda)\varepsilon_A(\lambda)\lambda^4 d\lambda \tag{5}$$

In eq 5 the integral accounts for the spectral overlap (striped region in Figure 1) of the normalized donor fluorescence spectrum $F_D(\lambda)$, with the absorption spectrum of the acceptor $\varepsilon_A(\lambda)$ ($M^{-1}cm^{-1}$). ϕ_f and n are the fluorescence quantum yield of the donor in the absence of acceptors and the refractive index of the host medium, respectively, and κ^2 is the orientation factor that accounts for the relative orientation of donor and acceptor transition dipole moments in the host medium. In the photophysical characterization of the latex NPs, $F_D(\lambda)$, $\varepsilon_A(\lambda)$, and $\phi_f = 0.70$ have been obtained. Taking into account that the mixture MMA/HEMA/GMA has a refractive index $n \sim 1.5$ and assuming $\kappa^2 \sim 0.476$ (static isotropic average), one obtains a Förster radius $R_0 = 47$ Å.

3.1.1. Acceptor Concentration Effects (AC Samples). It is common knowledge that the FRET efficiency is mostly influenced by the acceptor concentration,[46,48,49] provided that both donors and acceptors are homogeneously distributed. Hence, we first assessed the photophysical properties of NPs with a nearly fixed donor concentration ([Rh6G] ∼ 5.5 mM) and a variable acceptor one ([NB] = 0.5−11 mM, samples AC1 to AC9, Table 2).

Figure 2 shows the normalized (to the donor emission) fluorescence spectra of samples with low (sample AC1), medium (sample AC4), and high (sample AC9) loadings of NB (Figure 2a), as well as their fluorescence decay curves monitored at the donor (Figure 2b) and acceptor (Figure 2c) fluorescence peak wavelengths. Data obtained with sample D, incorporating just Rh6G and no acceptor, are also included in Figures 2a and 2b for comparison.

As can be seen in Figure 2a, as the amount of acceptor in the NPs increases, the fluorescence intensity corresponding to the NB increases with respect to that of the donor, indicating an improvement in the FRET efficiency. This is otherwise evident, as the higher the acceptor concentration is, the shorter the donor−acceptor mutual distances are and the stronger the transfer rate becomes (eq 4). Further evidence of the improvement in the FRET efficiency is the increase in the Rh6G emission deactivation rate (monitored at 560 nm) as the acceptor concentration is raised (Figure 2b and Table 2). As explained before, the fluorescence decay traces in Figure 2b follow a complex dynamic that, in some cases, requires a triexponential fit (Table 2). In this sense, the average lifetime of Rh6G goes from 4.37 ns in the absence of NB (sample D),

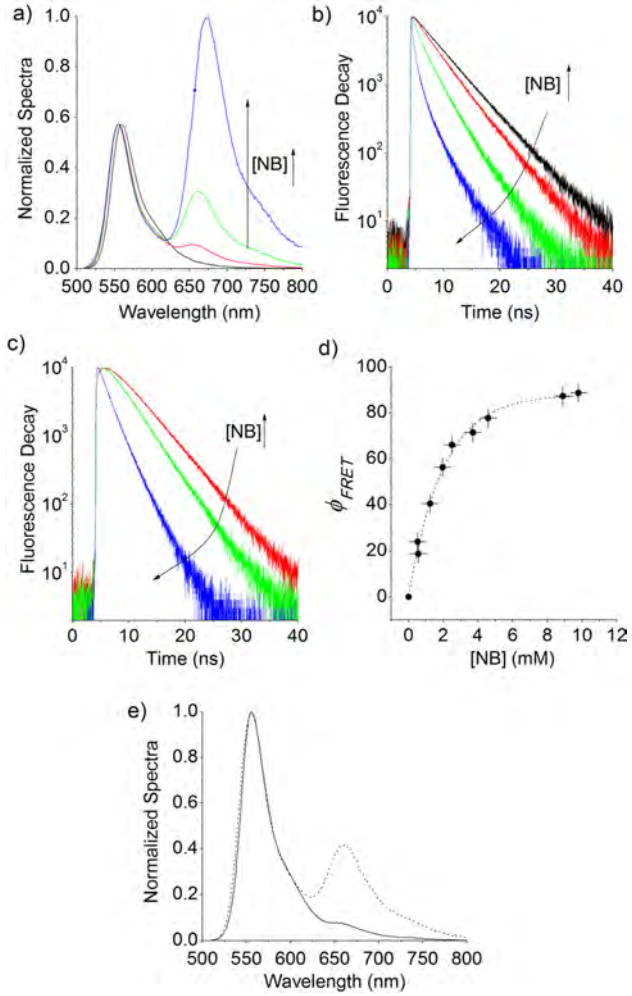

Figure 2. (a) Normalized to the donor emission fluorescence spectra under excitation at 470 nm of samples D, AC1, AC4, and AC9. (b) Fluorescence decay curves of Rh6G in samples D, AC1, AC4, and AC9. (c) Fluorescence decay curves of NB in samples AC1, AC4, and AC9. (d) FRET efficiency as a function of acceptor concentration for a fixed donor concentration of 5 mM. Error bars in (d) account for the experimental inaccuracies in the dye concentration determination. (e) Normalized fluorescence spectra under excitation at 500 nm of ethanol solution [Rh6G] = 5.5 mM and [NB] = 1 mM (solid line) and sample AC3 (dashed line). Sample-to-Color code for (a)−(c): D (black), AC1 (red), AC4 (green), and AC9 (blue).

down to 3.53, 2.18, and 0.53 ns in the samples AC1, AC4, and AC9, respectively (Table 2). These lifetimes, according to eq 2, correspond to FRET efficiencies of 25%, 54%, and 88%, respectively (Figure 2d). Such high values of ϕ_{FRET} can be expected for donor/acceptor pairs with the good spectral overlap shown by Rh6G and NB (Figure 1), provided high dye concentrations can be achieved without causing any problem regarding solubility, aggregation, or quenching.

On the other hand, the time evolution of the acceptor emission (monitored at 670 nm upon donor excitation) is characterized by an initial growth (Figure 2c and Table 2, $A_i < 0$)—which confirms that the NB excited state is populated by means of FRET from the excited Rh6G molecules—and an ulterior decay (Figure 2c and Table 2, $A_i > 0$) corresponding to a fluorescent deactivation. At low acceptor concentrations (0.5 mM, sample AC1) the FRET probability is low, and thus the acceptors are rather slowly populated (∼2 ns rise time, Figure

dx.doi.org/10.1021/jp503218z | J. Phys. Chem. C 2014, 118, 13107−13117

Table 3. Structural and Photophysical Properties of Samples under Study with a Fixed Acceptor Concentration ([NB] ∼ 5 mM)[a]

sample	NP wt %	d (nm)	[Rh6G] (mM)	[NB] (mM)	λ_{em} (nm)	$\tau_i[A_i]$ (ns)	$\langle\tau\rangle$ (ns)	ϕ_{FRET} (%)
DC1	7.3	41	1.2	5.9	560	0.28 [0.45]; 1.20 [0.39]; 3.18 [0.16]	1.10	76
					670	0.41 [<0]; 2.74 [>0]	-	
DC2	7.0	42	1.8	5.5	560	0.28 [0.44]; 1.22 [0.39]; 3.23 [0.17]	1.15	75
					670	0.41 [<0]; 2.78 [>0]	-	
DC3	7.2	43	2.2	4.3	560	0.30 [0.42]; 1.19 [0.43]; 3.10 [0.15]	1.10	76
					670	0.48 [<0]; 2.77 [>0]	-	
DC4 (AC7)	6.0	34	4.9	4.6	560	0.31 [0.44]; 1.17 [0.42]; 2.95 [0.14]	1.04	78
					670	0.38 [<0]; 2.82 [>0]	-	
DC5	6.7	40	7.3	5.6	560	0.29 [0.51]; 1.05 [0.39]; 2.88 [0.10]	0.85	82
					670	0.35 [<0]; 2.62 [>0]	-	
DC6	6.6	44	8.6	4.9	560	0.28 [0.53]; 1.02 [0.39]; 2.86 [0.8]	0.78	83
					670	0.33 [<0]; 2.62 [>0]	-	

[a]See Table 2 for definition of headers.

2c and Table 2). On the contrary, at very high acceptor concentrations (11 mM, sample AC9) the transfer probability is very high and the acceptor excited state is populated in just 100 ps (0.13 ns rise time, Figure 2c and Table 2). After the initial growth, the acceptor emission decays at a given rate, decreasing as the NB concentration increases. This decay rate, which ranges from 4.2 ns (sample AC1, Table 2) to 1.93 ns (sample AC9, Table 2), is not the NB intrinsic lifetime (2.4 ns at 6 mM, sample A, Table 1) but a combination of this with the population rate from the excited donors, as well as other photophysical effects. At low acceptor concentrations the transfer rate is slow, and it is extended in time (above 10 ns), whereupon the population of the acceptor excited states overlaps in time with—and counterbalances—the natural decay rate. This combination results in a lower effective deactivation rate (longer lifetime). As the acceptor concentration is increased, the transfer rate becomes very fast and stops overlapping with the natural decay rate. Hence, the observed decay rate approaches the acceptor intrinsic decay rate. The samples with the highest acceptor concentrations show lifetimes slightly shorter than that of sample A. This behavior can be understood as due to the changing distribution of the NB molecules inside the NPs as their concentration increases. As the amount of molecules encapsulated within the latex NP increases, some NB molecules are forced to the periphery of the NP, closer to the water/latex interphase (hairy layer), favoring a shorter lifetime, as explained before. In addition, the reduction in the lifetime that dyes suffer at high concentrations via the quenching processes[46] could be somewhat contributing to the observed lifetime shortening.

Figure 2d shows the FRET efficiency as a function of the acceptor concentration. The data shown in this figure follow an exponential behavior of the type $\phi_{FRET} \propto 1 - \exp(-[NB]/[NB]_C)$, with a fast rise in efficiency up to a given acceptor concentration ($[NB]_C$) and a saturation behavior above this concentration. The fit of the previous expression to the data in Figure 2d renders a critical acceptor concentration $[NB]_C \sim 2$ mM. At this concentration, the donors are located from their closest acceptors at a mean distance[59]

$$d_{mean} = \frac{0.554}{\sqrt[3]{C_{NB}}} \quad (6)$$

where C_{NB} is the volume density of acceptors in nm^{-3}. For $[NB]_C \sim 2$ mM, eq 6 renders $d_{mean} \sim 5.2$ nm, which is, interestingly, very similar to the Förster radius calculated before (eq 5, $R_0 = 47$ Å). This makes sense since R_0 is defined as the donor−acceptor separation for which the donor emits and transfers (to the acceptor) its energy with the same probability, i.e., the distance for which $\phi_{FRET} = 50\%$.

The true extent of the importance of the dye confinement in the effectiveness of the FRET process is revealed when comparing the results herein registered to those measured for the Rh6G/NB pair system in liquid solution. Unexpectedly, the highest NB concentration achieved in ethanol was around 1 mM, much lower than that allowed by their confinement in NPs (11 mM without problems of solubility or aggregation). Then, for comparison purposes we compared the FRET efficiencies in an ethanolic solution with donor/acceptor concentrations matching those of sample AC3 ([Rh6G] = 5.5 mM, [NB] = 1 mM). Under otherwise identical experimental conditions, the ethanolic solution showed energy transfer with an efficiency of 10%, which is 4 times lower than that achieved with sample AC3 (Table 2). At first glance this result is intriguing since the Förster radius (eq 5), and in turn the FRET rate (eq 4), should be higher in the ethanolic solution ($\phi_f = 0.85$, $n = 1.37$, $\kappa^2 \sim 2/3$, $R_0 = 55$ Å) than in the NP environment ($R_0 = 47$ Å). Several issues may be affecting the measured FRET efficiency. On one hand, the ethanolic solutions are so concentrated that, even using 10 μm path length cuvettes and front face configuration, the donor lifetime measurements are affected by reabsorption/re-emission effects, which are known to increase the observed lifetime.[46] In fact, the solution of Rh6G 5.5 mM in the absence of NB showed a lifetime of 6.08 ns, much longer than that in dilute solution (4.05 ns). This artifact hinders the correct estimation of the FRET efficiency, and hence, the 10% value is not trustful. Nevertheless, the comparison of the fluorescence spectra of the solution and the sample AC3 suggests that the latter presents a higher FRET efficiency, as evidenced by the higher NB intensity in its fluorescence spectrum (Figure 2e). On the other hand, other nonradiative deactivation processes (quenching) in the Rh6G molecules could be hindering the energy transfer among Rh6G and NB at such high concentrations in the ethanolic solution. To overcome these influences, we prepared a solution with the same NB concentration (1 mM) but much lower Rh6G concentration (0.5 mM) and measured it at the same experimental conditions (front-face and 0.01 mm pathway cuvette). Such a solution was negligibly affected by reabsorption/re-emission processes and showed a FRET efficiency of 57%, much higher than both the one of the

dx.doi.org/10.1021/jp503218z | J. Phys. Chem. C 2014, 118, 13107−13117

concentrated solution and the one of sample AC3. This result is more consistent with the expected outcome—FRET efficiency higher in solution than in NP—and evidences that the reduction in the FRET efficiency in the concentrated solution is due to both the reabsorption/re-emission artifact and the influence of donor quenching due to excess concentration. It still remains an open question why in the NPs such effects are not observed even at much higher concentrations.

3.1.2. Donor Concentration Effects (DC Samples). It is usually considered that the role of the donors in the FRET efficiency relies on their distribution and not on their particular concentration.[48,49] This is true at very low donor concentrations, where particular donor/donor interactions are negligible. At high donor concentrations, excitation energy migration may be effective, leading to a decrease in the ensemble fluorescence polarization anisotropy.[47] Energy migration may have a relevant influence on the overall FRET efficiency at the very high donor concentrations used to obtain laser emission in colloidal suspensions and, thus, merits to be studied in depth.

To gather information about the sole effect of the donor concentration in the FRET process, we synthesized samples with a nearly fixed acceptor concentration ([NB] ∼ 5.0 mM) and a variable donor one ([Rh6G] = 1−9 mM, Samples DC1 to DC6, Table 3). At these high concentrations the donor lifetime is slightly dependent on the particular concentration within the NP that, in turn, affects the calculated FRET efficiency (eq 2). To correct this influence, we synthesized NPs with donor alone in concentrations covering those of samples DC (Table S1, Supporting Information), and the lifetime of Rh6G was monitored as a function of its concentration (Table S1, Supporting Information). The values obtained at each concentration were used as a reference for the corresponding sample including acceptor (Table 3).

At low donor concentrations ([Rh6G] ≤ 2 mM, samples DC1 to DC3, Table 3), the FRET efficiency, within errors, is nearly constant (Figure 3a) and has a value around 76%, in agreement with what was observed in Figure 2d for acceptor concentrations around 5 mM. Nevertheless, at donor concentrations above 5 mM, the NPs show an increase in ϕ_{FRET}, with values reaching 84% (Figure 3a). Hence, the increase of the donor concentration, in contrast to what is usually claimed, has an effect on the FRET efficiency somewhat similar to what is observed when increasing the acceptor concentration (Figure 2d), albeit much less pronounced (compare scales in Figure 2d and Figure 3a).

The origin of this enhancement lays in the fact that Rh6G shows a significant overlap between its emission and absorption spectra (Figure 1), suggesting that energy transfer between donors (homo-FRET) is possible. Hence, as the donor concentration is increased, the migration of the excitation energy between donor molecules[47] is activated (Figure 3b). In fact, this migration was detected in our previous work by means of fluorescence anisotropy measurements.[51] This migration, in turn, increases the probability of energy transfer from Rh6G molecules to NB ones, which otherwise would not have access to this excitation due to an excessive separation (Figure 3b). In other words, the homo-FRET among donors mediates in the hetero-FRET between donors and distant acceptors. Nevertheless this enhancement is counterbalanced by the increase in the probability of emission from Rh6G after several energy hops, explaining the higher influence of the acceptor concentration in the FRET efficiency.

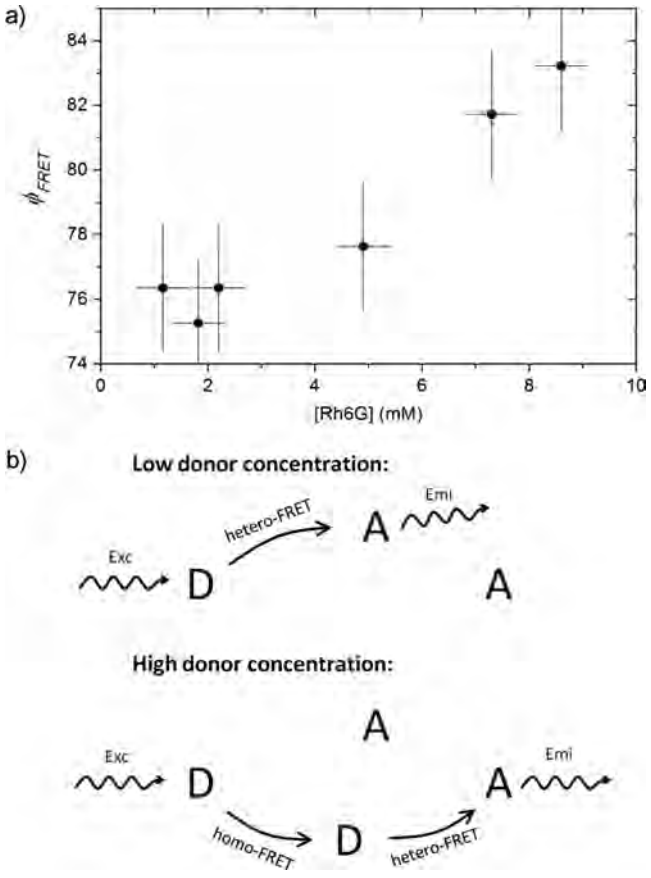

Figure 3. (a) FRET efficiency as a function of donor concentration for a fixed acceptor concentration of 5 mM. Error bars account for the experimental inaccuracies in the dye concentration determination. (b) Sketch of homo-FRET-mediated energy transfer. D = Donor, A = Acceptor.

The aforementioned homo-FRET process among donors is characterized as well by a Förster critical radius that, in the case of Rh6G in the present NPs, is as high as R_0 = 47 Å (eq 5), which is equal to that of the hetero-FRET among Rh6G and NB (R_0 = 47 Å). Hence, if the donor−donor mean distance is inferior to the donor−acceptor mean distance the excitation of the donor will be transferred with a higher probability to a different donor than to an acceptor. In other words, as mutual distance and concentration are linked (eq 6), the homo-FRET effects on ϕ_{FRET} should be noticeable at donor concentrations higher than those of the acceptor. In the set of samples DC, the acceptor concentration is nearly fixed at 5.0 mM, which means that ϕ_{FRET} should present a change at donor concentrations above or around 5.0 mM, and this is indeed the case, as can be clearly observed in Figure 3a.

Quite recently, it has been theoretically shown that the presence of donors in the vicinity of the acceptors results in an increase of the photon absorption rate of the latter due to a quantum interference effect emerging from the intermolecular coupling.[60] An increase in the absorption rate of the acceptor would lead to an increase of the Förster radius (eq 5) and, in turn, of the FRET efficiency. This quantum effect could be somewhat contributing to the observed behavior (Figure 3a), but most probably its effects would be screened by the homo-FRET effects.

3.1.3. Fixed Donor/Acceptor Molar Ratio (FR Samples). For completeness, we evaluated the energy transfer efficiency

dx.doi.org/10.1021/jp503218z | J. Phys. Chem. C 2014, 118, 13107−13117

Table 4. Structural and Photophysical Properties of Samples under Study with a Fixed Donor/Acceptor Ratio ([Rh6G]/[NB] ~ 0.9)[a]

sample	NP wt %	d (nm)	[Rh6G] (mM)	[NB] (mM)	λ_{em} (nm)	$\tau_i[A_i]$ (ns)	$\langle\tau\rangle$ (ns)	ϕ_{FRET} (%)
FR1	7.3	40	3.2	3.6	560	0.92 [0.63]; 3.02 [0.37]	1.70	63
					670	0.12 [<0]; 0.79 [<0]; 3.13 [>0]	-	
FR2 (DC4, AC7)	6.0	34	4.9	4.6	560	0.31 [0.44]; 1.17 [0.42]; 2.95 [0.14]	1.04	77
					670	0.38 [<0]; 2.82 [>0]	-	
FR3	6.7	40	7.6	7.8	560	0.21 [0.64]; 0.82 [0.31]; 2.81 [0.05]	0.53	88
					670	0.19 [<0]; 1.93 [0.88]; 3.00 [0.12]	-	
FR4	5.8	42	10.4	11.6	560	0.18 [0.64]; 0.76 [0.29]; 3.50 [0.07]	0.98	80
					670	0.17 [<0]; 1.75 [0.80]; 2.72 [0.20]	-	

[a]See Table 2 for definition of headers.

when increasing the total dye concentration in the NP at a fixed donor/acceptor molar ratio. We synthesized NPs with a donor/acceptor molar ratio ~0.9 and dye concentrations ranging from 3 to 11 mM (samples FR1 to FR4 in Table 4). As the amount of dye is increased, the FRET process becomes more efficient (Figure 4) since the donor/acceptor mutual distances are reduced. The hetero-FRET process among donors and acceptors (see section 3.1.1) and the homo-FRET-mediated energy transfer (see section 3.1.2) contribute to this increase in FRET efficiency. Efficiencies as high as 88% were obtained when dye concentrations around 8 mM were used (Figure 4). Nevertheless, the increase of dye content in the NP beyond this point does not lead to a FRET efficiency increase, but on the contrary, the energy transfer becomes less efficient. This is probably due to the fact that at such high concentrations ([Rh6G] = 10.4 mM and [NB] = 11.6 mM) there are other nonradiative processes that may lead to energy transfer rate reductions[46] (collisional deactivation, aggregation, static quenching, ...).

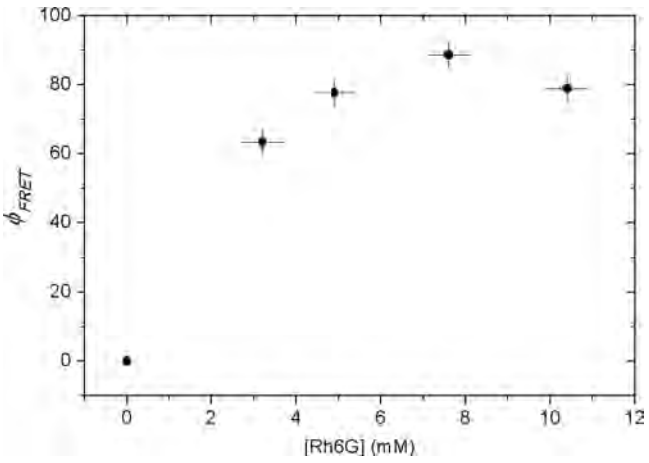

Figure 4. FRET efficiency as a function of donor concentration for a fixed donor/acceptor ratio ([Rh6G]/[NB] ~ 0.9). Error bars account for the experimental inaccuracies in the dye concentration determination.

In summary, the efficiency of the energy transfer under given photophysical experimental conditions depends on both the donor and acceptor concentration in a definite way: ϕ_{FRET} scales with the acceptor concentration due to the presence of more available energy traps and a reduction in the average donor/acceptor distances, and does it with the donor concentration due to the increase in the excitation energy migration between donor molecules, mediating in the hetero-FRET between donors and distant acceptors. When the concentration of both dyes is raised beyond a given value, the FRET efficiency is reduced due to the activation of competing quenching processes. Finally, the use of NPs not only allows achieving FRET efficiencies much higher than those attainable in liquid solution (88% vs 57%) but also opens the door to the study of FRET dynamics at concentrations beyond the solubility limit in liquid solutions (at least for the Rh6G/NB pair).

3.2. Lasing Properties. When performing laser emission experiments the process of energy transfer is highly modified. On one hand, the NP concentration is high enough to enable an acceptor molecule in a NP to absorb photons emitted by a

Table 5. Structural and Laser Properties of Selected Samples

						$\lambda_L{}^e$ (nm)		
sample	NP[a] wt %	d^b (nm)	[Rh6G][c] (mM)	[NB][c] (mM)	$\phi_L{}^d$ (%)	Rh6G	NB	$\phi_{LET}{}^f$ (%)
D	6.1	39	6.3	-	25	581	-	-
A	6.5	38	-	6.2	LIF	-	699.0	-
L1	6.8	41	2.2	3	6	568.1	682	10
L2 (AC3)	6.9	46	5.5	1.3	10	573	676	21
L3	5.2	40	8.2	3.9	10	573.4	690.5	78
L4 (DC6)	6.6	44	8.6	4.9	11	570.1	698.1	98
L5 (AC7, DC4)	6.0	34	4.9	4.6	9	565.8	699.8	99
L6 (DC5)	6.7	40	7.3	5.6	13	567.4	699.7	99.3
L7, (AC9)	5.3	41	5.5	11.4	7	-	703.2	100
L8	6.7	40	6.5	8.8	8	-	704.9	100

[a]Weight proportion of nanoparticles (NPs) in the suspension. [b]NP diameter. [c]NP dye concentration. [d]Laser efficiency. [e]Laser peak wavelength. [f]Laser energy transfer efficiency.

dx.doi.org/10.1021/jp503218z | J. Phys. Chem. C 2014, 118, 13107−13117

donor molecule surviving the FRET process within a distant NP; i.e., it gives place to radiative energy transfer between distant NPs, a fact that was avoided in the diluted suspensions used for the photophysical measurements. In other words, the radiative transfer favors the overall energy transfer process under laser conditions. In addition, and as mentioned above, ϕ_{FRET} depends on the concentration of donors and acceptors in the ground state. Under the experimental conditions of the photophysical measurements (pulse much shorter than lifetime and low pump energy), this concentration is practically identical to the total concentration of dyes in the NP. In contrast, under laser pumping conditions (pulse longer than lifetime and high pump energy), this is not the case, as the ground state of both dyes is highly depleted (Rh6G due to direct pumping and NB due to energy transfer and direct pumping), since population inversion to achieve laser emission must be reached. This means that the effective concentration of donor and acceptors in the ground state will be reduced during the lasing process, which, in turn, reduces the effective FRET efficiency.

These new contributions affect the overall energy transfer efficiency under laser pumping conditions. Hence, systematic laser measurements were performed on some of the samples previously evaluated to assess and compare the energy transfer processes under both experimental conditions. To this aim, total laser efficiencies (ϕ_L, ratio of emitted and pumped energies), laser energy transfer efficiencies (ϕ_{LET}), and laser peak wavelengths (λ_L) were assessed (Table 5).

To evaluate the energy transfer process under laser operation, we will introduce the laser energy transfer efficiency ϕ_{LET}, defined as the percent contribution of the acceptor emission to the total laser efficiency

$$\phi_{LET} = 100\% \frac{\int_{\Delta\lambda_{NB}} I_L(\lambda)\frac{hc}{\lambda}d\lambda}{\phi_L} \quad (7)$$

where $\Delta\lambda_{NB}$ is the wavelength interval corresponding to the NB laser emission and $I_L(\lambda)$ is the laser spectrum normalized so that $\int I_L(\lambda)hc/\lambda d\lambda$—integrated over all wavelengths λ—equals the laser efficiency ϕ_L, h being Planck's constant and c the speed of light in vacuum.

First, for comparison purposes, the laser emission from colloidal solutions of NPs containing only one dye, Rh6G or NB, was assessed. Whereas efficient laser emission was obtained with Rh6G (Table 5 and Figure 5), only laser-induced fluorescence (LIF) was obtained when NB was doped alone (Table 5). This lack of laser emission from the NB alone had been previously understood as a result of the combination of two factors:[51] first, MMA/HEMA/GMA is not the best solid host for the laser action of NB, which is favored in protic environments (alcohols), and on the other hand, the physically achievable NB concentrations within the NP are too low to provide the needed pump absorption and laser gain.

Table 5 summarizes the laser properties corresponding to the colloidal suspensions of NPs containing mixtures of dyes, and Figure 5 shows the normalized laser emission spectra ordered from lowest to highest ϕ_{LET} (eq 7). Interestingly, all of the samples presented some level of laser emission at a wavelength corresponding to NB (with laser thresholds of hundreds of microJoules), in contrast with sample A in which laser emission was not observed. ϕ_{LET} ranges from an approximately 10% in sample L1, where most of the laser emission remains at the Rh6G wavelength, to a full 100% in samples L7 and L8, in

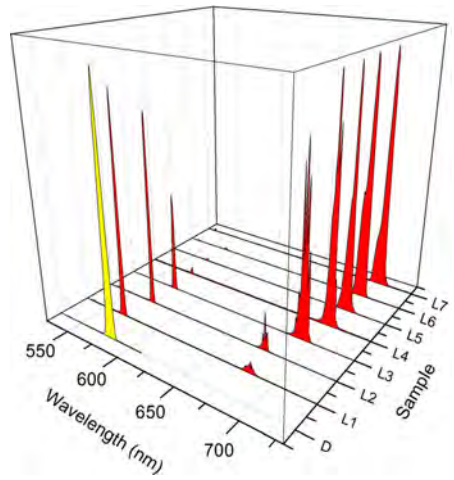

Figure 5. Normalized laser emission spectra from samples in Table 5 ordered from lowest to highest net energy transfer from donor to acceptor. Laser spectrum of sample D (yellow) is included for comparison.

which the laser emission has been fully transferred to the NB wavelength. In addition, under experimental conditions assuring ϕ_{LET} > 98% (samples L4–L8, Table 5), laser emission with efficiencies ϕ_L ranging between 13% (sample L6) and 7% (sample L7) can be obtained, testifying the advantages of the energy transfer approach.

As seen in Figure 6a and 6b, both ϕ_L and ϕ_{LET} vary significantly depending on the particular donor and acceptor concentrations within the NP. Higher dye concentrations lead to better ϕ_{LET} but lower ϕ_L, while lower concentrations give place to both poorer ϕ_L and ϕ_{LET} (Figure 6a and b). To explain this behavior it has to be first remarked that, in our system, the intrinsic laser efficiency of the acceptor is much lower than that of the donor, which justifies, to some extent, that the system exhibits lower final laser efficiency in spite of achieving better laser energy transfer efficiencies. In addition, this behavior is related to the complex nonlinear dynamics of the lasing process involving both radiative and nonradiative energy transfers, which depends on the donor and acceptor concentrations as well as on the pump intensity and the quenching processes, which become more relevant as the total dye concentration inside the NPs increases.

In an attempt to correlate the photophysical properties with the laser properties, Figure 6 shows as well the variation of ϕ_{FRET} as a function of donor and acceptor concentrations for the samples used in the laser experiments. As could be foreseen, the higher ϕ_{FRET} within the NP is, the higher ϕ_{LET} becomes, although there is not a linear correlation. Indeed, for low FRET efficiencies (low acceptor concentrations), $\phi_{LET} < \phi_{FRET}$, while at high FRET efficiencies, $\phi_{LET} > \phi_{FRET}$, with ϕ_{LET} reaching nearly 100% for ϕ_{FRET} >77%. This is again a consequence of the complex dynamics of the laser processes involving both radiative and nonradiative energy transfers. The fact that under laser experiments total energy transfer can be achieved is mostly a consequence of the appearance of radiative energy transfer processes (reabsorption/re-emission events) due to the high NP concentration and the long optical path traveled by the photons within the active medium (1 cm). Nevertheless, and as a final remark, a higher ϕ_{FRET} does not guarantee higher ϕ_L, as can be clearly seen comparing Figures 6a and 6c. In this sense, the best laser performance is shown by sample L6, which has

dx.doi.org/10.1021/jp503218z | J. Phys. Chem. C 2014, 118, 13107–13117

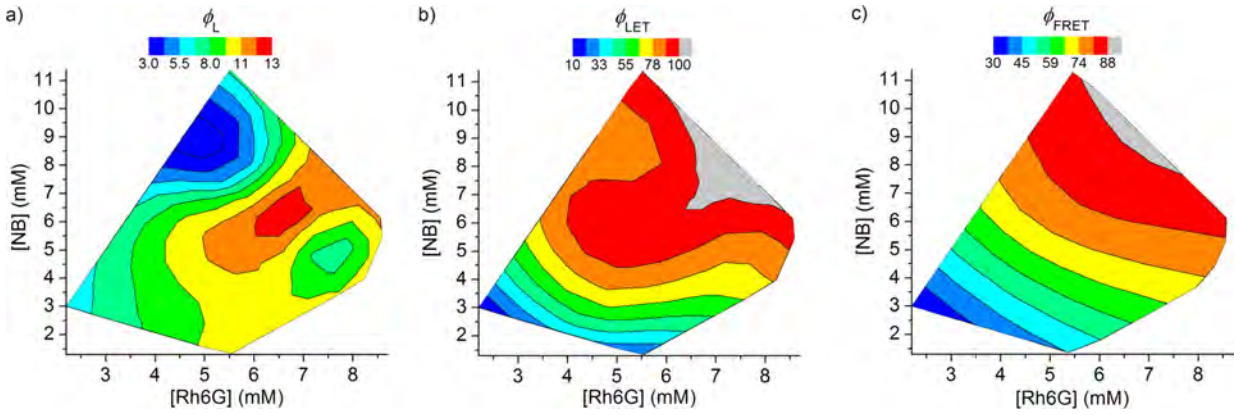

Figure 6. Contour plot of (a) laser efficiency (ϕ_L), (b) laser energy transfer efficiency (ϕ_{LET}, eq 7), and (c) FRET efficiency (ϕ_{FRET}) as a function of both donor and acceptor concentrations.

high ϕ_L (13%) and ϕ_{FRET} (82%), with a nearly complete ϕ_{LET} (99%).

CONCLUSIONS

We have systematically analyzed FRET-assisted emission in dye-doped latex NPs in terms of photophysical and laser properties. The control over the particle dye content has allowed an in-depth study of the influence of energy transfer on the photophysical and laser signatures of the NPs. The use of NPs not only allows achieving FRET efficiencies much higher than those attainable in liquid solution (88% vs 57%) but also opens the door to the study of FRET dynamics at concentrations beyond the solubility limit in liquid solutions and without the undesirable effects of reabsorption/re-emission processes (at least for the Rh6G/NB pair). The photophysics of these systems has revealed that the FRET efficiency is mostly influenced by the acceptor concentration since the probability of trapping the excitation energy by NB is enhanced and, in less extension, by the donor concentration. As the donor concentration is increased, the migration of the excitation energy between donors due to homo-FRET increases the probability of energy transfer from Rh6G molecules to NB ones, which otherwise would not have access to this excitation due to an excessive separation. When the concentration of both dyes is raised beyond a given value, the FRET efficiency is reduced due to the activation of competing quenching processes. With respect to the laser performance, we have observed that the higher the FRET efficiency within the NP, the higher the laser energy transfer efficiency becomes. In contrast, a higher FRET efficiency does not guarantee higher laser efficiencies in the system. This behavior is related to the complex nonlinear dynamics of the lasing process involving both radiative and nonradiative energy transfers as well as to the laser pumping conditions (pulse larger than dye lifetimes and high pump intensity). Finally, the findings achieved herein represent a rule of thumb applicable to other donor/acceptor pairs of laser dyes confined into NPs fulfilling the requirements to ensure efficient FRET processes.

ASSOCIATED CONTENT

Supporting Information

A table with structural and photophysical properties of NPs doped with Rh6G alone. This material is available free of charge via the Internet at http://pubs.acs.org.

AUTHOR INFORMATION

Corresponding Author

*E-mail: lcerdan@iqfr.csic.es.

Notes

The authors declare no competing financial interest.

ACKNOWLEDGMENTS

This work was supported by Spanish MICINN (projects TRACE2009-0144, MAT2010-20646-C04-01, and MAT2010-20646-C04-04). The authors thank Gobierno Vasco (IT339-10) for financial support and a predoctoral fellowship for L. Gartzia-Rivero.

REFERENCES

(1) Burns, A.; Ow, H.; Wiesner, U. Fluorescent Core-Shell Silica Nanoparticles: towards "Lab On a Particle" Architectures for Nanobiotechnology. *Chem. Soc. Rev.* **2006**, *35*, 1028−1042.

(2) Yan, J. L.; Estevez, M. C.; Smith, J. E.; Wang, K. M.; He, X. X.; Wang, L.; Tan, W. H. Dye-Doped Nanoparticles for bioanalysis. *Nano Today* **2007**, *2*, 44−50.

(3) Morgan, T. T.; Muddana, H. S.; Altinoglu, E. I.; Rouse, S. M.; Tabakovic, A.; Tabouillot, T.; Russin, T. J.; Shanmugavelandy, S. S.; Butler, P. J.; Eklun, P. C.; et al. Encapsulation of Organic Molecules in Calcium Phosphate Nanocomposite Particles for Intracellular Imaging and Drug Delivery. *Nano Lett.* **2008**, *8*, 4108−4115.

(4) Chan, C. P. Y.; Bruemmel, Y.; Seydack, M.; Sin, K. K.; Wong, L. W.; Merisko-Liversidge, E.; Trau, D.; Renneberg, R. Nanocrystal Biolabels with Releasable Fluorophores for Immunoassays. *Anal. Chem.* **2004**, *76*, 3638−3645.

(5) Cerdán, L.; Costela, A.; Enciso, E.; García-Moreno, I. Random Lasing in Self-Assembled Dye-Doped Latex Nanoparticles: Packing Density Effects. *Adv. Funct. Mater.* **2013**, *23*, 3916−3924.

(6) Cerdán, L.; Gartzia-Rivero, E.; Enciso, E.; Bañuelos, J.; López Arbeloa, I.; Costela, A.; García-Moreno, I. Focusing on Charge-Surface Interfacial Effects to Enhance the Laser Properties of Dye-Doped Nanoparticles. *Laser Phys. Lett.* **2014**, *015901*, 1−6.

(7) Resch-Genger, U.; Grabolle, M.; Cavaliere-Jaricot, S.; Nitschke, R.; Nann, T. Quantum Dots Versus Organic Dyes as Fluorescent Labels. *Nat. Methods* **2008**, *5*, 763−775.

(8) Harun, N. A.; Harrocks, B. R.; Fulton, D. A. A Miniemulsion Polymerization Technique for Encapsulation of Silicon Quantum Dots in Polymer Nanoparticles. *Nanoscale* **2011**, *3*, 4733−4741.

(9) Yang, Y.; Wen, Z.; Dong, Y.; Gao, M. Incorporating CdTe Nanocrystals into Polystyrene Microspheres: Towards Robust Fluorescent Beads. *Small* **2006**, *2*, 898−901.

(10) Joumaa, N.; Lansalot, M.; Théretz, A.; Elaissari, A. Synthesis of Quantum Dot-Taged Submicrometer Polystyrene Particles by Miniemulsion Polymerization. *Langmuir* **2006**, *22*, 1810−1816.

(11) Esteves, A. C. C.; Bombalski, L.; Trindade, T.; Matyjaszewski, K.; Barros-Timmons, A. Polymer Grafting from CdS Quantum Dots via AGET ATRP in Miniemulsion. *Small* **2007**, *3*, 1230−1236.
(12) Zhu, J.; Wei, S.; Patil, R.; Rutman, D.; Kucknoor, A. S.; Wang, A.; Guo, Z. Ionic Liquid Assisted Electrospinning of Quantum Dots/Elastomer Comosite Nanofibers. *Polymer* **2011**, *52*, 1954−1962.
(13) Wei, S.; Sampathi, J.; Guo, Z.; Anumadla, N.; Rutman, D.; Kucknoor, A.; James, L.; Wang, A. Nanoporous Poly(Methyl Methacrylate)-Quantum Dots Nanocomposites Fibers Towards Biomedical Applications. *Polymer* **2011**, *52*, 5817−5829.
(14) Zhu, C.; Liu, L.; Yang, Q.; Lv, F.; Wang, S. Water-Soluble Conjugated Polymers for Imaging, Diagnosis, and Therapy. *Chem. Rev.* **2012**, *112*, 4687−4735.
(15) Li, K.; Liu, B. Polymer Encapsulated Conjugated Polymer Nanoparticles for Fluorescence Bioimaging. *J. Mater. Chem.* **2012**, *22*, 1257−1264.
(16) Tuncel, D.; Demir, H. V. Conjugated Polymer Nanoparticles. *Nanoscale* **2010**, *2*, 484−494.
(17) Ahmed, E.; Morton, S. W.; Hammond, P. T.; Swager, T. M. Fluorescent Multiblock π-Conjugated Polymer Nanoparticles for In Vivo Tumor Targeting. *Adv. Mater.* **2013**, *25*, 4504−4510.
(18) Satapathi, S.; Kokil, A.; Venkatraman, B. H.; Lian, L.; Venkataraman, D.; Kumar, J. Sensitive Detection of Nitroaromatics With Colloidal Conjugated Polymer Nanoparticles. *IEEE Sens. J.* **2013**, *13*, 2329−2333.
(19) Liao, H.-C.; Hsu, C.-P.; Wu, M.-C.; Lu, C.-F.; Su, W.-F. Conjugated Polymer/Nanoparticles Nanocomposite for High Efficient and Real-time Volatile Organic Compounds Sensors. *Anal. Chem.* **2013**, *85*, 9305−9311.
(20) Baier, M. C.; Huber, J.; Mecking, S. Fluorescent Conjugated Polymer Nanoparticles by Polymerization in Miniemulsion. *J. Am. Chem. Soc.* **2009**, *131*, 14267−14273.
(21) Gu, J.-Q.; Shen, J.; Sun, L.-D.; Yan, C.-H. Resonance Energy Transfer in Steady-State and Time-Decay Fluoro-Immunoassays for Lanthanide Nanoparticles Based on Biotin and Avidin Affinity. *J. Phys. Chem. C* **2008**, *112*, 6589−6593.
(22) Li, L.-L.; Zhang, R.; Yin, L.; Zheng, K.; Qin, W.; Selvin, P. R.; Lu, Y. Biomimetic Surface Engineering of Lanthanide-Doped Upconversion Nanoparticles as Versatile Bioprobes. *Angew. Chem., Int. Ed.* **2012**, *51*, 6121−6125.
(23) Gnach, A.; Bednarkiewicz, A. Lanthanide-Doped Up-Converting Nanoparticles: Merits and Challenges. *Nano Today* **2012**, *7*, 532−563.
(24) Xu, W.; Bony, B. A.; Kim, C. R.; Baeck, J. S.; Chang, Y.; Bae, J. E.; Chae, K. S.; Kim, T. J.; Lee, G. H. Mixed Lanthanide Oxide Nanoparticles as Dual Imaging Agent in Biomedicine. *Sci. Rep.* **2013**, *3*, 3210.
(25) Charbonnière, L. J.; Rehspringer, J. L.; Ziessel, R.; Zimmermann, Y. Highly Luminescent Water-Soluble Lanthanide Nanoparticles Through Surface Coating Sensitization. *New J. Chem.* **2008**, *32*, 1055−1059.
(26) Vancaeyzeele, C.; Ornatsky, O.; Baranov, V.; Shen, L.; Abdelrahman, A.; Winnik, M. A. Lanthanide-Containing Polymer Nanoparticles for Biological Tagging Applications: Nonspecific Endocytosis and Cell Adhesion. *J. Am. Chem. Soc.* **2007**, *129*, 13653−13660.
(27) Seydack, M. Nanoparticle Labels in Immunosensing Using Optical Detection Methods. *Biosens. Bioelectron.* **2005**, *20*, 2454−2469.
(28) Sharma, P.; Brown, S.; Walter, G.; Santra, S.; Moudgil, B. Nanoparticles for Bioimaging. *Adv. Colloid Interface Sci.* **2006**, *123*−*126*, 471−485.
(29) Wolfbeis, O. S. Materials for Fluorescence-Based Optical Chemical Sensors. *J. Mater. Chem.* **2005**, *15*, 2657−2669.
(30) Stark, W. Nanoparticles in Biological Systems. *Angew. Chem., Int. Ed.* **2011**, *50*, 1242−1258.
(31) Demchenko, A. P. Nanoparticles and Nanocomposites for Fluorescence Sensing and Imaging. *Methods Appl. Fluoresc.* **2013**, *1*, 022001.
(32) Bogart, L. K.; Pourroy, G.; Murphy, C. J.; Puntes, V.; Pellegrino, T.; Resenblum, D.; Peer, D.; Lévy, R. Nanoparticles for Imaging, Sensing, and Therapeutic Intervention. *ACS Nano* **2014**, *8*, 3107−3122.
(33) Muddana, H. S.; Morgan, T. T.; Adair, J. H.; Butler, P. J. Photophysics of Cy3-Encampsulated Calcium Phosphate Nanoparticles. *Nano Lett.* **2009**, *9*, 1559−1566.
(34) Saxena, V.; Sadoqi, M.; Shao, J. Enhanced Photo-Stability, Thermal-Stability and Aqueous-Stability of Indocyanine Green in Polymeric Nanoparticulate Systems. *J. Photochem. Photobiol., B* **2004**, *74*, 29−38.
(35) Miletto, I.; Gilardino, A.; Zamburlin, P.; Dalmazzo, S.; Caputo, D.; Viscardi, G.; Martra, G. Highly Bright and Photostable Cyanine Dye-Doped Silica Nanoparticles for Optical Imaging: Photophysical Characterization and Cell Tests. *Dyes Pigm.* **2009**, *84*, 121−127.
(36) Enciso, E.; Costela, A.; Garcia-Moreno, I.; Martin, V.; Sastre, R. Conventional Unidirectional Laser Action Enhanced by Dye Confined in Nanoparticle Scatters. *Langmuir* **2010**, *26*, 6154−6157.
(37) Martin, V.; Bañuelos, J.; Enciso, E.; Lopez Arbeloa, I.; Costela, A.; Garcia-Moreno, I. Photophysical and Lasing Properties of Rhodamine 6G Confined in Polymeric Nanoparticles. *J. Phys. Chem. C* **2011**, *115*, 3926−3933.
(38) Monguzzi, A.; Frigoli, M.; Larpent, C.; Meinardi, F. Laser Dye Doped Nanoparticles for Highly Photostable Optical Nanoamplifiers. *RSC Adv.* **2012**, *2*, 11731−11736.
(39) Frigoli, M.; Ouadahi, K.; Larpent, C. A Cascade FRET-Mediated Ratiometric Sensonr for Cu^{2+} Ions Based on Dual Fluorescent Ligand-Coated Polymer Nanoparticles. *Chem.—Eur. J.* **2009**, *15*, 8319−8330.
(40) Rungta, P.; Bandera, Y. P.; Tsyalkovsky, V.; Foulger, S. H. Designing Fluoroprobes through Förster Resonance Energy Transfer: Surface Modification of Nanoparticles through "Click" Chemistry. *Soft Matter* **2010**, *6*, 6083−6095.
(41) Wu, C.; Zheng, Y.; Szymanski, C.; McNeill, J. Energy Transfer in a Nanoscale Multichromophoric System: Fluorescent Dye-Doped Conjugated Polymer Nanoparticles. *J. Phys. Chem. C* **2008**, *112*, 1772−1781.
(42) Peng, H.; Stolwijk, J. A.; Sun, L.-N.; Wegener, J.; Wolfbeis, O. S. A Nanogel for Ratiometric Fluorescent Sensing of Intracellular pH Values. *Angew. Chem., Int. Ed.* **2010**, *49*, 4246−4249.
(43) Ma, B.; Xu, M.; Zeng, F.; Huang, L.; Wu, S. Micelle Nanoparticles for FRET-Based Ratiometric Sensing of Mercury Ions in Water, Biological Fluids and Living Cells. *Nanotechnology* **2011**, *22*, 065501.
(44) Ouadahi, K.; Sbargoud, K.; Allard, E.; Larpent, C. FRET-Mediated pH-Responsive Dual Fluorescent Nanoparticles Prepared via Click Chemistry. *Nanoscale* **2012**, *4*, 727−732.
(45) Tian, Z.; Wu, W.; Li, A. D. Q. Photoswitchable Fluorescent Nanoparticles: Preparation, Properties and Applications. *ChemPhysChem* **2009**, *10*, 2577−2591 and references therein.
(46) Lakowicz, J. R., Ed. *Principles of Fluorescence Spectroscopy*, 3rd ed.; Kluwer Academic/Plenum Publishers: New York, 2006.
(47) Barberan-Santos, M. N.; Nunes Pereira, E. J.; Martinho, J. M. G. Stochastic Theory of Combined Radiative and Nonradiative Transport. *J. Chem. Phys.* **1997**, *107*, 10480−10484.
(48) Yekta, A.; Winnik, M. A.; Farinha, J. P. S.; Martinho, J. M. G. Dipole-Dipole Electronic Energy Transfer. Fluorescence Decay Functions for Arbitrary Distributions of Donors and Acceptors. II. Systems with Spherical Symmetry. *J. Phys. Chem. A* **1997**, *101*, 1787−1792.
(49) Farinha, J. P. S.; Martinho, J. M. G. Resonance Energy Transfer in Polymer Nanodomains. *J. Phys. Chem. C* **2008**, *112*, 10591−10601.
(50) Bojarski, P.; Kukal, L.; Walczewska-Szewc, K.; Synak, A.; Marzullo, V. M.; Luini, A.; D'Auria, S. Long-Distance FRET Analysis: A Monte Carlo Simulation Study. *J. Phys. Chem. B* **2011**, *115*, 10120−10125.
(51) Cerdán, L.; Enciso, E.; Martín, V.; Bañuelos, J.; López-Arbeloa, I.; Costela, A.; García-Moreno, I. FRET-Assisted Laser Emission in Colloidal Suspensions of Dye-Doped Latex Nanoparticles. *Nat. Photonics* **2012**, *6*, 621−626.
(52) Chen, N.-T.; Cheng, S.-H.; Liu, C.-P.; Souris, J. S.; Chen, C.-T.; Mou, C.-Y.; Lo, L.-W. Recent Advances in Nanoparticle-Based Förster

Resonance Energy Transfer for Biosensing, Molecular Imaging and Drug Release Profiling. *Int. J. Mol. Sci.* **2012**, *13*, 16598−16623.
(53) Xu, Z.; Liao, Q.; Shi, X.; Li, H.; Zhang, H.; Fu, H. Full-Color Tunable Organic Nanoparticles with FRET-Assisted Enhanced Two-Photon Excited Fluorescence for Bio-Imaging. *J. Mater. Chem. B* **2013**, *1*, 6035−6041.
(54) Xiong, L.; Shuhendler, A. J.; Rao, J. Self-Luminescing BRET-FRET Near-Infrared Dots fro In Vivo Lymph-Node Mapping and Tumour Imaging. *Nat. Commun.* **2012**, *3*, 1193.
(55) Lopez Arbeloa, F.; Urrecha Aguirresacona, I.; Lopez Arbeloa, I. Influence of the Molecular Structure and the Nature of the Solvent on the Absorption and Fluorescence Characteristics of Rhodamines. *Chem. Phys.* **1989**, *130*, 371−378.
(56) Lopez Arbeloa, F.; Lopez Arbeloa, T.; Lopez Arbeloa, I.; Costela, A.; Garcia-Moreno, I.; Figuera, J. M.; Amat-Guerri, F.; Sastre, R. Relations between Photophysical and Lasing Properties of Rhodamines in Solid Polymeric Matrices. *Appl. Phys. B: Laser Opt.* **1997**, *64*, 651−657.
(57) Dutt, G. D.; Doraiswamy, S.; Periasamy, N.; Venkataraman, B. Rotational Reorientation Dynamics of Polar Dye Molucular Probes by Picosecond Laser Spectroscopy Technique. *J. Chem. Phys.* **1990**, *93*, 8498−8513.
(58) de Oliveira, H. P. M.; Gehlen, M. H. Time-Resolved Fluorescence of Cationic Dyes Covalently bound to Poly(Methacrylic Acid) in Rigid Media. *J. Lumin.* **2006**, *121*, 544−552.
(59) Bhattacharyya, B.; Chakrabarti, B. K. The Mean Distance to the Nth Neighbour in a Uniform Distribution of Random Points: An Application of Probability Theory. *Eur. J. Phys.* **2008**, *29*, 639−645.
(60) Coles, M. M.; Leeder, J. M.; Andrews, D. L. Static and Dynamic Modifications to Photon Absorption: The Effects of Surrounding Chromophores. *Chem. Phys. Lett.* **2014**, *595*−*596*, 151−155.

3.3. DYE DIFFUSION IN CORE-SHELL NPS

It has been well demonstrated the high dependence that donor-acceptor average distance have on the FRET efficiency. Thus, to go in depth into this aspect the dye distribution within the NP was studied in multifunctional core/shell NPs (shell thickness ranging from 0.5 to 4 nm), where the location of donor and acceptor molecules can be preferentially selected (core, shell or both) looking for a fine tuning of the energy transfer efficiency [31-33]. Different anionic NPs with the same size and donor-acceptor concentrations but with different dye distribution (homogenous vs Rh6G in core/NB in shell) were compared (Figure 3.17).

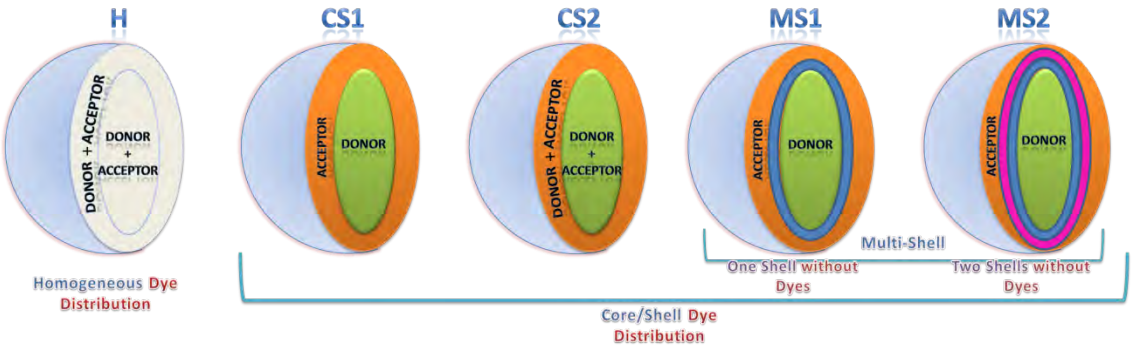

Figure 3.17. Sketch of latex NPs with homogeneous (H) and different core/shell (CS1, CS2) dye distributions. Shells without dyes are included as spacers (MS1, MS2). The homogeneous NP posses in reality a core/thin shell morphology induced by the charge of the surface and supported by a thorough photophysical study reported in the attached manuscripts.

The evolution of the donor fluorescence decay curve was the chosen tool to evaluate the FRET efficiency, as described previously. At the same time, the FRET dependence on donor-acceptor distance can be applied to verify the achievement of the target morphology of the NPs imposed in the synthesis together with the inner dye distribution. First, we started comparing diametrically different dye distributions: (i) homogeneous latex NPs with randomly distributed donor and acceptors, (ii) latex NPs with core/shell morphology in which the donor (Rh6G) was placed at the core and the acceptor at the shell and (iii) both dyes together mixed in core and in shell (Figure 3.17). Surprisingly, the experimental data showed that the calculated FRET efficiencies where almost comparable regardless of the morphologies; mixed donor-acceptor or separated by a barrier imposed by the core/shell morphology (Figure 3.18).

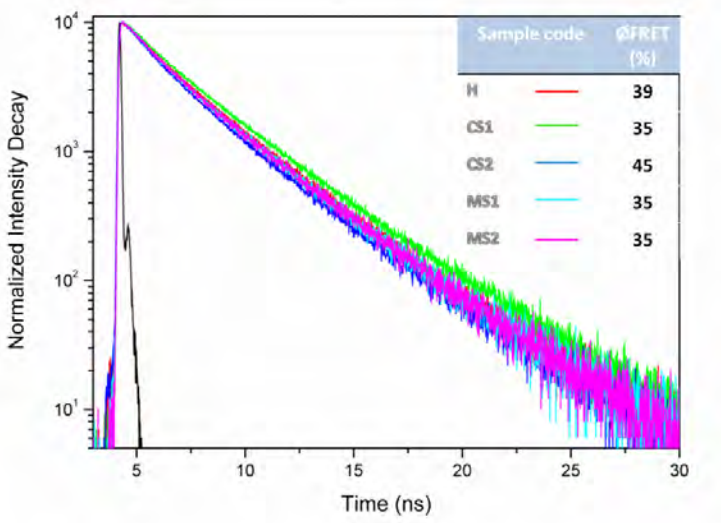

Figure 3.18. Donor fluorescence decay curves and FRET efficiencies in NPs with different morphologies and dye distribution: homogeneous, CS1, CS2, MS1 and MS2.

Moreover, NPs containing multiple shells were synthesized in which the donor was located in the core, the acceptor in the last shell and the inner empty shells as spacers to promote larger donor-acceptor distances (Figure 3.17). However, the results were analogous to that of the above samples (Figure 3.18).

These findings prompted us to wonder about the real distribution of the dyes within the NPs. The previously described theoretical method pointed out the need of including the dye diffusion to properly describe the experimental donor dynamics. Consequently, although the synthesis was performed in several steps and each dye was added in different stages, it was finally concluded that donor and acceptors are redistributed in the NPs due to the free diffusion leading to a homogeneous distribution along the whole NP. Such diffusion process could take place mainly from the core to the shell due the induced electrostatic attractive interactions by the negatively charged surface (hairy layer) of the anionic latex NPs on the cationic dyes. Besides, an additional driven force is related to different affinity or solubility of the dyes in each monomer mixture (divergent monomer compositions in the core and shell). Taking into account that the shell contains more HEMA than the core, a monomer in which both Rh6G and NB have a higher solubility than in MMA monomer, the dyes will accumulate preferentially in the region presenting the lower chemical potential (higher affinity or solubility). On the other hand, the dye motion from the shell to the core, ruled by hydrophobic forces, can also contribute to the dye mixing. As a result of these diffusion processes and regardless of the NP morphology, donors and acceptors tend to be in close contact, leading to high FRET efficiencies in all cases.

The electrostatic guided dye diffusion was supported by a kinetic study carried out mixing a sample containing Rh6G at the core of the NP with a solution of NB in order to track the evolution of the energy transfer by means of the fluorescence emission spectra recorded exciting the donor Rh6G (Figure 3.19). It is noteworthy that almost from the beginning (t=0) the emission of the NB was significantly high (in contrast with the same dye mixture in solution), indicating the presence of an extremely fast diffusion process of the NB from the aqueous solution to the NP surface. Elongated times (from t=0 to 20 hours) led to a progressive decrease of the donor signal in favour of the acceptor emission, indicating enhanced FRET efficiency, reaching values comparable to the above studied samples (Figure 3.18). In view of the initial fast kinetics, we monitored the fluorescence intensity of the NB (675 nm) during the first 20 minutes recording it every 1s (Figure 3.19 inset). The kinetic scan displayed two possible diffusion processes deduced from the divergent time gradients visible in the kinetic curve. The first one, faster and shorter (‹ 50s) could be assignable to the approach of the NB molecules to the NP surface, whereas the second and slower diffusion process might be due to the diffusion and redistribution of the NB within the `hairy layer´ or even towards the inner space of the NP.

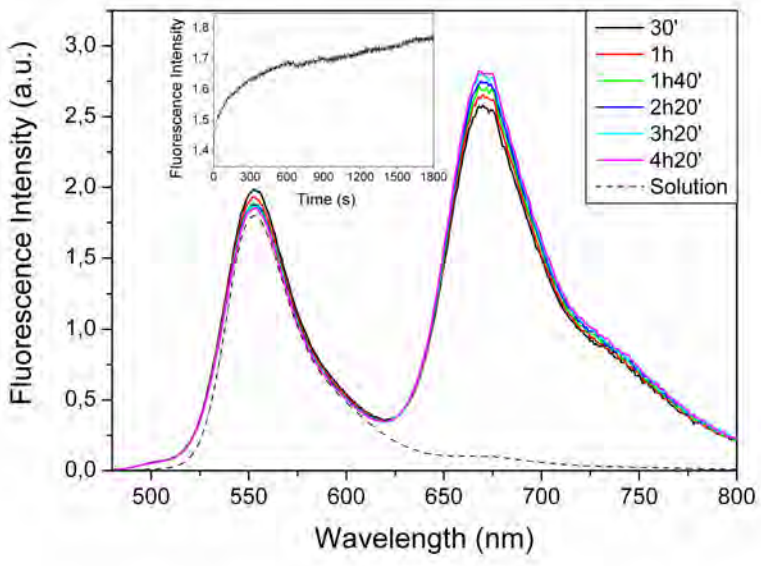

Figure 3.19. Kinetic study of the addition of a solution containing NB to a colloidal suspension of Rh6G-doped NPs. Emission spectra exciting the donor at 450 nm recorded at different times after the NB addition. Inset; kinetic curve monitoring the emission in the acceptor (670 nm). The spectrum of the same dye mixture in solution is included for comparison (dashed line).

Summarizing, the searched core-shell morphology with donors and acceptors located in each region was non-viable due to the fast dye diffusion occasioned by electrostatic dye-NP surface interactions and the differentiated monomeric affinities.

It has been also demonstrated that the FRET dynamics arise as a valuable "spectroscopic ruler" to obtain knowledge of the dye distribution inside the NP.

A more detailed FRET analysis of dye distribution in core/shell NPs is carried out in the attached article reported in the journal of *Royal Society of Chemistry Advances*.

RSC Advances

PAPER

A FRET analysis of dye diffusion in core/shell polymer nanoparticles†

Cite this: *RSC Adv.*, 2014, **4**, 22115

Luis Cerdán,*[a] Eduardo Enciso,[b] Leire Gartzia-Rivero,[c] Jorge Bañuelos,[c] Iñigo López Arbeloa,[c] Ángel Costela[a] and Inmaculada García-Moreno[a]

Received 17th March 2014
Accepted 30th April 2014

DOI: 10.1039/c4ra02342k

www.rsc.org/advances

In this paper we show that dye distributions within polymer core/shell nanoparticles (NPs), grown in multiple steps, are controlled not only by the synthesis route, but are also governed by dye diffusion between core and shell, resulting in dye distributions completely different from the targeted ones. We show that Förster Resonance Energy Transfer (FRET) dynamics can be used as a spectroscopic measure to determine the particular dye profiles along the NPs and thus to uncover the presence of dye diffusion. Finally, to confirm the previous results and with the aim to have a clearer understanding of the diffusion processes within core/shell NPs (equilibrium and transient dye distributions, time scales, *etcetera*), we analyze the behaviour predicted by existing diffusion models and infer that the dye diffusion is already finished at the end of the shell growth.

Introduction

Colloidal nanoparticles (NPs) are at the forefront of fundamental nanoscience, applied nanotechnology, biophotonics and nanomedicine thanks to their versatility, simplicity in manufacture, and, most importantly, due to the possibility of fine tuning their physical, optical and reactive properties in a controlled way.[1–3] In particular, core/shell NPs are being extensively used in sensing and diagnosis applications due to the possibility of obtaining multifunctional systems in which core and shell present different functionalities (catalytic, plasmonic, magnetic, imaging, drug delivery).[1,2,4,5] Although organic and inorganic compounds can be used and combined into a single core/shell NP,[5] full organic core/shell NPs are of special interest for *in vitro* and *in vivo* biophotonic and nanomedicine applications due to their biocompatibility, drug delivery capabilities and post treatment biodegradation properties.

In vivo and *in vitro* bioimaging techniques require of fluorescent probes with high brightness, high resistance to photodegradation, low toxicity and high water solubility.[6] Probes fulfilling all of these properties are scarce, but this limitation can be circumvented by using highly efficient and photostable probes embedded into NPs, which provides water solubility, reduced cytotoxicity, and selective tissue targeting through surface functionalization.[7] In addition, the fluorescence probes must emit in the red spectral region (>600 nm), as these wavelengths allow for deep tissue penetration and reduced interference with the background autofluorescence of biological samples. In this sense, Förster Resonance Energy Transfer (FRET), which is a physical process in which an excited donor transfers its energy to a nearby acceptor by means of dipole moments coupling,[8] allows for obtaining highly efficient red emitting probes while exciting at the blue or green spectral region. The FRET efficiency is highly dependent, among other parameters, on the particular donor–acceptor mutual distance distribution, so that when dealing with FRET-based multifunctional core/shell NPs, the location where FRET is taking place (core, shell, or both) must be accurately controlled, and the implications of the particular distribution choice clearly understood.

We have recently developed a series of dye doped latex NPs based on acrylic monomers, with sizes ranging from 20 to 350 nm in diameter, exhibiting outstanding laser performances when using one[9,10] or two laser dyes[11] as dopants for the NPs in colloidal solutions, as well as controllable random laser emission in dried self-assembled monoliths.[12] Given the control on the synthesis procedure attained with these NPs, they might serve as an appropriate test bed to prove the effects of the particular donor and acceptor distributions on the FRET efficiency and photophysics.

In this paper we evaluate the FRET process from Rhodamine 6G (Rh6G) to Nile Blue (NB), dyes with a very good spectral overlap,[11] in core/shell NPs composed of dissimilar mixtures of methacrylic monomers and grown in multiple steps. First, we experimentally verify whether the synthesized NPs are indeed core/shell or if new NPs are nucleated as a consequence of the multistep growing. Then, we compare the FRET efficiency of two

[a]*Instituto de Química-Física "Rocasolano", Consejo Superior de Investigaciones Científicas (CSIC), Serrano 119, 28006 Madrid, Spain. E-mail: lcerdan@iqfr.csic.es*

[b]*Departamento de Química Física I, Facultad de Ciencias Químicas, Universidad Complutense de Madrid, Ciudad Universitaria, 28040 Madrid, Spain*

[c]*Departamento de Química Física, Universidad del País Vasco-EHU, Aptdo. 644, 48080 Bilbao, Spain*

† Electronic supplementary information (ESI) available. See DOI: 10.1039/c4ra02342k

different NPs with the same size and donor and acceptor concentrations (in terms of number of molecules within each NP), but with diametrically different dye distribution (homogeneous *vs.* Rh6G in core/NB in shell). We make use of the FRET dynamics as a spectroscopic ruler to determine the particular dye profiles along the NPs and thus to uncover the presence of dye diffusion in the core/shell NPs. Finally, we evaluate theoretically the diffusion process in order to confirm the experimental results and gather the time scales involved.

Experimental and theoretical methods

Materials

Laser dyes Rhodamine 6G (Rh6G) (Fluka, >95% purity) and Nile Blue (NB) (Exciton, >99% purity and laser grade) were used as received. Methyl methacrylate (MMA) (Aldrich, 99%) was purified with a 0.1 M sodium hydroxide solution to remove inhibitor. 2-Hydroxylethyl methacrylate (HEMA) (Aldrich, 97%), glycidyl methacrylate (GMA) (Fluka, 97%), potassium persulfate (KPS) (Sigma, 99%), ethylenglycol dimethacrylate (EGDMA) (Aldrich, 98%) and Sodium Dodecyl Sulphate (SDS) (Sigma 99%) were used without further purification. Deionized water was obtained from a Direct QTM 5 Millipore.

Synthesis of core/shell nanoparticles

The particle seeds (core) were prepared from a batch emulsion polymerization following the procedure previously reported.[10] The proper amounts of dyes were dissolved in monomer mixtures of MMA:HEMA:GMA:EGDMA (see Table 1). SDS was added into the aqueous polymerization medium as surfactant stabilizer. After oxygen degassing with a nitrogen flux, the reactor was heated to 65 °C and the polymerization was initiated by adding a KPS aqueous solution, and performed for at least 60 minutes. The growth of the first shells was performed 60 minutes after the end of the seeds polymerization by introducing in the reactor further amounts of monomer mixture and the corresponding amount of dyes (see Table 1). The polymerization process of the shells was run for other 60 minutes. For additional shells growth, the process was repeated. The described synthesis route shows high polymerization yields (Table 1). The particle sizes and size distributions of the seeds and core/shell NPs were determined by quasielastic laser light scattering (QELS) with a Brookhaven Zetasizer (Brookhaven Instruments Ltd.) at 25 °C; for this, about 0.100 ml of each suspension was diluted with 2.9 ml of water immediately after polymerization. At the end of the synthesis, the solid content of the suspension was determined by drying 2.5 ml of original suspension in an oven at 45 °C up to constant weight.

Fluorescence decay dynamics measurement

The FRET processes were characterized in diluted samples (net dye concentration around 2 μM and optical pathway 1 cm) of the original aqueous solutions with the aim to avoid at maximum reabsorption/reemission effects. Fluorescence decay dynamics were monitored at the peak emission wavelengths corresponding to Rh6G (donor) after excitation at 470 nm with a diode laser (PicoQuant, model LDH470). These curves can be phenomenologically treated as a multi-exponential decay $I_F(t) = A_0 + \Sigma A_i \exp(-t/\tau_i)$. The fluorescence lifetime components (τ_i) were obtained from the slope after the deconvolution of the instrumental response signal from the recorded decay curves by means of an iterative method. The goodness of the exponential fit was controlled by statistical parameters (χ^2 and Durbin–Watson test statistics, automatically provided by the instrument). New exponentials (up to 3) were added to the fit until the residuals showed a homogeneous distribution (no bumps).

FRET parameters treatment

The efficiency of the FRET process in the latex nanoparticles can be obtained from the comparison of the fluorescence decay curves of the donor in the absence ($I_F^D(t)$) and presence ($I_F^{D+A}(t)$) of acceptors as[8]

$$\phi_{FRET} = 1 - \frac{\int I_F^{D+A}(t)\mathrm{d}t}{\int I_F^{D}(t)\mathrm{d}t}. \quad (1)$$

The fluorescence decay curve of a donor (Rh6G) in the presence of acceptors (NB) confined in systems with spherical symmetry undergoing FRET processes follows a complex dynamic which depends on the donor and acceptor radial distributions (see below), but is experimentally treated and fitted as a multi-exponential decay. Within this approximation, ϕ_{FRET} can be estimated according to the equation

$$\phi_{FRET} = 1 - \frac{\langle\tau\rangle}{\langle\tau_0\rangle}, \quad (2)$$

where $\langle\tau_0\rangle$ is the amplitude average lifetime of donor alone and $\langle\tau\rangle$ is the amplitude average fluorescence lifetime of the donor subjected to FRET processes, being defined as

$$\langle\tau\rangle = \sum A_i \tau_i \quad (3)$$

where the coefficients A_i are the weight of each contribution to the lifetime in the multiexponential.

The fluorescence decay curve of the donor in the presence of acceptors can be used as a tool to determine the distribution of donors and acceptors within the nanoparticle, since the resonance energy transfer is highly dependent on the donor–acceptor distance distribution.[8] In this work we have made use of the treatment developed by Martinho's group,[13,14] but slightly modified, which has been applied successfully to determine the dye distribution in different systems with spherical symmetry.[11,15,16] The donor decay function after a delta-pulse excitation is given by:

$$I_D(t) = 4\pi \exp\left\{-\frac{t}{\tau_D(r_D)}\right\} \int_0^{R_S} C_D(r_D) r_D{}^2 \exp\{-g(r_D,t)\}\mathrm{d}r_D$$

$$g(r_D,t) = \frac{2\pi}{r_D} \int_{r_{min}(r_D)}^{\infty} \left[1 - \exp\left\{-\frac{t}{\tau_D(r_D)}\left(\frac{R_0}{r}\right)^6\right\}\right]$$

$$\times \left[\int_{|r_D - r|}^{r_D + r} C_A(r_A) r_A \mathrm{d}r_A\right] r\mathrm{d}r \quad (4)$$

where r_D (r_A) is the radial position of the donor (acceptor), R_S is the NP radius, $\tau_D(r_D)$ is the lifetime of the donor in the absence of acceptor (which may depend on the position within the NP), r is the mutual distance between donor and acceptors, $R_0 = 4.9$ nm is the Förster critical radius for the Rh6G/NB system in the NPs (See ESI†), $C_D(r_D)$ and $C_A(r_A)$ are the concentration profiles (in nm^{-3}) of donors and acceptors, respectively, along the radius of the NP, and $r_{min}(r_D)$ is the minimum distance between donors and acceptors, which is approximately the mean distance to the 1st neighbor in a uniform distribution of random points. This distance (in nm) depends on the acceptor concentration as:[17]

$$r_{min}(r_D) = \frac{0.554}{\sqrt[3]{C_A(r_D)}} \quad (5)$$

In order to compare the theoretical predictions on the fluorescence decay curves $I_D(t)$, with the experimental ones $I_{exp}(t)$, $I_D(t)$ is convoluted with the instrument response function $L(t)$, to obtain:

$$I_{fit}(t) = L(t) \otimes I_D(t) = \int_0^t L(\tau) I_D(t-\tau) d\tau \quad (6)$$

and the fitting parameters are iterated until Pearson's χ^2 is no further reduced. A value of χ^2 closest to 0 is desired, but in our case $\chi^2 < 0.6$ is already considered a good fit.

For simplicity of treatment, the dye distributions $C_D(r_D)$ and $C_A(r_A)$ introduced into eqn (4) will be based on combinations of step functions of the Heaviside type ($H(r)$). Detailed expressions for the donor decay functions for the different dye distributions used through the paper can be found in the ESI.†

Results and discussion

Experimental verification of shell growing

The core and the shells in the synthesized NPs are both polymeric, although their monomer compositions and structures (*i.e.*, crosslinking degree) varies significantly in order to define layers with different properties such as polarity, hydrophobicity, solubility, free volume *etc.* The core is mostly comprised of MMA, HEMA and GMA, whereas the shells include as well EGDMA, a cross linking monomer (Table 1). In addition, the proportions of each monomer are different in the core and in the shell. For example, the MMA ratio in the shells is half that in the core. This implies that the shells are more prone to water swelling that the cores, but their increased polarity ensures a better environment for polar dyes such as Rh6G and NB.

In order to start the growing of shells around the cores, it has to be guaranteed that the polymerization process of the latter has terminated. During the core synthesis, the dispersion of the monomer components by the presence of SDS molecules in the aqueous solution, and the full solubility of the hydrophilic monomer HEMA, leads to a fast polymerization which can be followed by monitoring the temperature inside the reactor (Fig. 1a), since the free radical polymerization is an exothermic reaction and raises the temperature of the solution. The maximum temperatures were achieved around 20 minutes after initiator addition, while after 45 minutes the reactor temperature was set at a constant value of 65 °C, indicating that the polymerization is almost finished. In fact, DLS measurements rendered identical particle diameters after 60 and 120 minutes

Table 1 Compositional and structural properties of the particles synthesized in this study

Sample code	[a]wt%	η_P[b] (%)	NP site[c]	M : H : G : E[d] (wt%)	d_{NP}[e] (nm)	[Rh6G][f] (mM)	[NB][f] (mM)	Description
H	6.9	87	C	63 : 22 : 13 : 2	45.9	5.6	1.1	Homogeneous NP with Rh6G and NB
RH	6.1	77	C	69 : 20 : 11 : 0	39	6.3	—	Homogeneous NP with only Rh6G. Reference for sample H
CS1	5.5	72	C	68 : 21 : 11 : 0	42	5.6	—	NP with Rh6G in the core (C) and NB in shell (S1)
			S1	33 : 41 : 8 : 18	43.5 [0.75]	—	9.5	
CS2	7.0	90	C	67 : 21 : 12 : 0	41.5	5.4	1	NP with Rh6G and NB in core (C) and shell (S1)
			S1	33 : 41 : 8 : 18	44.3 [1.4]	5.4	1.5	
RCS	7.0	92	C	68 : 21 : 11 : 0	38.1	5.6	—	NP with Rh6G in core (C) and a shell (S1) without dyes. Reference for samples core/shell (CS)
			S1	34 : 41 : 8 : 17	41.3 [1.6]	—	—	
MS1	7.2	86	C	66 : 21 : 11 : 2	42.8	5.6	—	NP with Rh6G in core (C), a shell (S1) without dyes and a shell (S2) with NB
			S1	36 : 40 : 8 : 16	43.9 [0.55]	—	—	
			S2	33 : 43 : 8 : 16	46.5 [1.3]	—	9.5	
MS2	7.3	91	C	67 : 20 : 11 : 2	39.3	5.6	—	NP with Rh6G in core (C), two shells (S1&S2) without dyes and a shell (S3) with NB
			S1	34 : 42 : 8 : 16	41 [0.85]	—	—	
			S2	35 : 41 : 8 : 16	43.3 [1.15]	—	—	
			S3	33 : 41 : 9 : 17	46.8 [1.75]	—	11.2	
RMS	7.4	92	C	66 : 21 : 11 : 2	39.1	5.6	—	NP with Rh6G in the core, and two shells (S1&S2) without dyes. Reference for samples multishells (MS)
			S1	35 : 40 : 10 : 15	40.2 [0.55]	—	—	
			S2	35 : 40 : 8 : 17	42.5 [1.15]	—	—	

[a] Solid content in suspension after polymerization. [b] Polymerization yield. [c] NP site -core (C) or 1st, 2nd and/or 3rd shells (S1, S2, S3)- to which data in columns d to f refers to. [d] Weight ratio monomer mixture MMA:HEMA:GMA: EGDMA (in short, M:H:G:E). [e] NP mean diameter after subsequent growth. Values in brackets represent each shell thickness. [f] Dye molar concentration inside NP according the total monomer feed introduced in each polymerization step.

of reaction (39.4 and 39.1 nm at 60 and 120 minutes, respectively, for sample RMS).

One of the aims of the present work is to assess the influence of the nanoparticle morphology on the optical properties of the system without interference by other parameters, which is a challenge due to the fact that in nano-sized systems several physicochemical parameters are entangled. Taking into account that the optical properties of nanostructured materials are strongly dependent on their final size, the NPs herein synthesized have a thin shell, ranging from 0.5 nm to 4 nm. Since the shell thickness is so small as compared to the core radius, any random variable affecting the particle growth introduces large uncertainties in the shell sizes. However, the growth of the different shells followed by performing DLS measurements after each monomer mixture addition (Table 1) allows us to establish some qualitative behavior. According to the data in Table 1, the NPs diameter grows with each new monomer addition. If all of the added monomer feed introduced in the flask to grow the shells (M_S) were used to produced uniform and identical coatings over each NP, *i.e.*, there were no new particles formed, the final particle diameter d should raise according to

$$\left(\frac{d}{d_C}\right)^3 = 1 + r\,\frac{\rho_C}{\rho_S}, \tag{7}$$

where d_C is the diameter of the core before shell growth, $r = M_S/M_C$ is the ratio between the total monomer mass introduced in the reactor to grow the shells (M_S) and the cores (M_C), and ρ_C and ρ_S are the densities of the core and shell copolymers, respectively (See ESI† for derivation of this expression). As there are not important differences in the densities of the monomers used, the particular combination of monomers does not affect excessively the final density, hence, in ideal conditions, $\rho_C/\rho_S \sim 1$, and $(d/d_C)^3 \approx (1 + r)$.

By measuring the particle diameter in each growth step, we could test the dependency of d on r, and the obtained results are shown in Fig. 1b. These results show that there is a positive correlation between these two parameters, being an indication that the size of the particles increases with the sequential addition of new monomer feeds, *i.e.*, new shells are being form after each step. The dispersion observed in the values of d/d_C for a constant value of r, 7% standard deviation for the first growth, falls within the expected experimental reproducibility of the synthesis we follow in this paper. However, the measured diameters are slightly larger than those predicted by eqn (7) assuming $\rho_C/\rho_S \sim 1$ (Fig. 1b), indicating that the density of the shell would be lower than that of the core ($\rho_C/\rho_S > 1$). This could be ascribed to the water swelling in the shell resulting from the more hydrophilic nature of the monomers and compositions used for the shell, with respect to those of the core (MMA concentration in shell is half that in the core).

Even though, these results cannot fully confirm that all of the monomer feed added in the subsequent shell growths has been incorporated into the shells and, hence, they cannot rule out that a given fraction of the monomer has been turned into new particles or polymer solved in the interparticle medium.

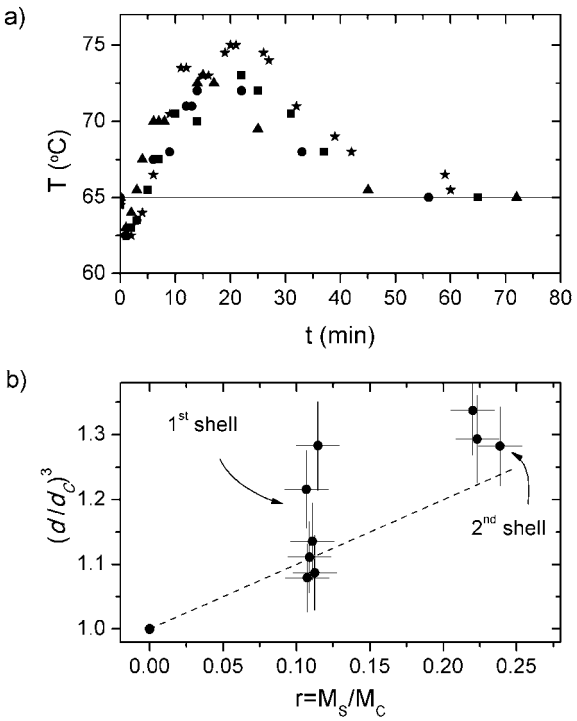

Fig. 1 (a) Reactor temperature during core formation for four randomly chosen samples synthesized in this work (H, CS1, RMS and MS2). The solid line marks the set temperature of the reactor. (b) NP diameters against mass of the monomer feeds. The values have been rescaled by the diameter and monomer feed of the core particles. The error bars in (b) accounts for fluctuations inherent to the synthesis procedure and apparatus resolution. The dashed line represents the predicted NP diameter after each shell growth assuming the absence of polymer swelling enhancement, full monomer feed inclusion into the final particles, and similar copolymers densities in core and shells (*i.e.*, $(d/d_C)^3 = 1 + r$).

Uncovering dye diffusion in core/shell NPs

The energy transfer process is highly dependent on the donor and acceptor distributions within the latexes, and may thus deeply affect the emission performance in these systems. Thus, it is important to correlate NP morphology (or dye distribution) with photophysical performance. Hence, our aim was to compare two different NPs with the same size and donor and acceptor concentrations (in terms of number of molecules within each NP), but with diametrically different dye distribution. Then, we synthesized two samples: latex NPs without shell and homogeneous donor and acceptor distributions (sample H, Table 1), and latex NPs with a core/shell morphology in which the donor dye Rh6G was placed at the core and the acceptor dye NB was placed at the shell (sample CS1, Table 1). Reference NPs without acceptor were prepared to extract information about the donor lifetime τ_D in the absence of acceptor and thus to calculate the FRET quantum yield ϕ_{FRET} with eqn (2) (samples RH and RCS, Table 1).

As the mean distance between donors and acceptors in samples H and CS1 is highly distinct, one could expect a quite different behavior with respect to the FRET process, but the data in

Table 2 and the fluorescence intensity decays of Rh6G in samples H and CS1 (Fig. 2a) suggested that there was not such a high difference, with samples H and CS1 presenting FRET efficiencies of 39% and 35%. In order to find the origin of this unexpected equality, we decided to fit the fluorescence intensity decays in Fig. 2a with theoretical expressions from which one can gather the donor and acceptor concentration distributions (see ESI†).

We began by evaluating the decay curve of sample H, as this kind of samples had been evaluated previously,[11] and had been successfully fitted with the so called "core/surface" distribution (Model 1 in ESI; eqn. (S7)–(S9)†). In this scenario the NP consists of a homogeneous polymer core in which both donors and acceptors are homogeneously and uniformly solved, and an extremely thin shell (hairy layer) surrounding the core, in which both donors and acceptors are adsorbed. In the core/surface model, the fitting parameters are C_A^S and C_A^C (surface and volume densities of acceptors in surface (S) and core (C), respectively), and the constraint $C_A^C/C_A^S = C_D^C/C_D^S$ applies (see ESI†). The reference sample RH shows two contributions to the lifetime of Rh6G in the NP (Table 2), the longest and main one being ascribed to the core ($\tau_{D,C}$), and the shortest and residual one to the hairy layer ($\tau_{D,S}$). Then, in eqn (S7) and (S8)† we used $\tau_{D,C} = 3.52$ ns and $\tau_{D,S} = 1.55$ ns. The best fit of eqn (S7)–(S9)† to the decay curve of Rh6G in sample H ($\chi^2 = 0.5988$, Fig 2a and b) rendered a total acceptor concentration $C_A = 2.4$ mM, with 68% of all donor and acceptor molecules solved in the core, and the rest adsorbed in the surface.

The best fit overestimates the acceptor concentration in the NP with respect to the experimental value ($C_A^{exp} \approx 1.1$ mM). At these donor concentrations (~5.5 mM) the excitation energy migration due to homo FRET among donors increases the probability of energy transfer from Rh6G molecules to NB ones which otherwise would not have access to this excitation due to an excessive separation. In other words, the homo FRET among donors mediates in the hetero FRET between donors and distant acceptors. In fact, the presence of homo FRET in this particular system was previously demonstrated.[11] As the used model (eqn (4)) does not account for this effect, and assumes that only the acceptor concentration governs the process, it "understands" the increase in the FRET efficiency due to the donors as an increase in the acceptor concentration, thus overestimating the latter. To modify the model considering the influence of homo FRET on the corresponding decay curves is neither a direct nor a simple task, but it would be necessary to enable gathering reliable information from highly loaded systems. Work is in progress in our labs towards this aim. Therefore, the information obtained from the fits is essentially qualitative, and must be treated as such.

Next, we evaluated the decay curve of sample CS1 by making use of a model considering a core/shell dye distribution (Model 2 in ESI; eqn (S10)–(S12)†), assuming that there were no donor in the shell ($C_D^S = 0$), and no acceptor in the core ($C_A^C = 0$), which were the targeted distributions. Hence, the only fitting parameter was C_A^S, the volume density of acceptors in the shell. In this case the reference sample RCS was a similar core/shell NP with donor molecules in the core but containing no dyes in the shell. Interestingly, the reference sample RCS shows only one contribution to the lifetime of Rh6G in the NP (Table 2), indicating that in the core/shell synthesis the surface dye population observed in the homogeneous NPs (sample RH) is not obtained. This means that somehow the shell growth is "cleaning" the hairy layer, or in other words, the newly included

Table 2 FRET parameters of NPs synthesized in this study

Sample code	τ_i $[A_i]^a$ (ns)	$\langle\tau\rangle^b$ (ns)	$\phi_{FRET}{}^c$ (%)
H	1.71 [0.45]; 3.64 [0.55]	2.77	39
RH	3.11 [0.21]; 4.70 [0.79]	4.37	—
CS1	1.80 [0.45]; 3.87 [0.55]	2.94	35
CS2	1.55 [0.52]; 3.52 [0.48]	2.50	45
RCS	4.52 [1]	4.52	—
MS1	1.48 [0.44]; 3.52 [0.56]	3.01	35
MS2	1.46 [0.43]; 3.50 [0.57]	3.01	35
RMS	4.66 [1]	4.66	—

[a] Fluorescence lifetimes (τ_i) and weights (A_i, $\Sigma A_i = 1$) obtained from multiexponential fit of decay curve. [b] Amplitude average fluorescence lifetime of the donor subjected to FRET processes (eqn (3)). [c] FRET quantum yield.

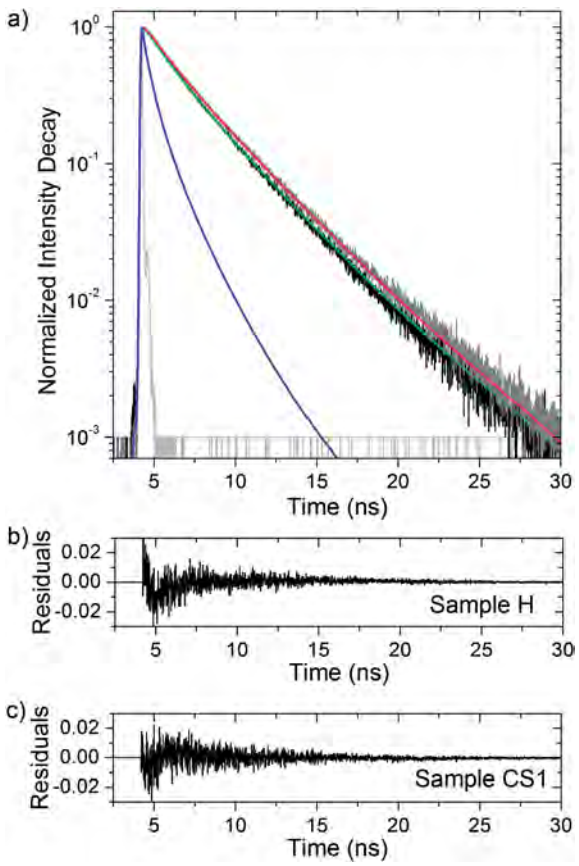

Fig. 2 (a) Fluorescence intensity decays of Rh6G for sample H (black line) and CS1 (dark gray line). The light gray line is the instrument response $L(t)$ after pulse excitation. The red and green lines are the best fits to CS1 and H decay data, respectively (Eqn (S10)–(S12) and eqn (S7)–(S9) have been used to samples CS1 and H, respectively). The blue line is the prediction of the core/shell model assuming $C_A^C = 0$ mM and $C_A^S = 9.5$ mM. Residuals of the fit to fluorescence decay of samples H and CS1 are plotted in (b) and (c), respectively.

monomers drag the dyes in the surface to the inner part of the NP. For the sample CS1, the best fit of eqn. (S10)–(S12)† to the decay curve ($\chi^2 = 0.6053$, not shown) rendered a shell acceptor concentration $C_A^S = 2.2$ mM, much lower than the value expected from the dye loaded in the synthesis procedure ($C_A^S = 9.5$ mM). Indeed, the predicted fluorescence intensity decay for a core/shell NP assuming $C_A^S = 9.5$ mM and $C_A^C = C_D^S = 0$ in eqn (S10)–(S12),† presents a much higher de-excitation rate (Fig. 2a) and thus would imply a much higher FRET efficiency. This discrepancy could be owed to different reasons: (a) there is a NB leakage from the shell to the solution after/during synthesis or even that the dye is not properly included in the shell during the synthesis, and (b) the NPs do not present the assumed core/shell dye distribution.

The first reason could be ruled out, since we dialyzed the sample CS1 for 48 hours, and the absorption spectra of the aliquots from the cleaning water did not show evidences of either Rh6G or NB. To check the second reason, we run again the core/shell model fit (Model 2 in ESI; eqn (S10)–(S12)†) but this time letting C_D^C, C_D^S, C_A^C and C_A^S free. As the donor and acceptor molecules have a very similar nature (both chemical and electrostatic) they will have similar affinities for a given monomer mixture. Hence, we assume, for simplicity, that both dyes will present the same dye distribution within the core/shell NP, *i.e.*, $C_A^C/C_A^S = C_D^C/C_D^S$. This constraint reduces the degrees of freedom to C_A^C and C_A^S. The best fit ($\chi^2 = 0.5521$, Fig. 2a and c) rendered a shell acceptor concentration $C_A^S = 3.5$ mM and a core acceptor concentration $C_A^C = 1.7$ mM, *i.e.*, the 80% of all dye molecules ends up in the core. In addition, the fitted total concentrations are much closer to the experimental ones than those obtained with the homogeneous model (Model 1). This fit shows that, unexpectedly, both donors and acceptors are distributed along the whole NP, implying that there would be diffusion processes from the shell to the core, and *vice versa*, while or after the shell polymerization. Hence, the fact that both dye distributions in sample CS1 are "spread" through the NP, explains by itself the observed similitude between the fluorescence intensity decay curves, and in turn of ϕ_{FRET}, of samples H, fully homogenized, and CS1, partially homogenized.

The information on the core/shell morphology and on the diffusion process has to be considered only qualitatively. On the one hand, the complexity of the system makes practically impossible to model all the process involved in the energy transfer. On the other hand, the errors on the shell thickness affects the determination of dye concentrations in the model, as was discussed above. For this reason and to assure whether the observed dye diffusion was not a mere coincidence due to a particular problem during the synthesis of sample CS1, we synthesized another NP with core/shell morphology in which both donor and acceptor were placed at the core and the shell such that $C_A^C \approx C_A^S$ and $C_D^C \approx C_D^S$ (sample CS2, Table 1). Again, the best fit of eqn (S10)–(S12)† to the decay curve ($\chi^2 = 0.4694$, not shown) rendered a shell acceptor concentration $C_A^S = 4.6$ mM and a core acceptor concentration $C_A^C = 1.8$ mM. This means that the acceptor concentration in the shell is nearly twice and half as much as the dye concentration in the core, indicating again that dye diffusion took place.

Once proved that dye diffusion was taking place in our core/shell NPs, we wanted to know if the diffusion was finished or was in process. To assess that, we measured again the fluorescence intensity decay of Rh6G in sample CS1 several weeks after the first measurements, but no differences were found either on the ϕ_{FRET} value or the fluorescence intensity decays, indicating that the diffusion was finished or at least frozen.

Finally, trying to avoid or partially reduce the dye diffusion, we synthesized NPs with multiple shells; the core containing the donor, the outer shell containing the acceptor, and the inner shell(s), intended as dye barrier(s), containing no acceptor (samples MS1 and MS2, Table 1). Nonetheless, the outcome was analogous to that of sample CS1, *i.e.*, there were important dye redistributions in the NPs due to free diffusion.

Then, it can be seen that the final dye distributions do not depend on the initial choice in the synthesis, but are governed by diffusion processes. The particular dye distributions obtained from the FRET decay curve fitting (acceptor concentrations in the shells 2 to 3 times higher than in the core) might be a consequence of the different solubilities of the dyes in the different regions. The shell contains more HEMA than the core (see Table 1), a monomer in which both Rh6G and NB have a higher solubility than in MMA monomer.[18] In this sense, the dyes would be more "comfortable" in the shell than in the core, thus explaining the higher concentration in the former.

Theoretical evaluation of dye diffusion in core/shell NPs

To confirm the previous results and with the aim to have a clearer understanding of the diffusion processes within core/shell NPs (equilibrium and transient dye distributions, time scales, *etcetera*), we decided to analyze the behavior predicted by existing diffusion models. In this sense, Fick's second law[19] predicts how diffusion causes the concentration of a given element to change in space and time for a given diffusion coefficient (dependent on the particular material properties). Since we are dealing with a chemical system in which every region—due to its different composition—presents a different affinity for the dyes, it is more adequate to work with chemical potentials. Fick's second law in spherical coordinates and in terms of chemical potentials reads (see ESI† for a detailed description on theoretical and numerical formalism used):

$$\frac{\partial \mu}{\partial t} = D\left(\frac{\partial^2 \mu}{\partial r^2} + \frac{1}{RT}\left(\frac{\partial \mu}{\partial r}\right)^2\right) + \frac{2D}{r}\frac{\partial \mu}{\partial r} + \frac{\partial D}{\partial r}\frac{\partial \mu}{\partial r} \qquad (8)$$

where $D = D(r)$ is the diffusion coefficient along the NP radius r in units of $cm^2\ s^{-1}$ and $\mu = \mu(r,t)$ is the time-dependant chemical potential along the NPs, which is defined as:

$$\mu(r,t) = \mu^0(r) + RT \ln C(r,t). \qquad (9)$$

In eqn (9), $C(r,t)$ is the time-dependant volume number concentration (nm^{-3}) of the diffusive element along the NP radius, $\mu^0(r)$ is the reference chemical potential of a solution (μ_C^0 in core and μ_S^0 in shell), $R = 8.31\ J\ K^{-1}\ mol^{-1}$ is the gas constant and $T = 300$ K is the matrix temperature. Particle regions with

large affinity for the dye (high solubility) will reduce the reference chemical potential and will enhance the dye concentration $C(r,t)$.

All systems evolve to the equilibrium by compensating the differences in the chemical potentials along the system, *i.e.*, at equilibrium $\mu(r) = \text{constant}\ \forall r$. For our particular case, this equilibrium condition implies that $\Delta\mu^0 = \mu_C^0 - \mu_S^0 = RT\ln(H)$, where $H = C_{eq}^S/C_{eq}^C$ is the partition ratio and C_{eq}^S and C_{eq}^C are the equilibrium concentrations in the shell and core, respectively. Hence, by making use of the C_A^S and C_A^C values obtained from the fit to the fluorescence intensity decay of sample CS1 (Fig. 2a), it can be heuristically inferred that, in the particular case of this sample, $\Delta\mu^0 \approx RT\ln(2)$. For simplicity, the diffusion coefficient will be assumed constant along the NP with a value $10^{-16}\,cm^2\,s^{-1}$.

By numerically solving the above system of equations with the adequate initial and boundary conditions (see details in ESI†), the dye distribution profiles along the NP were obtained as a function of time both for acceptor and donor concentrations (Fig. 3). At the very beginning ($t = 0$ seconds in Fig. 3), the donor is fully contained in the core, and the acceptor in the shell. Only 50 milliseconds (Fig. 3) later, the acceptor population in the shell is significantly depleted and inhomogeneously distributed, being spread towards the core, where it presents a characteristic bell shaped diffusion profile. On the other hand, the donor population quickly fills the shell, showing a huge concentration discontinuity at the core/shell frontier. After 0.2 seconds (Fig. 3) from the start, the acceptor concentration in the shell is half of the initial and it shows a moderate homogeneity, while the donor concentration in the shell is already at the same level of the initial donor core concentration. Interestingly, in spite of the assumed restrictive diffusion coefficient, the system nearly reaches the equilibrium state just after 18 seconds, showing that $C_A^S/C_A^C = C_D^S/C_D^C = 2$, as was expected (Fig. 3). For completeness, the time evolution of the corresponding chemical potentials is shown in Fig. S1,† where it can be clearly observed that the system evolves to a state in which $\mu(r)$ is constant over the entire system (core and shell), as was already explained.

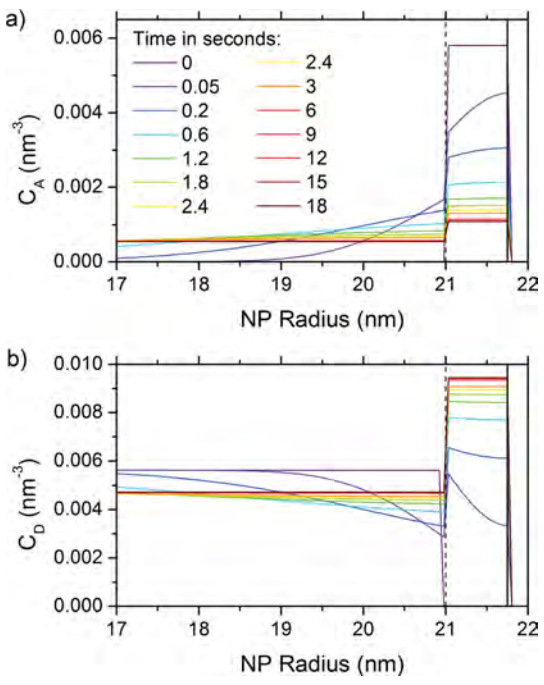

Fig. 3 Dye distribution profile along a NP analogous to CS1 as a function of time both for (a) the acceptor and (b) the donor. For better inspection, only the region around the core/shell transition is shown. The solid and dashed vertical lines indicate the position of the NP and core radii, respectively.

Hence, the previous simulation confirms what was observed experimentally: the final dye distributions do not depend on the initial choice in the synthesis, but are governed by the reference chemical potentials of the different regions, or what is the same thing, by the affinity or solubility of the dyes in each monomer mixture. In this sense, the higher the solubility of the dye in a region is, the higher the final concentration in that region becomes. In our case, the distribution obtained from the FRET decay curve fitting and the previous numerical simulation, is consistent with the fact that the shell contains more HEMA than the core, a monomer in which both Rh6G and NB have a higher solubility than in MMA monomer.[18]

Since the real problem is looser with respect to the diffusion restriction, the equilibrium state will be reached experimentally in much less time. Taking into account that the shell growth needs a minimum of 60 minutes at 65 °C, the dye diffusion from core to shell, and *vice versa*, will be already over by the synthesis end.

Conclusion

In summary, we have shown that dye doped core/shell polymer NPs do not present always a well controlled dye concentration profile, as free dye diffusion may lead to important dye redistributions. In addition, we have made use of the FRET dynamics as a spectroscopic ruler to determine the particular dye profiles along the NPs, and have revealed the presence of dye diffusion in the core/shell NPs. This fact explains why the experimental measured FRET efficiencies are almost unaffected when changing in the synthetic route the dye distribution or the number of shells in the NP. In our particular case, in which core and shell are composed of methacrylic monomers, we have shown that the equilibrium concentration for both the donor and the acceptor in the shell is 2 to 3 times higher than that in the core, indicating that the dyes dissolve better in the monomeric mixture of the former, most probably for its higher HEMA content. The equilibrium state of this redistribution has been shown to be determined by the chemical potentials of the dyes in the different regions of the NPs, with the dyes accumulating preferentially in the region presenting the lower reference chemical potential (higher affinity or solubility). The information obtained from the theoretical model of dye diffusion in core/shell NPs suggests that the diffusion process from the shell to the core, and *vice versa*, takes place at the very beginning of the shell growth.

In conclusion, if FRET-based multifunctional core/shell NPs are to be synthesized, the location where FRET is taking place (core, shell, or both) must be accurately controlled through a strict control of the dye diffusion. For example, by means of impermeable barriers between core and shell or covalently bonding the dyes to the monomers.

Acknowledgements

This work was funded by Spanish Ministerio de Economía y Competitividad (projects TRACE2009-0144, MAT2010-20646-C04-01 and MAT2010-20646-C04-04) and Gobierno Vasco (IT339-10). LGR thanks Gobierno Vasco for a predoctoral fellowship.

Notes and references

1 J. Shi, A. R. Votruba, O. C. Farokhzad and R. Langer, Nanotechnology in Drug Delivery and Tissue Engineering: from Discovery to Applications, *Nano Lett.*, 2010, **10**, 3223–3230.

2 A. S. Thakor, J. Jokerst, C. Zavaleta, T. F. Massoud and S. S. Gambhir, Gold Nanoparticles: A Revival in Precious Metal Administration to Patients, *Nano Lett.*, 2011, **11**, 4029–4036.

3 R. Taylor, S. Coulombe, T. Otanicar, P. Phelan, A. Gunawan, W. Lv, G. Rosengarten, R. Prasher and H. Tyagi, Small Particles, Big Impacts: A Review of the Diverse Applications of Nanofluids, *J. Appl. Phys.*, 2013, **113**, 011301.

4 S. Wei, Q. Wang, J. Zhu, L. Sun, H. Lin and Z. Guo, Multifunctional Composite Core/Shell Nanoparticles, *Nanoscale*, 2011, **3**, 4474–4502.

5 R. Ghosh Chaudhuri and S. Paria, Core/Shell Nanoparticles: Classes, Properties, Synthesis Mechanism, Characterization, and Applications, *Chem. Rev.*, 2012, **112**, 2373–2433.

6 S. Luo, E. Zhang, Y. Su, T. Cheng and C. Shi, A Review of NIR Dyes in Cancer Targeting and Imaging, *Biomaterials*, 2011, **32**, 7127–7138.

7 S. Santra, J. S. Xu, K. M. Wang and W. H. Tan, Luminescent Nanoparticle Probes for Bioimaging, *J. Nanosci. Nanotechnol.*, 2004, **4**, 590–599.

8 *Principles of Fluorescence Spectroscopy*, ed. J. R. Lakowicz, Kluwer Academic/Plenum Publishers, New York, 2nd edn, 1999.

9 E. Enciso, A. Costela, I. Garcia-Moreno, V. Martin and R. Sastre, Conventional Unidirectional Laser Action Enhanced by Dye Confined in Nanoparticle Scatters, *Langmuir*, 2010, **26**, 6154–6157.

10 V. Martin, J. Bañuelos, E. Enciso, I. Lopez Arbeloa, A. Costela and I. Garcia-Moreno, Photophysical and Lasing Properties of Rhodamine 6G Confined in Polymeric Nanoparticles, *J. Phys. Chem. C*, 2011, **115**, 3926–3933.

11 L. Cerdán, E. Enciso, V. Martín, J. Bañuelos, I. López-Arbeloa, A. Costela and I. García-Moreno, FRET-Assisted Laser Emission in Colloidal Suspensions of Dye-Doped Latex Nanoparticles, *Nat. Photonics*, 2012, **6**, 621–626.

12 L. Cerdán, E. Enciso, A. Costela and I. García-Moreno, Random Lasing in Self-Assembled Dye-Doped Latex Nanoparticles: Packing Density Effects, *Adv. Funct. Mater.*, 2013, **23**, 3916–3924.

13 A. Yekta, M. A. Winnik, J. P. S. Farinha and J. M. G. Martinho, Dipole-Dipole Electronic Energy Transfer. Fluorescence Decay Functions for Arbitrary Distributions of Donors and Acceptors. II. Systems with Spherical Symmetry, *J. Phys. Chem. A*, 1997, **101**, 1787–1792.

14 J. P. S. Farinha and J. M. G. Martinho, Resonance Energy Transfer in Polymer Nanodomains, *J. Phys. Chem. C*, 2008, **112**, 10591–10601.

15 J. P. S. Farinha, M.-T. Charreyre, J. M. G. Martinho, M. A. Winnik and C. Pichot, Picosecond Fluorescence Studies of the Surface Morphology of Charged Polystyrene Latex Particles, *Langmuir*, 2001, **17**, 2617–2623.

16 G. Marcelo, J. M. G. Martinho and J. P. S. Farinha, Polymer-Coated Nanoparticles by Adsorption of Hydrophobically Modified Poly(*N*,*N*-Dimethylacrylamide), *J. Phys. Chem. B*, 2013, **117**, 3416–3427.

17 B. Bhattacharyya and B. K. Chakrabarti, The Mean Distance to the Nth Neighbor in a Uniform Distribution of Random Points: An Application of Probability Theory, *Eur. J. Phys.*, 2008, **29**, 639–645.

18 A. Costela, I. García-Moreno and R. Sastre, Materials for Solid-State Dye Lasers, in *Handbook of Advanced Electronic and Photonic Materials and Devices*, ed. H. S. Nalwa, Academic Press, 2001, vol. 7, LiquidCrystals, Display and Laser Materials, pp. 161–208.

19 E. L. Cussler, *Diffusion*, Cambridge University Press, Cambridge, 1st edn, 1984.

Bibliography

[1] R. Costi, A. E. Saunders and U. Banin, *Angew. Chem. Int. Ed.,* **2010**, 49, 4878-4897.

[2] J. D. Debord, S. Eustis, S. Byul Debord, M. T. Lofye and L. A. Lyon, *Adv. Mater.,* **2002**, 14, 658-662.

[3] C. He, Y. Hu, L. Yin, C. Tang and C. Yin, *Biomaterials,* **2010**, 31, 3657-3666.

[4] E. Arunkumar, C. C. Forbes and B. D. Smith, *Eur. J. Or. Chem.,* **2005**, 4051-4059.

[5] Z. Cai, Z. Ye, X. Yang, Y. Chang, H. Wang, Y. Liu and A. Cao, *Nanoscale,* **2011**, 3, 1974-1976.

[6] A. Costela, I. García-Moreno, R. Sastre, F. López Arbeloa, T. López Arbeloa and I. López Arbeloa, *Appl. Phys. B,* **2001**, 73, 19-24.

[7] I. García-Moreno, A. Costela, M. Pintado-Sierra, V. Martín and R. Sastre, *Opt. Express,* **2009**, 17, 12777-12784.

[8] T. Kobayashi, J. Savatier, G. Jordan, W. J. Blau, Y. Suzuki and T. Kaino, *Appl. Phys. Lett.,* **2004**, 85, 185-187.

[9] K. H. Drexhage, *Structure and Properties of Laser Dyes,* in Topics in Applied Physics, Berlin, **1973**, p. 144-193.

[10] L. Cerdan, E. Enciso, V. Martin, J. Banuelos, I. Lopez-Arbeloa, A. Costela and I. García-Moreno, *Nat. Photon.,* **2012**, 6, 621-626.

[11] C. Lim, S. Kim, I. C. Kwon, C. Ahn and S. Y. Park, *Chem. Mater.,* **2009**, 21, 5819-5825.

[12] P. Zhang, W. Steelant, M. Kumar and M. Scholfield, *J. Am. Chem. Soc.,* **2007**, 129, 4526-4527.

[13] A. Costela, I. García-Moreno, L. Cerdan, V. Martin, O. Garcia and R. Sastre, *Adv. Mater.,* **2009**, 21, 4163-4166.

[14] V. Martín, J. Bañuelos, E. Enciso, I. López-Arbeloa, A. Costela and I. García-Moreno, *J. Phys. Chem. C,* **2011**, 115, 3926-3933.

[15] E. Enciso, A. Costela, I. García-Moreno, V. Martín and R. Sastre, *Langmuir,* **2010**, 26, 6154-6157.

[16] F. López Arbeloa, T. López Arbeloa, I. López Arbeloa, A. Costela, I. García-Moreno, J. M. Figuera, F. Amat-Guerri and R. Sastre, *Appl. Phys. B,* **1997**, 64, 651-657.

[17] F. López Arbeloa, I. Llona Gonzalez, P. Ruiz Ojeda and I. López Arbeloa, *J. Chem. Soc. , Faraday Trans. 2,* **1982**, 78, 989-994.

[18] R. W. Chambers, T. Kajiwara and D. R. Kearns, *J. Phys. Chem.,* **1974**, 78, 380-387.

[19] A. Devaux, G. A. Calzaferri, I. Miletto, P. Cao, P. Belser, D. Bruhwiler, O. Khorev, R. Haner and A. Kunzmann, *J. Phys. Chem. C,* **2013**, 117, 23034-23047.

[20] J. R. Lakowicz, H. Szmacinski, K. Nowaczyk, K. W. Berndt and M. Johnson, *Anal. Biochem.,* **1992**, 202, 316-330.

[21] E. M. Purcell, *Phys. Rev.,* **1946**, 69, 674-674.

[22] H. Schniepp and V. Sandoghdar, *Phys. Rev. Lett.,* **2002**, 89, 257403.

[23] C. Wu, Y. Zheng, C. Szymanski and J. McNeill, *J. Phys. Chem. C,* **2008**, 112, 1772-1781.

[24] L. Wang, Y. Liu, F. Chen, J. Zhang and M. Anpo, *J. Phys. Chem. C,* **2007**, 111, 5541-5548.

[25] J. R. Lakowicz, *Principles of Fluorescence Spectroscopy,* Springer, Singapore, **2006**.

[26] J. P. S. Farinha and J. M. G. Martinho, *J. Phys. Chem. C,* **2008,** 112, 10591-10601.

[27] A. Yekta, M. A. Winnik, J. P. S. Farinha and J. M. G. Martinho, *J. Phys. Chem. A,* **1997**, 101, 1787-1792.

[28] B. Valeur and M. N. Berberan-Santos, *Molecular Fluorescence: Principles and Applications,* Wiley-VCH, Weinheim, **2013**.

[29] I. López-Arbeloa, *J. Photochem.,* **1980,** 14, 97-105.

[30] N. J. Turro, V. Ramamurthy and J. C. Scaciano, *Modern Molecular Photochemistry of Organic Molecules,* University Science Books, Sausalito, **2010**.

[31] A. B. Descalzo, C. Somoza, M. Moreno-Bondi and G. Orellana, *Anal. Chem.,* **2013**, 85, 5316-5320.

[32] R. Ghosh Chaudhuri and S. Paria, *Chem. Rev.,* **2012**, 112, 2373-2433.

[33] S. Wei, Q. Wang, J. Zhu, L. Sun, H. Lin and Z. Guo, *Nanoscale,* **2011**, 3, 4474-4502.

CHAPTER 4

Energy Transfer Cassettes

In the preceding sections the studied energy transfer process was intermolecular via FRET pathway exclusively. One of the most spread alternatives to promote fully efficient EET is by a molecular assembly in which donor and acceptors are covalently linked via an adequate spacer [1,2]. The low donor-acceptor distances in such multichromophoric structures -called cassettes- ensures a highly efficient intramolecular FRET mechanism (through-space) [3,4], but, if the multichromophoric arrangement is the adequate, an energy transfer process via through-bond mechanism (TBET, see chapter 1 about energy transfer), characterized to be extremely fast (picoseconds/femtosecond scale), can be switched on [5,6].

The improvement of the EET efficiencies in these molecular cassettes have recently boosted their use to enhance and optimize the optical properties of fluorescent dyes as well as to overcome some of their inherent limitations and weaknesses, such as the low absorption capability over a broad spectral region and the high photobleaching rate [7]. Besides, their large pseudo-Stokes shift and improved photostability deserve special interest in biophysics science and technology due to the reduced background interferences in bioimaging and sensing applications, since the emission can be monitored far away from the excitation wavelength.

The molecular design is a key factor to achieve fully efficient EET processes in these cassettes. Thus, donor and acceptor should be linked at adequate positions via suitable bridges to retain their identity in the whole structure. While for FRET processes a suitable spectral overlap is the fundamental factor to enable the dipole-dipole coupling, for TBET process an orbital overlap (σ type, see sections 1.3 and 1.4) is required, which can be achieved with conjugated spacers. It is noteworthy that when FRET is the dominant mechanism the resolution/brightness of the system will be constrained by the spectral overlap integral of donor fluorescence and acceptor absorption bands, whereas if TBET prevails the resolution is no longer restricted by this overlapping grade. Therefore, the emissive properties of the cassettes will depend strongly on the energy-transfer mechanism taking place in the light-harvester molecular antenna. Anyway, in most of these dyads where the donor and acceptor are

covalently linked and arranged to promote TBET, it is very likely that the FRET mechanism is also taking place simultaneously, and it is not an easy task to discern the contribution of each one [8].

This powerful strategy in molecular engineering has been exploited in light-harvesting systems [9,10] and fluorescent molecular probes [11,12] but not often applied to enhance the lasing performance. To properly address this last issue the chapter will be focused on the development of TBET cassettes based on multichromophoric dyes (dyads) with enhanced photophysical and laser properties.

The molecular cassettes were synthesized by Prof. Y. Xiao (Dalian University of Technology, China) whereas the evaluation of their lasing properties was carried out by Prof. I. García-Moreno and Prof. A. Costela (Instituto Rocasolano, CSIC, Madrid). Additional information can be found in the corresponding attached articles.

4.1. TBET CASSETTES BASED ON BODIPY

As stated above in section 2.2.1, BODIPY dyes have received special attention by the scientific community in multitude and diverse application fields ranging from lasing to sensing or biomedicine due to their unique and excellent photophysical properties [13-15]. Probably, their most relevant characteristic is that the chromophoric core (boradiazaindacene) is ready available for a multitude of chemical reactions, which allows an exhaustive functionalization of the core with a large battery of functional groups. Moreover, such substitution pattern modulates the photophysical properties of the resulting BODIPY [16,17]. As a matter of fact, dyes with tailored spectral shifts can be nicely developed. In this sense, we took advantage of this straightforward procedure to tune the photophysical properties of the fluorophores and span the absorption over a broad spectral region simply using dyes coming from such family. Here, a novel BODIPY with extended conjugation via the attachment of acetylenephenyls at positions 2 and 6 has been accurately studied. The scaffolding of the molecular cassette was carried out by the direct integration of two BODIPYs (acting as energy donors) to the aryl ring of the above red-edge BODIPY (acting as energy acceptor) (Figure 4.1). The tailored design of the subunits forming the multicromophoric arrangement provides a system which absorbs and emits light in different parts of the electromagnetic spectrum thanks to the noticeable divergence in the molecular structures of the BODIPY dyes forming the cassette.

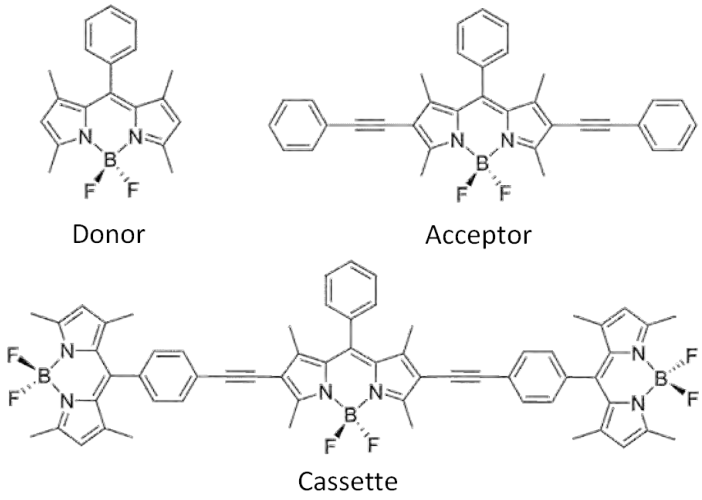

Figure 4.1. Molecular structure of the cassette based on BODIPY accompanied by donor and acceptor units.

The absorption spectrum (Figure 4.2.b) of the dyad is just the sum of the spectral bands corresponding to the free donor (500 nm) and acceptor (570 nm) fragments, confirming that each subunit retains its identity even after the covalent linkage, which means that the π system of the donor and the acceptor are electronically decoupled at least in the ground state. The methyl groups at positions 1 and 7 of the pendant side BODIPYs lock the aryl in a nearly orthogonal disposition (Figure 4.2.a). Therefore, the steric congestion of the rigid structure is enough to avoid the electronic coupling (resonant interaction) between both chromophores, supporting that the molecular design was adequate.

In this very weak coupling regime it is possible to excite selectively each fragment composing the cassette. The fluorescence spectrum of the multi-BODIPY under selective excitation of the donor moiety at 470 nm results in a very weak residual emission from the donor (510 nm) accompanied by a strong and dominant emission from the acceptor (600 nm) (Figure 4.2). Besides, the excitation spectrum recorded fixing the emission wavelength in the acceptor fluorescence region matches perfectly with the absorption spectrum (Figure 4.2), where the bands of the parent fluorophores are clearly distinguished. These results indicate that an extremely efficient intramolecular EET is taking place from the donor to the acceptor. One way to evaluate the EET efficiency is by the variation of the fluorescence quantum yield of the free acceptor upon presence of the donor (see chapter 1). Indeed, the fluorescence quantum yield of the cassette excited at 470 nm (0.59) is almost the same to that

recorded for the free acceptor excited at 575 nm (0.57) which is a clear proof of the high probability of EET in the cassette.

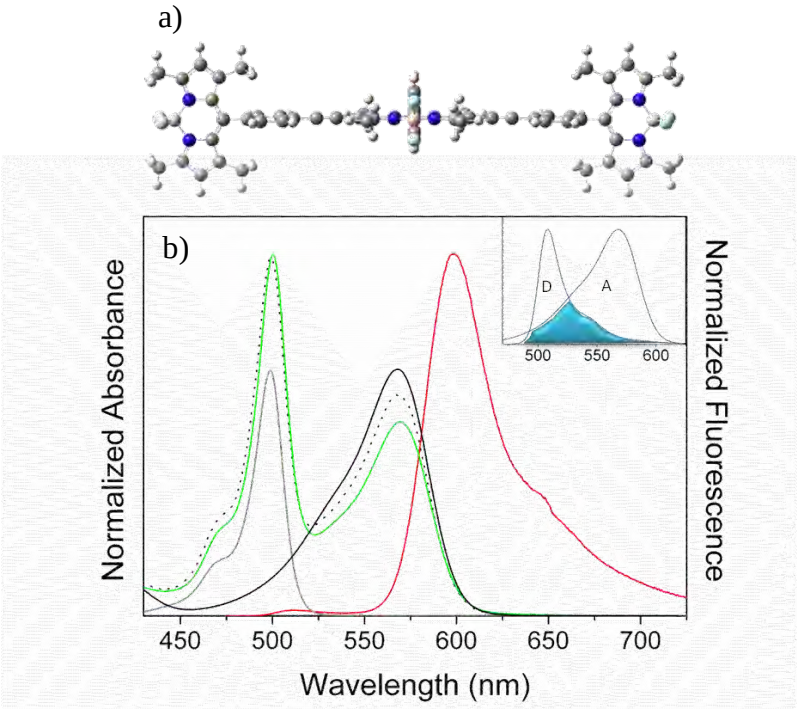

Figure 4.2. a) Ground state geometry of the BODIPY cassette optimized at b3lyp/6-31g level using Gaussian 09. b) Absorption (green), fluorescence (red) and excitation (dotted) spectra of the cassette. The absorption spectra of donor (grey) and acceptor (black) are also shown. Inset; spectral overlap between donor fluorescence and acceptor absorption bands.

As the emissive properties of the cassettes are strongly dependent on the energy transfer mechanism, such as "through-space" or "through-bond" pathways, it is convenient to ascertain the contribution of each one to the whole energy transfer process. Nevertheless, this is not a trivial task especially in cassettes where donor and acceptor distances are extremely short and the spectral as well as the orbital overlap is feasible (see sections 1.2 and 1.4). In the herein developed cassette, the imposed geometrical restrictions led to a nearly perpendicular disposition of the donor and acceptor transition moments (Figure 4.2.a), which are located along the longitudinal of the central indacene core, obstructing the dipole-dipole coupling (the orientation term κ^2 tends to zero in perpendicular arrangements) (see section 1.2). Therefore, it can be concluded that the intramolecular EET takes place mainly via TBET mechanism.

The dynamics of the EET process in the cassette can be nicely followed by time-resolved emission techniques. The time-resolved emission spectra (TRES) recorded upon donor excitation (470 nm) (Figure 4.3.a) showed a pronounced and fast quenching of the donor, while in turn the emission of the acceptor progressively increased due to the fast energy transfer process. Moreover, while the fluorescence

decay curve monitored at the acceptor moiety (600 nm) in the cassette is monoexponential (3.46 ns) and almost identical to that of the free dye (3.78 ns), the lifetime related to the donor part of the cassette (monitored at 510 nm) is strongly quenched and a multiexponential fit is required (Table 4.1). The shortest dominant lifetime (~ 20 ps; 92%), below the detection limit of our equipment, is assigned to non-radiative deactivation of the donor excited state via the ultrafast TBET process to the acceptor, whereas the longest lifetime (3.17 ns; 3%) is attributed to the residual donor emission. It is noteworthy to mention that when the emission is monitored at the acceptor moiety, the growing of the fluorescence decay curve (common in energy transfer processes) is negligible because of the rapidity of the process (TBET), undetectable by our fluorimeter.

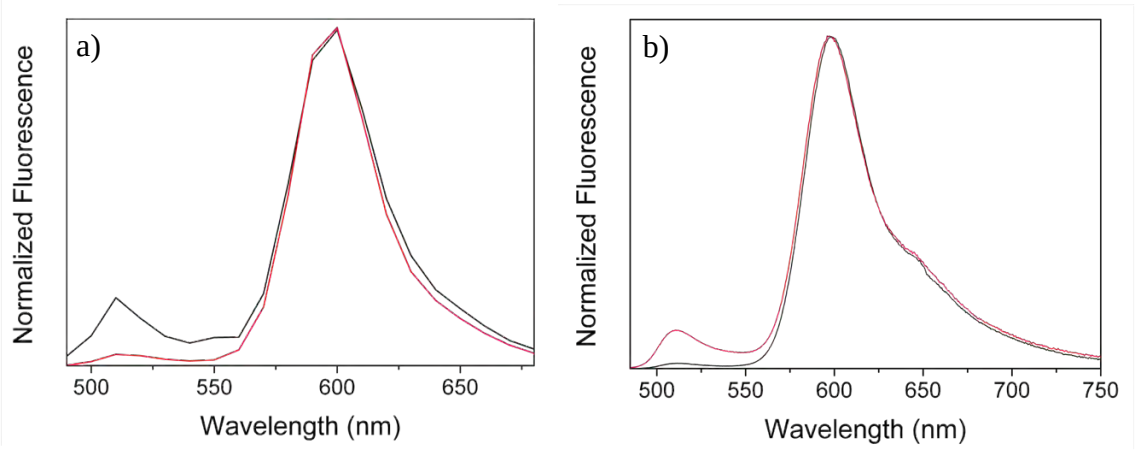

Figure 4.3. a) Normalized time-resolved emission spectra of the BODIPY cassette recorded at different times after excitation; 120 ps (black) and 4 ns (red). b) Normalized fluorescence spectra in diluted (black) and concentrated (red) solutions.

However, the assignment of the intermediate lifetime (1.68 ns; 5% contribution) was not clear at all. In order to get a deeper insight, the photophysical properties of the cassette were studied at higher concentrations (0.7 mM). The fluorescence spectrum (cuvettes pathway 0.1 mm in front-face configuration to minimize re-absorption/re-emission effects) after donor excitation at 470 nm (Figure 4.3.b) showed an increase of the residual emission of the donor when compared to diluted solutions. The corresponding fluorescence decay curve (Table 4.1) at those conditions also needed a triexponential deconvolution but differed with respect to the diluted solutions in some points. In concentrated solutions the short lifetime assigned to the TBET increased from 20 to 100 ps and its contribution was lower, while the longer lifetimes were

similar but with much higher contributions, especially in the intermediate lifetime (contribution › 50%).

Table 4.1. Photophysical properties of the cassette in diluted and concentrated solutions of ethyl acetate. The properties of the free donor are included for comparison.

Dye	λ_{exc}	λ_{em}	τ(ns)	λ_{exc}	λ_{em}	τ(ns)
Free donor	470	510	3.55	575	600	3.78
Cassette ($2\cdot10^{-6}$ M)	470	510	0.020 (92%) 1.68 (5%) 3.17 (3%)	575	600	3.46
Cassette (0.7 mM)	470	510	0.103 (27%) 1.91 (54%) 3.58 (19%)	470/ 575	600	3.48

These results point out that at high concentrations the distance between cassette molecules is close enough as to switch on an intermolecular FRET mechanism, apart from the unquestionable intramolecular TBET mechanism, being the former one the responsible of the intermediate lifetime. Indeed, The FRET process is usually slower than TBET, fact that is confirmed in the behaviour of the lifetimes (Table 4.1) [18]. The FRET probability increased remarkably at high concentrations because while for the intramolecular process the orientation factor κ^2 tends to 0, for the intermolecular process $\kappa^2 = 2/3$ owing to the random distribution of the molecules (see section 1.2). Nevertheless, the intermediate lifetime observed even in diluted solution (but with minor contribution) points out that an intramolecular FRET process slightly contributes to the whole EET process confirming that the κ^2 is nearly zero, which should be a consequence of a not perfect orthogonal disposition of the donor and acceptor transition dipole moments. Consequently, the contribution of each energy transfer mechanism changes with the concentration, thereby, at high concentrations the intermolecular through-space energy transfer gets more relevance.

To put the above results in a proper perspective and unambiguously assign the donor lifetimes in presence of acceptor, we prepared a concentrated donor/acceptor physical mixture to eliminate the contribution of the TBET process and exclusively analyze the intermolecular FRET mechanism. The mixture composition was fixed the same as that in the multichromophoric BODIPY (donor proportion twice of the

acceptor) for direct comparison. As expected, the acceptor emission was detected upon donor excitation, indicating that the FRET is viable at high concentrations (Figure 4.4.a). However, the donor emission prevailed over the acceptor one, supporting again that in the dyad the TBET rules the whole EET process. As consequence, the fluorescence decay curves of the physical donor/acceptor mixture differ from those of the chemically linked donor-acceptor (cassette), as reflected in the Figure 4.4.b. The fast lifetime recorded in the cassette was no longer detected, and the decay curve monitored at the donor was properly fitted as biexponential; the short and minor lifetime of 1.93 ns is assigned to the donor quenching by the intermolecular FRET, while the long and dominant one of 3.47 ns is ascribed to the donor emission itself.

Therefore, the assignation of each lifetime has been clearly confirmed in the BODIPY cassette: (i) the fastest lifetime to the intramolecular TBET donor quenching, (ii) the intermediate one to the FRET (enhanced at high concentration by the intermolecular process) and (iii) the longer one to the donor residual emission.

a)

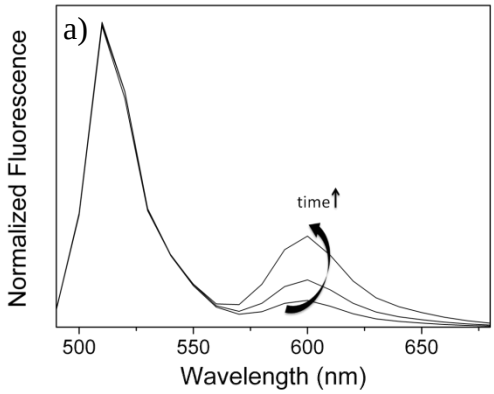

b)

Systems	τ(ns) λ_{exc} = 470 λ_{em} = 510	τ (ns) λ_{exc} = 470 λ_{em} = 600	τ (ns) λ_{exc} = 575 λ_{em} = 600
Cassette (0.7 mM)	0.103 (27%) 1.91 (54%) 3.58 (19%)	3.48	3.48
Physical donor/acceptor mixture	1.93 (18%) 3.47 (82%)	0.30 (< 0) 2.62 (< 0) 4.40 (> 0)	4.00

Figure 4.4. a) Normalized time-resolved emission spectra of a physical donor-acceptor mixture at high concentrations recorded at different times after excitation; 0.2 ns, 2.5 ns and 5 ns. b) Table containing the fluorescence lifetime data for the donor/acceptor physical mixture and the corresponding donor-acceptor covalently linked (cassette).

As consequence of the improvement of the BODIPY photophysical properties in the TBET cassette, this multicolour absorbing dye also exhibits highly efficient and photostable laser action under drastic pumping conditions compared to that of free donor and acceptor dyes. In fact, the laser properties of the free acceptor under 532 nm standard pumping are poor since it absorption capability is lower in this region, requiring a much higher concentrations (10 times superior) than in the cassette. Besides, pumping can be performed at the donor region (lower wavelengths) where more excitation standard sources are available. Even at the high concentrations required for the proper laser action of the free acceptor, its efficiency (15%) is less than

a half compared to that reached in the cassette (32%). Furthermore, the molecular cassette presents an improved photostability in comparison with the acceptor moiety alone, since it maintains 100% of its initial emission after $1x10^{15}$ pulses at a high repetition rate, whereas the free acceptor loses 10% of its initial emission under the same pumping conditions.

In conclusion, an efficient TBET cassette based on the direct integration of two donor BODIPY units to one acceptor BODIPY has been successfully developed. Efficient red-shifted fluorescence emission is achieved upon excitation over a broad spectral range, which is reflected in a highly efficient and photostable laser action in both, liquid solutions and solid-state, since the pumped dye differs from the emitting one. As a result, this molecular cassette can be considered as a suitable alternative to ameliorate the laser action and develop first class photonic systems for advanced applications in optoelectronics and biophotonics.

Further information comprising the photphysical and lasing properties of the multichromophoric BODIPY can be found in the enclosed article published in the *Chemical Communications*.

ChemComm

View Online
Dynamic Article Links

Cite this: *Chem. Commun.*, 2011, **47**, 11513–11515

www.rsc.org/chemcomm

COMMUNICATION

Unprecedented laser action from energy transfer in multichromophoric BODIPY cassettes†

Yi Xiao,*[a] Dakui Zhang,[a] Xuhong Qian,*[b] Angel Costela,[c] Inmaculada Garcia-Moreno,*[c] Virginia Martin,[c] M. Eugenia Perez-Ojeda,[c] Jorge Bañuelos,*[d] Leire Gartzia[d] and Iñigo López Arbeloa[d]

Received 29th June 2011, Accepted 1st September 2011
DOI: 10.1039/c1cc13874j

A cassette molecule, featuring direct integration of two donor BODIPY units to one acceptor BODIPY unit, was conveniently developed as the first highly "through-bond energy transfer" (TBET) laser dye. This multicolor absorbing dye exhibited highly efficient and photostable laser action under drastic pumping conditions.

Renewed interest has been focused on the design and synthesis of fluorophores with enhanced optical properties for newer applications in medical, analytic, physics, and biophysics science and technology.[1] Although a wealth of organic dyes are known, unfortunately they still have to overcome some limitations related to: (1) low absorption over broad spectral regions and (2) high photobleaching rate, which becomes especially important under drastic excitation conditions such as those required in single molecule detection methods.[2] An attractive approach to overcome these drawbacks has been the straightforward synthesis of energy transfer cassettes to span the absorption spectra of dyes, which result in large pseudo-Stokes shifts and, not least important, in improved photostability.[3] This powerful strategy has been exploited in light-harvesting systems and sensors but never focused to enhance lasing properties for advanced applications.

To address this issue, we have synthesized a rigid energy transfer cassette, **ET-2**, *via* a facile and efficient strategy tandem Sonogashira coupling (Chart 1 and ESI†). Different from other previous multichromophoric dyes with donor and acceptor connected by flexible and relatively long chains,[3] trifluorophoric **ET-2** features compact integration of two donor BODIPY (**BDP-1**) units to one acceptor BODIPY (**BDP-2**) by a single C–C bond which leads to a short donor–acceptor distance and favours ultrafast excited energy transfer. The strong steric congestion blocks the twist of the single bond spacer and forces the connected two parts to take a perpendicular orientation, avoiding the system to behave as a single conjugated dye.

The absorption spectrum of **ET-2** is essentially equal to the sum of the absorption bands of the free **BDP-1** donor (500 nm) and **BDP-2** acceptor (570 nm) components (Fig. 1). This indicates that the **ET-2** fluorophore behaves as a cassette since both chromophoric units are electronically decoupled in the ground state and remain as individual patterns in the multichromophoric compound, according to the theoretically predicted optimized ground-state geometry (Fig. 1, inset). The fluorescence spectrum of **ET-2** under excitation at 470 nm, where the donor absorbs intensively while the acceptor hardly absorbs, results in a very weak residual emission near 510 nm from the donor and a strong emission centred at 600 nm from the acceptor (Fig. 1). Thus, the shift between fluorescence and absorption maxima is higher than 6000 cm^{-1} exciting the cassette at the $S_0 \rightarrow S_1$ donor transition. In addition, the corresponding excitation spectrum of **ET-2**, recorded monitoring the emission in the acceptor region (660 nm), perfectly matches the corresponding absorption spectrum and clearly shows the absorption bands of the parent chromophores. These results indicate a highly efficient intramolecular excitation energy transfer from the donor to the acceptor. Fluorescence quantum yield data provide also solid evidence for this energy transfer phenomena. Since the corresponding bands from the donor and acceptor units are resolved in the **ET-2** fluorescence spectrum, separate quantum yields (Φ) for

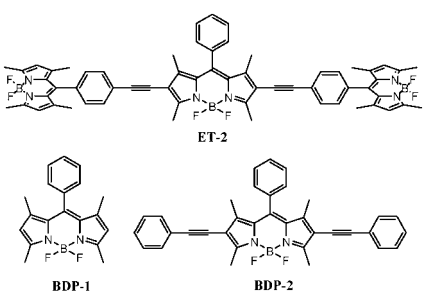

Chart 1 Molecular structures of **ET-2** cassette and donor **BDP-1** and acceptor **BDP-2** units.

[a] *State Key Laboratory of Fine Chemicals, Dalian University of Technology, Dalian 116012, China. E-mail: xiaoyi@dlut.edu.cn; Fax: 86 411 84986251; Tel: 86 411 84986252*
[b] *Shanghai Key Laboratory of Chemical Biology, East China University of Science and Technology, Shanghai 200237, China. E-mail: xhqian@ecuct.edu.cn*
[c] *Instituto de Química-Física "Rocasolano", CSIC, Serrano 119, 28006 Madrid, Spain. E-mail: iqrfm84@iqfr.csic.es*
[d] *Dpto Química Física, Universidad del País Vasco (UPV/EHU), 644, 48080 Bilbao, Spain. E-mail: jorge.banuelos@ehu.es*

† Electronic supplementary information (ESI) available: Experimental procedures and full characterizations data. See DOI: 10.1039/c1cc13874j

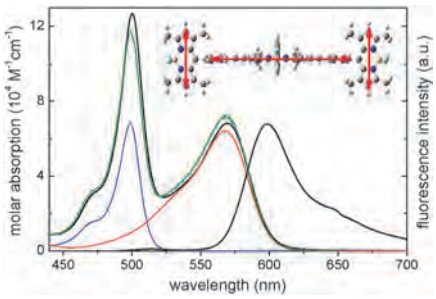

Fig. 1 Absorption (black), fluorescence (λ_{exc} = 470 nm, black) and excitation (λ_{em} = 660 nm, green) spectra of **ET-2**, together with transition moment orientations. The absorption spectra of **BDP-1** (blue) and **BDP-2** (red) are also shown.

both emissions can be defined and calculated (Table 1). The fluorescence quantum yield of **ET-2** (0.59) is almost independent of the excitation wavelength, within the donor and acceptor absorption ranges, and is quite similar to that exhibited by the free **BDP-2** component excited at 575 nm. The absence of the fluorescence quantum yield dependence suggests almost complete energy transfer from the donor to the acceptor. Furthermore, taking into account that the **BDP-2** dye excited at 470 nm exhibits a fluorescence quantum yield near zero, the **ET-2** dye allows reaching a significant "fluorescence enhancement", defined as the ratio of the fluorescence intensity of the cassette to that of corresponding acceptor excited at the short wavelength. The rigidity of the **ET-2** cassette plays a main role since this avoids the deactivation *via* internal conversion mechanism and enhances the efficiency of the energy transfer process. So, the cassette **ET-2** not only extents the absorption of **BDP-2** into the blue spectral region but also converts it in a more sensible chromophore activated for two donor fragments.

In the **ET-2** cassette, the donor and acceptor units connected by conjugated linker may transfer energy *via* different pathways,[4] including "through-space" energy transfer as well as other pathways usually referred to as "through-bond" energy transfer. To ascertain the contribution of each to the whole energy transfer process may not be a simple matter, especially in cassettes with donor and acceptor fragments relatively close and with flexible linkers. As shown in Fig. 1, the perpendicular disposition of the donor and acceptor transition moments in the **ET-2** molecule eliminates the orientation term κ in the Förster equation.[5] Thus, even though the spectral overlap between the donor emission and the acceptor absorption is good, the dipole–dipole contribution to the intramolecular energy transfer should be negligible, and, consequently, this process should take place *via* a through-bond mechanism.[6]

Table 1 Photophysical properties in ethyl acetate[a]

Dye	$\varepsilon/\lambda_{abs}$	λ_{exc}	λ_{em}	Φ	τ/ns
BDP-1	71600 (503)	470	510	0.66	3.55
BDP-2	65800 (568)	575	600	0.57	3.78
ET-2	127000 (503)	470	510	~0	0.020 (92%)
(2 μM)	68200 (569)				1.68 (5%)
					3.17 (3%)
		470	600	0.59	3.46
		575	600	0.59	3.46
ET-2		470	510		0.103 (27%)
(0.7 mM)					1.91 (54%)
					3.58 (19%)
		470/575	600		3.48

[a] $\varepsilon/M^{-1}cm^{-1}$: molar absorption; λ_{abs}, λ_{exc}, λ_{em} (nm): absorption, excitation and emission wavelengths, Φ: fluorescence quantum yield; τ: fluorescence lifetime.

Time-resolved emission techniques allow getting insight into the dynamics of the energy transfer process. The acceptor fluorescence time profile in the **ET-2** cassette appears to be monoexponential and is essentially identical to that of the free **BDP-2** dye. However, the lifetime of the donor, 3.55 ns, is drastically affected by the presence of the acceptor, since upon binding to **BDP-2** in **ET-2**, its fluorescence decay becomes multiexponential (Table 1). The lowest contributions correspond to a long lifetime (3.17 ns), assigned to the residual donor emission, and to an intermediate lifetime (1.68 ns) whose assignment will be discussed later. The main contribution corresponds to very short lifetime (~20 ps), in the limit of our single-photon counter time-resolution, which is assigned to the energy transfer process. This fast emission from the donor together to the highly increased fluorescence quantum yield from the acceptor (59%), confirm the high efficiency of the energy transfer ($k_{ET} \sim 5 \times 10^{10}$ s^{-1}) *via* a through-bond mechanism.[6] Scanning the gated fluorescence spectrum of **ET-2** at different delay times following excitation at 470 nm produces a sequence of time-resolved emission spectra (Fig. 2), which show a decay of the donor emission, quenched by this fast energy transfer, and the growth of the acceptor emission.

The photophysics of the **ET-2** cassette is sensitive to its concentration, which allows the unambiguous assignment of the intermediate lifetime observed above. The analysis of its fluorescence, upon excitation at 470 nm and at high concentration (0.7 mM), reveals an increase in the donor/acceptor emission ratio with respect to that recorded in diluted solutions together to a different weight of each lifetime in the multiexponential fit of the decay curve (Table 1). This result could be indicating that some energy may be transferred through an intermolecular Förster resonance process (*inter*-FRET) *via* dipole–dipole coupling assuming randomly distributed neighboring transition moments. Hence, the overall excitation energy transfer in **ET-2** should result from the contribution of intramolecular through-bond and intermolecular through-space mechanisms. Therefore, at high concentration, the lifetime component assigned to the through-bond energy transfer increases, from 20 to 100 ps, decreasing its contribution,

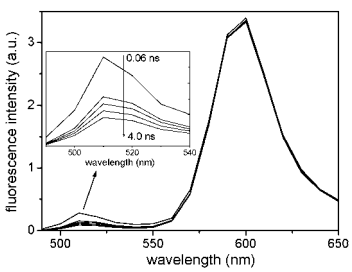

Fig. 2 Normalized time-resolved emission spectra of **ET-2** at different times after excitation; 0.06, 0.3, 1, 2 and 4 ns.

Table 2 Laser properties (efficiency, η and maximum output wavelength λ_{out}/nm) of **ET-2** and **BDP-2** dependent on pump sources and solvents

	ET-2						**BDP-2**					
λ_{pump}/nm	500		532		570		500		532		570	
c/M	1.4×10^{-4}		8.0×10^{-4}		2.2×10^{-4}		1.2×10^{-3}		4.0×10^{-4}		1.6×10^{-4}	
Solvent	η	λ_{out}	η	λ_{out}	η	λ_{out}	η	λ_{out}	η	λ_{out}	η	λ_{out}
Ethyl acetate	32%	609	32%	624	39%	610	15%	622	35%	619	36%	610
THF	21%	612	—	—	24%	615	10%	612	24%	622	24%	619
CH_2Cl_2	26%	613	23%	624	28%	616	11%	623	30%	619	28%	616

from 92 to 27%, to the total fluorescence decay curve of **ET-2** at 510 nm. At the same time, the contribution of the longest lifetime increases, according to the observed increase of the donor emission, which could be related to donor–donor energy migration (see ESI†). Even more significant is the increase of the intermediate lifetime, attributed to the donor–acceptor *inter*-FRET process, which appears also in diluted solution but with a ten times lower contribution (Table 1). The lifetime assignment is also confirmed adding free donor or acceptor to highly concentrated solutions of **ET-2** (ESI†).

The optimized photophysics of the **ET-2** cassette leads to its enhanced behaviour as a laser dye compared to that of the donor and acceptor components, since it lases efficiently under pumping at three different relevant wavelengths; 500, 532 and 570 nm (Table 2). Upon pumping at 500 nm, the laser properties of **BDP-2** are inferior due to its lower absorption in this region, which requires a concentration 10 times higher than that of **ET-2** (Fig. 3a). But even at this concentration, or because such a high concentration is required, the highest laser efficiency of **BDP-2** is only 15%, less than half the efficiency reached with **ET-2** (32%). In addition, under excitation at 500 nm, the lasing threshold of **BDP-2** (0.9 mJ) is much higher than that of **ET-2** (0.4 mJ). Moreover, **ET-2** exhibits excellent photostability, even better than that of **BDP-2**, since **ET-2** maintains 100% of its initial emission after 1×10^5 pump pulses at 10 Hz repetition rate, while **BDP-2** loses 10% of its initial emission under the same pumping conditions (Fig. 3b). These encouraging results led us to initiate a systematic investigation on the applications of **ET-2** in solid lasers. In a preliminary study, this dye dissolved in PMMA and pumped at 500 nm lases at 620 nm with an efficiency of 24% and high photostability, maintaining 93% of its initial emission after 1×10^5 pump pulses.

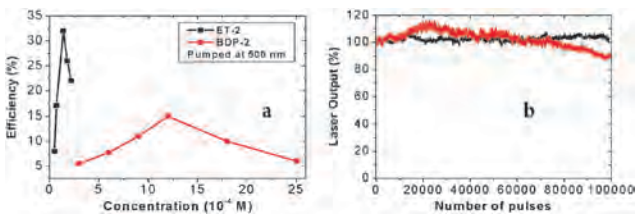

Fig. 3 (a) Laser efficiency of **ET-2** (black) and **BDP-2** (red) dependent on the concentrations in ethyl acetate (λ_{pump} = 500 nm) (b) normalized laser output of **ET-2**and **BDP-2** as a function of the number of pump pulses at 532 nm, 5.5 mJ and 10 Hz repetition rate.

In summary, the highly straightforward synthesis of an efficient "through-bond energy transfer" cassette allows enhancing significantly the already valuable photophysical and laser properties of BODIPYs. Compared to "unmodified" BODIPY dyes, the new multichromophoric system spans the absorption spectrum into a broad region, exhibiting high molar extinction coefficients with enhanced fluorescence emission and increased Stokes shifts. This enhanced photophysics assures an unprecedented highly efficient and photostable laser action under drastic pumping conditions from a cassette in both liquid solutions and solid-state, suggesting that the new photonic system could perform outstandingly in advanced applications in optoelectronics and biophotonics.

Y. X. thanks National Natural Science Foundation of China (No. 20876022) and the Fundamental Research Funds for the Central Universities (No. DUT10ZD114), and I. G.-M. and I. L. A. thank Spanish MICINN (MAT2010-20464-C04-01 and -C04-4, respectively, and TRACE2009-0144) for financial support.

Notes and references

1 (*a*) G. Ulrich, R. Ziessel and A. Harriman, *Angew. Chem., Int. Ed.*, 2008, **47**, 1184; (*b*) B. Abrams, Z. Diwu, O. Guryev, S. Aleshkov, R. Hingorani, M. Edinger, R. Lee, J. Link and T. Dubrovsky, *Anal. Biochem.*, 2009, **386**, 262; (*c*) G. Mitronova, V. Belov, M. Bossi, C. Wurm, L. Meyer, R. Medda, G. Moneron, S. Bretschneider, C. Eggeling, S. Jakobs and S. Hell, *Chem.–Eur. J.*, 2010, **16**, 4477.
2 (*a*) R. Tsien, L. Ernst and A. Waggoneri, Fluorophores for Confocal Microscopy: Photophysics and Photochemistry, in *Handbook of Biological Confocal Microscopy*, ed. J. Pawley, Springer, New York, 3rd edn, 2006, p. 338; (*b*) B. Huang, W. Wang, M. Bates and X. Zhuang, *Science*, 2008, **319**, 810; (*c*) J. Lippincott-Schwartz and S. Manley, *Nat. Methods*, 2009, **6**, 21.
3 (*a*) D. McQuade, A. Pullen and T. Swager, *Chem. Rev.*, 2000, **100**, 2537; (*b*) C. Wan, A. Burghardt, J. Chen, F. Bergström, L. Johansson, M. Wolford, T. Kim, M. Topp, R. Hochstrasser and K. Burgess, *Chem.–Eur. J.*, 2003, **9**, 4430; (*c*) A. Coskun and E. Akkaya, *J. Am. Chem. Soc.*, 2005, **127**, 10464; (*d*) X. Zhang, Y. Xiao and X. Qian, *Org. Lett.*, 2008, **10**, 29.
4 S. Speiser, *Chem. Rev.*, 1996, **96**, 1953.
5 J. Lakowicz, *Principles of Fluorescence Spectroscopy*, Kluwer Academic/Plenum Publisher, New York, 2nd edn, 1999.
6 (*a*) T. Kim, J. Castro, A. Loudet, J. Jiao, R. Hochstrasser, K. Burgess and M. Topp, *J. Phys. Chem. A*, 2006, **110**, 20; (*b*) R. Ziessel, C. Goze, G. Ulrich, M. Césario, P. Retailleau, A. Harriman and J. Rostron, *Chem.–Eur. J.*, 2005, **11**, 7366; (*c*) A. Harriman, L. Mallon, S. Goeb, G. Ulrich and R. Ziessel, *Chem.–Eur. J.*, 2009, **15**, 4553; (*d*) O. Bozdemir, Y. Cakmak, F. Sozmen, T. Ozdemir, A. Siemiarczuk and E. Akkaya, *Chem.–Eur. J.*, 2010, **16**, 6346; (*e*) J. Han, A. Loudet, R. Barhoumi, R. Burghardt and K. Burgess, *J. Am. Chem. Soc.*, 2009, **131**, 1642; (*f*) W. Lin, L. Yuan, Z. Cao, Y. Feng and J. Song, *Angew. Chem., Int. Ed.*, 2010, **49**, 375.

4.2. TBET CASSETTES BASED ON RHODAMINE-BODIPY PAIR

The conformation of these cassettes has been performed by the coupling of the two most widely known laser dyes nowadays; BODIPY (as energy donor) and rhodamine (as energy acceptor). Both components have been carefully chosen owing to their outstanding photophysical and lasing properties, taking advantage of their strong absorption and emission, and a high photostability compared to other common laser dyes. Besides, the suitable spectral overlap between the donor fluorescence and acceptor absorption bands of these fluorophores ensures the "through-space" energy transfer (FRET) process. In addition, to promote the TBET mechanism both fragments have been linked by rigid and conjugated linkers to allow the required electronic exchange [19,20]. The contribution of each mechanism to the whole EET process and the role that the structure of the cassette can play on it is one of the most interesting points to asses. To this aim, we have characterized in depth BODIPY-rhodamine dyads, which differ in the rigidity and length of the conjugated spacer groups (phenyl or acetylenephenyl) as well as in their linking positions (*meta* or *para* of the pendant aryl ring of the rhodamine) (Figure 4.5). In this way, we can carefully analyze the influence of the donor-acceptor distance and their relative orientation in the intramolecular EET efficiency.

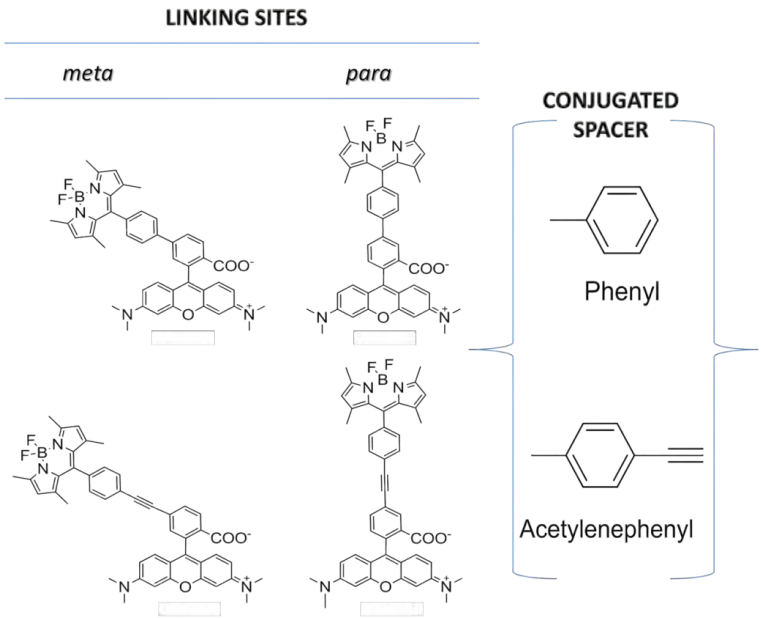

Figure 4.5. Molecular structures of BODIPY-rhodamine dyads linked by phenyl or para-acetylenephenyl spacer groups at the *meta* and *para* positions of the pendant ring of the xanthene.

The photophysical properties of these cassettes are controlled by the formation/opening of the spirolactone ring of the acceptor rhodamine (i.e., the interconversion between lactone (s) ↔ zwitterion (z) structures) which depends on the characteristics of the solvent (mainly polarity and acidity) (Figure 4.6) [21,22]. Accordingly, in apolar media the carboxylate attacks the central carbon in the xanthene leading to the spirolactone ring. As a result, the xanthene's delocalization is broken and their visible spectral bands are no longer present. Thus, just the absorption band of the BODIPY is detected in the cassette and the energy transfer process is interrupted (the dyad behaves as a single dye) leading to the emission from the BODIPY exclusively (Figure 4.6.b).

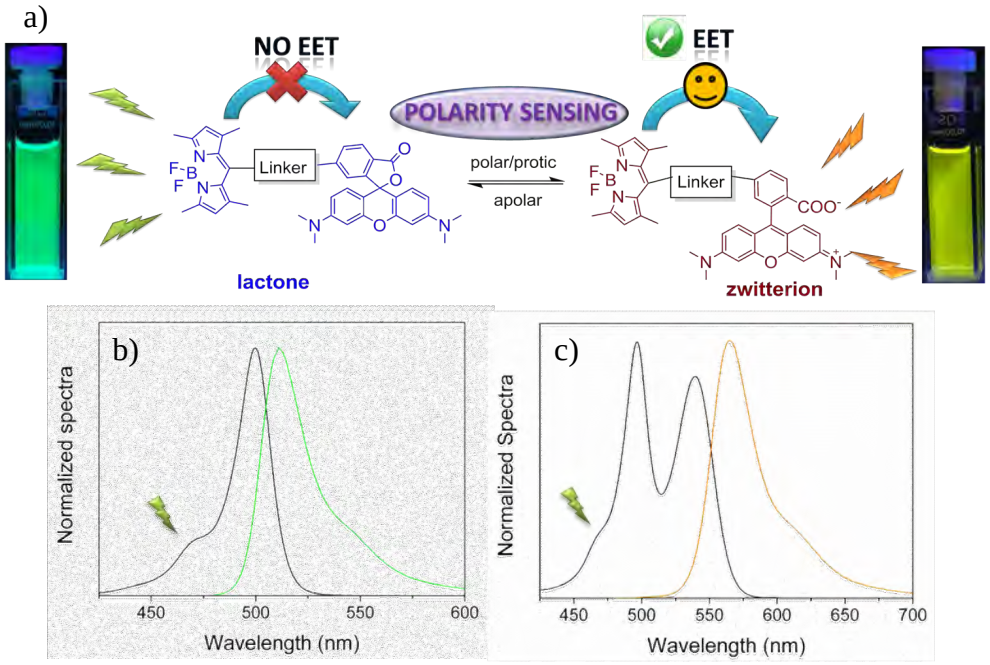

Figure 4.6. a) Schematic view of lactone (s) ↔ zwitterion (z) equilibrium of BODIPY-rhodamine cassettes and the implied on/off switching of the energy transfer process via variation of the polarity. b) Absorption (black) and fluorescence spectra (λ_{exc}=470 nm) (green) of a representative BODIPY-rodhamine cassette in apolar solvent (ethyl acetate). c) Absorption (black) and fluorescence spectra (orange) of the same dyad in a polar solvent (trifluoroethanol).

On the other hand, in polar protic solvents, the zwitterionic form is recovered and two absorption bands corresponding to the BODIPY (at higher energies) and rhodamine (at lower energies) units respectively are detected (Figure 4.6.c). The presence of both bands is ascribed to the electronic decoupling of the conjugated spacer with both, the BODIPY (steric hindrance induced by the 1 and 7 methyl groups of the BODIPY core adjacent to the aryl ring) and the rhodamine (the pendant phenyl is perpendicular with regard to the xanthene plane due to the sterical hindrance induced

by the *ortho* carboxilate). As consequence, the selective excitation of the BODIPY (470 nm) leads to a dominant rhodamine emission, indicating an efficient intramolecular EET process from the donor BODIPY to the acceptor rhodamine in these media (Figure 4.6.c).

Therefore, these novel cassettes are able to perform reversible on/off switching energy transfer processes by just varying the polarity of the media (Figure 4.6). Thereby, in apolar solvents the green emission corresponding to the BODIPY dye is exclusively achieved (no cassette, just a BODIPY bearing a bulky fragment), whereas as the solvent polartity/acidity increases the energy transfer process is allowed (multichromophoric cassette) and gradually enhanced, leading to the bright yellow-orange emission from the acceptor rhodamine upon donor excitation via a extremely fast EET. Indeed, the donor emission in the most polar media, where the spirolactone ring formation is completely avoided, is almost negligible. Accordingly, the donor is quenched and its decay curve is described by up to three exponential components (Figure 4.7.b), which became faster in polar media where the zwitterionic form prevails. This outstanding property makes these BODIPY-rhodamine cassettes suitable candidates not only for lasing purposes but also as molecular probes capable of monitoring the polarity of the surrounding media.

As aforementioned, it is not an easy task to asses the dominant EET mechanism in a system in which both FRET and TBET are ongoing simultaneously. One strategy to separate both mechanisms is by measurements at low enough temperatures, where activated electronic mechanisms (although the TBET mechanism is not well defined, most of the authors agree in the presence of an electronic exchange, see section 1) are hampered [4,23]. The direct comparison of the fluorescence spectra recorded upon donor excitation at room temperature and at 77 K (Figure 4.7) revealed that, although the EET was still present, the donor/acceptor emission ratio increased hugely at 77K, thus indicating that the EET was much less efficient. In the frozen solution the TBET was avoided and the recorded EET was exclusively characteristic of a FRET process. These results indicate that the extremely efficient EET processes of these cassettes at room temperature should be due to a TBET, appointing it as the main mechanism for the EET process. Besides, at 77 K the shortest lifetime disappeared and the fluorescence-decay curve was analyzed as biexponential (Figure 4.7.b), pointing out that the fastest lifetime present at room temperature conditions should be assigned to the TBET process, whereas the

intermediate lifetime could correspond to the quenching caused by the FRET process, as was observed in the multiBODIPY cassette of the preceding section 4.1.

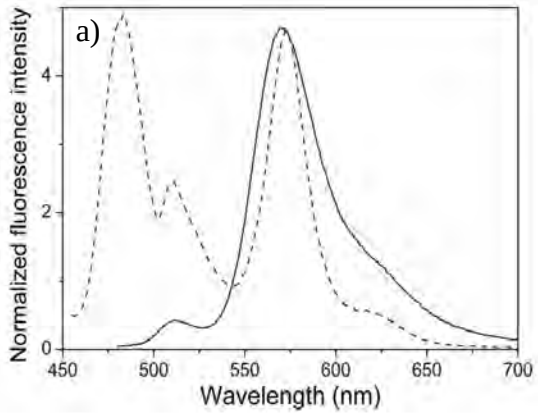

b)

τ (ns)	
T=25 ºC	**T=77 K**
0.05 (29%)	1.18 (47%)
1.24 (60%)	1.74 (53%)
2.72 (11%)	

Figure 4.7. a) Fluorescence spectra of the BODIPY-rhodamine dyad in ethanol upon donor (BODIPY) excitation recorded at 77 K (dashed line) and at room temperature (solid line). b) Table containing fluorescence emission lifetimes of the same dyad monitoring the emission in the donor (510 nm) under excitation of the donor (470 nm) at different temperatures.

Accordingly, the donor emission dynamics allow monitoring the efficiency of the EET process (Table 4.2); the fastest the donor decay the fastest the energy transfer. Thus, we will focus on the donor quenching to study the best spacer and donor-orientation to improve the EET efficiency. In this regard, the longer spacer (acethylenephenyl vs phenyl) and the *para* connection vs *meta* one ameliorate the EET efficiency as demonstrated by the shorter donor average lifetimes (Table 4.2).

To explain such trends the Förster analysis has been performed in each cassette to calculate the FRET rate constant (k_{FRET}), which depends on the spectral overlap (constant for each cassette) and the distance and mutual orientation of the transition dipole moments (κ^2) between donor-acceptor chromophores. Such values can be calculated by quantum-mechanical calculations and are given in Figure 4.8.

Table 4.2. Fluorescence lifetimes of rhodamine-BODIPY cassettes in solvents with increased polarity (ethyl acetate, ethanol and 2,2,2-trifluoroethanol) monitoring the emission in the donor region (λ_{exc} =510 nm) under excitation of the donor (λ_{exc} = 470 nm).

Spacer	Connection	Solvent		
		Ethyl acetate	EtOH	F_3-EtOH
Phenyl	***meta***	2.42	1.77	0.72
	para	2.47	1.54	0.65
Acetylenephenyl	***meta***	1.73	1.20	0.51
	para	1.80	0.84	0.16

For the phenyl spacer, it is noteworthy that the *para* disposition of the linker implied an increase of the donor-acceptor distance when compare to that of *meta* disposition (from 10.5 to 11.5 Å, whereas the κ^2 maintains invariable). Accordingly, the FRET probability (Figure 4.8) decreased for the former in disagreement with the experimentally observed increase of the EET efficiency, reflected by the shorter lifetime registered for the *para* arrangement (Table 4.2). Moreover, a lengthening of the spacer from phenyl to acetylenephenyl puts further away the donor from the acceptor with the consequent decrease of the FRET probability, again in discrepancy with the experimental trends.

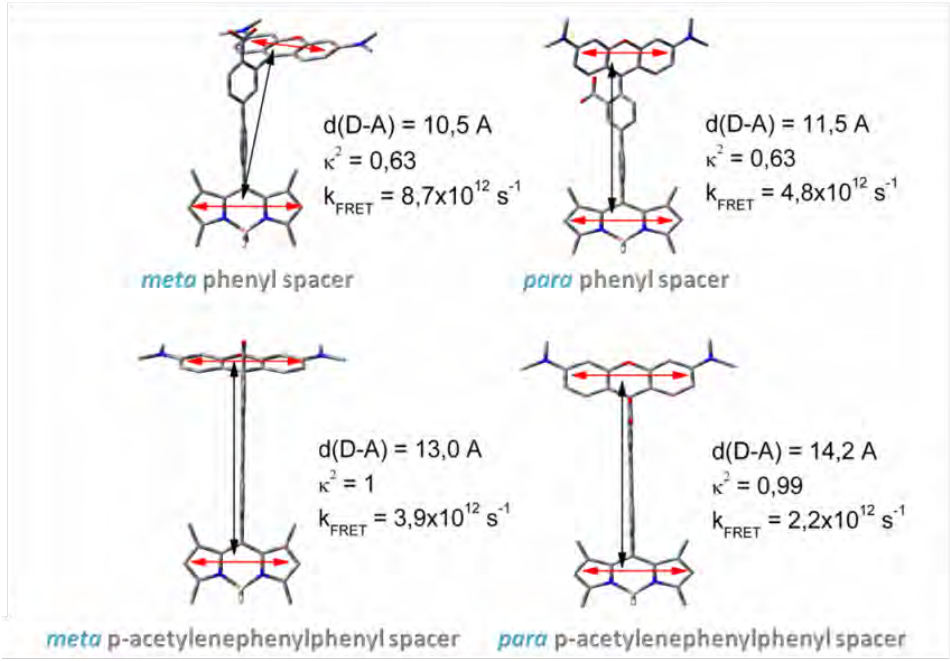

Figure 4.8. Ground state molecular structures of the cassettes optimized as the b3lyp/6-31g level, considering the solvent (methanol) as a continuum medium (PCM). The center to center donor-acceptor distance (black arrow) and the transition dipole moments (red arrow, placed along the longitudinal axis) are also represented. The Förster orientational factor κ^2 (calculated by means of $\kappa = \cos\theta_{DA} - 3\cos\theta + \theta_D\cos\theta_A$, where θ_{DA} is the dihedral angle between the transition moments, and θ_D and θ_A are the angles of each transition moment with the normal linking the mass centers) and rate constants are included.

These results highlight that albeit FRET process is taking place, this is not the main one. Thus, the key mechanism responsible of controlling the whole EET process in the cassette is the TBET. Consequently, the overall energy transfer efficiency is greatly enhanced when the electronic exchange is maximized rather than when the donor and acceptor are closer. Probably, whereas the *meta* connection of the spacer hindered the resonance interaction between the electronic clouds of the aromatic groups, a *para* disposition of the spacer enhanced the electronic delocalization along

the spacer. In the same line of reasoning, a more delocalized spacer (acetylenephenyl) implies a higher degree of conjugation and balanced the lengthening of the donor-acceptor distance. This is why the *para* connection through the longer but at the same time more conjugated spacer (acetylenephenyl group) provided the highest energy transfer efficiency, particularly in the most polar/protic media (2,2,2-trifluoroethanol) (Table 4.2).

In conclusion, the formation/opening of the spirolactone ring, which depends on the acidity/polarity of the surrounding environment, switches off/on a highly efficient TBET process from the BODIPY to the rhodamine (Figure 4.6). These photoactive cassettes are highly versatile since can be applied not only as efficient and photostable laser emitters, which can be pumped over a wide spectral region, but also as molecular probes for sensing the polarity of the surrounding media.

For a more detailed discussion of the photophysical and lasing properties of the cassettes based on BODIPY and Rhodamine pairs look up the attached article published in *Chemistry an Asian Journal*.

CHEMISTRY
AN ASIAN JOURNAL
ACES
FULL PAPER

DOI: 10.1002/asia.201300857

Photophysical and Laser Properties of Cassettes based on a BODIPY and Rhodamine Pair

Leire Gartzia-Rivero,[a] Haibo Yu,[b] Jorge Bañuelos,*[a] Iñigo López-Arbeloa,[a] Angel Costela,[c] Inmaculada Garcia-Moreno,[c] and Yi Xiao*[b]

Abstract: This work deals with the synthesis and the photophysical and laser properties of new BODIPY-rhodamine cassettes. These dyads differ in their rigid and conjugated spacer group (phenyl or acetylenephenyl) and in their linking positions (*meta* or *para*). The photophysical properties of these cassettes are controlled by the formation/opening of the spirolactone ring, which, in turn, switches off/on an energy-transfer process between the chromophores. Herein, we thoroughly describe the influence of the attached spacer group, as well as the distance and orientation between the donor–acceptor pair, on the excitation energy transfer. The observed fast dynamics and efficiency suggest that the process mainly takes place "through-bond", although the "through-space" mechanism also contributes to the whole process. As a result, efficient laser emission from the rhodamine is achieved upon excitation of the BODIPY, in particular for the cassette that contains an acetylenephenyl spacer group in a *para* disposition.

Keywords: BODIPY · dyes · energy transfer · laser chemistry · rhodamine

Introduction

Cassette molecules, which are composed of multiple dyes as donor and acceptor groups, have attracted considerable interest for excitation energy transfer (EET) processes. They have been widely applied as energy harvesters[1] in photoelectronics and as ratiometric fluorescent chemosensors[2] in chemical biology. Recently, we have begun to apply cassettes as laser materials with unprecedented performance, including high photostability, multiple pumping, and high laser efficiency.[3]

In addition to choosing a pair of suitable dyes as the donor and the acceptor, respectively, another key question is the design of a suitable linker to join the dyes together during the construction of the cassette. So far, most of these linkers have been long and flexible chains and, thus, "through-space" EET processes take place, in accordance with the recognized principle of FRET (Forster resonance energy transfer).[4] However, recently, several groups, that is, Burgess and co-workers,[5] Ziessel and Harriman,[6] Akkaya and co-workers,[7] Lin et al.,[8] and ourselves,[9] have used rigid, short, and conjugated linkers in the construction of such cassettes and a new concept of through-bond energy transfer (TBET) has been proposed.[10] Although the mechanism of TBET is not yet well-established, it is true that, in general, TBET is highly efficient (close to 100%) and ultrafast (in the picosecond range or even faster). Hence, TBET cassettes might be more advantageous as functional materials than FRET cassettes.

TBET cassettes that are based on BODIPY and rhodamine dyes should be very valuable materials, because both families of dyes take advantage of their strong absorption, intense emission, and high photostability compared to most other common fluorescent dyes. Owing to their outstanding photophysical properties, BODIPY and rhodamine have been widely used as fluorescent probes and laser dyes. Although each of these dyes has been frequently matched with other dyes in a wide variety of cassettes, it is uncommon for both to be combined in the same cassette. Indeed, to the best of our knowledge, the only TBET cassette that is based on BODIPY and rhodamine units was reported by ourselves in 2011 (**BDP-Rh**, Scheme 1). A **BDP-Rh** cassette with high EET efficiency (up to 99%) has been found to be a versatile scaffold for the development of sensors for bioimaging.[9]

Herein, we extend our work on the construction and application of cassettes that are based on the BODIPY-rhodamine pair (Scheme 1) to analyze the effects of different con-

[a] L. Gartzia-Rivero, Dr. J. Bañuelos, Prof. I. López-Arbeloa
Departamento de Química Física
Universidad del País Vasco (UPV-EHU)
Aptdo 644, 48080, Bilbao (Spain)
E-mail: jorge.banuelos@ehu.es

[b] Dr. H. Yu, Prof. Y. Xiao
State key laboratory of Fine Chemicals
Dalian University of Technology
Dalian, 116024 (China)
E-mail: xiaoyi@dlut.edu.cn

[c] Prof. A. Costela, Prof. I. Garcia-Moreno
Departamento de Sistemas de Baja Dimensionalidad
Superficies y Materia Condensada
Instituto Química Física "Rocasolano", C.S.I.C.
Serrano 119, 28006 Madrid (Spain)

Supporting information for this article, including the experimental details of synthesis and characterization of dyes, and techniques for photophysical and laser measurements, as well as additional photophysical data, absorption and fluorescence spectra and calculations of the FRET rate constants, is available on the WWW under http://dx.doi.org/10.1002/asia.201300857.

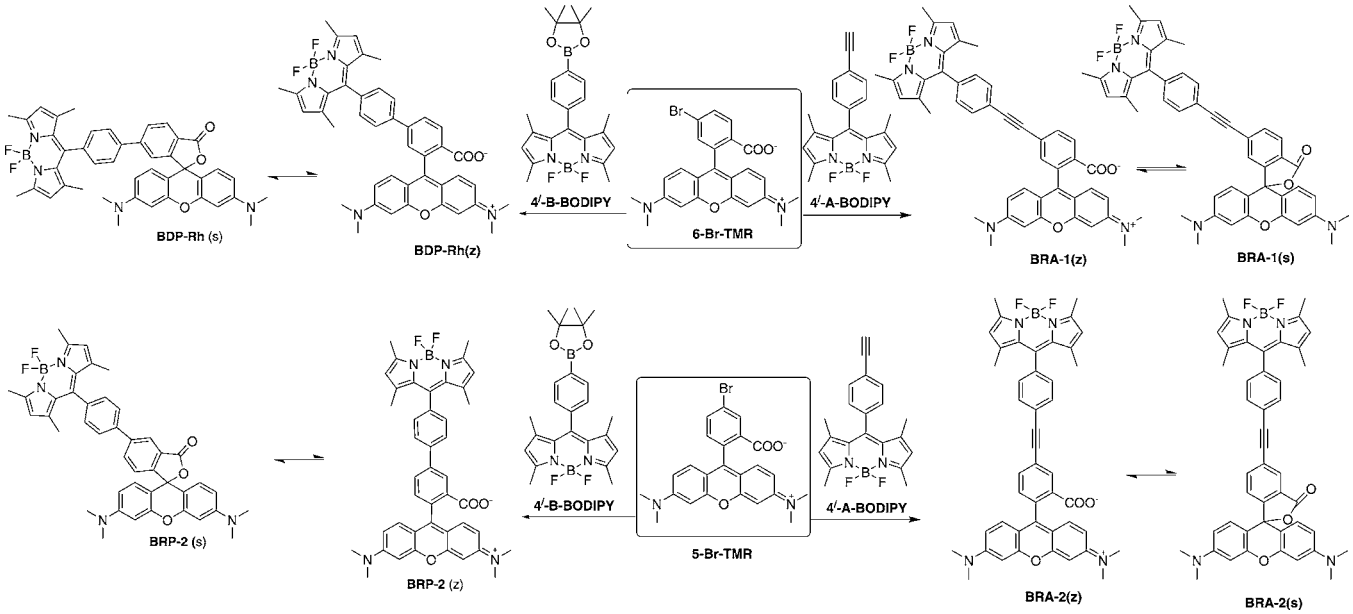

Scheme 1. Synthetic route to BODIPY-rhodamine dyads that are linked by phenyl or *para*-acetylenephenyl spacer groups at the *meta* and *para* positions.

jugated linkers, linking sites, and solvents or media on the photophysical and laser properties of these compounds. The motivation of this investigation is to find ways to tune the laser performance of TBET cassettes on the basis of the donor-acceptor distance and their mutual orientation.

Results and Discussion

1. Synthesis of the Dyes

To study the energy-transfer processes in cassettes that contained different spacer groups and different relative orientations of the donor and acceptor groups, four EET cassettes were synthesized in which a BODIPY donor was connected to a tetramethylrhodamine (TMR) acceptor (Scheme 1). Regioisomers **5-Br-TMR** and **6-Br-TMR** were employed as key starting materials for the development of these cassettes. A multigram-scale procedure to obtain pure **5-Br-TMR** and **6-Br-TMR** has been reported previously by our group.[1] Compounds **4′-B-BODIPY** and **4′-A-BODIPY** were prepared according to literature procedures.[2,3] The synthesis of the cassettes proceeded efficiently under Pd catalysis, such as Suzuki or Sonogashira coupling reactions. Cassette **BRP-2**, with a phenyl spacer, similar to previously reported **BDP-Rh**,[9] was obtained in a straightforward manner in high yield by coupling with **4′-B-BODIPY** in the presence of $Pd(OAc)_2$. Cassettes **BRA-1** and **BRA-2**, which contained an acetylenephenyl spacer, were efficiently prepared from intermediate **4′-A-BODIPY** by Sonogashira coupling.

2. Photophysical Properties

The presence of rhodamine as an acceptor unit in these cassettes determined their photophysical behavior because the carboxylate group in the *ortho* position forced the pendant phenyl group into a perpendicular position with respect to the xanthene core, thereby excluding it from the delocalized π system of the rhodamine. However, this arrangement of the anion was suitable for reacting with the central carbon atom of the xanthene group, thus leading to a lactone form (in apolar or aprotic media), in which the xanthene-like delocalization was broken (Scheme 2). Because the formation or opening of the spirolactone ring determine the photophysics of rhodamine[11] and, hence, of the resulting cassette, in the following sections we will analyze in depth the interconversion between such structures (lactone (s)↔zwitterions (z); Scheme 1 and Scheme 2), which depended on the characteristics of the solvent (mainly polarity and acidity). In addition to its zwitterionic neutral form ($Rh^{\pm}$), rhodamine can also adopt a cationic (RhH^{+}) molecular form (Scheme 2), albeit only in acidic environment.[12] Thus, its presence has been ruled out in this work, by considering that the zwitterion is the unique form that is present in polar/protic solvents.

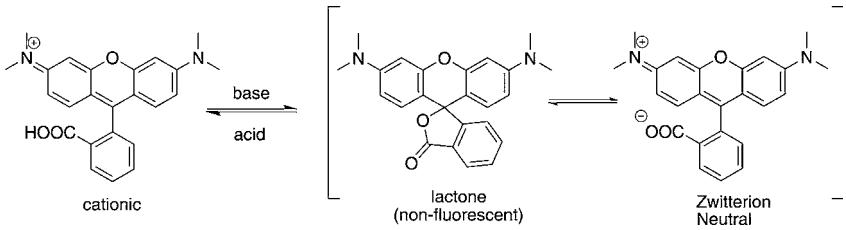

Scheme 2. Molecular forms of rhodamine compounds.[12]

2.1. Isomers with a Phenyl Spacer Group (*BDP-Rh* and *BRP-2*)

The absorption spectra of compounds **BDP-Rh** and **BRP-2** markedly depended on the characteristics of the surrounding media (as shown for **BDP-Rh** in Figure 1).

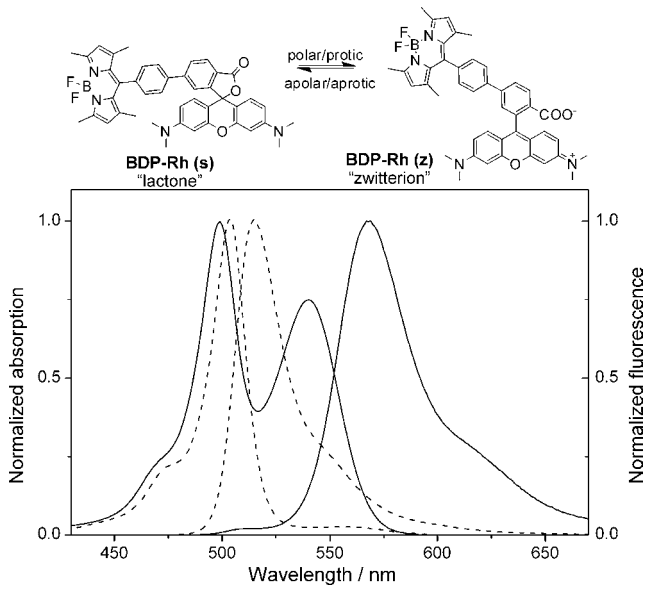

Figure 1. Normalized absorption and fluorescence spectra (upon excitation at the BODIPY wavelength, 470 nm) of **BDP-Rh** in cyclohexane (dashed line) and MeOH (solid line); the involved resonance structures are also included.

In polar/protic solvents, two absorption bands were present: One at higher energies, which corresponded to the BODIPY unit, and other at lower energies, which corresponded to the rhodamine unit. However, in apolar/aprotic solvents, only the absorption band of the BODIPY was present. In fact, the physicochemical characteristics of the solvent shifted the equilibrium between the isomers: Whereas polar protic media stabilized the zwitterionic form, owing to its inherent higher dipole moment and specific interactions with the carboxylate group, apolar/aprotic media stabilized the lactone form, in which the xanthene-like delocalization was broken down (Figure 1).[13]

Moreover, the fluorescence spectra in polar solvents (in which the zwitterionic form of rhodamine prevailed) showed substantial energy transfer from the BODIPY unit to the rhodamine unit, whereas, in apolar solvents (in which the lactone form of the rhodamine was favored), no appreciable energy transfer was noted and only the emission from BODIPY was detected (Figure 1). To understand the behavior of these compounds, we separately analyzed their photophysical properties in polar and apolar solvents.

In polar/protic solvents, such as alcohols, the delocalized π systems of the BODIPY and xanthene moieties were preserved. Moreover, there was no electronic coupling between the donor and acceptor units, because the phenyl spacer was perpendicular to both chromophores, owing to the steric hindrance that was induced by the adjacent methyl groups of BODIPY and the carboxylate group of rhodamine. Consequently, the bands of both chromophores were present in the absorption spectrum (Figure 1). Excitation in the BODIPY absorption region led to a dominant rhodamine emission (Figure 1), thus indicating efficient intramolecular energy transfer from the BODIPY donor to the TMR acceptor. The contribution of the intermolecular process was negligible because the measurements were performed in highly dilute solutions (2 μM), thereby ensuring that the molecules were far away from each other. As the acidity/polarity of the solvent increased (defined by Reichardt's parameter, $E_T^N(30)$;[14] Table 1), the EET efficiency was enhanced (see Figure 2 for **BRP-2** and the Supporting Information, Figure S1, for **BDP-Rh**), which was explained by a higher stabilization of the zwitterionic form of TMR in detriment of the lactone form.

Fluorescence-decay curves that were recorded at different emission and excitation wavelengths also confirmed the energy-transfer process. Table 1 shows the lifetimes (τ) of the donor (emission at 510 nm) and acceptor groups (emission at 565 nm) under excitation at the absorption bands of the donor (470 nm) and the acceptor (530 nm) in media in which the zwitterionic form of rhodamine prevailed. Owing to the energy-transfer process, the fluorescence-decay curve from the donor was analyzed by a multi-exponential fit, with up to three components contributing to the decay process, which became faster when the presence of the spirolactone ring was further avoided, that is, on increasing the solvent polarity (Figure 3 and Table 1). In these cases, a useful parameter is the amplitude average lifetime ($<\tau>_{aa}$), which is defined by Equation (1), in which the coefficient A_i represents the weight of each contribution to the lifetime.

$$<\tau>_{aa} = \Sigma A_i \tau_i \quad (1)$$

Therefore, the energy-transfer efficiency can be estimated according to $E = 1-(<\tau>_{aa}/\tau_0)$, where τ_0 is the lifetime of the donor alone. Thus, the smaller the value of $<\tau>_{aa}$, the higher the efficiency of the energy-transfer process. The average lifetime of the donor decreased (Table 1) as the polarity of the solvent increased, thereby correlating energy-transfer efficiency with increasing solvent polarity.

As clearly shown in Figure 1, there was a large spectroscopic overlap between the emission of the BODIPY donor and the absorption of the rhodamine acceptor. Therefore, the Förster mechanism should have been operative and energy transfer could take place "through-space" interactions. However, the high efficiency of the energy-transfer process (the donor emission was almost-completely quenched in most polar/protic media) suggested that, in addition to this contribution, a "through-bond" energy transfer (TBET) process could also take place, which was allowed by the conjugated spacer unit. Therefore, the overall energy-transfer process should comprise the contribution of both mechanisms. It is not easy to quantify the contributions of

Table 1. Fluorescence-emission lifetimes from the BODIPY donor (510 nm) and the rhodamine acceptor (565 nm) under excitation of the donor (470 nm) and the acceptor units (530 nm).[a]

Solvent	BDP-Rh(z)						BRP-2(z)				
	$\lambda_{ex}=470$ nm			$\lambda_{ex}=530$ nm		$E_T^N(30)$	$\lambda_{ex}=470$ nm			$\lambda_{ex}=530$ nm	
	λ_{em} [nm]	τ [ns] (%)	$<\tau>_{aa}$ [ns]	λ_{em} [nm]	τ [ns]		λ_{em} [nm]	τ [ns] (%)	$<\tau>_{aa}$ [ns]	λ_{em} [nm]	τ [ns]
1-decanol	510	3.17	3.17				510	2.44 (97)	2.51		
								4.71 (3)			
	565	2.20 (<0)		565	3.48	0.52	565	2.10 (<0)		565	3.52
		3.81 (>0)						3.72 (>0)			
EtOH	510	1.65 (88)	1.77				510	0.55 (11)	1.54		
		2.64 (12)						1.42 (78)			
								3.39 (11)			
	565	0.99 (<0)		565	3.05	0.65	565	0.64 (<0)		565	3.06
		3.18 (>0)						3.07 (>0)			
MeOH	510	0.61 (30)	1.52				510	0.04 (42)	1.05		
		1.43 (50)						1.06 (28)			
		3.11 (20)						2.46 (30)			
	565	0.09 (<0)		565	2.59	0.76	565	0.10 (<0)		565	2.58
		2.70 (>0)						2.59 (>0)			
2,2,2-trifluoroethanol	510	0.06 (66)	0.72				510	0.04 (77)	0.65		
		1.95 (16)						1.24 (9)			
		4.63 (8)						3.60 (14)			
	565	0.50 (<0)		565	3.97	0.90	565	0.23 (<0)		565	3.90
		4.08 (>0)						3.94 (>0)			

[a] $E_T^N(30)$ is the normalized Reinhardt parameter, which accounts for solvent polarity and acidity.

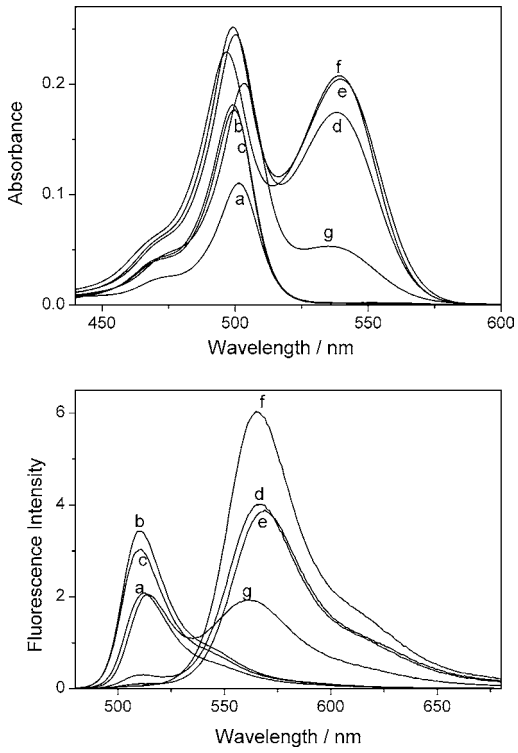

Figure 2. Absorption and fluorescence spectra ($\lambda_{ex}=470$ nm) of **BRP-2** in a) THF, b) EtOAc, c) acetone, d) EtOH, e) MeOH, f) 2,2,2-trifluoroethanol, and g) 1-decanol.

each mechanism to the whole EET process, although, in some specific cassettes, this quantification has been carried out by performing measurements at high pressures and low temperatures[15] or by performing transient absorption measurements on the femtosecond scale.[16]

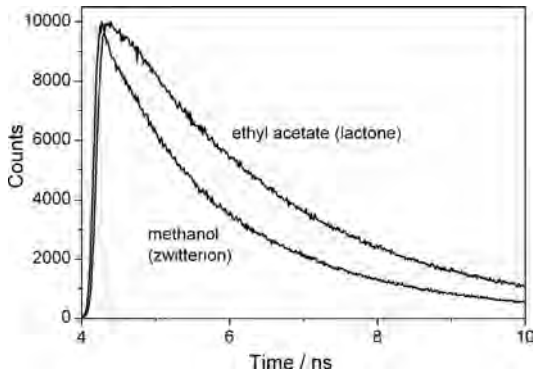

Figure 3. Fluorescence-decay curves of **BRP-2** ($\lambda_{ex}=470$ nm and $\lambda_{em}=510$ nm, which correspond to the BODIPY donor unit) in polar/aprotic solvent (EtOAc, in which the lactone form of the rhodamine acceptor prevails) and in polar/protic solvent (MeOH, in which the zwitterionic form prevails).

To clarify the influence of each mechanism, we recorded fluorescence spectra at low temperatures (Figure 4). Owing to the frozen environment, the emission bands showed a higher vibrational resolution and were shifted towards higher energies. Nevertheless, notably, although the fluorescence of the donor was dramatically quenched at room temperature by EET, its emission increased at 77 K, thus suggesting that the process was still present but was much less efficient (the emission intensities of the donor and the acceptor were almost equal). The TBET mechanism implies an electronic exchange through an activated energy process, which could be suppressed at low enough temperatures.[15] Thus, in the frozen solution, the recorded EET was solely due to a FRET process. Consequently, the high EET efficiencies of these cassettes at room temperature should be

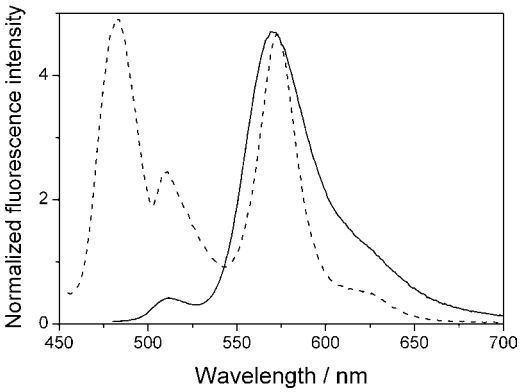

Figure 4. Fluorescence spectra of **BRP-2** in EtOH upon excitation of the BODIPY donor at 77 K (dashed line) and at room temperature (solid line).

due to TBET, which was the main pathway for the energy transfer under these experimental conditions. Moreover, at 77 K, the fluorescence-decay curve was analyzed as a biexponential, because the fastest lifetime disappeared. Thus, the three components that were required to properly analyze the fluorescence-decay curve of the donor at room temperature should be related to the quenching that was induced by the TBET and FRET processes for the fastest and intermediate components of the lifetime, respectively, whereas the longest lifetime could be assigned to residual emission from the BODIPY unit (Figure 3 and Table 1). As the polarity of the solvent increased, the contribution of the shortest lifetime became more relevant, according to the improved energy-transfer efficiency, whereas the contribution of the longest lifetime decreased significantly, in agreement with a negligible emission from the BODIPY unit (Table 1). On the other hand, the time evolution of the acceptor emission after excitation of the donor was characterized by an initial growth (thus indicating that the excited state of rhodamine was populated by EET) and a decay, which matched up with the lifetimes for the TMR unit after its direct excitation at 530 nm (Table 1).

Comparison of the results that were obtained with the **BDP-Rh(z)** and **BRP-2(z)** cassettes (Table 1) revealed that the efficiency of the energy-transfer process was higher in **BRP-2(z)**, because the decrease in its average lifetime in the BODIPY region was more evident (Table 1). Therefore, the *para* connection of the spacer seemed to benefit the energy-transfer process. Presumably, a *meta* connection of the rings hampered the resonance interaction between the electronic clouds of the phenyl groups, whereas a *para* disposition of the spacer enhanced the electronic delocalization between the aromatic rings and, hence, the efficiency of the TBET process, which involved an electronic process.[17] In fact, the fastest lifetime component in the fluorescence-decay curve of **BRP-2** in the BODIPY region decreased in value, but increased its contribution with respect to the values for **BDP-Rh** under identical conditions (Table 1). By contrast, the FRET mechanism mainly depended on the distance and orientation between both chromophores (see the Supporting Information, Figure S2).[18] In fact, quantum-mechanical calculations predicted that a change in the disposition of the linker from *meta* to *para* would hardly alter the dipole moment orientation parameter (κ^2) and increase the donor–acceptor distance (from 10.5 to 11.6 Å). Consequently, the FRET probability decreased from **BDP-Rh** to **BRP-2**, as confirmed by the rate constant that was calculated by using the Förster formalism (see the Supporting Information, Figure S2). In good agreement with this result, the contribution of the intermediate lifetime component was lower in the **BRP-2** cassette. From these results, we can state that the electronic coupling between the linker and the chromophoric units of the cassettes is the key factor in controlling the whole EET process, more than the donor–acceptor distance. In fact, the efficiency of the process increased when the TBET contribution was maximized by a specific linking attachment, which ensured effective electronic coupling, although the acceptor was further away from the donor.

Time-resolved emission spectroscopy (TRES) upon selective excitation at the donor unit revealed that most of the excitation energy had been transferred onto the acceptor within about ten picoseconds, because the emission of the acceptor had become more intense, whilst the fluorescence from the BODIPY donor had becomes residual within this timescale (Figure 5). These results highlight the high efficiency and the fast dynamics (well beyond the temporal resolution of our picosecond photon-counter) of the EET process in these cassettes. Taking into account the fact that ul-

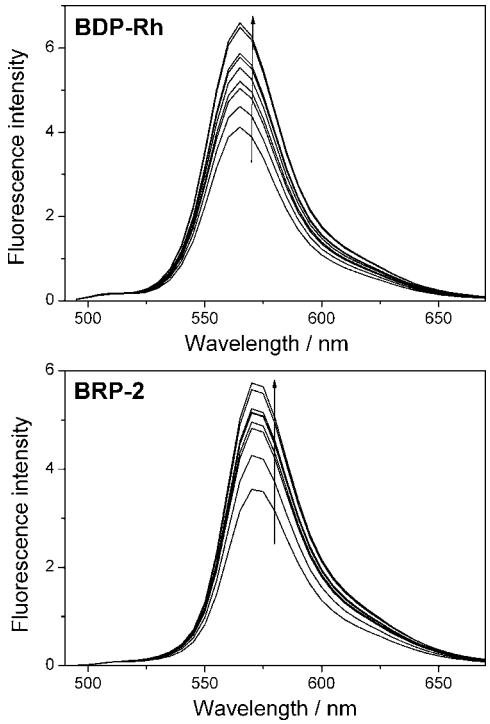

Figure 5. Normalized (at the donor region) time-resolved emission spectra for cassettes that contained a phenyl spacer at the *meta* (**BDP-Rh**) and *para* positions (**BRP-2**) in MeOH at different times after excitation: 0–0.1, 0.2–0.3, 0.4–0.5, 0.5–0.6, 0.6–0.8, 0.8–1, 1–1.2, 1.2–1.6, and 1.6–2 ns.

trafast measurements (femtoseconds) have previously been used to assign kinetics of a few picoseconds (around 5 ps) for TBET processes in cassettes that contained BODIPY and similar spacer groups,[16] the evolution of the acceptor emission in Figure 5 has to be attributed to the FRET process. Careful inspection of Figure 5 indicates that, for the same delay time after excitation, the donor emission is lower in the *para*-linked disposition, thereby confirming that this cassette is the most-efficient one and further supporting the assignment of the TBET mechanism as the main pathway in controlling the EET probability in these cassettes.

On the other hand, in apolar or aprotic media (i.e., cyclohexane, THF, EtOAc, and acetone), the stabilization of the carboxylate moiety was less efficient and this anion could attack the central carbon atom of the xanthene, thereby leading to the spirolactone ring.[13] As result, the xanthene-like delocalized π system was broken up and the spectroscopic bands of TMR were no longer detected (Figure 1 and Figure 2). Thus, when the lactone form was preferred, the system became monochromophoric; only the BODIPY emission was observed and the EET was switched "off".

The photophysical data of the lactone forms of isomers **BDP-Rh** and **BRP-2** are shown in the Supporting Information, Table S1. The fluorescence quantum yields (0.3–0.4, depending on the solvent) were much lower than that expected values for a BODIPY unit that contained a sterically hindered phenyl ring at the 8-position ($\phi \approx 0.7$–0.8). This result could be related to an increase in the non-radiative processes, because the bulky spirolactone group could induce photoelectron transfer processes and, owing to the linkage at the *para* position, could rotate, which partially quenched the emission from the BODIPY unit.[2]

The fluorescence-decay curves can be mainly described as monoexponential, although a biexponential fitting (characterized by a short lifetime with a minor contribution) could be forced for **BDP-Rh(s)** in some solvents. This result suggests that, although the environment is apolar, a minute contribution of the zwitterionic form may exist. Consequently, quite-small quenching of the BODIPY fluorescence can also take place through energy transfer, because the rhodamine (minority species) can trap part of the excitation light from the BODIPY. In fact, in the excitation spectra at long emission wavelengths (see the Supporting Information, Figure S3 for **BDP-Rh**), a weak band at lower energies does appear, which is attributed to the rhodamine unit (not well-observed in absorption).

*2.2. Isomers with an Acetylenephenyl Spacer Group (**BRA-1** and **BRA-2**)*

These cassettes followed the same trends as described above for the phenyl spacers. That is, the formation of the lactone in apolar/aprotic media was harmful for the cassette and should be avoided, because the xanthene chromophore was broken, thereby switching off the energy transfer (see the Supporting Information, Figure S4 and Table S2). In contrast, opening of the spirolactone in polar/protic environments allowed the recovery of the xanthene chromophore and yielded an effective EET process, which led to a strong emission from the rhodamine unit upon excitation of the BODIPY fragment (see the Supporting Information, Figure S4).

In spite of the lengthening of the spacer group, owing to the insertion of an acetylene group, which implied longer donor–acceptor distances (see the Supporting Information, Figure S2), the energy-transfer efficiency was still quite high, in particular in the most-polar media (2,2,2-trifluoroethanol), in which the emission from BODIPY was hardly detected (see the fluorescence spectra in the Supporting Information, Figure S4). The evolution of the fluorescence lifetimes in those media in which the zwitterionic form prevailed followed the same trends as previously observed for the **BDP-Rh(z)** and **BRP-2(z)** cassettes (Table 2): The decay curve in the BODIPY region was characterized by fast lifetimes, whereas the rhodamine lifetime was characterized by an initial growth, followed by decay.

The fluorescence spectra (see the Supporting Information, Figure S4) showed an enhancement of the energy-transfer efficiency between the BODIPY donor and the TMR acceptor when the polarity of the solvent increased and the zwitterion form prevailed. Indeed, the average lifetime ($<\tau>_{aa}$) of the donor progressively decreased as result of a more-efficient EET process (the shortest lifetime became faster and made a greater contribution), in agreement with the results described above (Section 2.1.). In addition, in Table 1 and Table 2, the average lifetimes of the donor in the cassettes with an acetylenephenyl spacer (**BRA-1** and **BRA-2**) were lower than those of the corresponding cassettes with a phenyl linker (**BDP-Rh** and **BRP-2**, respectively). These results indicated that the acetylenephenyl spacer maximized the EET process through TBET, probably because it implied a higher degree of conjugation in the spacer and counteracted the lengthening of the donor–acceptor distance (from 10.5 Å in **BDP-Rh** to 13.0 Å in **BRA-1**). Such an enlargement decreased the probability of FRET, in agreement with the calculated k_{FRET} (see the Supporting Information, Figure S2) by using the Föster formalism.

As observed in the cassettes with the phenyl spacer, the *para* disposition of the acetylenephenyl linker favored the energy-transfer process in **BRA-2(z)** with respect to **BRA-1(z)** (*meta*), as shown in Figure 6. Moreover, the fluorescence lifetime of the BODIPY donor in the **BRA-2** cassette was much shorter than that for the corresponding dye with the *meta* configuration (Table 2), owing to a higher probability of EET to the rhodamine unit through TBET, because the *para* connection allowed greater electronic delocalization (in terms of the Dexter formalism), as required for the TBET mechanism, than the *meta* connection. At the same time, the change from *meta* to *para* increased the donor–acceptor distance (from 13.0 Å in **BRA-1** to 14.2 Å in **BRA-2**), with the consequential decrease in FRET probability (see the Supporting Information, Figure S2). Therefore, the experimental results confirmed that the TBET mechanism determined the EET efficiency of these cassettes. Summing up, the acetylenephenyl group that connected both dyes

Table 2. Fluorescence-emission lifetimes from the donor (510 nm) and the acceptor (565 nm) under excitation of the donor (470 nm) and acceptor units (530 nm).

Solvent	BRA-1(z)					BRA-2(z)				
	$\lambda_{ex}=470$ nm			$\lambda_{ex}=530$ nm		$\lambda_{ex}=470$ nm			$\lambda_{ex}=530$ nm	
	λ_{em} [nm]	τ [ns] (%)	$<\tau>_{aa}$ [ns]	λ_{em} [nm]	τ [ns]	λ_{em} [nm]	τ [ns] (%)	$<\tau>_{aa}$ [ns]	λ_{em} [nm]	τ [ns]
1-decanol	510	2.23	2.23			510	0.43 (7)	2.09		
							2.22 (93)			
	565	1.10 (<0)		565	3.49	565	3.62		565	3.65
		3.65 (>0)								
EtOH	510	0.12 (6)	1.20			510	0.05 (29)	0.84		
		1.16 (89)					1.24 (60)			
		3.18 (5)					2.72 (11)			
	565	0.71 (<0)		565	2.99	565	0.59 (<0)		565	3.03
		3.02 (>0)					3.12 (>0)			
MeOH	510	0.05 (54)	0.89			510	0.02 (85)	0.22		
		1.21 (37)					0.96 (10)			
		4.64 (9)					2.15 (5)			
	565	0.04 (<0)		565	2.28 (77)	565	0.16 (<0)		565	2.58
		2.58 (>0)			3.13 (23)		2.66 (>0)			
2,2,2-trifluoroethanol	510	0.03 (83)	0.51			510	0.02 (94)	0.16		
		1.61 (8)					1.42 (3)			
		3.90 (9)					3.34 (3)			
	565	0.50 (<0)		565	2.90 (20)	565	0.51 (<0)		565	4.08
		3.96 (>0)			3.99 (80)		4.13 (>0)			

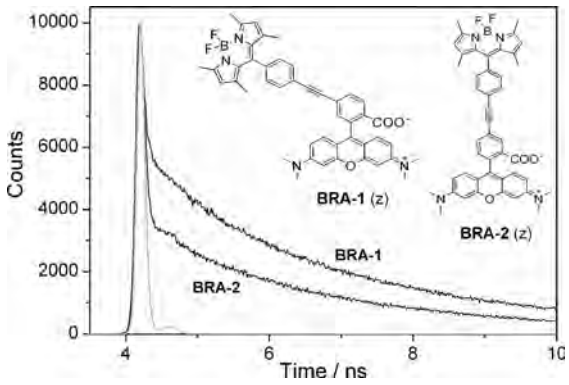

Figure 6. Fluorescence-decay curves of the BODIPY donor ($\lambda_{ex}=470$ nm and $\lambda_{em}=510$ nm) for cassettes that contained a *para*-acetylenephenyl spacer at the *meta* (**BRA-1**) and *para* positions (**BRA-2**) in 2,2,2-trifluoroethanol.

through their *para* positions was the best spacer group for improving the probability of energy transfer in these cassettes, as is accurately reflected in the average lifetimes (Table 1 and Table 2), which were the fastest among all of the studied derivatives, in particular in the most-polar/protic media (2,2,2-trifluoroethanol).

2.3. Fluorescence Quantum Yields for Emission from Rhodamine

To evaluate the probability of energy transfer and, hence, the fluorescence ability of the multichromophore cassettes, we recorded the fluorescence quantum yields for rhodamine emission after excitation of both the BODIPY donor (at 470 nm, ϕ_{470}) and the rhodamine acceptor (at 525 nm, ϕ_{525}) in MeOH and 2,2,2-trifluoroethanol (Table 3). The fluorescence quantum yields of TMR upon excitation of the donor approached those that were obtained after direct excitation, thereby indicating the remarkable efficiency of the energy-transfer process.

Table 3. Fluorescence quantum yields of the rhodamine unit after excitation at 470 nm (ϕ_{470}) and 525 nm (ϕ_{525}).

Solvent	BDP-Rh		BRP-2	
	ϕ_{470}	ϕ_{525}	ϕ_{470}	ϕ_{525}
MeOH	0.41	0.59	0.42	0.55
2,2,2-trifluoroethanol	0.52	0.79	0.51	0.73
	BRA-1		**BRA-2**	
	ϕ_{470}	ϕ_{525}	ϕ_{470}	ϕ_{525}
MeOH	0.49	0.52	0.49	0.52
2,2,2-trifluoroethanol	0.53	0.70	0.53	0.70

An increase in the fluorescence quantum yield on going from MeOH to 2,2,2-trifluoroethanol can be attributed to specific interactions between the rhodamine unit and the surrounding medium. The photophysical properties of amino-aromatic dyes is typically described by twisted intramolecular charge transfer (TICT)[19] or umbrella-like motion (ULM)[20] models. Thus, owing to the acidity of 2,2,2-trifluoroethanol, this solvent should interact with the lone pairs of the aromatic amines. In terms of the ULM model, such interactions decreased the probability of a hybridization change of the amine from sp^3 (non-planar) into sp^2 (planar) and, hence, impeded the internal-conversion processes. In a similar way, but considering the TICT model, the lone pair was localized on the amino group, owing to such specific interactions, thereby decreasing the probability of charge transfer to the chromophore and its quenching of the fluorescence emission.

3. Lasing Properties

According to their absorption properties, the lasing properties of the zwitterionic forms of the isomers were studied under pumping at 532 nm, whereas the lactone forms were pumped at 355 nm. Under our experimental conditions (transversal excitation and strong focusing of the incoming pump radiation), the concentration of the dyes needed to be high enough to ensure the total absorption of the pump radiation within the first millimeter of most of the solution, to obtain an emitted beam with near-circular cross-section, and to optimize the laser efficiency (ratio between the energy of the dye laser output and the incident pump energy on the sample surface). Some of the isomers that were studied presented low solubility in the appropriate solvents and could not be dissolved at the concentrations that were needed to obtain laser emission. This property was the case for isomers **BRP-2(s)** and **BRA-1(s)**, the laser properties of which could not be assessed.

In the first place, the concentrations of the compounds for optimized laser emission were determined by pumping solutions with different optical densities whilst keeping all of the other experimental parameters constant. Thus, herein, we report the results that were obtained with the optimal concentration of each derivative.

The lasing properties of the different isomers are presented in Table 4 and Table 5. There was good agreement between the lasing behavior and the photophysical properties of the different compounds: The higher the efficiency of the energy transfer or the fluorescence quantum yield, the higher the lasing efficiency. Notably, the compounds were pumped at standard wavelengths of 532 and 355 nm, whereas the maxima of the absorption bands was about 500 nm (Figure 1 and Figure 2). As expected, the laser efficiencies were higher when pumping at the absorption maxima. To confirm this result, an experimental setup was prepared that allowed the pumping of two of the derivatives at 500 nm. Thus, the laser efficiency increased from 41% to 60% for **BDP-Rh(z)** in EtOH and from 18% to 30% for **BDP-Rh(s)** in EtOAc.

Table 4. Laser properties of the zwitterionic isomers.

Solvent	**BDP-Rh(z)**			**BRP-2(z)**		
	Eff [%]	λ_L [nm]	I [%]	Eff [%]	λ_L [nm]	I [%]
EtOH	41(60)[a]	580(581)[a]	90	37	584	60
MeOH	43	586		39	587	
2,2,2-trifluoroethanol	50	579		40	584	
	BRA-1(z)			**BRA-2(z)**		
	Eff [%]	λ_L [nm]	I [%]	Eff [%]	λ_L [nm]	I [%]
EtOH	32	583	35	34	584	40
MeOH	34	586		37	587	
2,2,2-trifluoroethanol	38	581		43	584	

[a] Efficiency and laser wavelength with pumping at 500 nm are given in parentheses. Eff = laser efficiency (ratio between the energy of the laser output and the incident pump energy on the sample surface); λ_L = peak wavelength of the laser emission; I = intensity of the laser-induced fluorescence after 100000 pump pulses at a repetition rate of 10 Hz, referred to initial intensity. Pumping at 532 nm. Concentration of the isomers: 3×10^{-4} M (phenyl spacer), 2×10^{-4} M (acetylenephenyl spacer).

Table 5. Laser properties of the lactone isomers.

Solvent	**BDP-Rh(s)**			**BRA-2(s)**		
	Eff [%]	λ_L [nm]	I [%]	Eff [%]	λ_L [nm]	I [%]
EtOAc	18(30)[a]	542(537)[a]	30	8	528	20
THF	20	548		12	527	

[a] Efficiency and laser wavelength with pumping at 500 nm are given in parentheses. Pumping at 355 nm. Parameters are defined as in Table 4. In this case, I = intensity after 70000 pump pulses at a repetition rate of 5 Hz. Concentration of the isomers: 2×10^{-3} M (phenyl spacer), 1×10^{-3} M (acetylenephenyl spacer).

An important parameter for any practical application of dye lasers is their photostability under repeated pumping. Of the studied isomers, the one with the highest photostability was the zwitterionic **BDP-Rh(z)**, for which the laser-induced fluorescence remained at 90% of its initial value after 100000 pump pulses at a repetition rate of 10 Hz.

The encouraging results in liquid solution led us to investigate the lasing performance of these materials on their incorporation into solid matrices. Thus, in a preliminary study, isomers **BDP-Rh(z)** and **BDP-Rh(s)** were incorporated into solid matrices of poly(2-hydroxyethylmethacrylate) (PHEMA) and poly(methylmethacrylate) (PMMA), respectively. These polymers were chosen because they mimicked the solvents EtOH and EtOAc, respectively, thereby providing polar and apolar environments. The results are collected in Table 6.

The lasing efficiencies were somewhat lower than those in liquid solution, probably owing to the fact that the finishing of the surface of the solid samples relevant to the laser operation was not laser-grade; thus, higher efficiencies are expected with laser-grade surfaces. On the other hand, the photostabilities improved the values that were obtained in liquid solution, which make these compounds promising candidates for use in optoelectronic applications.

Table 6. Laser properties of the **BDP-Rh** isomers in a solid matrix.[a]

Sample	C [M]	Eff [%]	λ_L [nm]	I_n [%]
BDP-Rh(z)/PHEMA (pumping at 532 nm)	3×10^{-4}	34	594	99.7_{100000}
BDP-Rh(s)/PMMA (pumping at 355 nm)	2×10^{-3}	17	540	39.9_{62500}

[a] C = dye concentration; Eff = laser efficiency; λ_L = peak wavelength of the laser emission; I_n = intensity of the laser emission after n pump pulses in the same position of the sample at a repetition rate of 10 Hz, referred to as initial intensity.

Conclusions

In this study, with aid of the prior preparation of regioisomers **5-Br-TMR** and **6-Br-TMR**, we have constructed several intramolecular EET cassettes with BODIPY and rhodamine

fluorophores. These cassettes had the same energy donor (BODIPY) and acceptor (rhodamine), but the spacer group (phenyl or acetylenephenyl) and the relative orientation (*meta* or *para*) of the donor and acceptor were changed.

The photophysical properties of these cassettes were controlled by the formation of a spirolactone ring, which, in turn, depended on the characteristics of the surrounding medium. Thus, when the lactone form prevailed (in aprotic solvents), the xanthene π system was destroyed and no EET was detected. However, in protic media, the zwitterionic form of the rhodamine was predominant and the identities of both chromophores (BODIPY and rhodamine) were preserved. Consequently, an efficient energy-transfer process from the BODIPY donor to the rhodamine acceptor was switched "on", via "through-bond" and "through-space" interactions. The roles of the spacer group and the surrounding environment on the EET efficiency were nicely reflected by the average lifetime, as monitored in the donor region. Thus, placing the acetylenephenyl spacer group at the *para* position and in polar media is recommended, because the electronic coupling is maximized and the efficiency of the EET is improved. Indeed, once the BODIPY is excited, the emission of the rhodamine group is detected almost exclusively. Such evolution with the length and orientation of the spacer group cannot be explained by FRET and is due to the contribution of TBET, thus highlighting this mechanism as the key factor in BODIPY-rhodamine cassettes.

The studied isomers exhibited laser action in both liquid and solid media. In liquid solution, the laser emissions correlated well with the photophysical properties of the isomers. Under pumping at the standard wavelength of 532 nm, the zwitterionic isomer **BDP-Rh(z)** exhibited laser action with up to 50% laser efficiency and high photostability. The efficiency increased significantly when pumped at 500 nm, that is, at the wavelength that corresponded to the absorption maxima. When this compound was incorporated into a solid PHEMA matrix, the laser emission showed remarkable stability, that is, it remained at its initial level after 100000 pump pulses in the same position of the sample at a repetition rate of 10 Hz.

Experimental Section

The synthetic route, materials, and characterization of the herein reported cassettes, as well as the experimental procedures for 1) the preparation of liquid and solid samples and 2) conditions and techniques for photophysical and laser measurements can be found in the Supporting Information.

Acknowledgements

This work was supported by the Spanish MICINN (project nos MAT-2010-20646-01 and MAT-2010-20646-04). We also acknowledge Gobierno Vasco (project no. IT339-10 and for a PhD grant to L.G.-R.).

[1] a) R. K. Lammi, R. W. Wagner, A. Ambroise, J. R. Diers, D. F. Bocian, D. Holten, J. S. Lindsey, *J. Phys. Chem. B* **2001**, *105*, 5341–5352; b) H. Imahori, H. Norieda, H. Yamada, Y. Nishimura, I. Yamazaki, Y. Sakata, S. Fukuzumi, *J. Am. Chem. Soc.* **2001**, *123*, 100–110; c) X. Zhang, Y. Xiao, X. Qian, *Org. Lett.* **2008**, *10*, 29–32.
[2] X. Zhang, Y. Xiao, X. Qian, *Angew. Chem.* **2008**, *120*, 8145–8149; *Angew. Chem. Int. Ed.* **2008**, *47*, 8025–8029.
[3] Y. Xiao, D. Zhang, X. Qian, A. Costela, I. García-Moreno, V. Martín, M. E. Pérez-Ojeda, J. Bañuelos, L. Gartzia, I. López Arbeloa, *Chem. Commun.* **2011**, *47*, 11513–11515.
[4] K. E. Sapsford, L. Berti, I. L. Medintz, *Angew. Chem.* **2006**, *118*, 4676–4704; *Angew. Chem. Int. Ed.* **2006**, *45*, 4562–4588.
[5] a) T. G. Kim, J. C. Castro, A. Loudet, J. G.-S. Jiao, R. M. Hochtrasser, K. Burgess, M. R. Topp, *J. Phys. Chem. A* **2006**, *110*, 20–27; b) R. Bandichhor, A. Petrescu, A. Vespa, A. B. Kier, F. Schröder, K. Burgess, *J. Am. Chem. Soc.* **2006**, *128*, 10688–10689.
[6] R. Ziessel, A. Harriman, *Chem. Commun.* **2011**, *47*, 611–631.
[7] a) R. Guliyev, A. Coskun, E. U. Akkaya, *J. Am. Chem. Soc.* **2009**, *131*, 9007–9013; b) O. A. Bozdemir, Y. Cakmak, F. Sozmen, T. Ozdemir, A. Siemiarczuk, E. U. Akkaya, *Chem. Eur. J.* **2010**, *16*, 6346–6351.
[8] W. Y. Lin, L. Yuan, Z. M. Cao, Y. M. Feng, J. Z. Song, *Angew. Chem.* **2010**, *122*, 385–389; *Angew. Chem. Int. Ed.* **2010**, *49*, 375–379.
[9] H. Yu, Y. Xiao, H. Guo, X. Qian, *Chem. Eur. J.* **2011**, *17*, 3179–3191.
[10] J. Fan, M. Hu, P. Zhan, X. Peng, *Chem. Soc. Rev.* **2013**, *42*, 29–43.
[11] M. J. Culzoni, A. Muñoz de La Peña, A. Machuca, H. C. Goicoechea, R. Babiano, *Anal. Methods* **2013**, *5*, 30–49.
[12] I. López Arbeloa, P. Ruiz Ojeda, *Chem. Phys. Lett.* **1981**, *79*, 347–351.
[13] C. J. Stephenson, K. D. Shimizu, *Org. Biomol. Chem.* **2010**, *8*, 1027–1032.
[14] C. Reichardt, *Chem. Rev.* **1994**, *94*, 2319–2358.
[15] a) M. A. H. Alamiry, J. P. Hagon, A. Harriman, T. Bura, R. Ziessel, *Chem. Sci.* **2012**, *3*, 1041–1048; b) D. Bai, A. C. Benniston, J. Hagon, H. Lemmetyinen, N. V. Tkachenko, W. Clegg, R. W. Harrington, *Phys. Chem. Chem. Phys.* **2012**, *14*, 4447–4456; c) J. Iehl, J. F. Nierengarten, A. Harriman, T. Bura, R. Ziessel, *J. Am. Chem. Soc.* **2012**, *134*, 988–998.
[16] Y. Ueno, J. Jose, A. Loudet, C. Pérez-Bolívar, P. Anzenbacher, K. Burgess, *J. Am. Chem. Soc.* **2011**, *133*, 51–55.
[17] a) C.-W. Wan, A. Burghart, J. Chen, F. Bergström, L. B.-A. Johansson, M. F. Wolford, T. G. Kim, M. R. Topp, R. M. Hochstrasser, K. Burgess, *Chem. Eur. J.* **2003**, *9*, 4430–4441; b) A. Harriman, L. J. Mallon, S. Goeb, G. Ulrich, R. Ziessel, *Chem. Eur. J.* **2009**, *15*, 4553–4564.
[18] a) R. Ziessel, C. Goze, G. Ulrich, M. Cesário, P. Retailleau, A. Harriman, J. P. Rostron, *Chem. Eur. J.* **2005**, *11*, 7366–7378; b) R. Ziessel, M. A. H. Alamiry, K. J. Elliot, A. Harriman, *Angew. Chem.* **2009**, *121*, 2810–2814; *Angew. Chem. Int. Ed.* **2009**, *48*, 2772–2776.
[19] Z. R. Grabowski, K. Rotkiewicz, W. Rettig, *Chem. Rev.* **2003**, *103*, 3899–4032.
[20] a) I. López Arbeloa, K. K. Rohatgi-Mukkerjee, *Chem. Phys. Lett.* **1986**, *128*, 474–479; b) I. López Arbeloa, K. K. Rohatgi-Mukkerjee, *Chem. Phys. Lett.* **1986**, *129*, 607–614; c) F. López Arbeloa, T. López Arbeloa, I. López Arbeloa, *Trends Photochem. Photobiol.* **1994**, *3*, 145–155.

Received: June 28, 2013
Published online: September 10, 2013

Bibliography

[1] B. Albinsson and J. Martensson, *J. Photochem. Photobiol. A,* **2008**, 9, 138-155.

[2] J. Fan, M. Hu, P. Zhan and X. Peng, *Chem. Soc. Rev.,* **2013**, 42, 29-43.

[3] D. Collado, P. Remón, Y. Vida, F. Najera, P. Sen, U. Pischel and E. Perez-Inestrosa, *Chem. Asian. J.,* **2014**, 9, 797-804.

[4] D. Bai, A. C. Benniston, J. Hagon, H. Lemmetyinen, N. V. Tkachenko, W. Clegg and R. W. Harrington, *Phys. Chem. Chem. Phys.,* **2012**, 14, 4447-4456.

[5] W. Lin, L. Yuan, Z. Cao, Y. Feng and J. Song, *Angew. Chem. Int. Ed.,* **2010**, 49, 375-379.

[6] G. Jiao, L. H. Thoresen and K. Burgess, *J. Am. Chem. Soc.,* **2003**, 125, 14668-14669.

[7] K. H. Drexhage, *Structure and Properties of Laser Dyes,* Springer, Berlin, **1973**, p. 144-193.

[8] F. C. De Schryver, T. Vosch, M. Cotlet, d. A. Van, K. Müllen and J. Hofkens, *Acc. Chem. Res.,* **2005**, 38, 514-522.

[9] M. J. Ahrens, L. E. Sinks, B. Rybtchinski, W. Liu, B. A. Jones, J. M. Giaimo, A. V. Gusev, A. J. Goshe, D. M. Tiede and M. R. Wasielewski, *J. Am. Chem. Soc.,* **2004**, 126, 8284-8294.

[10] M. R. Wasielewski, *Acc. Chem. Res.,* **2009**, 42, 1910-1921.

[11] R. Guliyev, A. Coskun and E. U. Akkaya, *J. Am. Chem. Soc.,* **2009**, 131, 9007-9013.

[12] X. Zhang, Y. Xiao and X. Qian, *Angew. Chem.,* **2008**, 120, 8145-8149.

[13] T. Kalai and K. Hideg, *Tetrahedron,* **2006**, 62, 10352-10360.

[14] N. Adarsh, R. R. Avirah and D. Ramaiah, *Org. Lett.,* **2010**, 12, 5720-5723.

[15] M. E. Pérez-Ojeda, V. Martín, A. Costela, I. García-Moreno, I. J. Arroyo Córdoba and E. Peña-Cabrera, *Appl. Phys. B,* **2012**, 106, 911-914.

[16] J. Bañuelos, V. Martín, C. F. A. Gómez-Durán, I. J. A. Córdoba, E. Peña-Cabrera, I. García-Moreno, Á Costela, M. E. Pérez-Ojeda, T. Arbeloa and Í L. Arbeloa, *Chem. Eur. J.,* **2011**, 17, 7261-7270.

[17] A. Loudet and K. Burgess, *Chem. Rev.,* **2007**, 107, 4891-4932.

[18] S. Speiser, *Chem. Rev.,* **1996,** 96, 1953-1976.

[19] Y. Gong, X. Zhang, C. Zhang, A. Luo, T. Fu, W. Tan, G. Shen and R. Yu, *Anal. Chem.,* **2012**, 84, 10777-10784.

[20] Y. Zhao, Y. Zhang, X. Lv, Y. Liu, M. Chen, P. Wang, J. Liu and W. Guo, *J. Mater. Chem.,* **2011**, 21, 13168-13171.

[21] C. J. Stephenson and K. D. Shimizu, *Org. Biomol. Chem.,* **2010**, 8, 1027-1032.

[22] H. Yu, Y. Xiao, H. Guo and X. Qian, *Chem. Eur. J.,* **2011**, 17, 3179-3191.

[23] M. A. H. Alamiry, J. P. Hagon, A. Harriman, T. Bura and R. Ziessel, *Chem. Sci.,* **2012**, 3, 1041-1048.

CONCLUSIONS

The results presented in this thesis demonstrate the viability of several strategies to promote energy transfer processes in host-guest materials and molecular systems. The main purpose has consisted in the development of artificial antenna systems where light over a wide spectral region is harvested and transported by successive energy transfer hops and finally converted into light of the desired energy.

The design and suitable selection of the components forming the light-harvesting systems has been crucial to establish the energy transfer mechanism that is taking place and its efficiency, which will determine the final emission properties of the photoactive material or molecular cassette, and hence its best application field; from lasers (mainly working in the red-edge of the visible) to light modulators (white-light emission) or molecular probes.

Among the photoactive materials studied in this thesis, we can distinguish between organic-inorganic hybrid materials, i.e. dye-doped LTL zeolite materials with tunable size and morphology, and entirely organic materials, i.e. dyes confined in polymeric NPs with controlled size and chemical composition. On the other hand, the covalent linkage of suitable laser dyes allows obtaining molecular assemblies or cassettes with intramolecular energy transfer efficiencies about 100%. In all cases, the main target consisted in promoting EET processes and assessing the key factors that determine its efficiency to achieve a fine modulation of the process.

In the following lines we will highlight the main results and advantages of each approach:

DYE-DOPED LTL ZEOLITE

We have develop a synthetic protocol assisted by microwave heating to attain LTL zeolites with high crystallinity, tunable size (from few nm to 3 μm) and defined morphology (from coin or discs to barrels). The employed strategy of allocating suitable dyes into the pores, which protects the dye and align it in a preferential disposition avoiding "sandwich"-type aggregates even at high loadings, or plugging the entrances of LTL zeolite, has been proved as a successful approach to achieve highly

organized antenna materials guided by FRET processes. Thus, these photoactive hybrid materials are able to harvest light from a wide range of the electromagnetic spectrum (UV-Vis) and convert it efficiently into red light. Moreover, the FRET efficiency can be modulated by suitable dye combinations (regarding the spectral overlap). Such tuning gives rise to very versatile photoactive materials where not only red emission can be obtained but also white-light emission (simultaneous blue, green and red emission). Accordingly, a high FRET efficiency is required to push the antenna effect (red emission), whereas partial efficiency is mandatory for white-light emitting materials, where the light can be modulated over a broad spectral range.

DYES CONFINED IN POLIMERIC NPS

The encapsulation of laser dyes into polymeric nanocarriers ensures higher compatibility and overcomes the common drawbacks inherent to dyes such as low water solubility and poor photostability. Therefore, dye-doped latex NPs improves the fluorescence capacity and lasing efficiency, as well as reduces the photobleaching as compared with the performance of the same dye in solution. Moreover, it should be emphasized the proper correlation of the photophysical properties with the lasing efficiency, although the last one is more sensitive to the modification of the structural and chemical properties of the NPs, owing to the high optical density required in the active media.

The encapsulation of Rh6G and NB laser dyes into subwavelength nanoparticles lead to FRET processes which subsequently enhance the laser efficiency and photostability of the red-emitting laser dye NB by means of direct excitation of the photostable donor Rh6G, which efficiently absorbs the pump radiation at 532 nm. The confinement effect ruled by the NP size promotes the proximity between dyes and enables FRET processes even in diluted solutions (~10^{-6} M). Besides, it is noteworthy to emphasize the possibility of studying FRET dynamics at dye concentrations inside the NP beyond the solubility limit in aqueous and most organic solvent solutions, reaching FRET efficiencies much higher than those obtained in solution.

It has been also revealed that the FRET efficiency can be modulated by means of donor/acceptor ratio, dye concentration and NP size. Accordingly, the FRET is boosted by a higher number of available energy traps and energy migration between donors, which enables the energy transfer to acceptors placed far away from the excited donors. However, a higher dye loading does not imply always an improved FRET, since the RET processes are more feasible and back up the non-radiative pathway. As result,

there is an optimal donor and acceptor content to maximize the FRET process, i.e., to visualize the red emission from the NB upon Rh6G excitation. Finally, it is well confirmed that FRET dynamics arise as a valuable spectroscopic ruler to obtain knowledge of the dye distribution inside the NP.

MOLECULAR CASSETTES

One alternative to the EET processes ruled by FRET is the promotion of TBET in molecular assemblies where the donor and the acceptor are covalently linked via an adequate spacer. A right molecular design is essential to enable the TBET, since each fragment should retain its identity at least in the ground state to allow the selective excitation of each chromophore. The herein developed cassettes based on multiBODIPYs and BODIPY-rhodamine dyads, respectively, fulfill all these requirements. Thus, the selective excitation of the donor moiety leads almost exclusively to the acceptor red emission via EET, reaching efficiencies around of 100%, since the donor emission is completely quenched. It is noteworthy that in these cassettes both the TBET and FRET mechanisms are feasible, but the measurements at low temperatures and in dyads with controlled donor-acceptor distance and orientation revealed the TBET as the main EET pathway.

The possibility of exciting the emitting dye indirectly through an energy transfer process explains why these kinds of multichromophoric structures are postulated as a convenient alternative to overcome problems of photostability and availability of excitation sources in laser action, or background interferences in sensing and bioimaging applications. In this regard, the ongoing EET in BODIPY-Rhodamine cassette markedly depends on the solvent properties. Thus, it is switched on in polar-protic solvents but switched off in apolar ones due to the formation of a spirolactone ring which breaks the delocalization framework of the rhodamine. In conclusion, this cassette behaves not only as a highly photostable laser dye, but also as a molecular probe to monitor the polarity of the environment, i.e., as a reversible polarity on/off switch.

Summing up, as a result of the work carried out during the period of the thesis several photoactive materials and fluorophores undergoing energy transfer processes and working as artificial antenna systems have been developed. In this way, the best alternative can be chosen for the target application, for instance, hybrid materials are more suitable for achieving white-light emission, while dye-doped latex NPs and molecular cassettes are recommended for red-emitting dye lasers.

Outlook

The herein reported work demonstrates the successful approaches carried out to develop artificial antenna systems by way of photoactive nanomaterials or molecular cassettes. A clear proof of such statement is that the searched energy transfer process, either via FRET or TBET, arises favorably in all cases, which allow achieving red emission regardless of the excitation wavelength. Nevertheless, there are some remaining challenges to improve the workability of these systems and at the same time fulfill new prospects opened along this thesis work. Several strategies that are being currently considered will be addressed in the following lines.

- **Hybrid Materials**

  The main advantage of this kind of constrained hosts is the high organization degree of the material, which promotes energy transfer just in one direction. However, the specific interaction of the enclosed guest molecules with the surrounding framework (mainly with the acid adsorption sites) hampers the final fluorescence response of the material. To this aim, perylene dyes are being considered as a promising alternative to overcome the above mentioned drawbacks. The perylenimide chromophore is highly photostable and chemically "inert", while the bulky side substituents act as spacers and hinder intermolecular interactions with adjacent chromophores, ensuring a tight fitting into the pores of the host. Besides, the absorption and emission region can be shifted from the orange to the red by the substitution pattern of the perylenimide. Current experimental (in collaboration with the organic research group headed by Prof. M. J. Ortiz from the Universidad Complutense, UCM, in Madrid) and theoretical work is being carried out in our group to attain LTL zeolites doped with perilenes as luminescent antenna systems.

  Besides, the multi-channelled structure of the LTL zeolite allows the encapsulation of high amounts of photostable and fluorescent laser dyes (perylenes or other suitable chromophores) in their monomeric form, leading to photoactive materials with promising prospects to be used as nanolasers. To this aim, we are working in collaboration with the group headed by Prof. Inmaculada García-Moreno from the institute of Physical Chemistry "Rocasolano"-CSIC.

- **Dye-doped polymeric NPs**

  These colloidal nanoparticles outstand by their high fluorescence and laser efficiency in the red edge of the visible. The laser performance is of special interest when the emission is recorded via a tunable and enhanced FRET process from the irradiated donors. One of the main future perspectives in this field would be the possibility of studying such FRET process under the time-resolved fluorescence confocal microscopy. To this aim we are in collaboration with the group managed by Prof. E. Enciso from UCM who is developing big enough (more than 2 micrometer) latex particles doped simultaneously with donor and acceptor molecules. The time-resolved fluorescence confocal microscope will provide valuable information about dyes distribution and FRET dynamics.

- **Molecular Antenna Systems**

  One of the main features of these multichromophoric donor-acceptor dyads is the huge energy transfer efficiencies (almost 100%) achieved due to the successful promotion of both FRET and TBET mechanisms. Probably, this is one of the more straightforward ways to obtain highly photostable laser dyes in the red edge of the visible with the detection and excitation regions well separated. Actually, and again in collaboration with Prof. M. J. Ortiz and Dr. S. de la Moya from UCM, we are working in the development of novel cassettes with improved geometrical designs to boost the energy transfer efficiency in which donor and acceptor moieties are tightly linked by rigid spiranic bonds. In fact, some of these preliminary results have been recently published in the journal "Chemical Comunications" in a article entitled "Spiranic BODIPYs: a ground-breaking design to improve the energy transfer in molecular cassettes". Nevertheless, this article has not been included in this thesis report because it was published during the last period of its redaction. Besides, the attachment of a third dye working in the blue edge of the visible is thought to be an outstanding strategy to span the absorption range. These molecular assemblies should afford a considerable improvement in the light-harvesting efficiency thanks to the broadening of the absorption window over the whole ultraviolet-visible spectral region and its full conversion into red light via fast and efficient energy transfer processes.

List of Publications

The work carried out during the period of the thesis has yielded the following publications.

Articles included in the thesis report:

In Chapter 2 and organized as in the thesis:

1. L. Gartzia-Rivero, J. Bañuelos, U. Izquierdo, V. L. Barrio, K. Bizkarra, J. F. Cambra, I. López-Arbeloa, "Microwave Synthesis of LTL Zeolites with Tunable Size and Morphology: An Optimal Support for Metal-Catalyzed Hydrogen Production from Biogas Reforming Processes", *Particle*, 2014,31, 110-120. (Invitation to contribute to the Basque Country Special Issue)
2. U. Izquierdo, V.L. Barrio, K. Bizkarra, A. M. Gutierrez, J. R. Arribi, L. Gartzia, J. Bañuelos, I. López-Arbeloa, J.F. Cambra, "Ni and Rh-Ni catalysts supported on Zeolites L for hydrogen and syngas production by biogas reforming processes", *Chem. Eng. J.*, **2014**, 238,178-188.
3. H. Manzano, L. Gartzia-Rivero, J. Bañuelos, I. López-Arbeloa, "UltravioletVisible Dual Absorption by Single BODIPY Dye Confined in LTL Zeolite Nanochannels", *J. Phys. Chem. C*, **2013**, 117, 13331-13336.
4. L. Gartzia-Rivero, J. Bañuelos-Prieto, V. Martínez-Martínez, I. López-Arbeloa, "Versatile Photoactive Materials Based on Zeolite L Doped with Laser Dyes", *ChemPlusChem*, **2012**, 77, 61-70.

In Chapter 3 and organized as in the thesis:

1. L. Cerdán, L. Gartzia-Rivero, E. Enciso, J. Bañuelos, I. López-Arbeloa, A. Costela, I. García-Moreno, "Focusing on charge-surface interfacial effects to enhance the laser properties of dye-doped nanoparticles", *Laser. Phys. Lett.*, **2014**, 11, 015901-015907.
2. L. Gartzia-Rivero, L. Cerdán, J. Bañuelos, E. Enciso, I. López-Arbeloa, A. Costela, I. García-Moreno, "Förster Resonance Energy Transfer and Laser Efficiency in Colloidal Suspensions of Dye-Doped Nanoparticles: Concentration Effects", *J. Phys. Chem. C*, **2014**, 118, 13107-13117.

3. L. Cerdán, E. Enciso, L. Gartzia-Rivero, J. Bañuelos, I. López-Arbeloa, A. Costela, I. García-Moreno, "A FRET analysis of dye diffusion in core/shell polymer nanoparticles", *RSC Adv.*, **2014**, 4, 22115-22122.

In Chapter 4 and organized as in the thesis:

1. Y. Xiao, D. Zhang, X. Qian, A. Costela, I. García-Moreno, V. Martin, M. E. Perez-Ojeda, J. Bañuelos, L. Gartzia, I. López Arbeloa, "Unprecedented laser action from energy transfer in multichromophoric BODIPY cassettes", *Chem. Commun.*, **2011**, 47, 11513-11515.
2. L. Gartzia-Rivero, H. Yu, J. Bañuelos, I. López-Arbeloa, A. Costela, I. Garcia-Moreno, Y. Xiao, "Photophysical and Laser Properties of Cassettes base don BODIPY and Rhodamine Pair", *Chem. Asian J.*, **2013,** 8, 3133-3141.

Articles not included in the thesis report:

1. V. Martínez-Martínez, C. Corcóstegui, J. Bañuelos Prieto, L. Gartzia, S. Salleres, I. López Arbeloa, "Distribution and orientation of dyes intercalated into single sepiolite fibers. A confocal fluorescence microscopy approach", *J. Mater. Chem.*, **2011**, 21, 269-276.
2. E. M. Sánchez-Carnerero, L. Gartzia-Rivero, F. Moreno, B. L. Maroto, A. R. Agarrabeitia, M. J. Ortiz, J. Bañuelos, I. López-Arbeloa, S. de la Moya, "Spiranic BODIPYs: a ground-breaking design to improve the energy transfer in molecular cassettes", *Chem. Commun.*, **2014**, 50, 12765-12767.